Modelling of nonneutral plasmas trapped by electric and magnetic fields relevant to gyrotron electron guns

Guillaume Michel LE BARS

■ École
polytechnique
fédérale
de Lausanne

2023

All sorts of things can happen
when you're open to new ideas
and playing around with things.
— Stephanie Kwolek

To my wife Eliane.

Abstract

Gyrotrons are a class of high-power vacuum-electronics microwave sources, which are envisioned to play an important role in the domain of magnetically confined fusion plasmas. Indeed, only gyrotrons are capable of producing continuous electromagnetic waves at sufficient power (more than 1 MW) and in the frequency range ($\sim$ 100 GHz) matching to one of the highest frequency collective normal modes of a magnetized plasma: electron cyclotron waves. The use of millimetre waves at the highest normal mode frequency has the added potential to very locally deposit energy and eventually control instabilities of a fusion plasma, as well as heating it.

The impressive advances in the gyrotron R&D in the past decades makes the electron cyclotron heating system be today the reference and most promising auxiliary heating system in a future fusion power plant. Despite this success, the gyrotron complexity is such that some gyrotron components still deserve some R&D. One of the key components is the electron gun, where an annular electron beam is formed and accelerated in a region with externally applied crossed electric and magnetic fields. For some gyrotrons, high-voltage arcing events, as well as significant leaking currents, have been observed in the gun region and are believed to be associated to the formation of trapped secondary electrons clouds, i.e. not belonging to the main electron beam. These arcing events are disruptive and prevent the reliable operation of the device. Despite the very high-vacuum level inside the tube, it is hypothesized that trapped electron clouds are formed by ionization of the residual neutral gas and are locally confined in regions where the combination of the externally applied electric and magnetic field form a Penning-like structure also called a potential well. These clouds are categorized as annular nonneutral plasmas, but are in an exotic parameter regime where limited literature exists. This is due to their high electron density, strong externally driven azimuthal flow, non-negligible electron neutral collisions, strong dependence on the confining electrodes geometries and the fact that they form without a controlled external electron source.

The theoretical study of the formation, evolution and possible equilibrium of these electron clouds in the unexplored parameter range is the main motivation of this work. For this a new 2D (axial-radial) particle-in-cell code, called FENNECS, has been developed which is capable of simulating the real electron gun geometry while keeping structured grids, by using a novel finite element method based on weighted extended b-splines. This method reduces the numerical costs and avoids the cumbersome meshing step, thus facilitating the implementation of new geometries. FENNECS also includes: electron-neutral collisions and secondary electron emissions caused by fast ions colliding with the electrodes, which allows the simulation of the self-consistent formation and dynamics of the clouds in the gun. This code is then verified using manufactured solutions

Abstract

and physical systems with analytical solutions, which leads to the first simulations of trapped electron clouds formation, based on first principles, in gyrotron electron guns.

In a second step, FENNECS is used to study the conditions of cloud formation in a simplified geometry, and guiding the derivation of a 0D analytical fluid model describing the trapped electron clouds quasi steady-state. This allows the derivation of analytical scaling laws for the maximum trapped cloud density and corresponding leaking current, as a function of the applied external parameters, which can produce fast estimates. In addition, this shows that the electrons are lost from the cloud due to a radial drifts imposed by collisional drag forces caused by electron-neutral collisions. Furthermore, FENNECS is successfully validated using experimental measurements obtained with a gyrotron suffering from problematic leaking currents, which allows the first simulation of trapped electron clouds spontaneously forming in a realistic gyrotron gun geometry, and shows that not all potential wells are problematic, thus supporting the relaxation of the "no potential-well" design criteria currently used in gyrotron gun design.

The code is finally used to support the design of a new experiment, called T-REX, which is planned to study experimentally the trapping of electron clouds in conditions similar to the ones present in gyrotron electron guns, with dedicated and more precise diagnostics than what is physically possible in gyrotrons. FENNECS simulations led to the design of three electrode configurations and to the selection of the experimental diagnostics.

Furthermore, the trapped electron clouds are annular and highly susceptible to fast (compared to the cloud build-up time-scales) azimuthal "Kelvin-Helmoltz-like" instabilities, called diocotron instabilities, which cannot be simulated in FENNECS due to its assumed azimuthal symmetry. A finite difference eigenvalue solver is used to study the linear stability of the clouds to diocotron normal modes, assuming an electron cloud of infinite longitudinal extent along an homogeneous magnetic field and using the radial density profiles of clouds obtained from FENNECS simulations. These simulations indicate that this instability will develop in electron clouds trapped in gyrotron electron guns, but that the instability should depend on the externally applied bias. This result opens the door to exploring further this instability in the context of gyrotrons.

Résumé

Les gyrotrons sont une classe de sources micro-ondes électroniques sous vide de haute puissance, qui devraient jouer un rôle important dans le domaine des plasmas de fusion confinés par champ magnétiques. En effet, seuls les gyrotrons sont capables de produire des ondes électromagnétiques continues à une puissance suffisante (plus de 1 MW) et dans la gamme de fréquences ($\sim 100\,\text{GHz}$) correspondant à l'un des modes normaux collectifs de plus haute fréquence d'un plasma magnétisé : les ondes cyclotroniques électroniques. L'utilisation d'ondes millimétriques à la fréquence du mode normal le plus élevé a le potentiel supplémentaire de déposer très localement de l'énergie et éventuellement de contrôler les instabilités d'un plasma de fusion, ainsi que de le chauffer.

Les progrès impressionnants de R&D sur les gyrotrons au cours des dernières décennies font que le système de chauffage électron-cyclotron est considéré aujourd'hui comme le système de chauffage auxiliaire de référence et le plus prometteur dans une future centrale à fusion. Malgré ce succès, la complexité du gyrotron est telle que certains de ses composants peuvent bénéficier de plus de R&D. L'un des composants clés est le canon à électrons, où un faisceau annulaire d'électrons est formé et accéléré dans une région où des champs électriques et magnétiques croisés sont imposés de manière externe. Pour certains gyrotrons, des arcs électriques à haute tension, ainsi que des courants de fuite importants, ont été observés dans la région du canon et ont été associés à la formation de nuages d'électrons secondaires piégés qui n'appartiennent pas au faisceau d'électrons principal. Ces arcs électriques sont perturbateurs et empêchent le fonctionnement fiable de l'appareil. Malgré le niveau de vide très élevé à l'intérieur du tube, il est supposé que les nuages d'électrons piégés sont formés par l'ionisation du gaz neutre résiduel, et sont localement confinés dans des régions où la combinaison du champ électrique et du champ magnétique externe forme une structure de type Penning aussi appelée puit de potentiel. Ces nuages sont classés dans la catégorie des plasmas annulaires non neutres, mais se trouvent dans un régime de paramètres exotiques pour lequel la littérature est limitée. Cela est dû à leur forte densité d'électrons, à l'importance du flux azimutal induit par les champs externes, aux collisions non négligeables entre électrons et neutres, aux effets importants de la géométrie des électrodes de confinement et au fait que les nuages se forment en l'absence d'une source contrôlée d'électrons.

L'étude théorique de la formation, de l'évolution et de l'équilibre éventuel de ces nuages d'électrons dans la gamme de paramètres inexplorée est la principale motivation de ce travail. Pour ce faire, un nouveau code 2D (axial-radial) de type "particle-in-cell", appelé FENNECS, a été développé. Il est capable de simuler la géométrie réelle du canon à électrons tout en conservant des grilles structurées pour résoudre l'équation de Poisson en utilisant une nouvelle méthode d'éléments finis basée sur des b-splines étendues et pondérées. Cette méthode réduit le coût numérique et évite l'étape fastidieuse du maillage, facilitant ainsi la mise en oeuvre de nouvelles géométries. FENNECS inclut également : les collisions électron-neutre et les émissions d'électrons secondaires causées par la collision d'ions rapides sur les électrodes, ce qui permet la simulation de la formation et la dynamique autoconsistantes des nuages dans le canon. Ce code est ensuite vérifié à l'aide de solutions fabriquées et de systèmes physiques ayant des solutions analytiques. Ceci conduit à la première simulation, basée sur des principes premiers, de nuages d'électrons piégés dans un canon à électron.

Résumé

Dans un deuxième temps, FENNECS est utilisé pour étudier les conditions de formation des nuages, dans une géométrie simplifiée, et pour dériver un modèle fluide analytique 0D décrivant les nuages d'électrons piégés en quasi équilibre. Cela permet de dériver des lois d'échelle analytiques pour la densité maximale du nuage piégé et le courant généré, en fonction de paramètres expérimentaux imposés. FENNECS est également validé à l'aide de mesures expérimentales obtenues avec un gyrotron souffrant de problèmes de courant indésirables à haute tension. Ces simulations constituent la première simulation de formation cohérente de nuages d'électrons piégés dans une géométrie réaliste de canon à électrons de gyrotron, et montrent que tous les puits de potentiel ne sont pas problématiques, ce qui permet d'assouplir les critères de conception des futurs canons à électrons de gyrotron.

Le code est finalement utilisé pour soutenir la conception d'une nouvelle expérience, appelée T-REX, conçue pour étudier expérimentalement le piégeage des nuages d'électrons dans des conditions similaires à celles présentes dans les canons à électrons de gyrotrons, avec des diagnostics dédiés, plus précis que ce qui est physiquement possible dans les gyrotrons. Des simulations par FENNECS ont conduit au choix des diagnostiques expérimentaux et au choix de trois géométries pour les électrodes.

De plus, du fait que les nuages d'électrons piégés sont annulaires et donc très sensibles aux instabilités azimutales rapides (par rapport aux échelles de temps de formation des nuages), de type Kelvin-Helmholtz, appelées instabilités diocotron. Celles-ci ne peuvent pas être simulées dans FENNECS en raison de la symétrie azimutale imposée dans le code. Un solveur aux valeurs propres basé sur les différences finies est utilisé pour étudier la stabilité linéaire des nuages aux modes normaux diocotron, en supposant un nuage d'électrons d'extension longitudinale infinie le long d'un champ magnétique homogène et en utilisant les profils de densité radiale des nuages d'équilibre, obtenus à partir de simulations FENNECS. Ces simulations indiquent que l'instabilité diocotron se développera dans les nuages d'électrons piégés dans les canons à électrons du gyrotron, mais que cette instabilité devrait dépendre du biais externe. Ce résultat ouvre la porte vers une exploration plus approfondie de cette instabilité dans le contexte des gyrotrons.

Mots-clés— Gyrotron, Plasmas non-neutres, Particle-in-cell, Méthode d'éléments finis, Confinement, Diocotron.

Contents

Contents

1 Introduction

1.1 Magnetically confined fusion research

With the rise in world population and the industrialization of developing countries, the need for abundant and clean energy has become a worldwide problem. This is particularly relevant as our current main energy source, fossil fuels, has both catastrophic effects on the earth climate and a limited availability, and the current alternatives each present their own challenges. In the group of renewable energies, wind and solar electricity production is inherently intermittent and necessitates the development and construction of costly storage solutions, while hydroelectric production is reaching its maximum power in western countries and geothermal energy poses some geological risks. The nuclear fission reactors remain the best available technological solution to the energy crisis thus far. However, they pose the problem of long-term storage of the nuclear waste, and can affect a wide area and a large population in case of a major nuclear accident. To address these challenges, a potential clean, safe, and reliable energy source is the nuclear fusion reaction, which is also the energy source of the Sun.

The fusion reaction is done by combining two light elements in order to form one heavier element and release energy in the process. During this process, the mass of the fusion products is lower than its reactants, causing the release of large amounts of energy (several MeV per reaction) in the form of kinetic energy of its products. In the case of nuclear fusion for energy production, the reactants are a deuterium and a tritium atom, two isotopes of hydrogen, and the products are a helium atom and a neutron,

$$D + T \rightarrow He + n + (17.6 \text{ MeV}). \tag{1.1}$$

This is the reaction envisaged for a fusion power plant because it maximizes the fusion cross-section (see Figure 1.1) which maximizes the reachable reaction rate. For this reaction to occur, the two light elements must possess a sufficient kinetic energy to overcome the strong Coulomb repulsion that exists between the two positively charged nuclei. For the matter to have average kinetic energies maximizing the fusion collision cross-sections (of the order of 10 keV), the temperature of the D-T fuel must reach approximately 100 million degrees Kelvin. At these temperatures the matter is fully ionized and is in the plasma state.

On Earth, reaching these high temperatures is challenging and necessitates a confinement of the plasma to keep it isolated from its environment. In addition, to reach a net positive fusion power balance, the plasma needs to be confined with a sufficient temperature, density, and energy confinement time defined by the Lawson criterion [1]. The energy confinement time is the characteristic time over which the energy of the
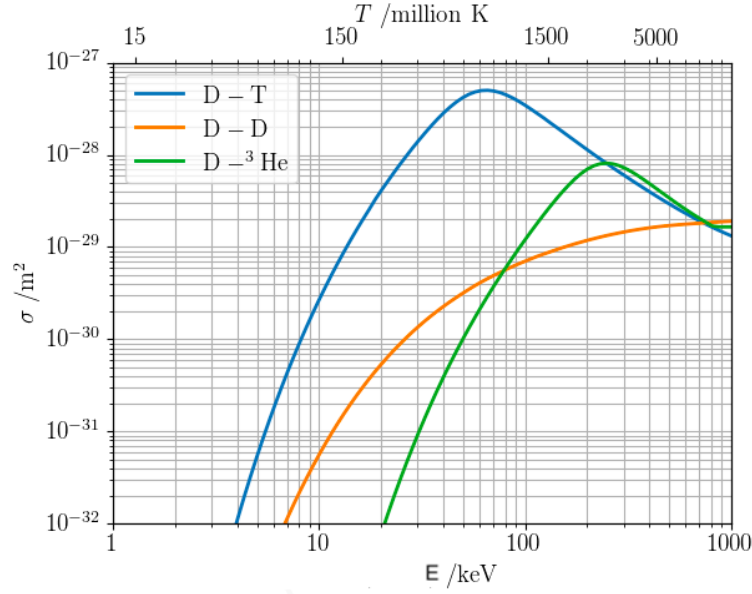
Figure 1.1: Fusion cross-section as a function of the ion temperature for a thermalized plasma.

plasma is lost. One of the most promising confinement schemes is based on magnetic confinement, in which the plasma's charged particles are confined by closed helically wound magnetic field lines forming a toroidal magnetic cage. The current two main solutions to generate such magnetic configurations are the tokamak and the stellarator. In a tokamak, as represented in Figure 1.2, the toroidal magnetic field is generated using external coils and the main poloidal magnetic field is self-generated by the toroidal plasma current. Here, the terms poloidal and toroidal directions refer to the short and long paths around the torus respectively (see Figure 1.2). External poloidal field coils can also be used to modify the poloidal magnetic field, thus allowing the shaping and control of the plasma cross-section and of the magnetic field lines. This configuration is used for example at EPFL in the Tokamak à Configuration Variable (TCV) experiment [2] and will be used for the future International Thermonuclear Experimental Reactor (ITER) [3]. In a stellarator, the magnetic field is fully generated using external coils. This has some interesting stability properties for the plasma, as no toroidal plasma current is necessary. However, the complex shape of the coils needed to produce the external magnetic field is challenging from an engineering perspective. This configuration is currently used in the Wendelstein 7-X experiment [4]. Both the TCV and Wendelstein 7-X configurations are shown in Figure 1.3.

To reach the high temperatures necessary for a net fusion power, Ohmic heating, which heats the plasma by inducing a current in the torus and using the plasma resistivity to transform electric energy into heat, is not sufficient in tokamaks. This is due to the fact that the plasma resistivity decreases with its temperature. Similarly, this technique is not desired in stellarators as the presence of a plasma current can lead to the same problematic instabilities present in tokamaks and defeats the purpose of using a stellarator. To alleviate this problem, several methods have been devised such as Neutral Beam Heating (NBH), Ion Cyclotron Resonance Heating (ICRH), Lower Hybrid and Electron Cyclotron Resonance Heating (ECRH) [3, 6–8]. The ECRH uses high power microwaves to heat the electrons in the plasma and, because of its wave frequency range, has the advantage of allowing the use of wave-guides to transport the wave from the source to the tokamak or the stellarator, therefore reducing the physical footprint of the heating device close to the machine [9]. To heat the electrons, a high power microwave is launched into the plasma with a frequency
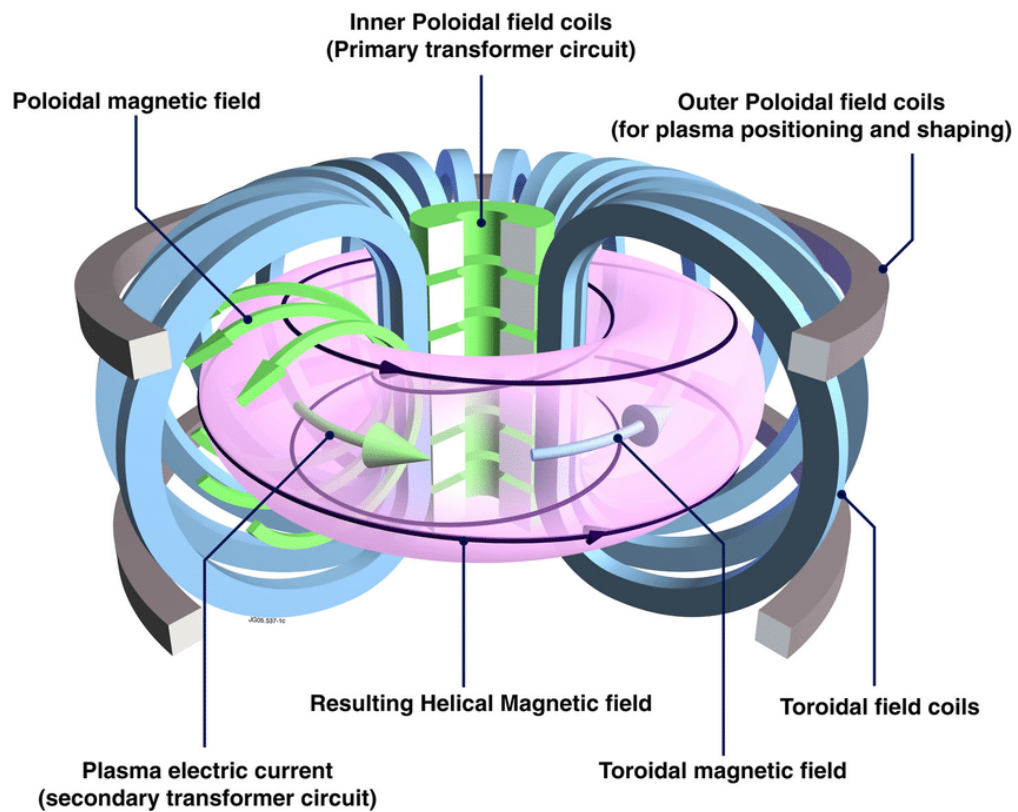
Figure 1.2: Schematic of a tokamak representing the generation of the confining magnetic fields [5].
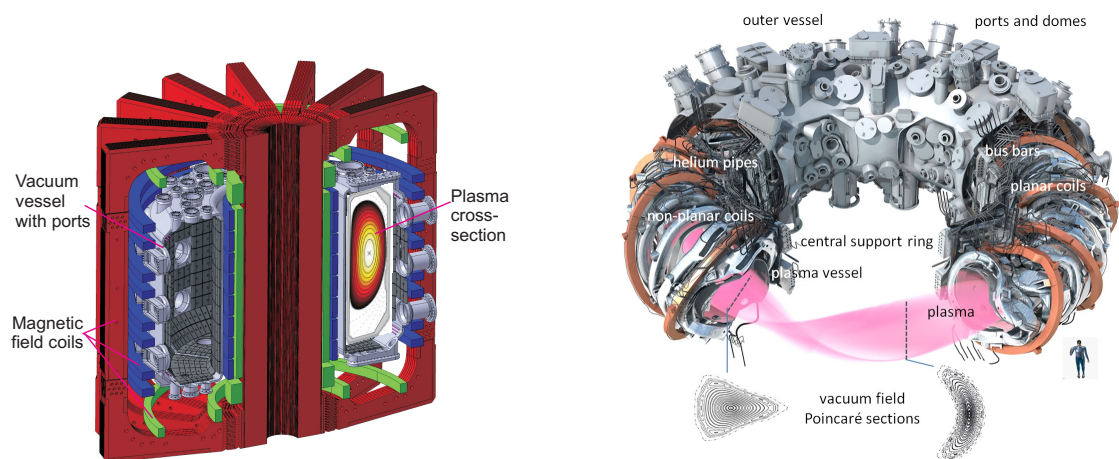
Figure 1.3: Left: Schematic of the TCV tokamak with an example plasma profile (courtesy of Matthieu Toussaint). Right: Schematic of the Wendelstein 7-X stellarator [4].
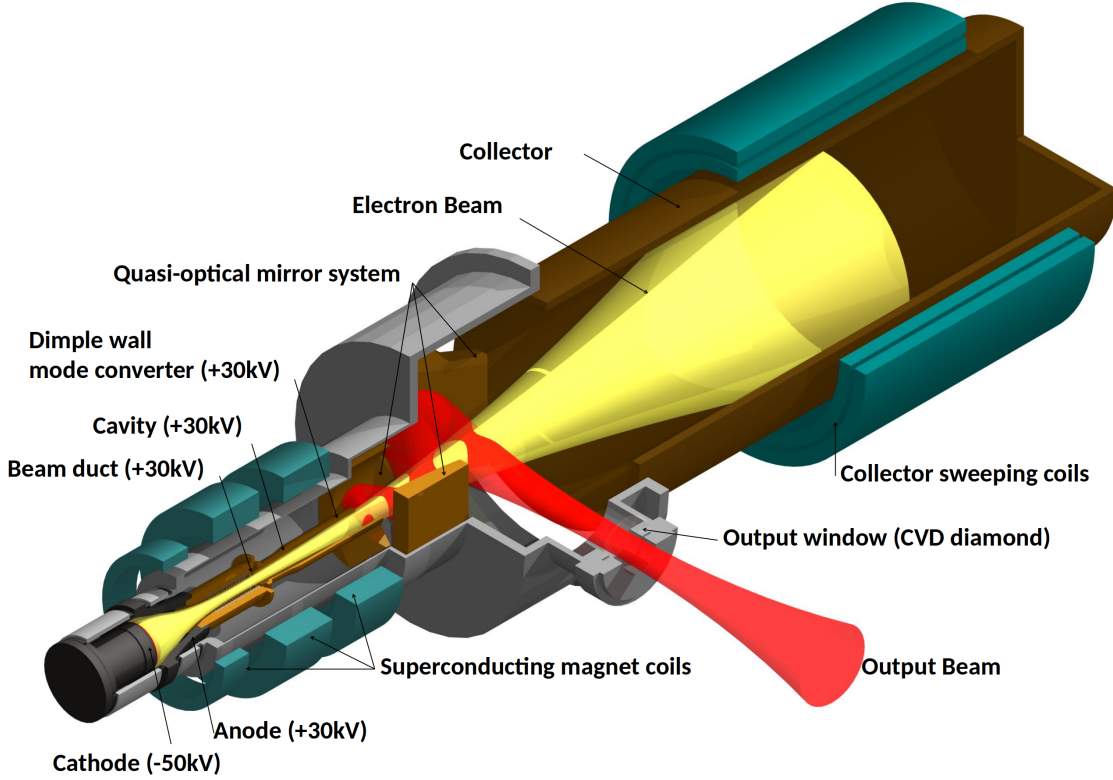
Figure 1.4: Schematic of a gyrotron oscillator with its main components. The electron beam is represented in yellow and the wave is shown in red. Courtesy of Jean-Philippe Hogge.

equal to the local electron cyclotron frequency $\Omega_{ce} = eB/m_e$, or one of its harmonics, of the region of plasma that needs to be heated. Here e is the electron charge, B is the local magnetic field amplitude and m_e is the electron mass. This energy transfer from the wave to the plasma will only happen at the position where the wave frequency ω_{rf} is equal to a harmonic of Ω_{ce}, which allows for localized heating or current drive of the plasma and can be used to control or suppress problematic plasma instabilities [6, 10]. However, depending on the mode of injection of the electromagnetic wave (X or O-mode [11]), the magnetic field amplitude or the plasma density along the path of the wave, a cut-off region can be reached where the wave is reflected [6, 11]. This can be very problematic as the plasma is then not heated and the rf power can be dissipated on parts of the tokamak vacuum-vessel that are not designed to withstand such a load. However, wave frequencies that are above the cut-off frequencies can reach the interaction region. This motivates the use of microwaves at harmonics of Ω_{ce}. Only one type of coherent rf source is currently capable of reaching the frequency (in excess of 100 GHz) at MW-level in continuous mode needed for fusion applications. This device is called a gyrotron and is the main motivation for the studies presented in this thesis [12–15].

1.2   The gyrotron oscillator

Gyrotrons are a class of coherent electromagnetic wave sources operating at frequencies in the range of a few GHz to THz and at power between 0.1 and 2 MW [12, 13]. They can operate both in pulsed modes or in continuous wave (CW) with overall power efficiencies between 30% and 50%. These devices are
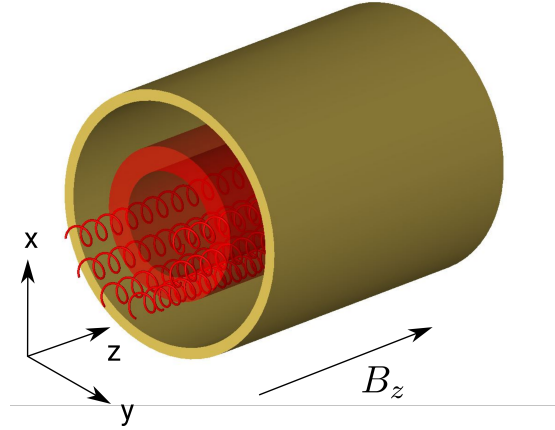
Figure 1.5: Schematic of a cylindrical gyrotron cavity with the annular electron beam in red traversing the cavity axially. The spirals show the Larmor motion of the electrons. The electron Larmor radius is increased for readability, but it is usually two orders of magnitude smaller than the cavity radius (see Figure 1.7).

part of the vacuum-electronics microwave sources and exploit the electron cyclotron maser instability (ECMI) [16] to excite the wave. An example of such a device is represented in Figure 1.4.

This instability can appear when a strongly magnetized and weakly relativistic annular electron beam passes through a cylindrical cavity (see Figure 1.5) and interacts with the electromagnetic modes supported by the cavity. Due to thermal noise, all these modes are present in the cavity at extremely low intensities and can serve as a seed for the ECMI. Depending on the relative phase between the electron cyclotron motion and the wave, electrons are either accelerated or decelerated by the wave. Due to their weakly relativistic energy, this will in turn change their respective relativistic cylcotron frequency Ω_{ce}/γ causing the accelerated electrons to rotate slower as γ increases and the decelerated electrons to rotate faster as γ decreases. Here, $\gamma = 1/\sqrt{1 - v^2/c^2}$ is the Lorentz relativistic factor of the electron, with v the electron velocity and c the speed of light in vacuum. Due to this interaction, most of the electrons will obtain a similar gyrophase, which is the azimuthal phase of their cyclotron motion, in what is called a phase bunching [16]. As seen in Figure 1.6, this process will generate electron bunches on the Larmor circle, and these bunches will rotate at a frequency close to the cyclotron frequency of the electrons.

Once a bunch is formed, collective interactions and effective energy exchange can develop between the beam and the wave, depending on the relative phase between them. Three cases can be distinguished. First, if the bunch is exactly in phase with the wave, no net energy transfer happen between the wave and the beam as half of the electrons are accelerated, and the other half is decelerated. As with individual electrons, if the bunch phase is greater than the wave phase, the bunch remains in the accelerated region and a net energy is transferred from the wave to the beam. This configuration happens when the frequency of the wave ω_{rf} is slightly smaller than the cyclotron frequency or its harmonics. Inversely, if the bunch phase is smaller than the wave phase, the bunch remains in the decelerated region and statistically more electrons are decelerated, leading to a net energy transfer from the beam to the wave. This configuration happens when the frequency of the wave ω_{rf} is slightly larger than the cyclotron frequency or its harmonics, and is the basis of electromagnetic wave excitation in gyrotron cavities. For this instability to occur, the angular
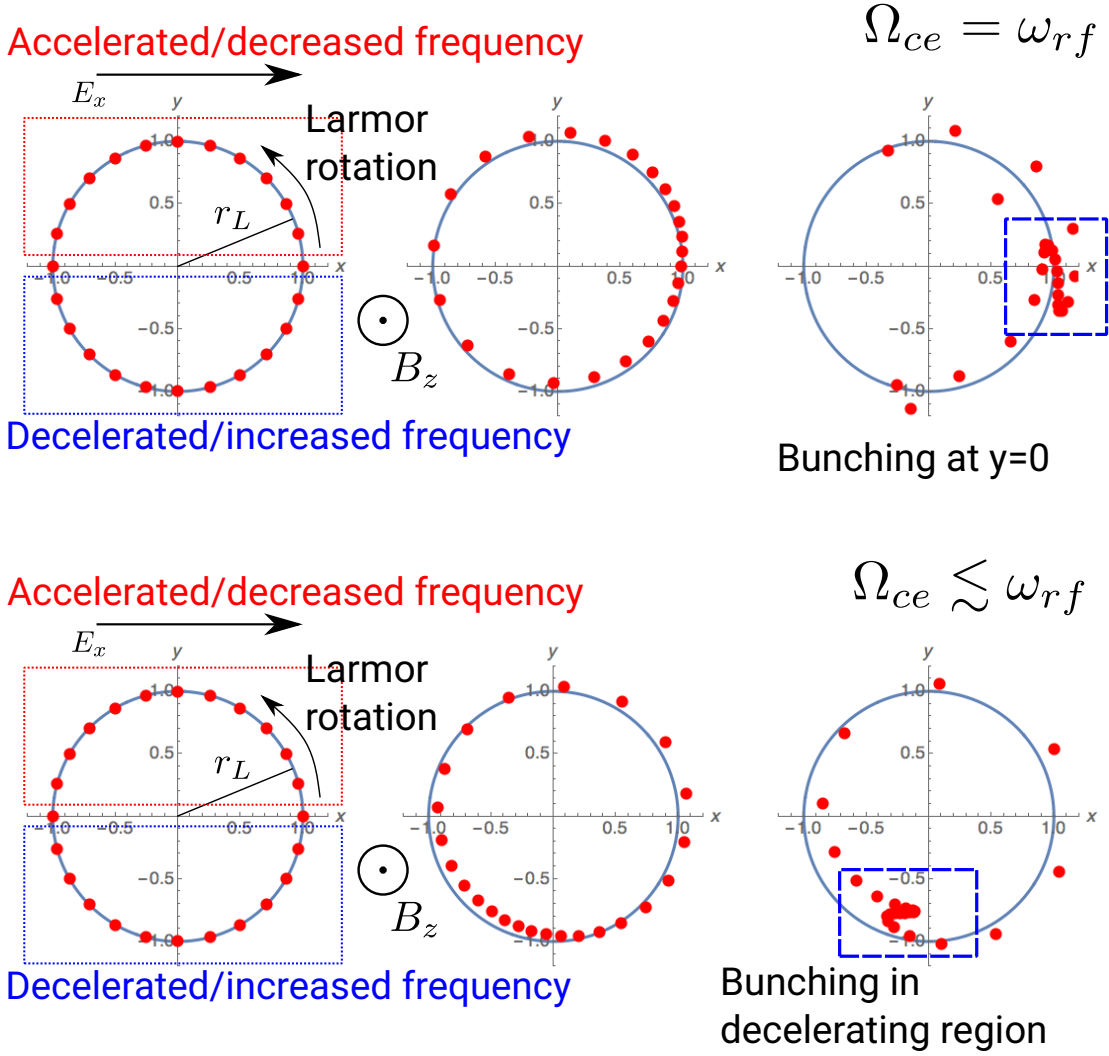
Figure 1.6: Process of bunching of the electrons (red dots) due to the ECMI viewed at three moments in time, in the reference frame of the electric field rotating at the frequency ω_{rf}. In this frame the electric field is always in the x direction. The blue circle highlights the initial Larmor trajectory with radius r_L. Top: The electrons are initially rotating at their cyclotron frequency $\Omega_{ce} = \omega_{rf}$ with uniform distribution in the gyrophase and form a bunch at $y = 0$. No net energy transfer is achieved. Bottom: The electrons are initially rotating at their cyclotron frequency $\Omega_{ce} \lesssim \omega_{rf}$ with uniform distribution in the gyrophase and form a bunch in the decelerating region. A net energy transfer is achieved from the beam to the wave.
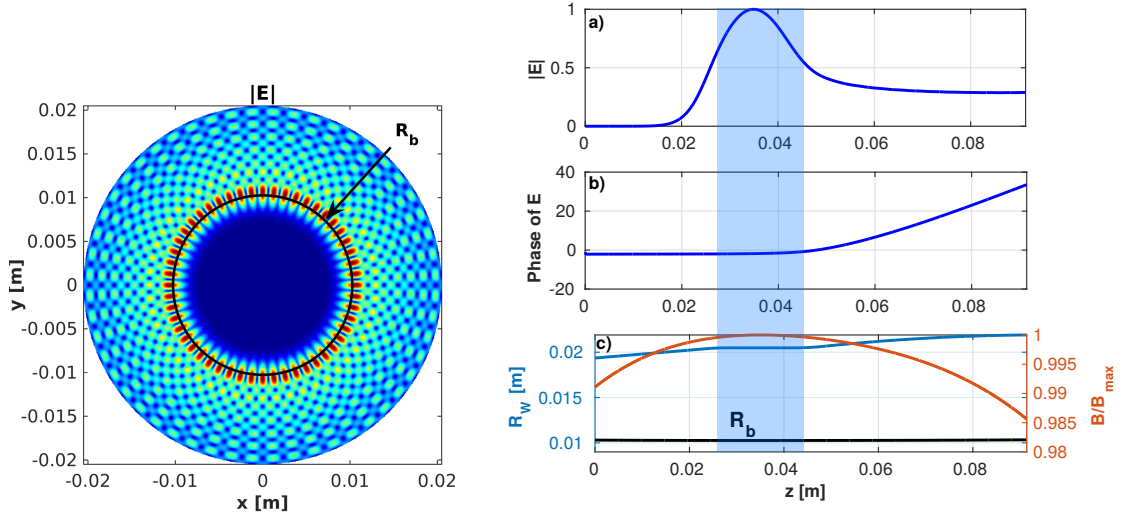
Figure 1.7: Left: Amplitude of the electric field profile of the $TE_{27,6,1}$ nominal mode of the dual-frequency gyrotron operated at TCV [17]. The black circle highlights the position of the annular electron beam, of radius R_b, used to excite this mode. Right: a) b) Amplitude and phase of the electric field profile of the TCV dual-frequency gyrotron nominal mode at 128GHz obtained with the spectral code TWANGlinspec [18]. c) Wall radius (blue), beam radius (black) and normalized magnetic field amplitude (red) in the region around the cavity. The blue shaded region highlights the axial extent of the cavity. Plots courtesy of Jérémy Genoud

frequency of the wave ω_{rf} must match the relativistic cyclotron frequency of the beam Ω_{ce}/γ with

$$\omega_{rf} \approx \frac{\Omega_{ce}}{\gamma}. \tag{1.2}$$

In a gyrotron, the electric field of the wave is purely perpendicular to the cavity axis ($E_z = 0$), which is called a Transverse Electric (TE) mode. The TE modes are designated by their $TE_{m,p,q}$ number where m is the azimuthal mode number, p is the radial wave number and q is the longitudinal wave number. An example of a $TE_{26,7,1}$ mode, used for the dual-frequency gyrotron of TCV [17], is represented in Figure 1.7.

1.2.1 The gyrotron components

To create the right conditions for the ECMI to develop and to transfer enough power to the wave, the gyrotron needs several components presented in the sketch of Figure 1.8, and in more details in Figures 1.4 and 1.9.

Starting from the bottom, there is first a Magnetron Injection Gun (MIG), which produces an annular electron beam of typically 3 MW at 40 A, $75 - 80$ kV accelerating bias, and which will be the main focus of this thesis. It is composed of an annular cathode (emitter ring), biased negatively, generating electrons through thermionic emissions, and one or two accelerating electrodes set at higher potentials to impose an accelerating radial and axial electric field. The two electrodes configuration is called a diode gun, and the three electrodes configuration is a triode. An example of a triode configuration is represented in
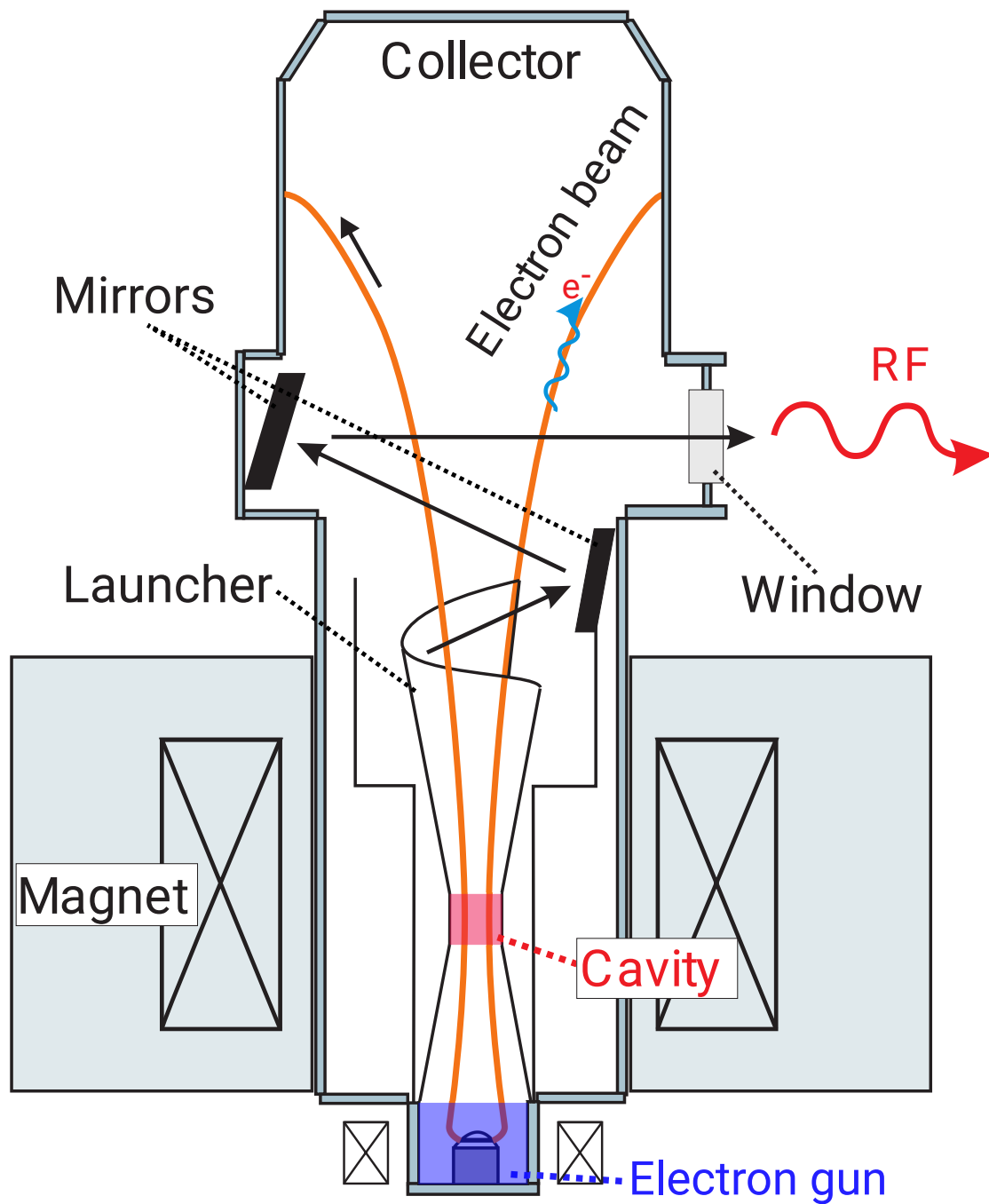
Figure 1.8: Simplified schematic of a gyrotron oscillator. The electron beam is indicated with orange lines and the rf wave trajectory is indicated with black arrows. The beam-wave interaction happens in the cavity represented in red. The electron gun region, which is the part of interest for this thesis, is delimited in blue.

Figure 1.9, and, using the design of this figure, a diode configuration would have the same potential for the body and the anode (see Figure 1.4). The electrode geometries and the amplitude of the applied voltages characterize the beam energy γ and the pitch-angle $\alpha = v_\perp/v_\parallel$, which is the ratio of the electrons' velocity perpendicular and parallel to the magnetic field. The pitch-angle needs to be maximized to increase the energy transfer to the wave, as only the perpendicular kinetic energy is available for the interaction, but needs to remain sufficiently low to prevent reflection of electrons towards the gun due to magnetic mirror effects (see Figure 1.9). The advantage of the triode gun is that changing individually the applied voltages on the anode, cathode, and body allows the separate control of α and γ, while in the diode gun these two quantities are co-dependent and modified simultaneously by a change of applied potentials.

After generation, the electron beam is accelerated by the electrodes along the magnetic field lines, generated by a set of superconducting coils, from a region of low magnetic field (~ 0.2 T), close to the gun, to a region of high magnetic field ($3 - 7$ T) in the cavity (see Figure 1.9). This increase of magnetic field amplitude will cause a compression of the beam, and a conversion of the electrons' kinetic energy from parallel to perpendicular, due to the conservation of magnetic moment of the electrons.

In the cavity, the beam-wave interaction takes place, inducing a large transfer of beam perpendicular kinetic energy to the wave. By properties of the TE modes, the amplitude of the electric field is non-uniform and, in the transverse plane, a localized ring exists where the electric field envelope is maximum (see Figure 1.7). To maximize the beam-wave interaction, the annular electron beam must be radially located on this same region of high electric field amplitude. Since the magnetic field in the cavity is imposed by the excited wave frequency and the electrons' γ, and the electrons follow the magnetic field lines from the cathode to the cavity, the beam radius can only be controlled by the annular cathode radius and the magnetic field amplitude at the cathode which imposes constraints on the gun design.

After interaction with the wave, the beam follows the magnetic field lines and is collected at the top of the gyrotron in what is called a collector. The excited wave leaving the cavity is first converted from the TE mode of the cavity to a quasi Gaussian mode by a mode converter called the "launcher". This wave is then reflected by a set of mirrors and exits through a diamond window, where it can be guided by wave-guides or mirrors toward the target.

1.3 The problem of trapped electrons in gyrotron electron guns

Gyrotrons are technically challenging because they combine several advanced domains of engineering, which are high-power rf devices, ultra-high vacuum, mm-wave propagation, supra-conducting magnets, continuous operation, low-temperature, high-temperature and extreme heat deposition density. Each of these topics bring their own complexity and need to cohabit to allow the production of one gyrotron. Most of the gyrotron components presented in this section necessitated long development and still need R&D. In this thesis, we will focus on one component: the electron gun, which produces the main electron beam of the gyrotron, and is represented at the bottom of Figure 1.8.

In some gyrotron electron guns, problematic currents (i.e. not associated to the main electron beam) have been measured between the cathode and anode of the MIG. At large amplitudes, these currents have caused damage to the electrodes or other parts of the gun [19]. Even at low amplitudes, these currents need to be sustained by a polarizing power supply (PS), either anode or body PS, that is generating the accelerating electric field for the main beam, and which is distinct from the Main High Voltage Power Supply (MHVPS) that produces the main electron beam (see Figure 1.9). Typically, exceeding a critical current as low as a
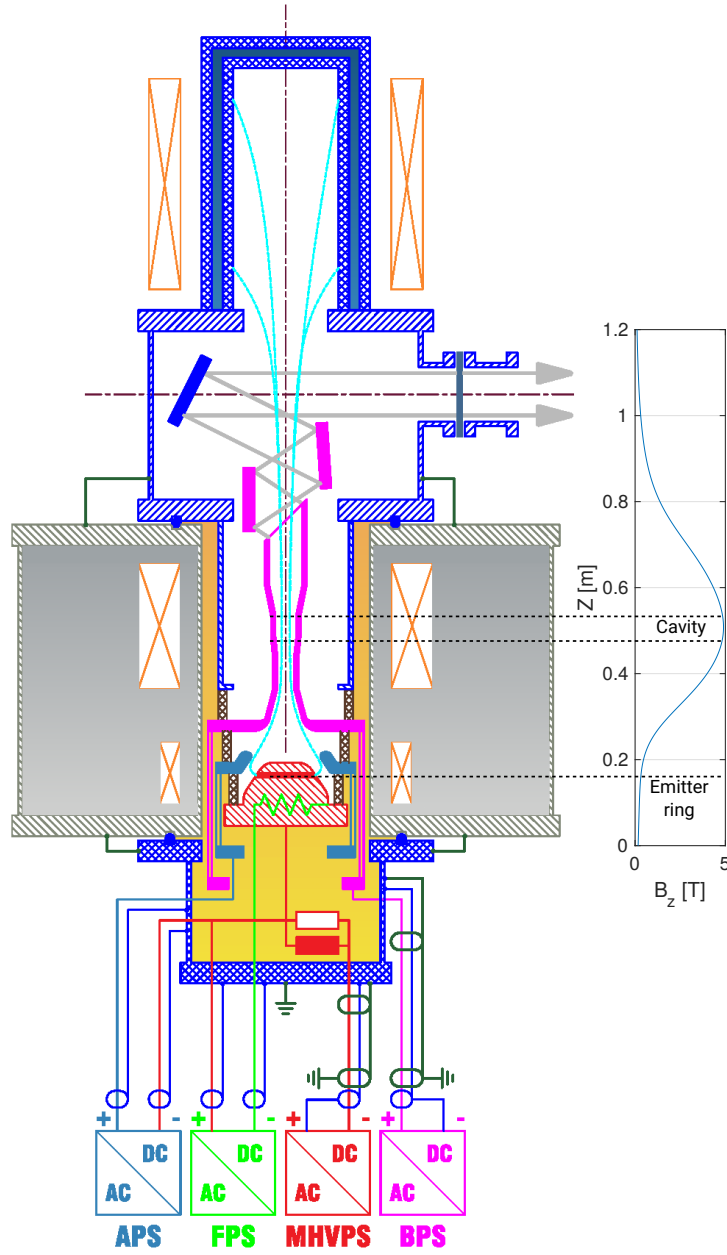
Figure 1.9: Electrical schematic of the TH1510 bi-frequency gyrotron used at TCV with the 4 individual power supplies powering the gyrotron. This gyrotron uses a triode configuration. APS (light blue) is the anode power supply, which biases the anode w.r.t. the cathode potential. FPS (green) is the filament power supply, which heats the emitter ring to permit thermionic emission. MHVPS (red) is the main high voltage power supply, which imposes the negative cathode potential w.r.t. ground and provides the beam current. BPS (pink) is the body power supply, which imposes the body positive potential w.r.t. ground. The casing of the gyrotron, vacuum vessel, and the collector (dark blue) are set to ground. In addition, the amplitude of the axial magnetic field B_z on the symmetry axis is represented on the right. Schematic courtesy of Ugo Siravo.

Figure 1.10: Schematic of the electron gun used in the first prototype of the European 170GHz 2MW coaxial gyrotron developed for ITER [23, 24]. This geometry was subject to both potential well and magnetic mirror trapping in different regions of the gun. The gray parts denote an electrode and orange denotes an insulator. The yellow surface highlights the emitter ring, where the main electron beam is produced. The dashed lines show the magnetic field lines and the green arrows show the electric field direction. The red boxes highlight the regions of trapping.

few tens of mA will cause the polarizing PS to switch itself off to protect its internal components, and, therefore, prevent the gyrotron operation [20]. In addition, these currents combined with the high biases imposed between the electrodes (∼ 100 kV) cause an important localized power deposition on the electrode surface, which could cause outgassing in the vacuum vessel and hamper the tube functioning.

These detrimental currents have been linked to the trapping of electrons not belonging to the main electron beam, in the electron gun region, either by electrostatic potential wells (described in more detail in section 1.3.1) or by magnetic mirror traps generated by the strong axial variation of magnetic field amplitude [21]. An example of a MIG suffering from both types of trapping is shown in Figure 1.10 as an illustration. This example considers a diode coaxial gun, but both types of trapping also occur in conventional diode and triode guns. First, an initial population forms in the trapping region, either by ionization of the vacuum vessel background gas by background radiation, or by electrons generated by field-emission [22] on the electrode surfaces. This initial trapped population will then gain, by the effect of the externally applied electric field, sufficient kinetic energy to ionize the residual neutral gas (RNG) present in the vacuum vessel. This can lead to the build-up of a cloud with significant space-charge that can modify the local electric field. This can both perturb the energy and pitch-angle properties of the main electron beam, and modify the trapping potential of the cloud, leading to the constant release of electrons generated by the trapped population, and to the collection of an electronic current on parts of the gyrotron.

1.3.1 Potential well trapping

Potential wells can be formed in MIG guns by the combination of externally applied electric and magnetic fields, and have some analogy to the ones used in Penning traps [25]. As can be seen in Figure 1.11, this kind of trapping can happen if a magnetic field line crosses the same electric equipotential line twice. In this case, the projection of the electric field on the magnetic field line changes sign between the two cross-points and a potential well is formed that can trap either positively or negatively charged particles depending on the electric field direction. In the example of Figure 1.11, negatively charged particles would remain trapped, while positively charged particles would be repelled. As a result, such a potential well
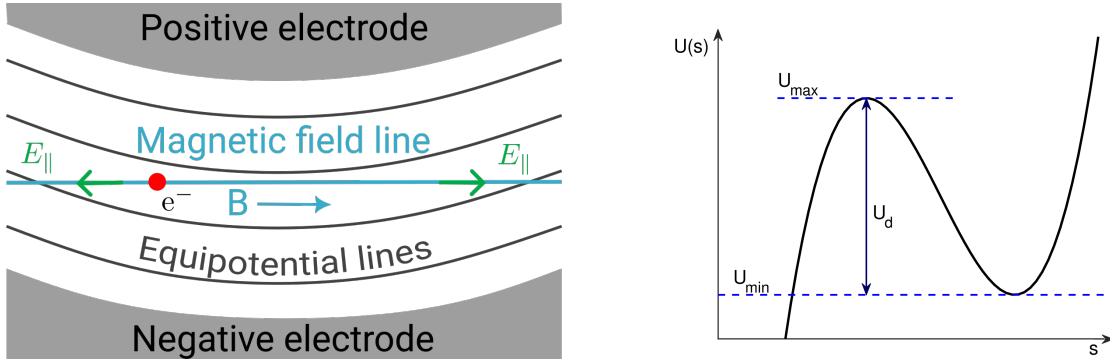
Figure 1.11: Left: Schematic of the trapping mechanism in potential wells. In this case, a magnetized electron is moving along the blue magnetic field line and is subjected to a trapping non-uniform electric field. Right: Example of electric potential as seen by a particle travelling along a magnetic field line. The maximum potential well depth U_d is defined for a specific magnetic field line as the difference between the local maxima of electric potential energy U_{max} and the highest local minimum U_{min} along the magnetic field line coordinate s.

could lead to the formation of a nonneutral plasma.

In negative charge trapping potential wells, the well depth $U_{well}(s)$, at the magnetic field line coordinate s, is defined on each field line by computing the difference between the normalized local electric potential energy in electronvolts, $U(s) = e\phi(s)$, and the highest reachable minimum on each side along the same magnetic field line coordinate $U_{min} = min(U(s))$ [21, 26]. Here ϕ is the electric potential, and reachable is understood in the sense that the magnetic field line is not intersecting a wall, and a particle travelling along the field line would therefore not be captured. This definition translates mathematically to

$$U_{well}(s) = U(s) - U_{min}. \tag{1.3}$$

The maximum depth is $U_d = U_{max} - U_{min}$ as represented in Figure 1.11. This definition reverses the maximum and minimum for positive charge potential wells. However, as this work focuses on electron cloud trapping, potential wells will only be defined for negatively charged particles trapping, and a potential well will be present if the value of the electric potential along a magnetic field line presents a local maximum. We remark that the values of U_d, for a given magnetic field configuration, result from a combination of the externally imposed electric field as well as that generated by the space-charge. Furthermore, the equilibrium charge density depends on the potential well properties. The equilibrium potential well can therefore only be known by solving a complex non-linear set of equations. However, in vacuum the potential well depends only on the magnetic field topology and on the electrodes geometries. This allows for a given magnetic field configuration to define a normalized potential well depth depending on the applied bias. An example of a potential well is given in Figure 1.12 for the geometry of Figure 1.10 using the nominal magnetic field of this gyrotron. In this configuration, a deep potential well is formed with a maximum depth $U_d = 30$ keV for an applied bias between the cathode and the anode of $\Delta\phi = 90$ kV. In gyrotron guns, the potential wells typically occupy volumes of the order of hundreds of cm^3 with depths ranging from 1 keV to tens of keV.
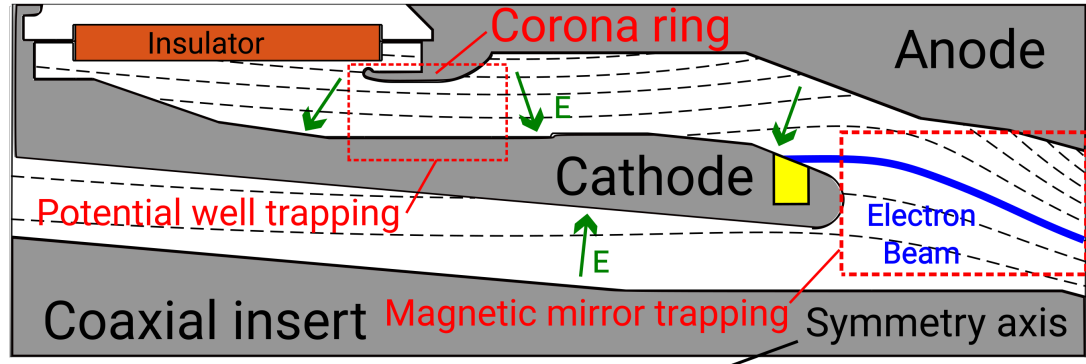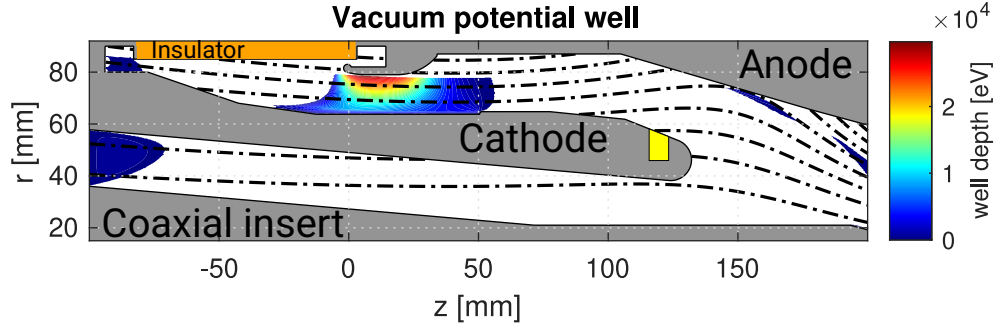
Figure 1.12: Potential well in vacuum for the geometry of the electron gun used in the first prototype of the European 170 GHz 2 MW coaxial gyrotron developed for ITER [23, 24] at the nominal magnetic field configuration (see Figure 1.10). The Cathode is set at a potential $\phi_{cathode} = -90\,\text{kV}$ and the other electrodes are set at ground. A potential well of depth $U_d = 30\,\text{keV}$ is formed. The black dashed-dotted lines represent the magnetic field lines, and the yellow surface highlights the emitter ring, where the main electron beam is produced.

1.3.2 Magnetic mirror trapping

Depending on the electrons' initial pitch-angle and on the ratio of magnetic field amplitude between the gun and the cavity, some electrons can be reflected towards the gun by the effect of magnetic mirror before entering the cavity. These reflected electrons will become confined by the electric potential close to the gun and the magnetic mirror in the direction of the cavity [27, 28]. This trapping mechanism is due to the combined conservation of the adiabatic invariant $\mu = \gamma m_e v_\perp^2 / 2B$ and the electron kinetic energy, causing the increase of $v_\perp$ and the decrease of $v_\parallel$ for an increasing magnetic field amplitude [29]. For this reason, this kind of trapping is also called adiabatic trapping.

In this type of trapping, electrons can escape due to a change of pitch-angle not induced by magnetic effects. This can be induced for example by electron-neutral collisions, or by axial acceleration caused by the space-charge generated electric field. If the losses are towards the cavity, the secondary electrons are simply collected in the collector with a limited effect. However, electrons can also be released towards the cathode and hit the electrode surface with energies up to the order of a few keV and free secondary electrons at the impact point [27]. The release of secondary electrons is usually not on the emitter ring surface and the energy and pitch-angle parameters of these secondary electrons is typically compatible with magnetic trapping, leading to an increase of the number of trapped electrons. The accumulation of trapped electrons modifies the local electric field close to the emitter ring, which perturbs the properties of the main electron beam (pitch angle and beam current), and can reduce the interaction efficiency in the cavity [21].

1.3.3 Current solutions

To avoid the formation of electron clouds in potential wells, the current solution is to avoid the formation of any potential well at the nominal electric and magnetic field configuration of the gyrotron. This is done by carefully adapting the electrode geometry of the gun [20, 21, 30]. However, this process is challenging from an engineering point of view as local changes, as small as a few millimetres, in the geometry or magnetic field topology can create deep potential wells with a depth of the order of several keV [30]. This

sensitivity to small geometric changes is illustrated in chapter 4. In addition, this criterion comes last in the design requirements of the gun, as the conditions of electric and magnetic field amplitude and direction in the gun must first be set to ensure the correct beam parameters at the entrance of the cavity.

Concerning the magnetic mirror trapping, the secondary electron emission on the cathode can be mitigated using materials with lower electronic yield around the emitter ring. In addition, the cathode geometry can be adapted to favour a normal incidence of the reflected electrons on the cathode surface, thus reducing the secondary electron yield. In some cases, the anode geometry has also been modified, with limited success [31], to capture the reflected electrons in what is called a Halo shield [21], thus preventing the build-up of the electron cloud.

1.3.4   Open questions

Experimental results in MIGs have shown that in some cases a deep potential well (several keV) could be present while no problematic currents were measured [30]. These results highlight the lack of understanding in electron cloud formation in gyrotron electron guns. The physical process of formation of these nonneutral plasmas is not yet well understood, no satisfactory model exists to predict the cloud density and the resulting current, and the oscillatory behaviour of the collected currents remains to be explained. While the existing knowledge on nonneutral plasmas is broad [32], in particular at low temperature and low densities, there remain unexplored nonneutral plasma regimes. This is for example the case for high-density nonneutral plasmas subjected to large externally imposed flows and subjected to electron-neutral collisions. Furthermore, laboratory nonneutral plasmas are usually created using an external electron source (e.g. Penning traps, main beam of the gyrotron, magnetrons...), and not formed self-consistently due to ionization of the neutral gas, which significantly alters the dynamic of the electron cloud formation. Nonneutral plasmas formed self-consistently by neutral ionization can typically occur in gyrotron electron guns, therefore a deeper study of such configurations would also represent a deeper understanding of more exotic, unexplored nonneutral plasma regimes.

1.4   Nonneutral plasmas

Contrary to fusion plasmas formed by a combination of positive and negative particles, and where quasi-neutrality is ensured, nonneutral plasmas possess a strong charge imbalance and are typically composed of only one type of charges. These plasmas can appear in astrophysics, for example in the magnetosphere of pulsars [33], or on earth in the study of elementary particle physics [34–36], in particle accelerators [32], or in rf sources such as the gyrotron [16, 19]. Even if nonneutral plasmas possess by definition strong non-neutrality and produce important space-charge effects, they exhibit the same properties of Debye shielding and long-range collective behaviours [32] as neutral plasmas. Regarding the Debye shielding, the main difference between the neutral and nonneutral plasmas is in the amplitude of the average electric field. Indeed, in a neutral plasma at equilibrium, the average electric field is zero due to quasi-neutrality, while in a nonneutral plasma at equilibrium, the average space-charge effects induce an important zeroth order electric field not screened by the response of the nonneutral plasma.

Because of the non-neutrality causing strong Coulomb repulsion between the charged particles, the plasma particles can only be trapped either by rf fields, or by a combination of static electric and magnetic fields [25, 32]. The most common trapping configuration, called the Penning trap and represented in Figure 1.13, consists of a cylindrical vessel, subjected to an axial magnetic field, and two biased end electrodes
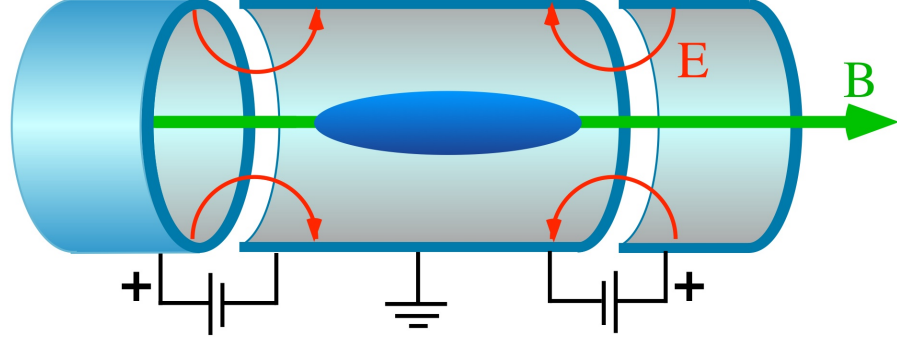
Figure 1.13: Schematic of a Penning trap, where a nonneutral electron plasma in the middle (dark blue) is radially trapped by the axial magnetic field (green) and axially trapped by the axial electric field (red) [41].

generating an axially confining electric field. Nonneutral plasmas in Penning traps exhibit extraordinary stability to electrostatic modes [37], allowing the storage of charged particles for long time periods ranging from hours to days [38]. Indeed, the conservation of energy and canonical angular momentum in these plasmas establishes a constraint on the mean-square radius of the plasma, for cylindrical plasmas in the absence of asymmetries and collisions with neutrals [39, 40]. This means that the percentage of lost particles can be bound to small values by controlling the magnetic field amplitude and the vacuum vessel radius. This result is however only valid for cylindrical plasmas trapped in cylindrical geometries. Indeed, an annular plasma trapped in a coaxial geometry, as is the case in MIGs, could have some of the particles drifting inwards and some drifting outward, conserving the same mean-square radius of the plasma and leading to the collection of the particles on the inner and outer electrodes.

In Penning traps, to ensure that the equilibrium state exists over very long time-scales [42], many dedicated theoretical and experimental studies have been carried out to avoid disruptive instabilities such as the azimuthal diocotron instability [43–53] and, to a lesser extent, axial resonant space-charge effects [25]. The confining electric potential along the magnetic field lines, which is imposed externally, is generally of the order of tens of V and the trapped plasma densities are low with a Brillouin ratio $f_b = 2\omega_p^2/\Omega_c^2 \ll 1$, where $\omega_p = \sqrt{q^2 n/(\epsilon_0 m)}$ is the plasma frequency and Ω_c is the cyclotron frequency [25]. Here, q is the trapped particle charge and m its mass, n is the plasma density, and ϵ_0 is the vacuum permittivity. In most laboratory nonneutral plasmas, the cloud temperature is initially determined by the mechanisms of electron generation and injection, and the cloud is often further cooled to temperatures of the order of a few eV, through cylcotron radiation cooling [54], to reduce the electron neutral collision cross-sections and increase the confinement time, or cooled to extremely low temperatures (a few K) to study quantum effects [25].

1.4.1 The rigid rotor equilibria [32]

To illustrate the type of equilibrium reached by nonneutral plasmas in Penning traps, an ideal nonneutral plasma configuration is presented in this section. This example considers an infinitely long pure electron plasma column of density n_0 confined radially by a uniform axial magnetic field $\vec{B} = B_0 \hat{e}_z$ as represented
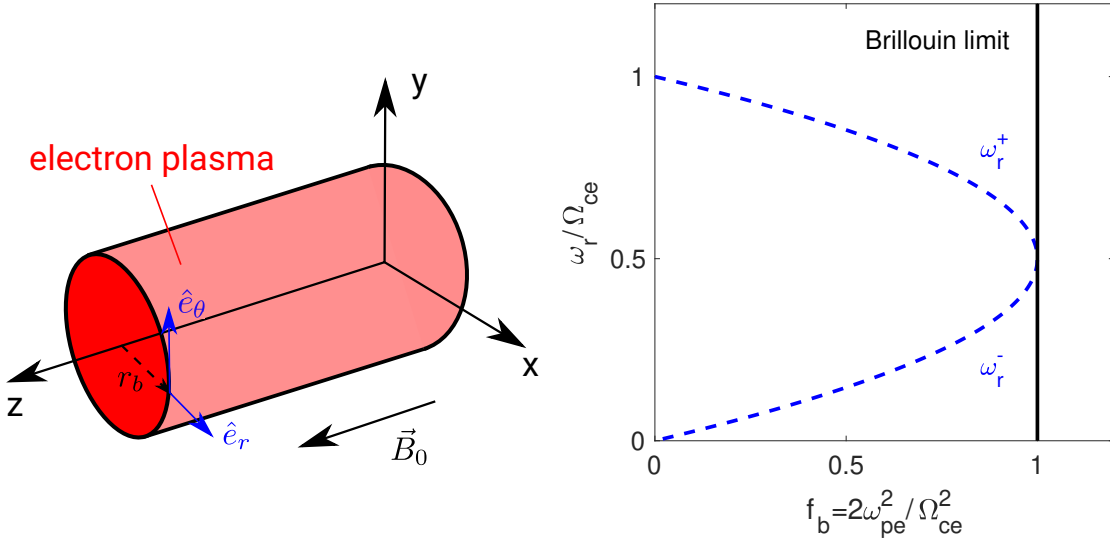
Figure 1.14: Left: Plasma column configuration considered for the rigid rotor equilibrium. Right: Equilibrium azimuthal angular velocity for a fluid element of the rigid rotor equilibrium as a function of the Brillouin ratio.

in Figure 1.14. The plasma is considered at equilibrium using a cold fluid description in cylindrical coordinates (r, θ, z). For this configuration, the radial density is defined as

$$n(r) = \begin{cases} n_0 & 0 \leq r \leq r_b, \\ 0 & r > r_b, \end{cases} \tag{1.4}$$

with r_b the radial dimension of the column. This electron cloud generates a radial electric field due to the space-charge

$$E_r(r) = \begin{cases} \frac{m_e}{2q_e} \omega_{pe}^2 r & 0 \leq r \leq r_b, \\ \frac{m_e}{2q_e} \omega_{pe}^2 \frac{r_b^2}{r} & r > r_b, \end{cases} \tag{1.5}$$

with m_e the electron mass, q_e the electron charge, $\omega_{pe} = \sqrt{q_e^2 n_0/(\epsilon_0 m_e)}$ the electron plasma frequency. At equilibrium, the radial force balance on an electron fluid element is expressed as a balance between the outward centrifugal and electric forces and the inward magnetic force:

$$\frac{m_e u_\theta^2(r)}{r} + q_e E_r(r) + q_e u_\theta(r) B_0 = 0, \tag{1.6}$$

with $u_\theta(r)$ the azimuthal fluid velocity. Using the expression for the radial electric field (1.5) in (1.6) leads to the expression of the two equilibrium fluid azimuthal angular velocities

$$\omega_r^\pm \equiv \frac{u_\theta}{r} = \frac{1}{2}\Omega_{ce}\left(1 \pm \sqrt{1 - \frac{2\omega_{pe}^2}{\Omega_{ce}^2}}\right), \tag{1.7}$$

which is represented in Figure 1.14. The value of ω_r is independent of r, therefore the azimuthal motion of the column corresponds to a rigid rotation around the axis of symmetry. In the case $\omega_r = \omega_r^-$, the column rotates at a slow angular velocity close to the $E \times B$ velocity. On the contrary, in the case $\omega_r = \omega_r^+$, the

plasma rotates at a fast angular velocity close to the cyclotron frequency Ω_{ce}. In addition, this result shows that, for an equilibrium to exist, the ratio $f_b = 2\omega_{pe}^2/\Omega_{ce}^2 \leq 1$. For $f_b = 1$, defined as the Brillouin density limit, the slow and fast rotation frequencies are equal with $\omega_r^+ = \omega_r^- = \Omega_{ce}/2$. This case is reached for a critical electron density $n_{e,crit} \approx 4.9 \times 10^{18} \,\text{m}^{-3}\,\text{T}^{-2}$. Indeed, if $f_b > 1$ the space-charge force, combined with the centrifugal force, are too important to be compensated by the magnetic force, and the electrons are lost radially. Experimentally, equilibria with both ω_r^+ and ω_r^- could be formed for several values of f_b and showed a good agreement between the experimental measurement and the analytical prediction of (1.7) [55].

The configuration considered in this section is relatively simple and is used as an introduction to the concept of nonneutral plasma. However, it is not sufficient to study the problem of trapped electrons in gyrotron MIGs as the trapping geometries are more complicated and other effects, such as electron-neutral collisions or ion induced electron emission are not considered. Taking into account these effects will generally require numerical modelling and more complex governing equations.

1.5 Goals of the thesis

The main goal of this thesis is to investigate the problem of electron cloud trapping in MIGs due to the potential well mechanism and to increase our understanding of the conditions of their formation. This is motivated by the fact that producing a design that avoids the existence of any potential well is very challenging. In addition, some experimental results have shown that some potential wells, under conditions still to be determined, can be present in MIGs and not cause detrimental current [30]. To this end, the thesis focuses on studying electron clouds trapped by electrostatic potential wells in coaxial geometries, and subjected to large externally imposed radial electric fields and azimuthal flows. The ultimate goal of this study would be to derive new relaxed design criteria for future gyrotron electron guns that could be applied in the vacuum configuration and would not need long and costly simulations to determine the risk of electron trapping. This thesis also aims at advancing the fundamental understanding of exotic, unexplored nonneutral plasma regimes, namely high-density, strong externally imposed azimuthal flows, non-negligible ionizing electron-neutral collisions, and annular shape, through numerical simulations and analytical models.

Since the gyrotron is a complex and sealed device, it is difficult to measure experimentally and understand the behaviour of trapped electrons in the electron gun region. For this reason, two parallel methods for studying this problem, are pursued. The first one is the use of first principle numerical simulations, allowing for detailed diagnostics of the clouds and the study of the trapped electrons' distribution function. To this end, it is necessary to develop a new particle-in-cell code, called FENNECS (Finite Element NonNeutral Electron Cloud Simulator), capable of simulating the complex electrode geometry of MIGs and the electron neutral collisions. The necessity of a new code is supported by the fact that available codes lack the capacity of either simulating the exact electron gun geometry, simulating electron-neutral collisions or simulating the dynamics of the cloud (see Chapter 2). In addition, the combination of large regions of vacuum in the gun and complex electrodes' geometries prompts the use of a novel numerical method, based on weighted extended b-splines (web-splines [56]), to impose the geometry in the simulations. This code also considers the self-consistent electron cloud build-up due to ionization of the RNG and the collision of the released ions with the electrodes, generating ion induced electron emission. With this newly developed numerical tool, the conditions of trapping and loss mechanisms are studied in simplified and realistic geometries. This allows, in a second step, to derive simple scaling laws relating the electron cloud properties and gun operational parameters. FENNECS is validated against experimental measurements and will be used,

during the design process of future gyrotron electron guns, to predict the onset of detrimental currents. The second method of study, is experimental and motivates the design, construction, and operation of a new experiment called T-REX. The experimental part of this project is led by Francesco Romano, a post-doctoral fellow at SPC, but the design and diagnostic device selection is supported by FENNECS simulations.

In line with the first method, analytical modelling is also used to supplement the numerical modelling and increase our understanding of the underlying mechanisms of cloud formation, electron losses and equilibrium conditions. To this end, a 0D fluid model is derived that is capable of producing fast estimates of the trapped electron density and of the resulting leaking currents, using only externally imposed operational parameters. This model is also capable of reproducing and explaining simple scaling laws, that have been observed in numerical simulations, for the key quantities in terms of the operational parameters.

1.6   Thesis outline

Chapter 2 focuses on the numerical code FENNECS mentioned in the previous section, and used to study the electron cloud trapping. In this chapter, the novel numerical method used to define the electrodes geometry and the Monte-Carlo algorithms used to simulate the different interactions of the electrons with the RNG or the electrodes are presented. Verification cases are shown to support the robustness and accuracy of the code. Finally, the parallelization methods of the code are described, and numerical scaling and parallelization efficiency results are given.

Chapter 3 considers the self-consistent formation of an electron cloud in a simplified coaxial geometry retaining the critical components of a gyrotron electron gun. Namely, the large, mostly axial magnetic field, and the large radial electric field. The electron source and loss mechanisms are identified, and the cloud formation is modelled as a balance between the RNG ionization and losses due to radial drifts caused by collisional drags. The results of parametric scans on the external parameters (applied bias, magnetic field amplitude, RNG pressure and type) are presented and used to derive analytical scaling laws between the electron cloud density and resulting current, and the external control parameters. Finally, a semi-analytical model is presented, that is capable of predicting the order of magnitude of the electron cloud density and the collected current in a range of external parameters.

Chapter 4 presents simulations results in realistic MIG geometries. In this chapter, the refurbished MIG geometry of the GT170 170 GHz 2MW coaxial gyrotron designed for ITER [23] is used. In this geometry, results of simulations with various magnetic field configurations and applied gun biases are presented and compared to experimental results. This serves as a validation of the numerical model implemented in FENNECS. In addition, the importance and consequence of including ion induced electron emission on the electrode surfaces is discussed by comparing simulations with and without this effect. Finally, a quantitative validation of FENNECS is attempted in the prototype geometry of the GT170 electron gun.

Chapter 5 is dedicated to results of simulations using the electrode geometries considered for the TRapped Electron eXperiment (T-REX) being built at the Swiss Plasma Center. These simulations are used to guide the design of the T-REX electrode geometries and show the relevance of this experiment to study the problem of electron clouds trapped in MIGs. Simulations are also presented that investigate the effects of (i) non-ideal power supply to impose the confining bias and (ii) ion induced electron emission (IIEE).

Chapter 6 considers the linear stability of nonneutral plasmas in ring clouds to diocotron normal modes. To this end, a linearized fluid model used to characterize the diocotron stability is presented and implemented

in a spectral code, in order to study realistic electron clouds. This study is done in the GT170 prototype geometry and considers the diocotron stability of the electron cloud during its formation. This work is motivated by the fact that annular electron clouds are highly susceptible to the diocotron instability [32], which is azimuthal in nature and cannot be simulated with the 2D (axial-radial) FENNECS code. This investigation also indicates that the diocotron instability is bias dependent and should develop in MIGs configurations. This result opens the door to exploring further this instability.

Chapter 7 summarizes the main results presented in this thesis and presents the conclusions of this work. In addition, possible extensions and future use cases for the code FENNECS will be discussed, as well as possible future steps for the study of trapped electrons in MIGs.

In the appendices, the derivation of the self-consistent electric field for an annular electron cloud of infinite length confined in a biased coaxial geometry is first presented. This derivation is used in the semi-analytic model described in Chapter 3. Then an equilibrium nonneutral plasma is presented, where we demonstrate that high densities ($f_b > 1$) can be achieved. The algebraic development and finite difference implementation of a more general electrostatic eigenvalue equation to study diocotron normal modes is presented in the third appendix [57]. This equation has the benefit of relaxing the low plasma density assumption used in Chapter 6, but the numerical implementation could not be verified to sufficient accuracy. The last appendix presents a list of the input parameters to FENNECS and can be used in combination with chapter 2 as a preliminary user manual for FENNECS.

2 The particle-in-cell code FENNECS

To understand the conditions of formation and evolution of trapped electron clouds in gyrotron electron guns, a particle-in-cell code called FENNECS (Finite Element NonNeutral Electron Cloud Simulator) has been developed and is the subject of this chapter. Current codes considering neutral and nonneutral plasma discharges are either proprietary (LSP [58], MAGIC [59]), or are limited to simple electrode geometries (NINJA [60]) due to the method used to solve the Poisson equation. In the domain of gyrotrons, electron gun simulations are carried out with codes capable of simulating the complex geometry of the gun. However, the most common codes such as EGUN [61], ESRAY [62], DAPHNE [63] or ARIADNE++ [64] do not consider electron-neutral collisions and assume a beam-optics framework, that only simulates equilibrium, and can therefore not simulate the fast electrostatic modes that can arise in high density electron clouds. Another candidate, the WARP [65–67] code, is both capable of simulating electron-neutral collisions and the complex electrodes geometries used in gyrotron electron guns. However, due to the finite difference method on staggered grids used to solve Poisson's equation, simulations of complex geometries require potentially costly grid refinements.

The 2D electrostatic axisymmetric particle-in-cell code FENNECS presented in this chapter considers a novel Finite Element Method (FEM) that allows the exact definition of the electrodes geometry and somewhat decouples the grid definition and the geometry of interest when solving for the electrostatic potential. This method has been successfully used in several domains of physics, for example to solve elastic deformation problems [56], electromagnetic wave propagation in wave-guides [68], or the stationary Stokes problem [69], and is used here for the first time in plasma physics, to the best of our knowledge [70, 71]. The code is also capable of simulating electron-neutral collisions, considering elastic and inelastic (ionization) collisions, and resolves the fast timescale associated with plasma waves and electron cyclotron motion. This is of great importance for simulating high-density trapped electron clouds for which the Brillouin ratio is close to one. The magnetic fields generated by the electron clouds are neglected in front of the strong externally applied magnetic field that is assumed to dominate the dynamics. This code has already been successfully used to study the self-consistent formation of trapped electron clouds in gyrotron electron guns and to derive scaling laws for the electron cloud density and resulting current as a function of external parameters [26]. In the same context, FENNECS was successfully validated against experimental measurements [72]. The code is currently used to study gyrotron electron guns. However, the governing equations are sufficiently general that it could be used in the domain of Penning traps [25], or be easily adapted to study cathodic arcs [73]. In addition, the code and its dependencies will soon be open-source, which facilitates its modification, enables further improvements, and simplifies the beginning of new collaborations. The code and the list of its dependencies are stored in a git repository that can be

accessed at https://c4science.ch/source/fennecs/.

2.1 Physical model

2.1.1 Governing equations

FENNECS is an axisymmetric 2D3V electrostatic particle-in-cell code that solves the Boltzmann-Poisson system for an electron distribution function $f(\vec{r}, \vec{v}, t)$ and the electrostatic potential $\phi(\vec{r}, t)$ with the addition of electron-neutral collision operators. The neutral gas is considered as a background gas of uniform density n_n and at room temperature $T_n = 300\,\text{K}$. For each simulation, only one neutral gas species is considered, and it is assumed that n_n does not change in time. The gas species is a control parameter of the code, and, in this thesis, the considered gases are Ne, H_2, Ar and He to allow different comparisons with experiment and to understand the effect of a change in species. In the current model, only elastic and single ionization collisions are considered with their respective collision cross-sections σ_{ela} and σ_{io}. This choice is supported by the fact that, due to the large radial electric field in gyrotron electron guns, the newly formed ions are lost on a timescale $\tau_{ion,loss}$ much smaller than the second ionization collision timescale. Similarly, due to the large electron kinetic energies (more than several hundred eV), the collision time-scales for excitation of the neutral gas are at least one order of magnitude larger than both the elastic and single ionization time-scales and are therefore neglected [26, 74]. In elastic and ionization collisions, we assume anisotropic scattering cross-sections using a screened-Coulomb scattering cross-section [75]. For an ionization event, the remaining kinetic energy after collision (initial kinetic energy minus the ionization energy) is split between the freed and the incoming electron using a double differential cross-section $\frac{\partial^2 \sigma_{\text{io,sec}}}{\partial\Omega\partial E_p}$ for the energy of the secondary electron, and a second double differential cross-section $\frac{\partial^2 \sigma_{\text{io,sca}}}{\partial\Omega\partial E_p}$ for the energy of the scattered electron. This energy splitting assumes that the energy transferred to the ion is negligible due to the large mass difference between electrons and ions. The double differential cross-sections depend on the solid scattering angle Ω and the incoming electron energy E_p [76]. They are defined such that, in ionization events, the total energy is conserved $E_p = E_{\text{io}} + E_{\text{sca}} + E_{\text{sec}}$. Here, E_{io} is the first ionization energy of the neutral gas, E_{sca} is the energy of the scattered electron and E_{sec} is the energy of the secondary electron.

The magnetic field $\vec{B}_0^{\text{ext}}$ is imposed externally, and the magnetic field generated by the electron cloud is neglected. Perfectly absorbing boundary conditions for the particles are used at the electrodes, thereby representing a loss term L_{wall}. In addition, a volumetric seed source S_{seed} can be imposed, and electron emission due to ions impacting the electrode surfaces can be simulated, introducing a surface source S_{IIEE}. In this case, the Boltzmann equation becomes

$$
\begin{aligned}
&\left[\frac{\partial}{\partial t} + \vec{v} \cdot \frac{\partial}{\partial \vec{r}} - \frac{e}{m_e} \left(\vec{E} + \vec{v} \times \vec{B}_0^{\text{ext}}(\vec{r}) \right) \cdot \frac{\partial}{\partial \vec{v}} \right] f(\vec{r}, \vec{v}, t) = \\
&+ n_n |\vec{v}| \int \frac{d\sigma_{\text{ela}}(|\vec{v}|)}{d\Omega} [f(\vec{r}, \vec{v}'(\Omega), t) - f(\vec{r}, \vec{v}, t)] d\Omega \\
&+ \frac{n_n |\vec{v}|}{E_k} \left(\int_{E_k + E_{\text{io}}}^{2E_k + E_{\text{io}}} \int E_p \frac{\partial^2 \sigma_{\text{io,sec}}}{\partial\Omega\partial E_p} f(\vec{r}, \vec{v}'(\Omega), t) d\Omega dE_p \right. \\
&+ \left. \int_{2E_k + E_{\text{io}}}^{\infty} \int E_p \frac{\partial^2 \sigma_{\text{io,sca}}}{\partial\Omega\partial E_p} f(\vec{r}, \vec{v}'(\Omega), t) d\Omega dE_p \right) \\
&- n_n |\vec{v}| \sigma_{\text{io}}(|\vec{v}|) f(\vec{r}, \vec{v}, t) \\
&+ S_{\text{seed}} + S_{\text{IIEE}} - L_{wall}.
\end{aligned} \tag{2.1}
$$

Here, Ω is the solid scattering angle; $\vec{v}'$ is an integration variable for all the electron velocities that are scattered by a solid angle Ω to $\vec{v}$ [77]; $E_k = m_e|\vec{v}|^2/2$ is the electron kinetic energy at velocity $\vec{v}$. On the right-hand side, the first term accounts for the scattering by elastic collisions [77], the second term describes the emission of secondary electrons by ionization, the third term accounts for the scattering of incoming electrons during an ionization collision and the fourth term describes the electrons removed from the distribution by ionization [78]. If the right-hand side is integrated over $\vec{v}$, its first term will be 0 and the second, third and fourth term will combine to an ionization source term $n_e n_n < \sigma_{\mathrm{io}} v >_f$. Here, n_e is the local electron density, and $<>_f$ denotes the average over the distribution function. The electric potential ϕ is solved self-consistently using Poisson's equation

$$\nabla^2 \phi(\vec{r}, t) = -\frac{\rho}{\epsilon_0} = \frac{e}{\epsilon_0} \int f(\vec{r}, \vec{v}, t) d^3\vec{v} \tag{2.2}$$

and the charge density ρ, and considering the boundary conditions imposed by the electrodes. At the electrodes, in addition to fixed potentials imposed by ideal power supplies, the resistive and capacitive effects of a non-ideal power supply can be simulated (see Section 2.2.7).

2.1.2 Normalizations

To improve the numerical precision of the code, all the physical quantities are normalized by physical constants relevant to the problem. To this end, four reference quantities are used: B_0, an input parameter usually set to the maximum amplitude of the magnetic field in the simulation domain; c, the speed of light in vacuum; e, the electron charge; and m_e, the electron mass. The time is normalized by the inverse of the cyclotron frequency $t_N = 1/\Omega_{ce} = m_e/eB_0$, velocities are normalized by $v_N = c$, lengths are normalized by $r_N = v_N/t_N$, the magnetic field is given in units of $B_N = B_0$, and the electric potential and fields are respectively normalized by $\phi_N = B_N v_N r_N$ and $E_N = v_N B_N$.

2.1.3 Geometries of interest

As FENNECS is a 2D axisymmetric code, it is capable of simulating geometries with an azimuthal symmetry. Namely, in cylindrical coordinates (r, θ, z) all fields can depend on r and z but not on θ. For coaxial gyrotron electron guns, the typical geometry of interest, as represented in Figure 2.1, is composed of an inner cathode and an outer cylindrical anode described by an arbitrary radial profile $r(z)$. However, the code is more flexible in the definition of the electrodes and multiple concentric electrode rings can be defined. Similarly, regions where only the outer electrode is present are also possible. This is important to simulate all types of gyrotron electron guns, but can also be useful to study nonneutral plasmas in other physical settings. In addition, independent potentials can be applied to each simulated electrode. Furthermore, the particles are subjected to an axisymmetric external magnetic field with both radial and axial components. In the configurations typical of gyrotron guns, the electron clouds usually have an annular shape (see Figure 2.1) confined axially by magnetic mirrors, due to the electrons large perpendicular velocity, or by electrostatic potential wells imposed externally [21, 26]. However, cylindrical clouds (clouds extending to $r = 0$) can also be simulated.
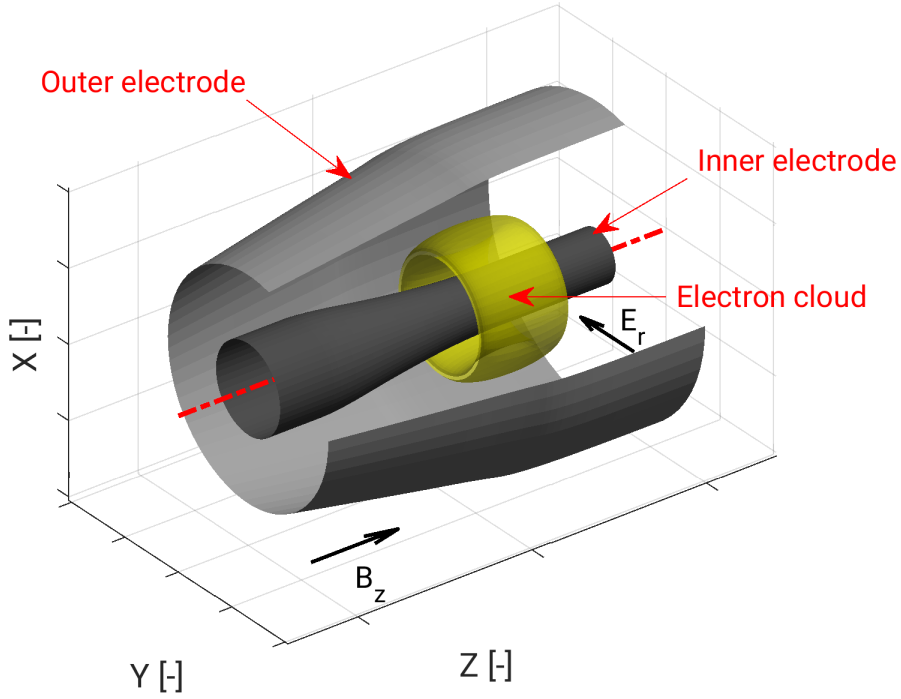
Figure 2.1: Typical geometry of interest used in FENNECS. The yellow ring represents an example of an electron plasma cloud. The gray/black parts are the electrodes on which a fixed potential can be applied. The red dotted-dashed line highlights the axis of symmetry.

2.1.4 Timescale separation

Typical electron clouds trapped in gyrotron electron guns are subject to physical phenomena happening on various time-scales. These can span up to ten orders of magnitude, between the fast electron cyclotron motion at Ω_{ce}, and the slow ionization collision frequency f_{io} and effective elastic collision frequency for momentum exchange f_d, as illustrated in Figure 2.2. In between these slow (f_{io}, f_d) and fast (Ω_{ce}, ω_{pe}) scales lies typically an intermediate scale $f_\parallel \approx v_\parallel / L$, namely the electron bounce frequency in a trap of length L along the magnetic field lines, and with average velocity $v_\parallel$ parallel to the magnetic field line. The length L can be either the potential well dimension along the magnetic field line or the distance between the two cusp points in a magnetic mirror configuration (see Section 1.3). This large timescale separation prevents the complete simulation of all the timescales due to the numerical cost of the task. However, as $f_{\mathrm{io}} = n_n < \sigma_{\mathrm{io}} v >$ and $f_d = n_n < \sigma_{\mathrm{ela}} v >$ are linearly proportional to n_n, the collision timescales can be shortened by considering, in the simulations, an increased neutral gas density $n_{n,simu} = \alpha n_{n,phys}$ compared to the physical density of interest [26, 72]. This factor $\alpha > 1$ must be selected such that a sufficient timescale separation is kept between the slow and fast timescales, namely such that $f_{\mathrm{io}}, f_d \ll f_\parallel$. Assuming that the dynamics is dominated by the slow timescales, the simulation characteristic times (e.g. the particle losses or cloud oscillations) can then be rescaled to the physical timescales using the same parameter α. For simulating realistic gyrotron configurations, α is chosen to be of the order of $\alpha \approx 10^4$.

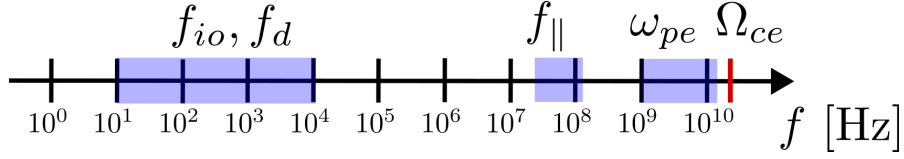Figure 2.2: Relevant timescales for electron clouds of interest simulated by FENNECS. f_{io} and f_d are the ionization collision frequency and the effective elastic collision frequency for momentum exchange; $f_\parallel \approx v_\parallel / L$ is the electron bounce frequency in the trap of length L along the magnetic field lines; ω_{pe} is the electron plasma frequency; Ω_{ce} is the electron cyclotron frequency. The blue shaded area indicates the range of possible time scales for $n_e \approx 10^{14} \rightarrow 10^{17} \mathrm{m}^{-3}$ and $n_n \approx 10^{13} \rightarrow 10^{17} \mathrm{m}^{-3}$. The red line gives Ω_{ce} for $B = 0.3\,\mathrm{T}$.

2.2 Numerical methods

To solve the Boltzmann equation (2.1) and the Poisson equation (2.2), the particle-in-cell (PIC) method is employed. The distribution function f is sampled using a finite number of macro-particles i at position $\vec{r}_i$ with velocity $\vec{v}_i$ and each representing N_i electrons, such that

$$f(\vec{r}, \vec{v}, t) = \sum_i N_i \delta(\vec{r} - \vec{r}_i) \delta(\vec{v} - \vec{v}_i). \tag{2.3}$$

Here $\delta(\vec{x})$ is the Dirac delta function. This representation of the particles has been chosen to reduce the number of computations necessary to calculate the right-hand side of Poisson's equation, to facilitate the particles removal at the boundaries, and to facilitate the parallelization of the code. On the other hand, this choice forces the use of a relatively large number of macro-particles in order to minimize numerical noise.

Starting from an initial distribution of macro-particles, the code performs the following steps to advance in time the particles and the fields according to the Boltzmann-Poisson system described in equations (2.1) and (2.2). At each time-step, the code:

1. Localizes each particle in the geometry and calculates its FEM cell index. Removes the particles that are outside the vacuum region. In Message Passing Interface (MPI) parallelism, the particles that are leaving or entering the local domain simulated by each process are exchanged between the neighbouring processes.

2. Runs the Monte Carlo collision routine for each particle and scatter/reduce their velocity vector accordingly, and adds the freed electrons due to ionization of the neutral gas (Sec. 2.2.8).

3. Injects the new particles according to the seed source distribution function (Sec. 2.2.10).

4. Computes the new applied bias according to the collected current on the electrodes when the non-ideal power supply module is activated (Sec. 2.2.7).

5. Computes the right-hand side of Poisson's equation by looping on all the macro-particles (Sec. 2.2.4).

6. Solves Poisson's equation (Sec. 2.2.4).

7. Computes for each particle the value of $\vec{E}$ and $\vec{B}$ at their position and advances in time their velocity (Sec. 2.2.5 and 2.2.2).

8. Saves on file the requested diagnostic quantities (particles positions and velocities, electric field evaluated on the grid, moments of the distribution function evaluated on the grid...) (Sec. 2.3).

9. Advances in time the particles positions (Sec. 2.2.1).

10. Restarts the cycle.

2.2.1 Particle trajectory: Boris algorithm

To advance in time the macro-particle positions and velocities, according to the left-hand side of Boltzmann equation (2.1), the Boris algorithm is used [79]. This method was selected for its simplicity and reliability, and for its capability of integrating both classical and relativistic trajectories with very little change in the code. This allows the user of FENNECS to select at run-time if the classical or relativistic Newton's equation is solved during the simulations, by means of an input flag.

The Boris algorithm is a second order in time ($O(\Delta t^2)$) explicit integrator based on a leap-frog scheme, meaning that the particles positions and velocities are never known at the same time-step. Instead, the positions are known at times t_i and the velocities are known at times $t_{i+1/2} = t_i + \Delta t/2$. This is important to take into account during the initialization of the particles and when calculating diagnostics quantities as a naive evaluation will lead to a reduced accuracy of $O(\Delta t)$. To advance in time the velocities at position $\vec{r}_t$ from $\vec{v}_{t-\Delta t/2}$ at $t - \Delta t/2$ to $\vec{v}_{t+\Delta t/2}$ at $t + \Delta t/2$, the algorithm

1. accelerates the velocity by half the electric field to $\vec{v}_-$,

2. rotates the velocity due to the magnetic field force to $\vec{v}_+$,

3. accelerates the velocity by half the electric field to $\vec{v}_{t+\Delta t/2}$.

To solve the relativistic Newton equation, the new variable $\vec{u} = \gamma \vec{v}$ is used, with $\gamma = (1 - v^2/c^2)^{-1/2}$ the Lorentz relativistic factor. This gives in equation form:

$$\vec{u}_- = \vec{u}_{t-\Delta t/2} + \frac{q\Delta t}{2m}\vec{E}_t(\vec{r}_t), \tag{2.4}$$

$$\vec{u}' = \vec{u}_- + \vec{u}_- \times \vec{t}, \tag{2.5}$$

$$\vec{u}_+ = \vec{u}_- + \vec{u}' \times \vec{s}, \tag{2.6}$$

$$\vec{u}_{t+\Delta t/2} = \vec{u}_+ + \frac{q\Delta t}{2m}\vec{E}_t(\vec{r}_t). \tag{2.7}$$

Here used has been made of the two rotation vectors

$$\vec{t} = \frac{q\vec{B}(\vec{r}_t)}{\gamma_t m}\frac{\Delta t}{2}, \tag{2.8}$$

and

$$\vec{s} = \frac{2\vec{t}}{1 + t^2}, \tag{2.9}$$

with q the macro-particle charge, m its mass and $\gamma_t = (1 - v_-^2/c^2)^{-1/2}$. The classical Newton equation is recovered if $\gamma \equiv 1$ is imposed numerically. The particles' position is finally advanced with:

$$\vec{r}_{t+\Delta t} = \vec{r}_{t-\Delta t} + \Delta t\vec{v}_{t+\Delta t/2}. \tag{2.10}$$

2.2.2 Magnetic field

The magnetic field is imposed externally, assuming azimuthal symmetry. It is also assumed that the external magnetic field amplitude is large enough so that the contribution from the electron cloud current can be neglected. It can be defined either using an analytical magnetic field vector potential that, e.g., approximates a magnetic mirror close to the magnetic axis, as described in Sec.2.4.2, or it can be calculated on a grid using standard Biot-Savart solvers and be used as an input for the simulations. The magnetic field is then interpolated using third order b-splines to the FEM solver grid points. Finally, at the particle position, the magnetic field is computed using linear interpolation from the FEM grid points values to reduce the computational cost of the evaluation. The need for b-spline interpolation comes from the fact that the Biot-Savart solver is currently run using an external code and does not necessarily guarantee that the grid points of this solver correspond to the grid-points of the FEM solver, especially when the FEM grid needs to be adapted, or the simulation domain needs to be changed. This induces some imprecision on the value of the magnetic field that remains acceptable if the Biot-Savart solver grid is sufficiently fine. However, there are plans to include the magnetic field solver directly in FENNECS to avoid the b-spline interpolation step.

2.2.3 The b-spline basis functions

As b-splines are used extensively in FENNECS, we present in this section a few of their properties and a method to generate a b-spline basis. b-splines are piecewise basis polynomials with compact support, that are used in some FEM and can be used to smoothly interpolate data with freedom in the C^m continuity. Here m is the degree of the b-spline basis considered.

A spline basis of degree m is defined on a finite interval $[a, b]$ divided into N_x sub-intervals with:

$$a = r_0 \leq r_1 \leq r_2 ... \leq r_{N_x} = b, \tag{2.11}$$

where the intervals do not need to be uniform. The control points r_l, also called knots, and spline degree m define unequivocally the spline basis. The lth spline of degree m on this interval can be defined using the recurrence relation of de Boor [80] starting from the constant spline

$$b_l^0(x) = \begin{cases} 1 & \text{if } r_l \leq x < r_{l+1}, \\ 0 & \text{otherwise,} \end{cases} \tag{2.12}$$

and calculating the spline of higher order with

$$b_l^m(x) = \frac{x - r_l}{r_{l+m} - r_l} b_l^{m-1}(x) + \left(1 - \frac{x - r_{l+1}}{r_{l+m+1} - r_{l+1}}\right) b_l^{m-1}(x). \tag{2.13}$$

It can be observed from this definition that if N_x intervals are defined, a spline basis of degree m will be formed of $N_x + m$ orthogonal basis functions. Examples of basis of degree 1, 2 and 3 on the interval $[0, 1]$ with $N_x = 5$ are represented on Figure 2.3.

The b-splines have several useful properties that are relevant for FEM and interpolation:

- Positivity and local support: b_l^m is positive on (r_l, r_{l+m+1}) and vanishes outside this interval,

- Smoothness: b_l^m is $m - 1$ times continuously differentiable with discontinuities of the mth derivative

at the break points $r_l, .., r_{l+m+1}$,

- They form a partition of unity: $\sum_l b_l^m(x) = 1 \ \forall x \in [a, b]$,

- The derivative of a spline of degree m is a weighted sum of splines of degree $m - 1$,

- For a basis of degree m, only $m + 1$ b-splines are non-zero on the interval $[r_l, r_{l+1}]$.
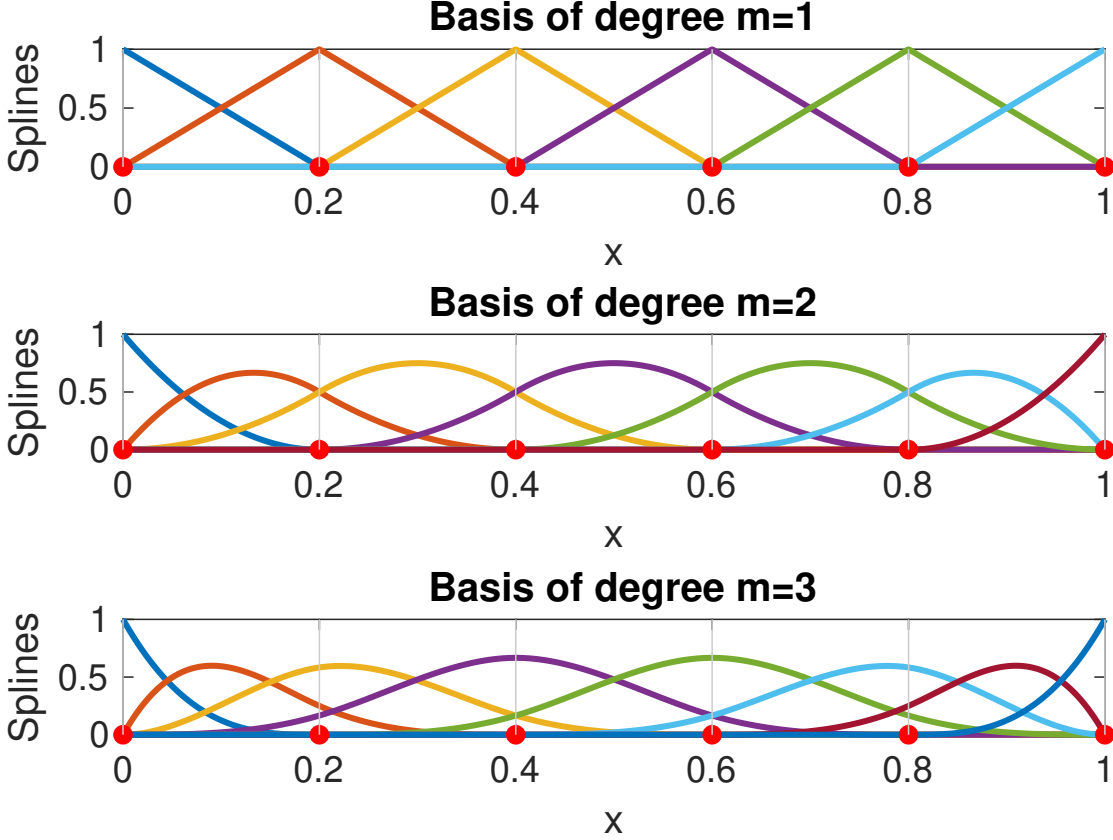
Figure 2.3: B-spline basis of degrees 1, 2 and 3 defined with $N_x = 5$ intervals on $[0, 1]$. The knots are highlighted by the vertical gray lines and the red dots. Each basis spline b_l^m is coloured individually.

With these properties, they can be used to approximate functions by assigning scalar or vector coefficients u_l to each b-spline. If $p(x)$ is a polynomial of degree m on $[a, b]$, a b-spline basis of degree $\geq m$ can represent it exactly by calculating the correct coefficients u_l, and $p(x)$ can be rewritten as

$$p(x) = \sum_l u_l b_l^m(x). \tag{2.14}$$

b-splines basis can also be used to define curves in n-dimensions by changing the coefficients from scalar to vectors $\vec{u}_l = (u_{l,1}, u_{l,2}, ..., u_{l,n})$. Similarly, one can define multivariate b-splines, for example bivariate b-splines are generated by defining two orthogonal spline spaces $b_l^m(x)$ on $[a_1, b_1]$ and $b_k^m(y)$ on $[a_2, b_2]$. The bivariate functions are then interpolated by defining u_{lk} coefficients such that

$$p(x, y) = \sum_k \sum_l u_{lk} b_l^m(x) b_k^m(y). \tag{2.15}$$

In this representation, the splines order of the two splines basis do not need to be equal, and the coefficients u_{lk} can also be multidimensional to be able to define e.g. surfaces in 3D. In the rest of this chapter, the notations will be simplified by generalizing the concept of 1D splines to ND splines, imposing the same degree on all directions and noting the multivariate spline basis with b_l^m. This can be done for the 2D case by going from a double index (l, k) to a linear index $i = (l - 1)N_x + k$. For brevity, this index i will be renamed l.

2.2.4 Poisson: Web-spline method

The Poisson equation, for a scalar field ϕ and a source term Q, is solved on the domain D, closed by boundaries ∂D, using a FEM based on bivariate b-splines of any order [71, 81, 82]. Dirichlet boundary conditions are imposed on boundaries ∂D_i and Neumann boundary conditions are imposed on boundaries ∂D_k such that:

$$-\nabla^2 \phi = Q \text{ in } D, \ \phi = g_i \text{ on } \partial D_i, \ \nabla_{\perp k} \phi = 0 \text{ on } \partial D_k, \tag{2.16}$$

where $\nabla_{\perp k}$ denotes the normal derivative perpendicular to ∂D_k. To define these boundary conditions on curved surfaces, the web-spline method is used for the first time in plasma physics, to the authors' knowledge. This chapter will be limited to the description of the method and of the points necessary for the implementation. Details regarding the numerical stability and accuracy of the method can be found in references [70, 71].

To derive a variational formulation, the electric potential ϕ is first rewritten to eliminate the inhomogeneous boundary conditions by setting

$$\phi = u + \tilde{g}, \tag{2.17}$$

with u a function that vanishes on ∂D_i and $\tilde{g}$ an extension of the Dirichlet boundary conditions g_i to all D. $\tilde{g}$ can be set to any smooth function such that $\tilde{g}(\vec{x}) = g_i(\vec{x}) \ \forall \vec{x} \in \partial D_i$. The Poisson equation is then multiplied by a test function ψ and integrated over D leading to the weak formulation:

$$\int_D \nabla u \nabla \psi = \int_D (Q\psi - \nabla \tilde{g} \nabla \psi). \tag{2.18}$$

To construct the Ritz-Galerkin approximation of the solution, the function ψ is taken to be a set of n_b basis polynomials Ψ_l^m of degree m with compact support on mesh cells of D, and the solution is approximated by a function $\phi_h = u_h + \tilde{g}$ such that

$$u_h = \sum_{l=1}^{n_b} u_l \Psi_l^m. \tag{2.19}$$

To ensure by construction that the Dirichlet boundary conditions are respected, the basis functions Ψ_l^m are defined such that they are 0 on ∂D_i. Solving the Ritz-Galerkin approximation of the solution then reduces to solving a system of linear equations for the coefficients u_l:

$$\overleftrightarrow{A} \cdot \vec{u} = \vec{\lambda}, \tag{2.20}$$

with $\overleftrightarrow{A}$ a matrix with coefficients

$$A_{lk} = \int_D \nabla \Psi_l^m \nabla \Psi_k^m, \tag{2.21}$$

and $\vec{\lambda}$ a vector with coefficients

$$\lambda_l = \int_D Q\Psi_l^m - \nabla \tilde{g} \nabla \Psi_l^m. \tag{2.22}$$

One can define a set of basis functions Ψ_l^m using weighted b-splines by defining a smooth geometric weight function w such that $w(\vec{x}) = 0 \,\forall \vec{x} \in \partial D_i$, and w is positive inside the domain $D/\partial D_i$ and negative outside D. In this case: $\Psi_l^m \equiv w b_{l,h}^m$, with $b_{l,h}^m$ the n-variate tensor product of b-spline of degree m, with grid width h, and support $(l_1, ..., l_n)h + [0, m+1]^n h$. Since the grid is regular (h is the same for all b-splines of the basis), the index h will be neglected for the rest of this chapter. The weighted b-spline (wb-spline) method is known to show bad numerical convergence as the grid width is reduced due to a strong, sudden and unpredictable increase of the condition number of the Ritz-Galerkin matrix $\overleftrightarrow{A}$ [70] (see Figure 2.4). This problem comes from the effect of boundary b-splines whose intersection between their support and the simulation domain becomes small. To alleviate this problem, Höllig and co-authors [70] combined boundary and inner b-splines to form a new basis called the web-spline basis.
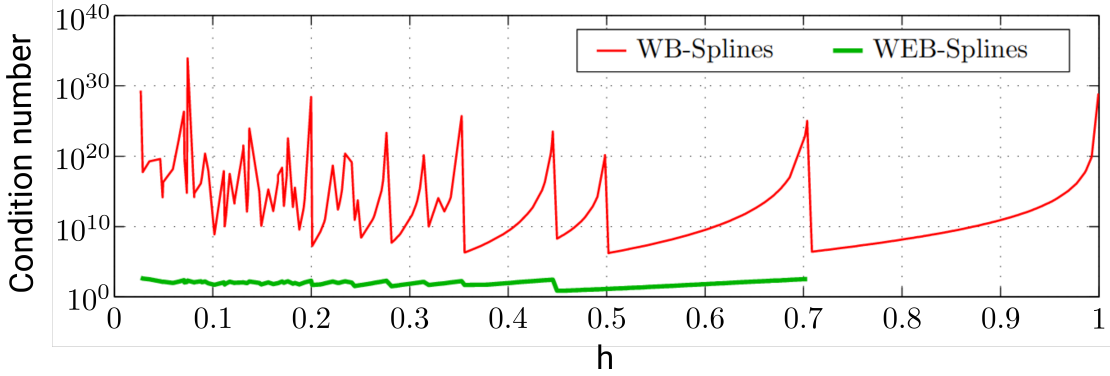

Figure 2.4: Evolution of the Ritz-Galerkin matrix condition number for weighted b-splines (red) and web-splines (green) as a function of the grid width h for the Poisson problem solved on the unit disc [83]. As h is reduced, splines with too small support in D appear randomly due to the non-conforming boundaries causing numerical error for w-splines, but these are stabilized by the web-spline method.

To understand the web-spline basis, it is necessary to define inner, outer, and boundary b-splines, depending on the intersection between the support of the b-spline and the domain D. Inner b-splines need to have at least one grid-cell in their support that is fully inside D; for outer b-splines, the intersection between their support and D is $\emptyset$; and boundary b-splines are all the other b-splines. An example of this classification is represented in Figure 2.5, using the geometry defined in subsection 2.4.1 and quadratic b-splines. For the rest of this section, the ensemble L of inner b-splines are identified as b_l^m using the subscript l (see green dots of Figure 2.6) and the ensemble K of boundary b-splines are identified as b_k^m using the subscript k (see red dots of Figure 2.6).

A web-spline basis $\Psi_{l,web}^m$ is defined by combining boundary and inner b-splines while keeping the correct approximation order of the initial b-spline space. To this end, the approximated solution u_h is separated between the contribution of inner and boundary b-splines

$$u_h = \sum_{l \in L} u_l b_l^m + \sum_{k \in K} u_k b_k^m. \tag{2.23}$$

According to Marsden's identity [84], if u_h is a polynomial of degree $\leq m$ the coefficients u_l and u_k can be calculated by a polynomial $\tilde{u}(i) = u_i$ of degree $\leq m$ dependent on the spline index i. In this case, the outer coefficients u_k can be interpolated, for the n-variate b-splines in a space of dimension n, from any $(m+1)^n$ inner indices without affecting the approximation power of the spline space. In practice, the
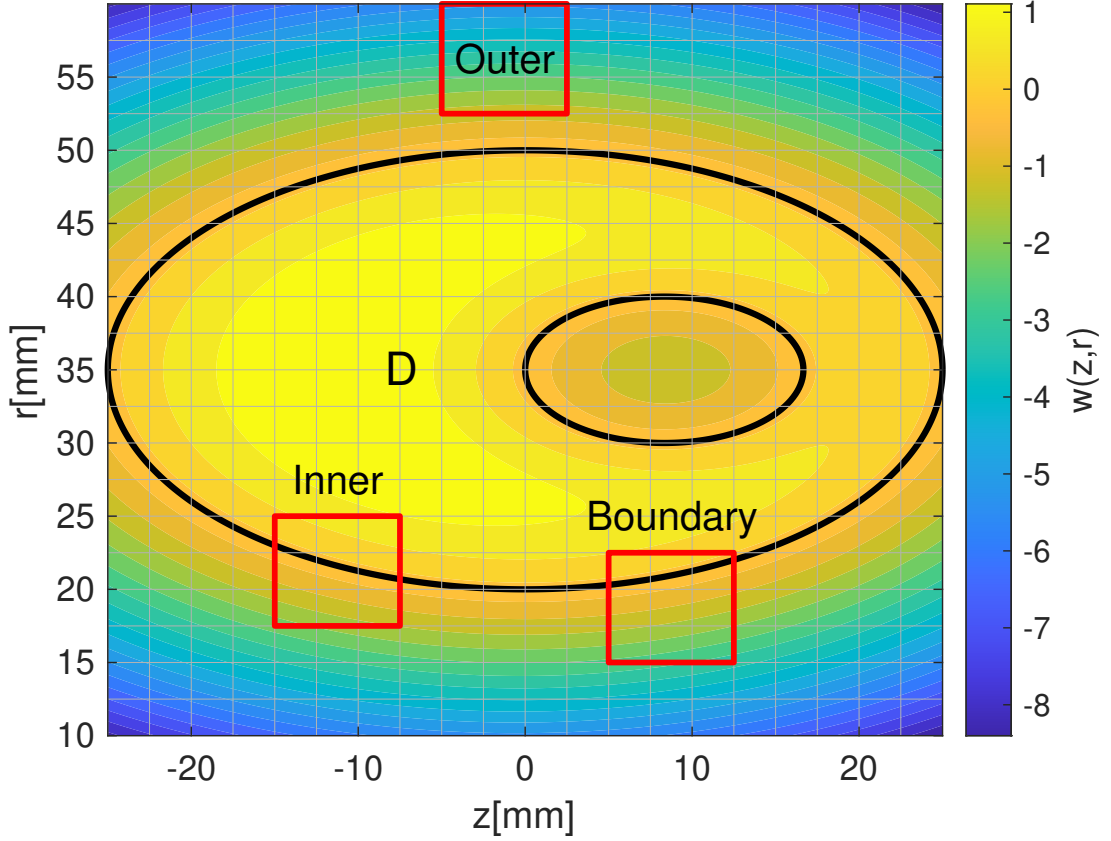
Figure 2.5: Geometric weight w and domain boundary (in black, where $w = 0$) for the test case presented in Section 2.4.1 (black). The gray lines show the FEM grid, and the red squares show the boundary of the support of 3 types of quadratic b-splines.

interpolant indices are taken as the closest $(m + 1)^n$ inner indices l, and the coefficients u_k are interpolated using Lagrange polynomials such that

$$u_k = \sum_{l \in L} u_l e_{lk}. \tag{2.24}$$

This assumes that the grid width h is sufficiently small for this list to exist. The coefficients e_{lk} are defined as

$$e_{lk} = \prod_{\nu=1}^{n} \prod_{\mu=0}^{m} \frac{k_\nu - p_\nu - \mu}{l_\nu - p_\nu - \mu}, \tag{2.25}$$

with n the dimension of D and p_ν the lower index in each dimension of the inner interpolating splines. An example of the value of these coefficients is represented in Figure 2.6. In addition to the interpolation of the external coefficients u_k, the web-spline basis is also rescaled by the weight evaluated at x_l, the centre of a grid cell belonging to the support of b_l^m and fully inside D (see Figure 2.6). The final web-spline basis is finally defined as

$$\Psi_{l,web}^m = \frac{w}{w(x_l)} \left[b_l^m + \sum_{k \in K(l)} e_{lk} b_k^m \right], \tag{2.26}$$

with $K(l)$ the ensemble of boundary b-splines for which the inner b-spline l is used to interpolate u_k. An

Figure 2.6: Illustration of coefficients e_{lk} for inner b-splines l (green) and boundary b-splines k (red). The lower left corner of the support of the cubic bivariate b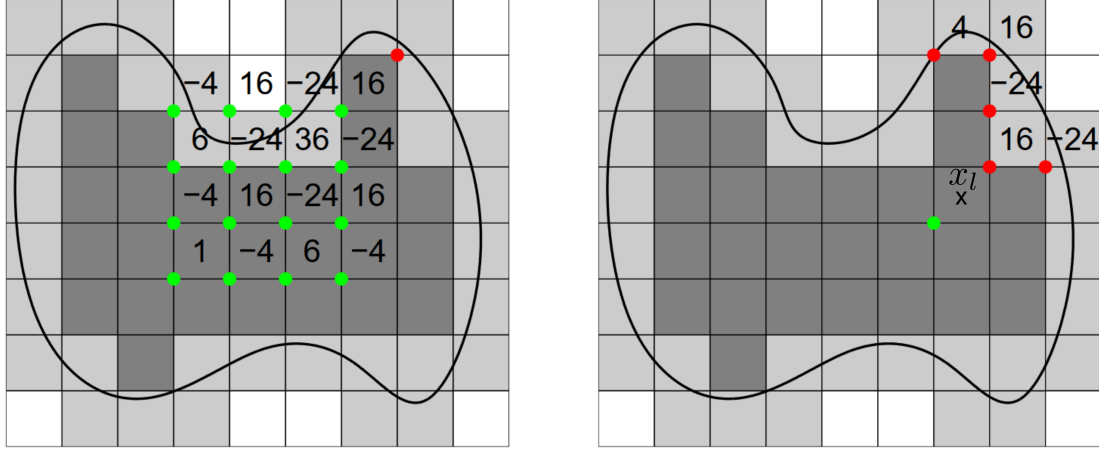-splines is highlighted by a coloured dot. The internal cells are shown in dark gray, the boundary cells in light gray and the external cells in white. [83]

illustration of a web-spline basis function is represented in Figure 2.7. The Ritz-Galerkin matrix obtained using this new web-spline basis has a condition number which is reduced and remains stable as the grid width is reduced. This greatly improves the numerical stability of the finite element method and allows for arbitrary small grid width. In addition, this method allows keeping a regular grid and thus greatly simplifies the localization of the particles in the grid and facilitates the code parallelization with domain decomposition. Finally, it was shown that the web-spline methods necessitates less free parameters than standard triangulation methods. Indeed, in a study calculating the cut-off wave number of wave-guides of arbitrary geometry [68], the authors showed that the number of nodes and computational time was reduced by approximately two orders of magnitude for the same numerical accuracy.

In FENNECS, since the distribution function is sampled with point-like macro-particles defined with Dirac δ functions, the evaluation of the first term of λ_l is straightforward. This term becomes, for an electron distribution function,

$$
\begin{aligned}
\int_D Q \Psi_l^m &= -\frac{e}{\epsilon_0} \int_D \int_v f(\vec{r}, \vec{v}, t) d\vec{v} \Psi_l^m = -\frac{e}{\epsilon_0} \int_D \sum_i N_i \delta(\vec{r} - \vec{r}_i) \Psi_l^m \\
&= -\frac{e}{\epsilon_0} \sum_i N_i \Psi_l^m(\vec{r}_i).
\end{aligned}
\tag{2.27}
$$

In practice, since the basis functions Ψ_l^m have a compact support on mesh cells, only $(m + 1)^n$ basis functions need to be evaluated for each macro particle i. The source term is therefore calculated by looping through all the macro-particles and accumulating their contribution to the $(m + 1)^n$ elements λ_l, for which $\Psi_l^m(\vec{r}_i)$ is non-zero.
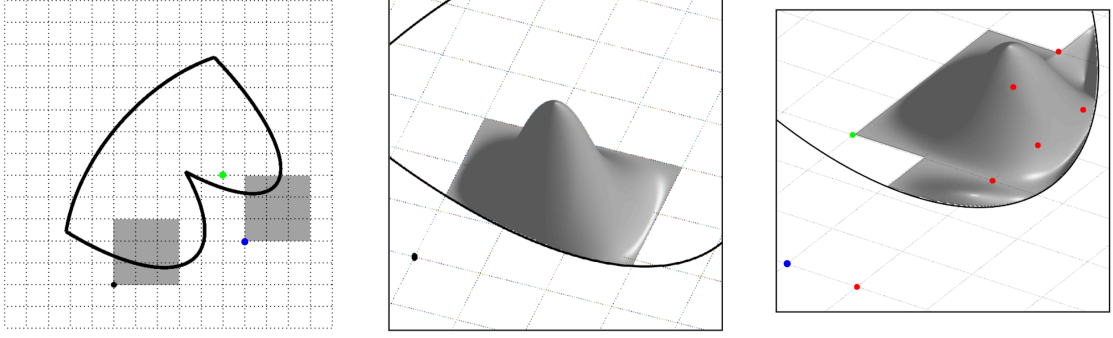
Figure 2.7: Left: Representation of an illustration domain delimited by the solid black line. The colored dots denote the lower left corner of three relevant b-splines used in the two other representations of this figure. Middle: Weighted internal b-spline highlighted by a black dot in the lower left corner of its support. Right: Web-spline constructed by the inner b-spline denoted by the green dot and boundary b-splines denoted by the red and blue dots. The red dots are not represented in the left image for clarity. [83]

2.2.5   Implementation of the web-splines method

As described in Section 2.2.4, the Poisson equation is effectively solved by using the linear system of equations

$$\overleftrightarrow{A} \cdot \vec{u} = \vec{\lambda}, \tag{2.28}$$

where the matrix and vectors are defined with the web-spline basis

$$\Psi_{l,web}^m = \frac{w}{w(x_l)} \left[b_l^m + \sum_{k \in K(l)} e_{lk} b_k^m \right]. \tag{2.29}$$

This basis is however not easy to manipulate numerically. This is the case both during the integration of the basis to generate the linear system of equations and during the evaluation of the solution. One easier method is to work first in a regular weighted b-spline (wb-spline) basis to calculate a matrix $\overleftrightarrow{A}'$ with coefficients

$$A_{ij}' = \int_D \nabla(wb_i^m)\nabla(wb_j^m), \tag{2.30}$$

and a right-hand side vector $\vec{\lambda}'$ with coefficients

$$\lambda_i' = \int_D Qwb_i^m - \nabla\tilde{g}\nabla(wb_i^m). \tag{2.31}$$

This can be calculated directly by looping on the grid cells and the b-spline functions, and using standard numerical integration methods (e.g. Gauss-Legendre quadrature integration). In a second step, all the b-splines are catalogued in the three inner, outer, and boundary splines and a transformation matrix from wb-spline to web-spline space $\overleftrightarrow{E}$ is calculated, with coefficients

$$E_{l,j} = \frac{1}{w(x_l)} \begin{cases} 1 & \text{for } j = l, \\ e_{l,k} & \text{for } j = k \in K(l), \\ 0 & \text{otherwise.} \end{cases} \tag{2.32}$$

With this definition the web-spline basis is equivalent to

$$\Psi^m_{l,web} = \sum_j wb^m_j E_{l,j}. \tag{2.33}$$

The web-spline linear system is then obtained from the wb-spline system through a basis transformation

$$\overleftrightarrow{A} = \overleftrightarrow{E}\overleftrightarrow{A}'\overleftrightarrow{E}^t, \tag{2.34}$$

and

$$\vec{\lambda} = \overleftrightarrow{E}\vec{\lambda}'. \tag{2.35}$$

Here, the superscript t indicates the transposed matrix. The system

$$\overleftrightarrow{A} \cdot \vec{u} = \vec{\lambda}, \tag{2.36}$$

is then solved and the wb-spline coefficient vector $\vec{u}'$ can be obtained through an inverse transformation

$$\vec{u}' = \overleftrightarrow{E}^t \vec{u}. \tag{2.37}$$

The final solution

$$u_h = \sum_i u'_i wb^m_i, \tag{2.38}$$

is also easier to evaluate numerically using standard b-spline libraries in the wb-spline basis than in the web-spline basis.

2.2.6 Boundaries and boundary conditions definitions

With the web-spline method, Dirichlet boundary conditions are imposed by defining the weight function $w(x)$ and the value at the boundary is set with the function $\tilde{g}(x)$. There is freedom in defining $w(x)$ and $\tilde{g}(x)$. In this section, two main methods will be described to create these functions, that are both systematic and robust. For illustration, a 2D domain is considered, but this method can also be applied to 3D. The first method used to define w, that sets the simulation domain D, is based on analytical geometric functions w_i that define elementary geometric shapes. These functions can define, for example, a half-plane, a disc, or a square. One such geometric function w_1 can be the equation delimiting the inside of an ellipse of minor radius a, major radius b and centre (x_0, y_0)

$$w_1(x, y) = 1 - \left(\frac{x - x_0}{a}\right)^2 - \left(\frac{y - y_0}{b}\right)^2. \tag{2.39}$$

These elementary weight functions can be combined by using Rvachev functions to define the union, intersection, or complementary of these elementary domains [85]. This allows the construction of C^1 continuous weight functions everywhere except at the points where both w_1 and w_2 are 0. The union (+) and intersection (-) of two weights w_1 and w_2 can be calculated with

$$w(x, y) = w_1(x, y) + w_2(x, y) \pm \sqrt{w_1^2(x, y) + w_2^2(x, y)}. \tag{2.40}$$

Similarly, the complementary of a domain D is defined by taking the negative of the weight function. This method is used in Sec.2.4.1 to combine two elliptical domains of different major and minor radii and of different centres. For this type of weight, the function $\tilde{g}$ used to impose the Dirichlet boundary conditions

can be defined using transfinite interpolation of the potentials g_i imposed on n_i boundaries ∂D_i and using weights w_i [86]. In this case, the transfinite interpolation of the potentials g_i is:

$$\tilde{g} = \sum_{i=1}^{n_i} g_i \frac{\prod_{j=1; j \neq i}^{n_i} w_j}{\sum_{k=1}^{n_i} \prod_{j=1; j \neq k}^{n_i} w_j}. \tag{2.41}$$

This function ensures that $\forall \vec{x} \in \partial D_i$, $\tilde{g}(\vec{x}) = g_i$. Furthermore, if all w_i are continuous, then $\tilde{g}$ is also continuous and that is needed for the stability and physicality of the solution.

The second method to define a boundary is to use spline curves defined using a set of control points, called "knots", in 2D or 3D. The total weight function w, induced by the boundaries ∂D_i can be computed, in this case, using a smoothed distance function to the curves, blended with a plateau of value 1 inside the domain.

$$w = 1 - \sum_{i=1}^{n_i} \max(1 - d(x, y; \partial D_i)/d_0, 0)^3, \tag{2.42}$$

where $d(x, y; \partial D_i)$ is the shortest distance between the point (x, y) and a point on the boundary ∂D_i, and d_0 is the characteristic fall length from the plateau to 0. This variable d_0 is an input parameter and needs to be chosen such that the shortest distance between two boundaries is always greater than d_0 ($d(\partial D_i; \partial D_j) > d_0$). With this method, $w = 1$ on almost all D and $w < 1$ only at a distance $d < d_0$ of the boundaries. This is useful to ensure that at each position in the domain, only one distance function needs to be calculated. This limits the number of calls to the distance function, as this evaluation is numerically expensive and needs to be computed for each macro-particle. The cubic power in w ensures the C^2-continuity of the weight at the plateau boundary. For this type of boundary conditions, since at most one boundary affects the weight in any position, $\tilde{g}$ can be defined using

$$\tilde{g} = \sum_{i=1}^{n_i} g_i \max(1 - d(x, y; \partial D_i)/d_0, 0)^3. \tag{2.43}$$

Since by the choice of d_0, only one boundary ∂D_i can be at a distance smaller than d_0 anywhere, the relevant boundary i can be pre-computed in each grid cell during the initialization of the geometry and at most one distance must be computed anywhere. Furthermore, for points sufficiently inside the domain, $w = 1$ and $\tilde{g} = 0$, which is equivalent to the classic b-spline FEM. This greatly reduces the execution time of the code.

To impose natural boundary conditions, only the integration domain D needs to be adapted, as the FEM ensures by construction $\nabla_{\perp k} \phi = 0$ on ∂D_k. To define D, the current solution is to consider another weight function $w_N(\vec{x}) = 0 \ \forall \vec{x} \in \partial D_k$ which is used to calculate on each grid-cell, and in each direction, the integration boundaries of D, by finding the roots of w_N. In its current form, FENNECS permits only the definition of Neumann boundary conditions with $\nabla_{\perp k} \phi = 0$ on ∂D_k. However, the web-spline method is more general and the code could be modified with limited effort to include more general Neumann boundary conditions. For the case $\nabla_{\perp k} \phi = g_k$ on ∂D_k, this boundary condition can be imposed by adding a term $\sum_k \int_{\partial D_k} g_k \Psi_l^m$ to λ_l in equation (2.22).

2.2.7 Non-Ideal power supply

In addition to a constant bias imposed on each electrode of the domain, the code can simulate the effect of a non-ideal power supply (PS) imposing the confining biases between two selected electrodes. This

is particularly relevant to reproduce experimental measurements where the bias was imposed using high impedance PS. Indeed, when currents are collected on the electrodes and flow through the high impedance PS, the PS needs to deliver a current which leads to a significant reduction of the applied bias, even for currents of the orders of mA. To reproduce this behaviour, a PS and load circuit in this case are approximated by the circuit of Figure 2.8, in a simplified first attempt to reproduce experimental behaviour of a PS by neglecting inductive effects and the internal capacity of the power supply. The power supply is configured to impose a set voltage V_S supposed to be constant in time, and has an internal resistance R_S. The plasma cloud is described as a current source generating a current $i_p(t)$. In addition, the capacitive effects of the geometry and of the cables connecting the PS and the electrodes is simulated by a capacitor with capacitance C_G connected in parallel with the plasma cloud. This configuration imposes a bias $V_p = V_A - V_B$ between the electrodes and is included in the code by changing in time the values g_j corresponding to the boundaries j (see Sec. 2.2.6) connected to the PS. The ordinary differential equation of this circuit for the potential V_p is

$$\frac{\mathrm{d}V_p(t)}{\mathrm{d}t} = \frac{V_S - R_S i_p(t) - V_p(t)}{R_S C_G}. \tag{2.44}$$
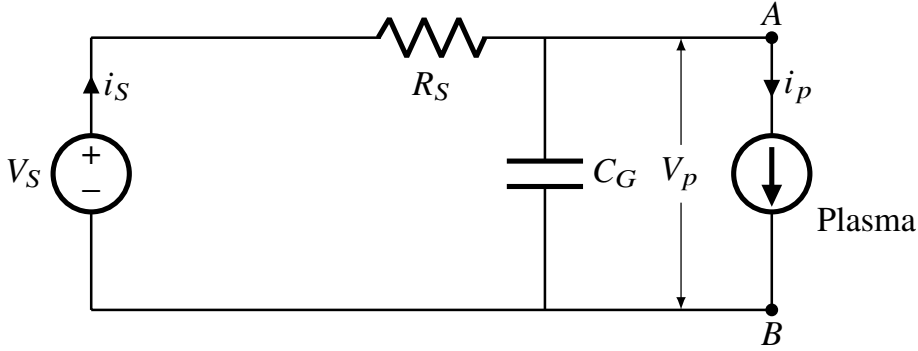

Figure 2.8: Circuit considered to simulate the effect of a non-ideal power supply imposing the external bias between the positive electrode at A and negative electrode at B.

The applied bias V_p is advanced in time using a 4th order Runge-Kutta method every N_s time-steps of the particle advance, by assuming that $i_p(t)$ is only function of time and is given by the PIC simulations. Here, N_s is an input parameter. The plasma current $i_p(t)$ is measured every $N_s/2$ time steps, by accumulating the charge $q(t_i)$ collected at each time step t_i on the electrodes, giving:

$$i_p(t_{i+N_s/2}) = \frac{1}{\Delta t N_s/2} \sum_{j=i+1}^{i+N_s/2} q(t_j). \tag{2.45}$$

Here, Δt is the numerical time step used to evolve the particles position. Since the PS has a fixed characteristic response time, independent of the neutral pressure $p_n = n_n T_n$, and due to the artificial reduction of the timescale separation defined by the parameter α (see Section 2.1.4), the time response of the PS must be rescaled in the simulation. Similarly, as the collected current is linearly proportional to the neutral gas density [26, 72], i_p must be adapted in the simulations. This is particularly important if simulations need to be run for experimental cases in high and ultra-high vacuum. To this end, the value of R_S is rescaled in the simulations defining $R_{S,\mathrm{simu}} = R_{S,\mathrm{phys}}/\alpha$. This has the effect of rescaling the power supply time-scale $\tau_{PS} = R_S C_G$, and is equivalent to rescaling the numerical current $i_{p,\mathrm{simu}}(t)$ by $1/\alpha$ due

to the term $R_S i_p(t)$ in the differential equation (2.44).

2.2.8 Electron-neutral collisions

The electron-neutral collisions are simulated using a standard Monte Carlo approach [87]. For this process, each macro-particle is temporarily treated as a single particle of the simulated species. At each time step, the collision cross-sections σ_{io} and σ_{ela} are evaluated, from tabulated data [74, 88], for each type of interaction and each macro-particle. For each particle i, a random number $x_{i,1} \in [0, 1]$ is generated according to a uniform distribution function and is used to determine if the particle i of kinetic energy E_i and velocity v_i undergoes a collision event.

1. If $x_{i,1} < 1 - \exp(-n_n(\sigma_{\mathrm{io}}(E_i) + \sigma_{\mathrm{ela}}(E_i))v_i\Delta t)$, with Δt the time step, a collision is triggered.

2. The type of collision is determined using a new random variable $x_{i,2}$. If

$$x_{i,2} < \frac{\sigma_{\mathrm{ela}}(E_i)}{\sigma_{\mathrm{io}}(E_i) + \sigma_{\mathrm{ela}}(E_i)}, \tag{2.46}$$

   an elastic collision is triggered, otherwise an ionization event takes place.

3. In case of an elastic event, the first scattering angle χ, in the plane containing the initial electron trajectory and the target, is calculated using a singly differential cross-section for screened Coulomb Collision [75, 89], and a third random number $x_{i,3}$, according to

$$\cos(\chi) = 1 - \frac{2x_{i,3}(1 - \xi)}{1 + \xi(1 - 2x_{i,3})}. \tag{2.47}$$

   Here, $\xi = 4E_i/(E_h + 4E_i)$ and $E_h = \hbar^2/(m_e a_0^2) = 27.21\mathrm{eV}$ is one Hartree, the atomic unit of energy, with $\hbar$ the reduced Planck constant and a_0 the Bohr radius. The second scattering angle $\theta = 2\pi x_{i,4}$, in the plane perpendicular to the initial electron velocity, is obtained with a fourth random number. The electron velocity is then rotated using χ and θ.

4. In case of an ionization event, the energy splitting between the two resulting electrons is determined using a normalized differential cross-section obtained from experimental data [76] with a random number $x_{i,5}$. The scattered electron kinetic energy E_{sca} is

$$E_{\mathrm{sca}} = E^* \tan\big(x_{i,5} \arctan((E_i - E_{\mathrm{io}})/(2E^*))\big), \tag{2.48}$$

   with E^* a fitted scattering factor that depends on the neutral gas [76] and E_{io} the ionization energy of the gas. A new macro-particle is created in the simulation at the position of the particle i and with velocity v_i rescaled such that the kinetic energy of the new particle E_{sec} ensures energy conservation $E_{\mathrm{sec}} = E_i - E_{\mathrm{io}} - E_{\mathrm{sca}}$. The kinetic energy of the incoming particle is then also rescaled to E_{sca}.

5. Both scattered and freed electrons undergo a scattering event using the same differential cross-section as for the elastic collision. The same procedure as in point 3 is used for both electrons.

Depending on the physical system being simulated, the generated ion can either be added to a second species and be tracked in the simulation or not simulated. Ignoring the generated ions is justified in cases where the ions are lost rapidly and where ion induced electron emission happens in regions devoid of trapping mechanism. This rapid loss happens when the ions' Larmor radius is larger than the dimensions of the vacuum vessel, which is typically the case in gyrotron electron gun simulations due to the large

electric field, leading to a large perpendicular velocity, and a comparatively small magnetic field leading to a too small cyclotron frequency. This result will be shown in sections 2.4.4, 4.3.3 and 5.2.4.

2.2.9 Ion induced emission

In simulations with large electrode bias (above 1 kV), the ions generated due to an ionization event are accelerated toward the electrodes and gain large energies, e.g. of the order of several keV. In this regime, their collision with the electrodes can cause ion induced electron emission (IIEE). This process is currently simulated in the code for several types of metallic surfaces, and H or H_2 ions. The electronic yield implemented is the one for H on metals due to the available data, but experimental results indicate that the yield due to H_2 bombardment is close to the one for H bombardment on clean metals in the energy range expected in MIGs [90]. However, for improved comparison with experiments, yield for H_2 on metallic targets are desirable. The IIEE module can therefore only be used with the electron-neutral collision module configured with H_2 gas. The implementation and verification of this module was done in the frame of an EPFL internship [91]. To calculate the electronic yield $\gamma(E_i)$, defined as the average number of electrons released by one impinging ion, two collision regimes are considered depending on the ion kinetic energy E_i. At low kinetic energies, $E_i < 1$ keV, the electrons of the metal are extracted due to the potential energy of the incoming ions [92]. In this case, the yield depends on the ionization energy E_{io} necessary to form the incoming ion, the Fermi energy ϵ_F and the work function Φ of the metal, but is independent of the ion kinetic energy,

$$\gamma_{pot} \approx \frac{0.2}{\epsilon_F}(0.8E_{io} - 2\Phi). \tag{2.49}$$

At large kinetic energies $E_i > 1$ keV, the energy used to free the metallic electron comes from the kinetic energy of the ion and the yield is calculated using a model derived by Schou [90]

$$\gamma_{kin}(E_i) = \Lambda\beta \left(\frac{\mathrm{d}E}{\mathrm{d}x}\right)_e. \tag{2.50}$$

Here, Λ is a material constant, β is a coefficient that accounts for energy transport by recoiling electrons and by back scattered ions, and $\left(\frac{\mathrm{d}E}{\mathrm{d}x}\right)_e$ is the inelastic stopping power of the impacting ion which depends on the ion type and kinetic energy, and on the material type. As the code currently only considers IIEE by Hydrogen atoms, an experimental parameter $\Lambda\beta = \Lambda_{exp} \approx 0.1$ Å eV^{-1} is used, which is independent on the metal type [90, 93]. The inelastic stopping power is taken from tabulated data based on experimental data and theoretical predictions [94, 95]. As both types of collision events can happen in the same simulation, the two yields are blended in the range $0 \leq E_i \leq 1$ keV using a linear interpolation between γ_{pot} and $\gamma_{kin}(1 \text{ keV})$ as seen in Figure 2.9.

To simulate IIEE in the code, the ions generated by electron-neutral collisions are simulated and tracked. Once an ion reaches an electrode, its kinetic energy E_i and yield $\gamma(E_i)$ are calculated. Since the code uses a discrete number of macro-particles, it is usually not possible to generate γ macro-particles. However, this value can be approximated on average by considering events generating an integer number of macro-particles. Since these are rare events, they are well described by the Poisson distribution function. For this reason, to determine the number of macro-electrons generated, a random number k is generated according to a Poisson distribution with mean $< k >= \gamma(E_i)$ such that the probability of freeing k electrons is

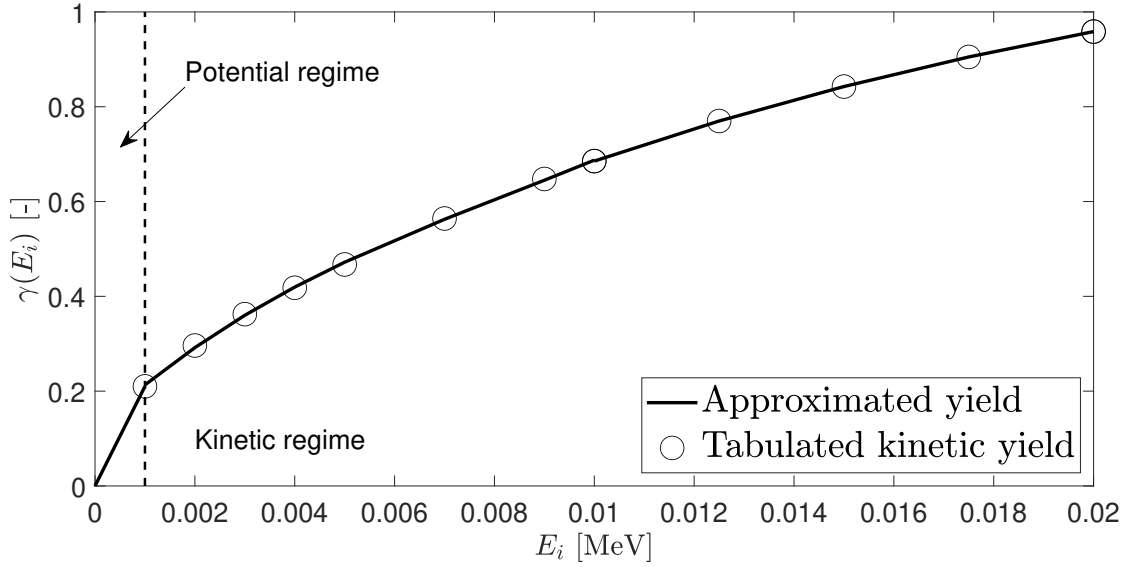$$P(k) = \frac{\exp(-\gamma(E_i))}{k!}. \tag{2.51}$$

Figure 2.9: IIEE yield used in FENNECS for Hydrogen atoms hitting aluminium electrodes as a function of the incoming ion kinetic energy. The circles show the effective yield calculated using (2.50) and tabulated inelastic stopping power [94, 95]. For this electrode material $\gamma_{pot} = 0$.

k macro-electrons are then generated at the last known position of the ion inside the domain. As a first approximation, the k resulting electrons are given a velocity normal to the electrode surface, since it is the most probable direction of emission [90]. To simulate the emitted electron energy spectra [90], the kinetic energy of the generated electrons E_e is given using a gamma distribution function which best fits experimental measurements [96]. We recall here the probability density function of the gamma distribution with parameters κ and θ and mean $< x >= \kappa\theta$:

$$f_\gamma(x) = \frac{1}{\Gamma(\kappa)\theta^\kappa} x^{\kappa-1} \exp\left(-\frac{x}{\theta}\right). \tag{2.52}$$

Here $\Gamma(\kappa)$ is the gamma function

$$\Gamma(\kappa) = \int_0^\infty t^{\kappa-1} e^{-t} dt. \tag{2.53}$$

As a first approximation, the parameters $\kappa = 4$ and $\theta = 0.5$ of the distribution function are independent of the electrode material and impose a mean kinetic energy of the generated electrons $< E_e >= 2\,\mathrm{eV}$, which is consistent with experimental measurements [90]. This approximation is supported by the fact that, in gyrotron gun simulations, large electric fields are externally imposed, and the initial electron kinetic energy becomes negligible compared to the one gained by electric field acceleration.

2.2.10 Seed sources

In addition to the electron sources resulting from the ion-induced electron emission and the impact ionization of the neutrals, a volumetric seed source is implemented in the code. This source can generate electrons in a fixed volume according to various types of distribution functions in velocity. For example, a Maxwellian distribution function with temperature T or a mono-velocity beam can be used. The amplitude and spacial distribution of the source can also be chosen. This source can be used to simulate the effect of

neutral ionization due to background radiation, or to simulate the effect of field-emissions on the electrodes. Indeed, it is sometimes necessary to ensure that some electrons are present at all times in the simulation domain and can start the cloud formation cascade [26]. Without this source, the initial electron cloud population might be entirely lost due to electron-neutral friction drifts and no new electron cloud could be generated.

2.3   Post-processing

In addition to the Fortran PIC code, FENNECS is also bundled with a set of post-processing routines, implemented in MATLAB, to allow the extraction of several physical quantities relevant to the problem at hand. These routines allow the loading and easy manipulation of the raw simulation data. They provide an abstraction layer that reads HDF5 simulation result files, and present to the user standard MATLAB structures and classes, which facilitates the manipulation of the data and reduces the complexity of figures generation. For example, a set of graphical user interface routines have been created to display dynamically the time evolution of the electron density, the fluid velocities, the electrostatic potential and electric field, or the pressure tensor.

The raw data is saved at user-defined regular intervals. This can either be by saving the individual particles physical quantities for studying the full distribution of the simulated species, or by calculating at each grid-point the 0th,

$$n(\vec{r}, t) = \int_{\mathbb{R}^3} f(\vec{r}, \vec{v}, t) d^3 v, \tag{2.54}$$

first,

$$n\vec{u}(\vec{r}, t) = \int_{\mathbb{R}^3} \vec{v} f(\vec{r}, \vec{v}, t) d^3 v, \tag{2.55}$$

and second order,

$$nE_{ij}(\vec{r}, t) = \int_{\mathbb{R}^3} \frac{m_e}{2} v_i v_j f(\vec{r}, \vec{v}, t) d^3 v \tag{2.56}$$

moments of the distribution function in each direction. From these moments, the density and fluid velocity are directly accessible and evaluated at discrete time-steps. The pressure tensor can be calculated with

$$\mathcal{P}_{ij} = \int_{\mathbb{R}^3} m_e (v_i - u_i)(v_j - u_j) f(\vec{r}, \vec{v}, t) d^3 v = n \left(-m_e u_i u_j + 2E_{ij} \right). \tag{2.57}$$

This information is then accessible in the MATLAB class representing the simulation result.

Standard routines have also been written to calculate the potential well in vacuum and in the presence of the electron clouds. Similarly, the electric currents generated by the particles reaching the electrodes can be easily calculated from the particles flux obtained at the grid-cells integrated over the electrode surfaces, and plotted as a function of time. These routines have been used extensively in this thesis to generate the various plots presented.

2.4   Verifications

To verify the correct implementation of the code, a set of test cases have been run and are presented in this section.
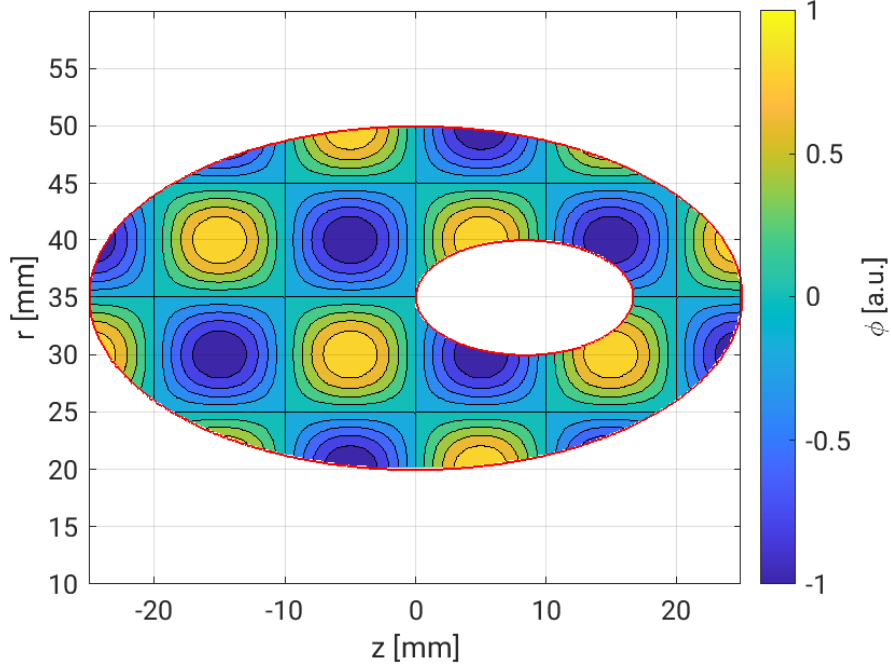
Figure 2.10: Domain and manufactured solution of the potential used to verify the implementation of the FEM solver.

2.4.1 General complex geometry Poisson solver

The Poisson solver is verified using a manufactured solution of the form

$$\phi(r, z) = \sin\left(\pi \frac{z - z_0}{L_z}\right) \sin\left(\pi \frac{r - r_0}{L_r}\right), \tag{2.58}$$

which satisfies the Poisson equation with the source term:

$$
\begin{aligned}
Q(r, z) = &\left(\frac{\pi}{L_z}\right)^2 \sin\left(\pi \frac{z - z_0}{L_z}\right) \sin\left(\pi \frac{r - r_0}{L_r}\right) \\
&+ \frac{\pi}{L_r} \sin\left(\pi \frac{z - z_0}{L_z}\right) \left[-\frac{1}{r} \cos\left(\pi \frac{r - r_0}{L_r}\right)\right. \\
&\left. + \frac{\pi}{L_r} \sin\left(\pi \frac{r - r_0}{L_r}\right)\right],
\end{aligned}
\tag{2.59}
$$

on a domain defined using the Rvachev intersection of two domains defined with ellipses, as represented in Figure 2.10. For this test case, the function $\tilde{g}$ is defined with

$$\tilde{g}(\vec{r}) = \sin\left(\pi \frac{z - z_0}{L_z}\right) \sin\left(\pi \frac{r - r_0}{L_r}\right)(1 - w(\vec{r})), \tag{2.60}$$

and represented in Figure 2.11. Here, $w(\vec{r})$ is the geometric weight function, and the factor $(1 - w(\vec{r}))$ ensures that $\tilde{g} \neq \phi$ to avoid the trivial solution $u = 0$ for which all the spline coefficients u_l are identically 0. The spline grid is defined with $-25 \leq z \leq 25$ mm and $10 \leq r \leq 60$ mm and for an increasing number
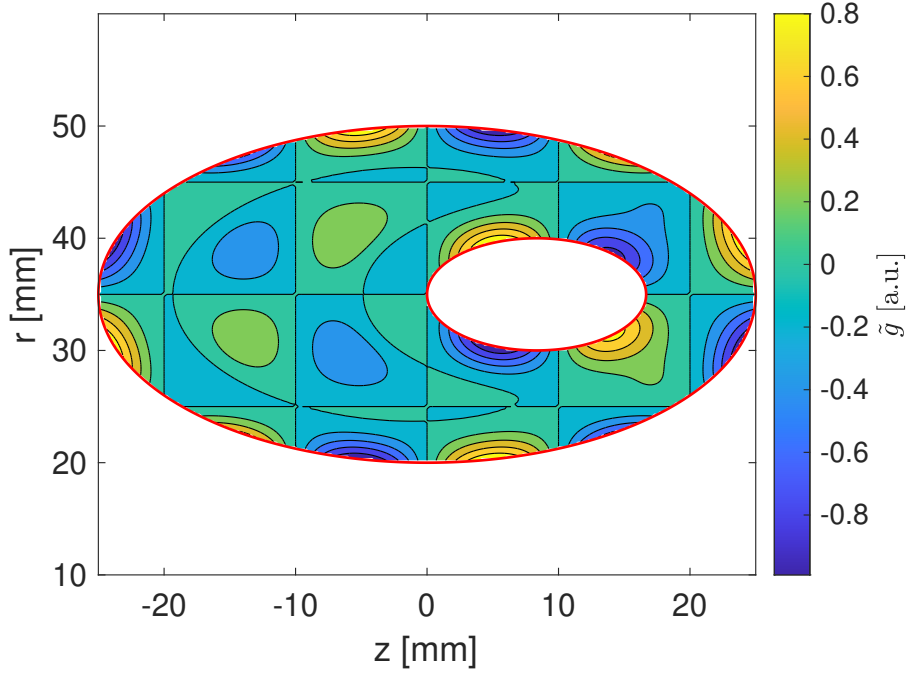
Figure 2.11: Domain and function $\tilde{g}$ used to verify the implementation of the FEM solver.

of grid cells per dimension, from 20 to 960. The manufactured solution parameters are $r_0 = 35$ mm, $z_0 = 0$ mm, $L_r = 10$ mm and $L_z = 10$ mm. The inner ellipse is defined with the geometric weight

$$w_1 = \left(\frac{r - 35}{8.3}\right)^2 - \left(\frac{z - 8.3}{8.3}\right)^2 - 1, \tag{2.61}$$

and the outer ellipse is defined with

$$w_2 = 1 - \left(\frac{r - 35}{15}\right)^2 - \left(\frac{z}{25}\right)^2. \tag{2.62}$$

Here r and z are defined in mm. The total geometric weight w is finally

$$w = w_1^2 + w_2^2 - \sqrt{w_1^2 + w_2^2}. \tag{2.63}$$

The error in the solution is evaluated using both the L^2 and the H^1 norms defined respectively as

$$e_2 = ||\phi_h - \phi||_{L^2} = \left(\int_D (\phi_h - \phi)^2 dV\right)^{1/2}, \tag{2.64}$$

and

$$e_1 = ||\phi_h - \phi||_{H^1} = \left(\int_D (\phi_h - \phi)^2 + |\nabla(\phi_h - \phi)|^2 dV\right)^{1/2}. \tag{2.65}$$

Here, ϕ_h is the numerical solution obtained with the web-splines Poisson solver. It can be shown [82] that $e_1 \sim O(h^{m-1})$ as $h \to 0$ when using web-splines of order m. Similarly, it can be shown that $e_2 \sim O(h^m)$ as $h \to 0$ when using web-splines of order m. Evaluations of the relative error using the H^1 and L^2 norms

Figure 2.12: H1 norm of the relative error for spline orders from 2 to 5 ($\circ, \diamond, \triangle, \square$) and varying grid width h. The dotted line highlights the ideal convergence for each spline order. Each order is colour coded (black, red, blue, magenta) for readability.
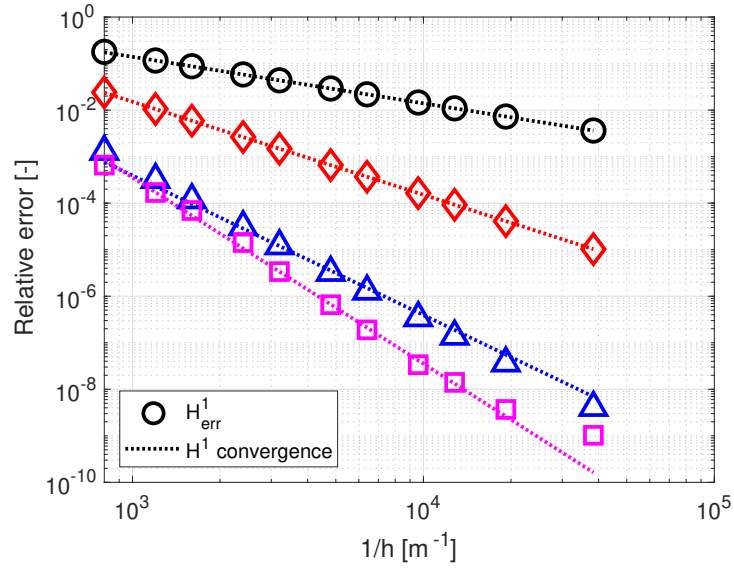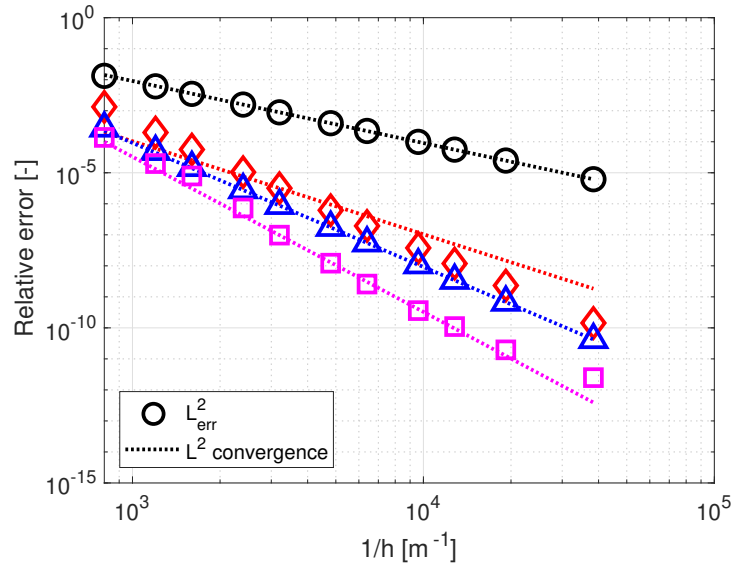

Figure 2.13: L2 norm of the relative error for spline orders from 2 to 5 ($\circ, \diamond, \triangle, \square$) and varying grid width h. The dotted line highlights the ideal convergence for each spline order. Each order is colour coded (black, red, blue, magenta) for readability.
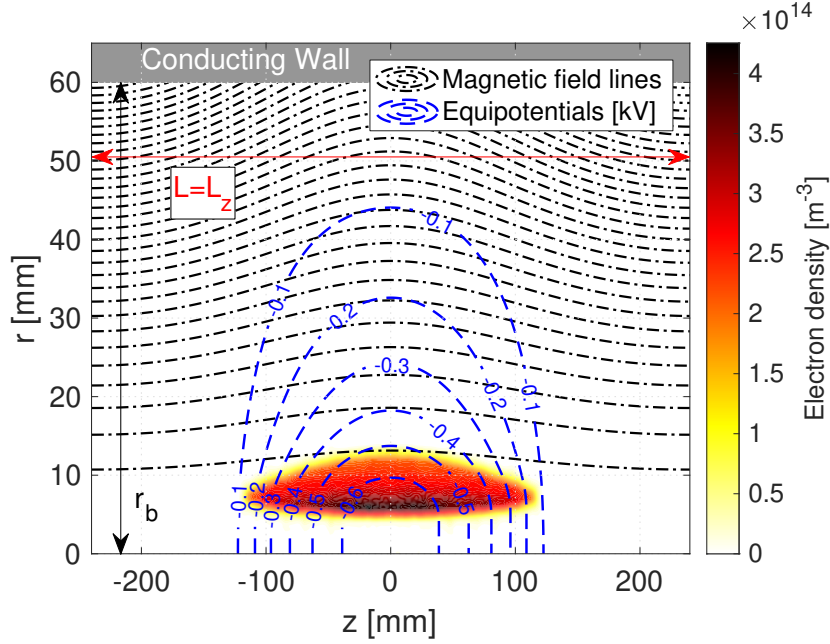
Figure 2.14: Configuration of the test annular electron cloud trapped axially by a magnetic mirror of length L and mirror ratio R. The electric equipotential in equilibrium (dashed blue) and magnetic field lines (dash-dotted black) are represented.

are represented in Figure 2.12 and Figure 2.13 using the manufactured solution previously defined. We observe that the correct convergence rates are recovered for different orders of the web-spline basis.

2.4.2 Equilibrium of a ring of charges trapped in a magnetic mirror

In this section, we present the results of simulations of a pure electron plasma equilibrium for which an analytical solution exists. This particular Vlasov (collisionless) electrostatic equilibrium, shown in Figure 2.14, considers an annular electron cloud trapped radially by a strong magnetic field and trapped axially by a magnetic mirror of length L [32, 97]. This equilibrium is studied analytically in more details in Appendix B. The magnetic vector potential for an externally imposed mirror field, that is needed to compute the canonical angular momentum, is described analytically by

$$A_0^{\text{ext}}(r, z) = \frac{1}{2} B_0 \left[r - \left(\frac{L}{\pi} \frac{R-1}{R+1} \right) I_1 \left(\frac{2\pi r}{L} \right) \cos \left(\frac{2\pi z}{L} \right) \right], \quad (2.66)$$

with B_0 the magnetic field amplitude on axis at $z = \pm L/4$, I_1 the modified Bessel function of order one, L the distance between the mirror coils, and R the mirror ratio defined by $R \equiv B_{max}/B_{min} = B_0^{\text{ext}}(r = 0, z = \pm L/2)/B_0^{\text{ext}}(r = 0, z = 0)$. The distribution function is written in terms of conserved quantities, namely the total energy $H = p^2/(2m_e) - e\phi(r, z)$, with $\vec{p} = m_e \vec{v}$, and the canonical angular momentum $P_\theta = r[p_\theta - eA_0^{\text{ext}}(r, z)]$,

$$f_e(H, P_\theta) = \frac{n_0 R_0}{2\pi m_e} \delta(H - H_0) \delta(P_\theta - P_0). \quad (2.67)$$

Here, n_0 is the maximum electron density in the cloud, R_0 is a reference radial position at which $n_e(R_0) = n_0$, H_0 and P_0 are positive constants, and p_θ is the electron momentum in the azimuthal direction. Equation (2.67) is a solution of the Vlasov equation, which is equation (2.1) with the right-hand-side set to zero. For this equilibrium, one can show that an envelope function describing the electron cloud in space, $\zeta(r, z)$ can be defined [97]:

$$\zeta(r, z) = \frac{p_\perp^2(r, z)}{2m_e H_0} = 1 + \frac{e\phi}{H_0} - \frac{1}{2m_e H_0} \left[\frac{P_0}{r} + eA_0^{\text{ext}} \right]^2, \tag{2.68}$$

such that the curve where $\zeta(r, z) = 0$ denotes the limit of the electron cloud. Here, $p_\perp$ is the momentum perpendicular to $\hat{e}_\theta$ and ϕ is the self-consistent electric potential. The electron density is therefore:

$$n_e(r, z) = \frac{R_0}{r} n_0 U[\zeta(r, z)], \tag{2.69}$$

with $U[x]$ the Heaviside step function. To verify the code implementation, a cloud of electrons is loaded in FENNECS with $H_0 = 3.2 \times 10^{-14}$ J and $P_0 = 8.66 \times 10^{-26}$ kg m^2 s^{-1} in the region where $\zeta_0 = 1 - \frac{1}{2m_e H_0} \left[\frac{P_0}{r} + eA_0^{\text{ext}} \right]^2 > 0$ using a radially uniform and axially non-uniform density distribution function as seen in Figure 2.15. The number of loaded macro-particles is 2116800 with a macro particle weight $w_p = 1.018 \cdot 10^4$ such that the reference density in steady state is $n_0 = 5 \times 10^{14}$ m^{-3}. The simulation domain is defined with a cylindrical volume of radius r_b and length L_z as shown in Figure 2.15. The volume is enclosed radially by a cylindrical conductor of radius r_b at ground. The system and numerical parameters are given in Table 2.1.

B_0	0.21 T
R	1.5
$L = L_z$	0.48 m
r_b	0.06 m
Δz	1.9×10^{-3} m
Δr	2.8×10^{-4} m
Δt	5×10^{-12} s $\approx 0.2 m_e / eB_0$
n_0	5×10^{14} m^{-3}
R_0	0.005 m
H_0	3.2×10^{-14} J
P_0	8.66×10^{-26} kg m^2 s^{-1}

Table 2.1: Physical and numerical parameters used in the simulation of the annular electron cloud trapped in a magnetic mirror.

The simulation is run with a time step $\Delta t = 5 \times 10^{-12}$ s $\approx 0.2/\Omega_{ce}$ and the total kinetic and potential energies of the cloud are monitored. As shown in Figure 2.16, the total energy summed over all particles E_{tot} is conserved on average and the relative error on the energy is kept below 10^{-4} over long time scales as compared to the mirror bounce time of electrons.

During the simulation no particles are lost, and after a time $t = 364$ ns $\approx 460/\omega_{pe}$, the system is in a steady state and successfully retrieves the analytical solution of the equilibrium. In particular, the $1/r$ radial dependency of the electron cloud density, as predicted by equation (2.69), is well reproduced and the cloud remains limited by the envelope function as can be observed in Figure 2.17 and Figure 2.18.

Figure 2.15: Zoom on the initial density loading of the electron cloud and steady-state $\zeta = 0$ contour (dotted magenta). In addition, the electric equipotential (dashed blue) and magnetic field lines (dash-dotted black) are represented.

Figure 2.16: Left: Time evolution of the total (yellow), kinetic (blue) and potential (red) energies during the simulation. Right: Relative error on the total energy conservation during the simulation.
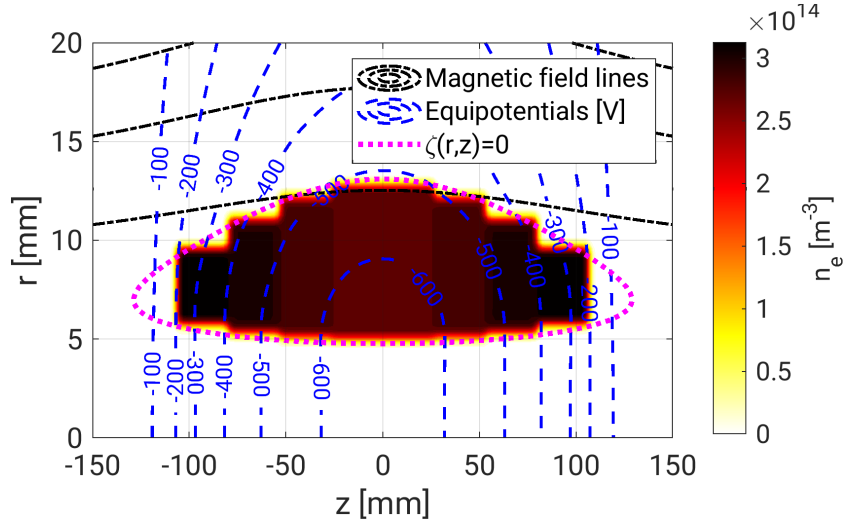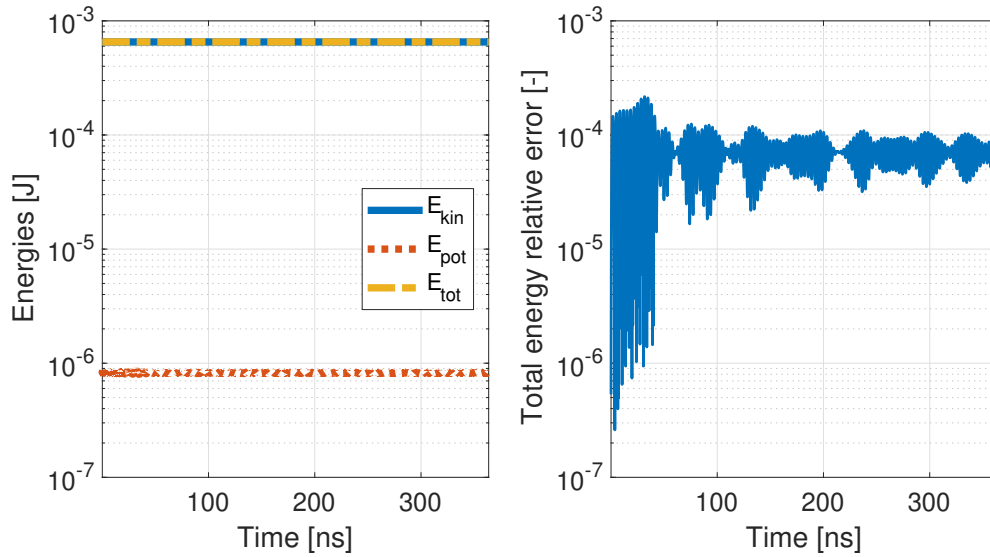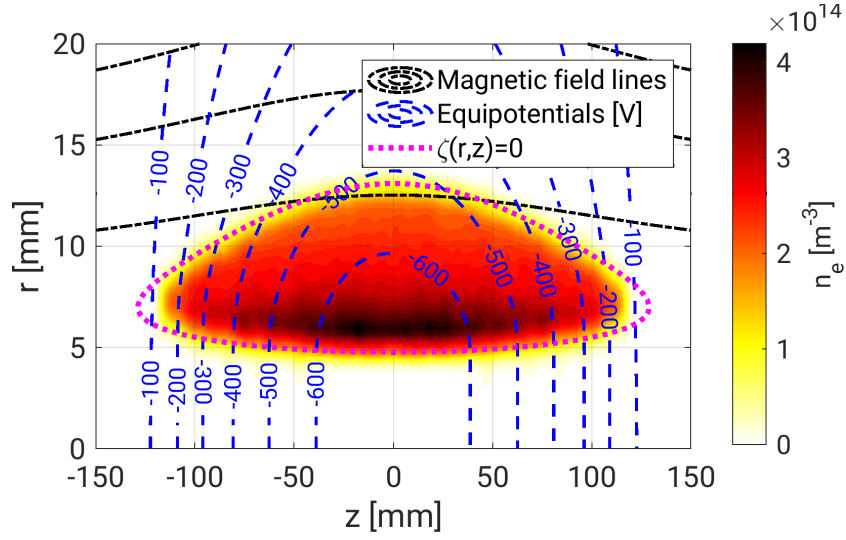
Figure 2.17: Zoom on the final density of the electron cloud and steady-state $\zeta = 0$ contour (dotted magenta). In addition, the electric equipotential (dashed blue) and magnetic field lines (dash-dotted black) are represented.
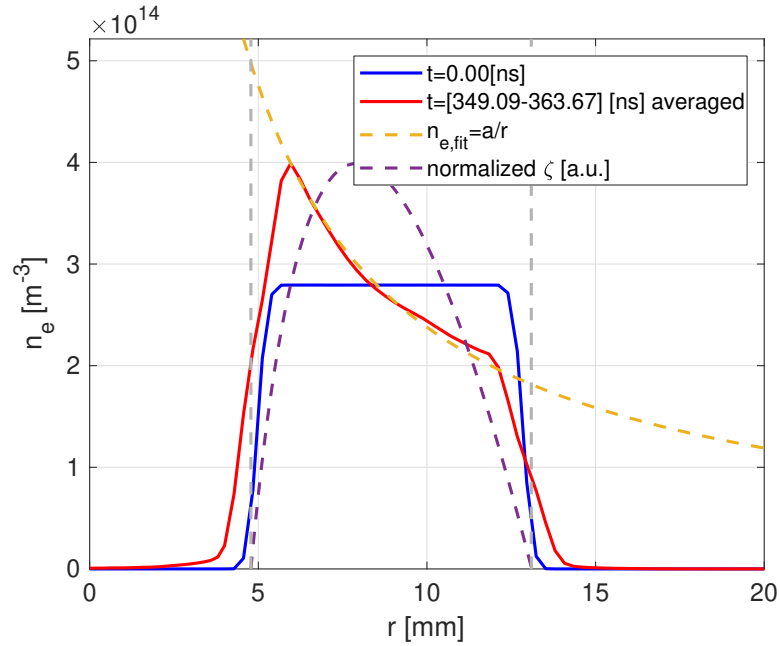
Figure 2.18: Initial (solid blue) and steady-state (solid red) radial density profile at $z = 0$ mm, $1/r$ fit of the steady-state density profile (dashed yellow) and normalized ζ (dashed purple) at the same axial position. The vertical gray dashed lines highlight the radial positions for which $\zeta = 0$.

2.4.3 Radial drifts due to collisions

To verify the electron-neutral collision implementation, an annular electron cloud is considered in a coaxial configuration of infinite length, subjected to a uniform axial magnetic field, and to elastic collisions with a residual neutral gas (ionization is "turned off"). Assuming that the electron distribution function remains close to isotropic, we can study the system using a fluid model [26]. In this model the force balance equation is

$$n_e m_e \frac{d\vec{u}}{dt} = -n_e e \left(\vec{E} + \vec{u} \times \vec{B} \right) - n_e m_e \nu_{ela,mom} \vec{u} - \nabla P. \tag{2.70}$$

Here, $\vec{u}$ is the fluid velocity of the electrons, n_e is the local electron density, $\nu_{ela,mom} = n_n < \int \frac{d\sigma_{ela}}{d\Omega} v d\Omega >_f$ is the averaged collision frequency for momentum exchange, $<>_f$ denotes the average over the distribution function, and P is the pressure. Due to the assumed azimuthal symmetry, the pressure force is identically 0 in the azimuthal direction. Neglecting all inertial terms, equation (2.70) in the azimuthal direction gives the radial electron flux $\Gamma_r(r) = n_e u_r$ caused by the collisional drag:

$$\Gamma_r(r) = -n_e \frac{u_\theta \nu_{ela,mom}}{\Omega_{ce}}. \tag{2.71}$$

In the simulations, the system is defined with a coaxial configuration of "infinite length", using periodic boundary conditions for the particles and natural boundary conditions for the fields. A bias $\Delta\phi = 300\,\text{V}$ is applied between the electrodes and the system is also subjected to a uniform external magnetic field of amplitude $B_0 = 0.28\,\text{T}$. In this configuration, a cloud of uniform density $n_e^0 = 2.5 \times 10^{15}\,\text{m}^{-3}$ and uniform velocity, as represented in Figure 2.19 is loaded on an annulus between $r = 70\,\text{mm}$ and $r = 76\,\text{mm}$. The applied bias, combined with the cloud space-charge, and the static magnetic field impose an azimuthal $\vec{E} \times \vec{B}$ velocity u_θ from which a radial flux is expected according to (2.71). The simulation is then run
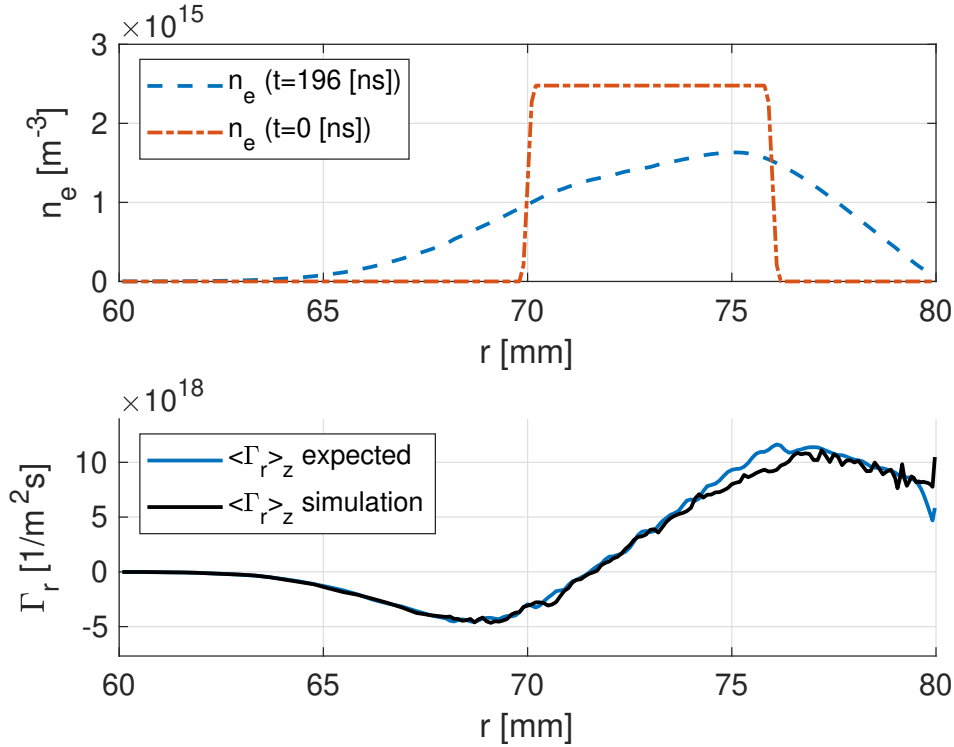

Figure 2.19: Top: Initial and final radial electron density profile. Bottom: Expected (blue) and simulated (black) radial flux at the end of the simulation.

for several elastic collision characteristic times. The simulation results show indeed that the distribution function remains isotropic and that the inertial terms are small compared to the Lorentz and collisional drag terms (data not shown). The radial flux is measured in the code and compared to the prediction obtained using the fluid model (2.71). The fluid azimuthal velocity is extracted from the code, and the averaged collision frequency is evaluated with the electron distribution function extracted from the simulation results. Both the expected and simulated fluxes are averaged along the axial direction to reduce the numerical noise. As shown in Figure 2.19, both fluxes exhibit the same behaviour throughout the simulation domain, with a maximum relative error of 20% at $r = 76$ mm.

2.4.4   Ion induced emission

The IIEE module is verified with a coaxial configuration with an inner electrode at $r_a = 1$ mm and an outer electrode at $r_b = 10$ mm with an axial uniform magnetic field of amplitude $B_0 = 0.21$ T. A bias $\Delta\phi = 20$ kV is imposed between the electrodes and three clouds of 1000 Hydrogen ions each are loaded at different radial positions $r_1 = 3$ mm, $r_2 = 5$ mm and $r_3 = 8$ mm with zero velocity. In this configuration, the ions are accelerated radially towards the central electrode, gaining a kinetic energy $E_{kin}(r_j) \equiv E_j = e(\phi(r_j) - \phi(r_a))$ that depends on their initial radial position r_j. The effective yield obtained in the simulation is then compared to the theoretical yield $\gamma_{kin}(E_j)$ for each initial position r_j. The results of these simulations are given for three electrode materials in Table 2.2, and show an agreement between the theoretical yields γ_{exp} and simulation yields γ_{sim} within 2%.

Material	^{304}SS	r_1	r_2	r_3
	γ_{exp}	1.311	1.623	1.870
	γ_{sim}	1.299	1.627	1.891
	Rel. error	0.9%	0.2%	1.1%
Material	Cu	r_1	r_2	r_3
	γ_{exp}	1.237	1.522	1.746
	γ_{sim}	1.229	1.518	1.760
	Rel. error	0.6%	0.3%	0.8%
Material	Al	r_1	r_2	r_3
	γ_{exp}	0.920	1.133	1.297
	γ_{sim}	0.910	1.115	1.293
	Rel. error	1.0%	1.6%	0.3%

Table 2.2: Expected and simulation yield obtained for the IIEE verification case considering: stainless steel 304, copper and aluminum as electrode material, and 3 initial radial position of the ions.

2.5   Parallel performance

The code is parallelized using a hybrid OpenMP/MPI approach. Indeed, the code is first parallelized using MPI and a non-uniform axial domain decomposition. This choice is supported by the fact that the particle distribution is usually not uniform axially, as illustrated by the test case described in Sec.2.4.2. Thus, to ensure a good load balancing for the computation of the particle trajectories between each task, the axial length covered by each task must be different as illustrated by Figure 2.20 showing the axial domain decomposition for 6 MPI tasks in the configuration of Sec.2.4.2. On each node, OpenMP parallelism is
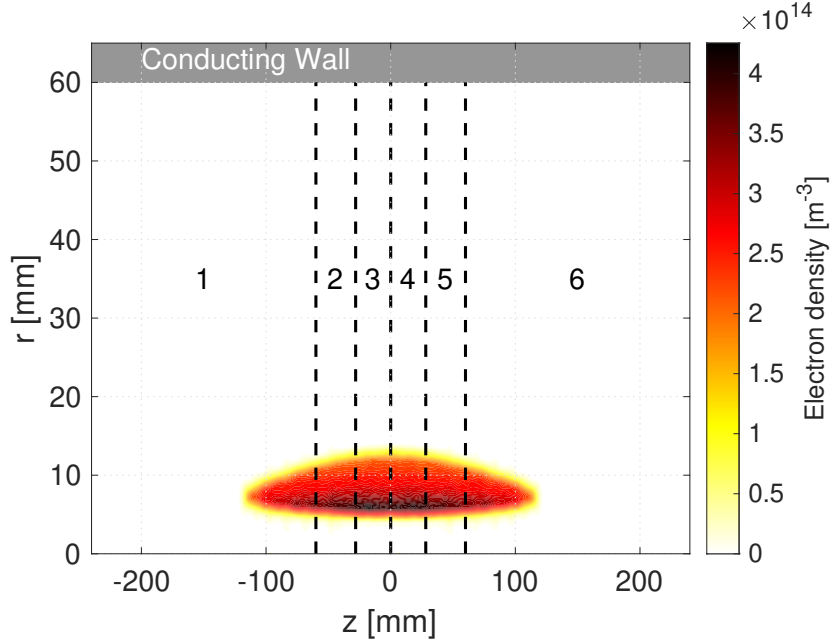
Figure 2.20: Axial domain decomposition for the test case of Sec. 2.4.2 considering 6 MPI tasks. The dashed vertical lines show the axial limits of the domain considered by each MPI task. The subdomains are axially non-uniform to ensure a good particle load balancing between MPI tasks.

used to parallelize the computation of the particle trajectories. The Poisson solver is currently using the MUMPS library in serial mode, but the solver could, in principle, be adapted to leverage the OpenMP and MPI parallelism if larger problems are studied. Strong scaling studies, that measure the reduction in wall clock time for simulations of the same size but with more CPUs available, have been run on the jed cluster of EPFL [98] using an increasing number of tasks and 4 threads per task as shown in Figure 2.21. For this study, we considered a coaxial geometry in which 10 million particles are simulated on a (100x156) grid. Strong scaling studies have been run, which measure the reduction in simulation wall-clock time as a function of the computational resources provided to the code, for a fixed problem size. The strong scaling results show a parallel efficiency above 90% for up to 4 tasks, with each 4 OpenMP threads corresponding to a total of 16 CPUs. The parallel efficiency η_{par} is defined as the ratio between the time t_1 to run the task with a given number of cores, and N times t_N the time needed to run when N times more cores are used ($\eta_{\mathrm{par}} = t_1/(Nt_N)$).

In most simulations using FENNECS, the code is run with 6 tasks and 6 OpenMP workers per task. The number of particles in steady-sate is of the order of 6 million macro-particles with a time-step $\Delta t \approx \frac{2\pi}{30\Omega_{ce}}$. The axial and radial grid width in the trapping region is set to $\Delta r = \Delta z \approx 3 \times 10^{-4}$ m in order to resolve correctly the cloud density profile and the Debye length. With these parameters, the simulations take between 1 and 3 days of wall clock time to reach a steady-state.

2.6 Summary and conclusions

This chapter describes the code FENNECS solving the Boltzmann-Poisson equations for a nonneutral plasma subject to strong electric fields generated by electrodes of complex shapes and space-charge effects,
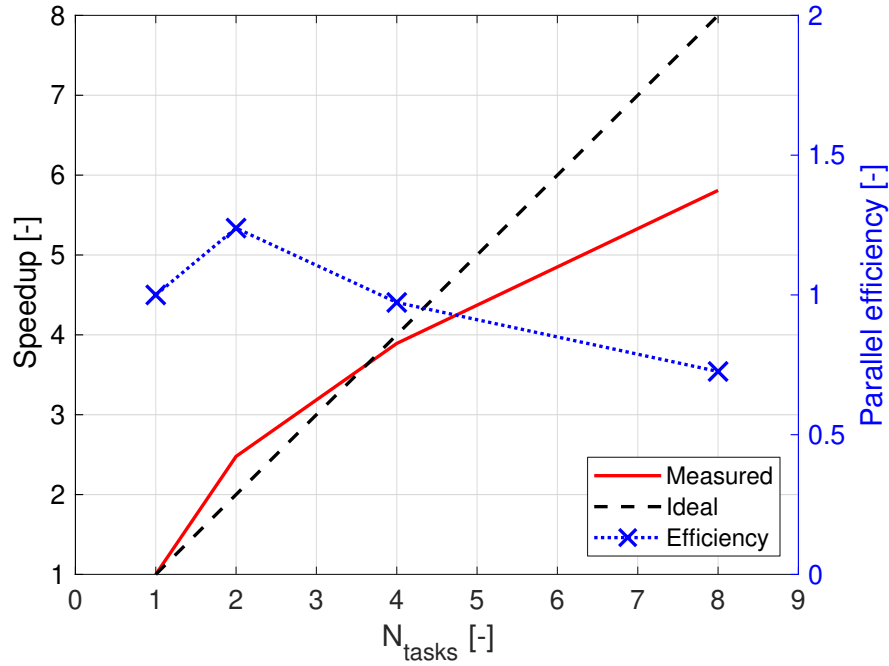
Figure 2.21: Strong scaling and parallel efficiency of FENNECS for a case considering 10M macro-particles in a coaxial geometry. Each task is set to use 4 OpenMP threads.

and to strong external magnetic fields. The novel web-splines numerical method used to simulate the complex electrode geometries present in gyrotron electron guns is also described. The different electron sources considered in the code are presented. More specifically, the Monte Carlo method used to simulate the electron-neutral collisions (elastic and ionization), and the emission of electrons at the electrode surfaces due to collisions of energetic ions on the electrode surfaces are also described. A set of verification cases are presented and confirm the correct implementation of the governing equations. In addition, the cases underline the efficiency of the novel web-spline method and demonstrate its capability of reaching arbitrary precision for the electrostatic potential.

The code is parallelized using a hybrid OpenMP/MPI approach, allowing to leverage the capabilities of modern computers and computational clusters. Scalability studies have shown a reasonable speed-up of the code for workstations and small cluster use. This allows the code to be used for parametric studies and to guide the design of electron guns.

FENNECS is used throughout this thesis to study trapped electron clouds in existing gyrotron electron guns [26, 72] and to show its relevance as a design tool for future gyrotron electron gun. It is also used to support the design of the T-REX experiment [99] and to define the relevant diagnostics and geometries to study the problem of trapped electron clouds in a more controlled environment. Furthermore, the governing equations are expected to be sufficiently general so that the code can also be applied to study arc formations, and more conventional Penning-Malmberg traps. As the code is soon to be open-source, it can easily be adapted to study other problems of plasma physics, where electrode geometric effects are important.

3 Theoretical and numerical studies of trapped electron clouds subjected to fast azimuthal flow

In this chapter, trapped electron clouds are studied in a potential well generated by a simple geometry. This configuration allows access and control to elementary physical quantities while retaining the key components of gyrotron electron guns, mainly the strong magnetic field, the high externally imposed radial electric field and the presence of a residual neutral gas (RNG). In this configuration, represented in Figure 3.1, the dynamics of the cloud and its trapping region are first studied. Then, systematic studies are presented, where a set of external parameters have been varied. Next, a reduced fluid model is derived and verified that explains the relation between the simulated quantities and the control parameters of the scans. Finally, this model is put in closed form using assumptions on the trapped electron cloud geometry, and is used to obtain predictions for the PIC simulation results.

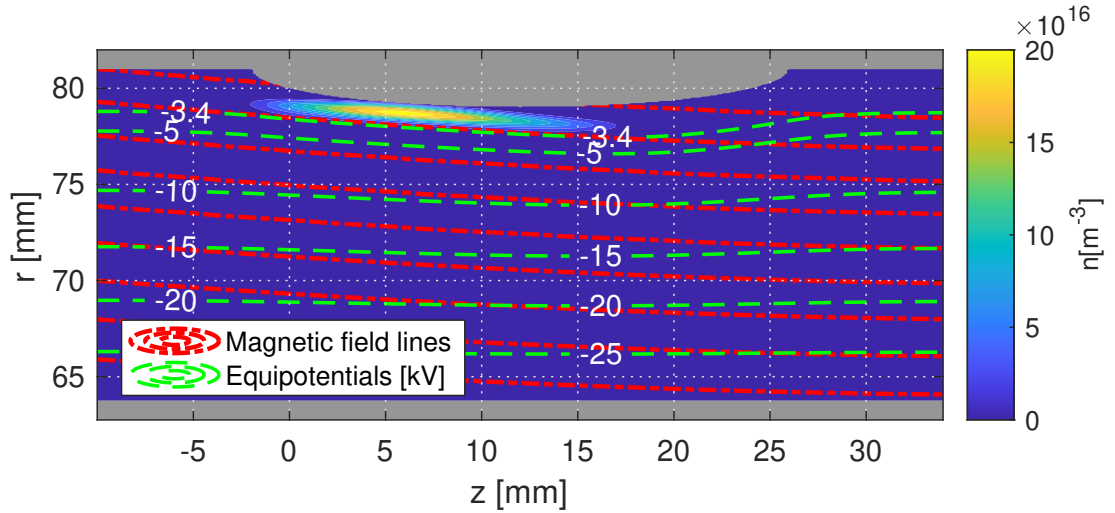Figure 3.1: Geometry and simulation domain. The top and bottom grey parts represent the metallic boundary conditions with an externally imposed bias of $\Delta\phi = 30\,\text{kV}$. The peak magnetic field amplitude in this domain, here in the lower right corner, is $B_{max} = 0.28\,\text{T}$. The cloud density and self-consistent electric equipotential lines are represented at a time when the number of trapped electrons is maximum.

3.1   Simplified geometry and numerical parameters

The geometry used in this chapter, is based on the electron gun geometry used in the first prototype [20] of the 170 GHz 2 MW coaxial gyrotron designed for ITER which will be described in more details in chapter 4, see Figure 3.2. This particular Magnetron Injection Gun (MIG) was subject to voltage breakdown and detrimental leakage currents for specific magnetic field configurations, and had to be redesigned to allow nominal operation [20]. The configuration of this study focuses on the corona ring region of the original prototype gun (red dashed region of Figure3.2), and uses the same magnetic field used for the prototype gyrotron with $B \sim 0.28$ T [100]. This region can be approximated by a coaxial configuration as represented in Figure 3.1, with a central conductor of radius $r_a = 63.75$ mm, and an outer cylinder of radius $r_b = 81$ mm. On the outer cylinder, a region with a half ellipsis shape centred at $r_0 = 81$ mm, $z_0 = 12$ mm, with "major axis" $\delta z = 14$ mm, and "minor axis" $\delta r = 3$ mm is added. Between the central and the outer metallic parts, a bias $\Delta\phi$ is applied which, combined with the externally applied magnetic field $\vec{B}$, induces a strong azimuthal $\vec{E} \times \vec{B}$ drift. Furthermore, due to the upper elliptic region, the electric equipotential lines combined with the magnetic field lines topology lead to the formation of a potential well, see Figure 3.3. In the selected case, the well depth spans the range $U_d = 200 - 3600$ eV for a bias $\Delta\phi$ ranging from 5 to 90 kV. We remark that the value of U_d results from a combination of the externally imposed electric field as well as that generated by the space-charge, and so it can only be known after the simulation is run. In Figure 3.3 both the externally imposed well in vacuum and the self-consistent well in the presence of the cloud are displayed.
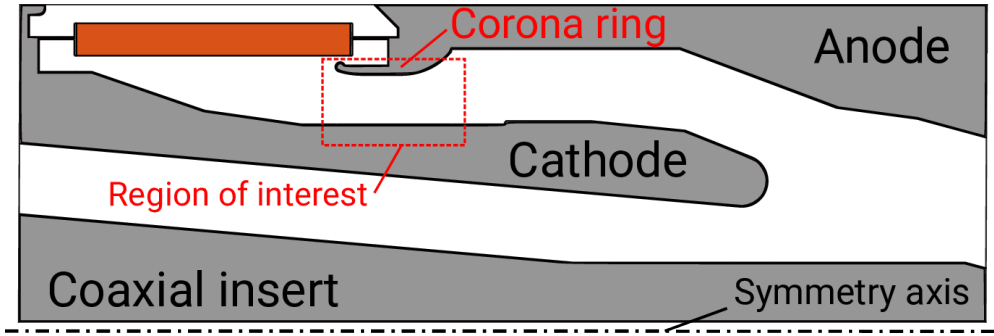

Figure 3.2:   Cut-view of the electron gun used in the first prototype of the 170 GHz 2 MW coaxial gyrotron designed for ITER. This configuration is used as a model for the geometry considered in this study, see Figure 3.1. This representation assumes azimuthal symmetry. Grey indicates a metallic component, orange indicates an insulator, and white represents vacuum.

As described in chapter 2, in the simulations, the RNG pressure is artificially increased to allow running for several collision times while resolving the cyclotron motion. In this study, the neutral pressure is increased to 10^{-1} mbar. The relatively high pressure sets the collision time scales ($\tau_d \sim 5 \times 10^{-9}$ s) closer to the cyclotronic ($\tau_{ce} \sim 1 \times 10^{-10}$ s at $B \sim 0.28$ T), and plasma time scales ($\tau_{pe} \sim 2.5 \times 10^{-10}$ s at $n \sim 2 \times 10^{17}$ m^{-3}), while keeping sufficient timescale separation, such that $\tau_d \gg \tau_{ce}$ and $\tau_d \gg \tau_{pe}$. Despite this timescale "compression", the wall-clock time of a single simulation can be as large as $\sim$ 1 day when running on 36 CPUs. As shown later in Section 3.3.3, the results of this study show that simple scaling laws exist for RNG pressure effects that support the choice of high pressures for numerical simulations. This also allows direct extrapolation of the results to arbitrarily low neutral pressures. In addition, due to the general availability of total and differential cross-section data, the default background gas considered in the simulations of this chapter is Ne. However, other gases relevant to experimental
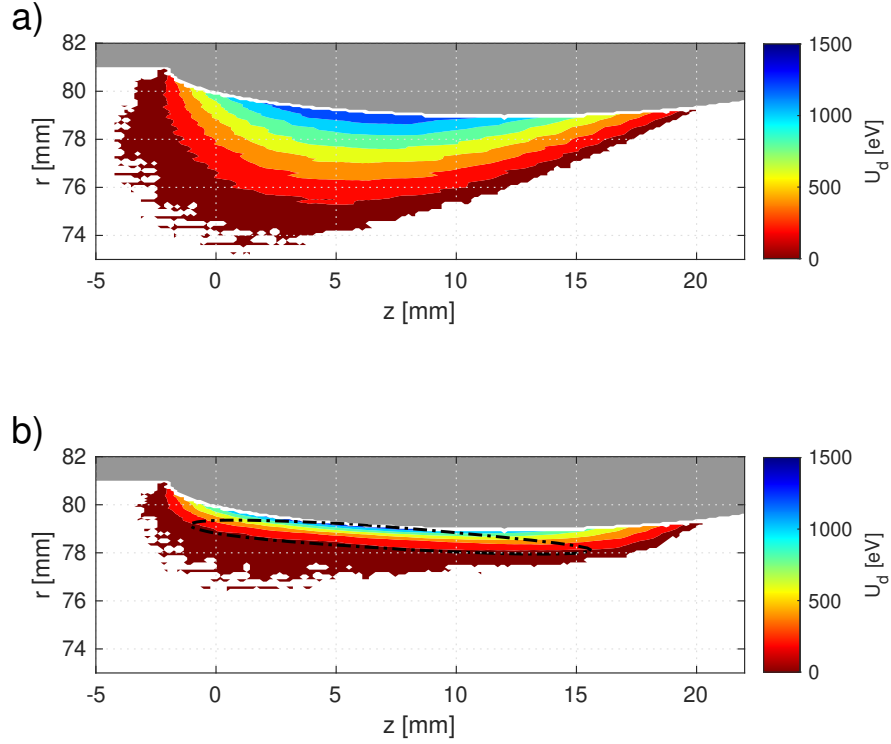
Figure 3.3: Potential well position and depth for the geometry of Figure 3.1. The plots are zoomed on the well region for readability. In a) the potential well is represented in the vacuum condition: no electron cloud is present. In b) the potential well is represented at peak electron density. The black dashed-dotted line represents the cloud edge defined as the positions where $n_e = 0.2\, n_{e,max}$.

setups and gases typically present in vacuum vessels [101] are also used in some simulations and in the following chapters.

3.2 Cloud dynamics

3.2.1 Time evolution

The simulations are initialised, in the presence of a Ne gas background, with a homogeneous low density electron cloud following a Maxwellian distribution with $n_0 = 1 \times 10^{15}\,\mathrm{m}^{-3}$ and temperature $T_0 = 1\,\mathrm{eV}$ acting as a seed for the ionisation process. The electrons outside the vacuum potential well, see Figure 3.3, are rapidly lost axially. The remaining trapped electrons collide with the RNG, leading to the formation of a cloud. This cloud is located close to the elliptic region where the potential well is deepest, see Figure 3.1. The cloud density then slowly increases over time due to ionisation and trapping of the newly created electrons. As shown in Figure 3.4 and illustrated in Figure 3.5, as the cloud density increases, a radial current

$$I_r(r_+) = \int_0^{2\pi} \int_{-L/2}^{L/2} \int_{\mathbb{R}^3} e r_+ v_r(r_+) f(\vec{r}, \vec{v}) d^3 v\, dz\, d\theta, \tag{3.1}$$
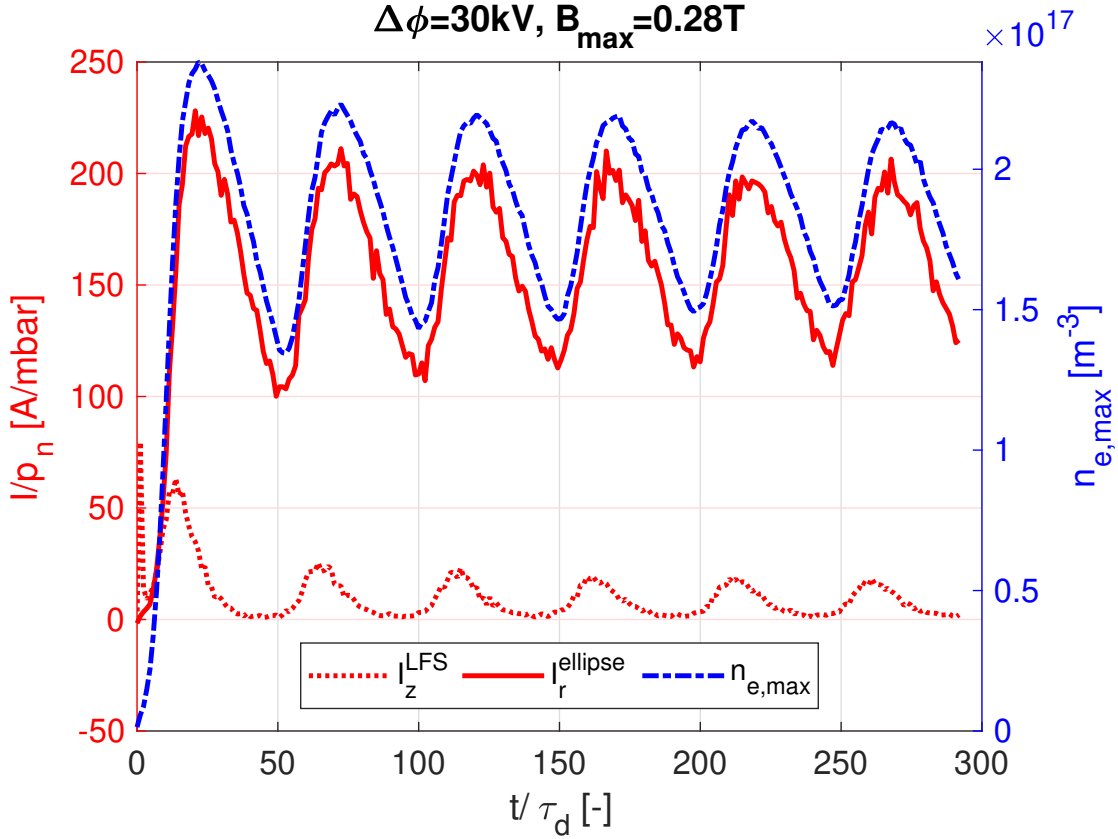
and a comparatively smaller axial current

Figure 3.4: Time evolution of the peak electron density in the simulation domain (blue) and total axial and radial currents (red). The currents are divided by the RNG pressure in mbar and the time is normalised to the total collision characteristic timescale for the momentum exchange. I_z^{LFS} is the axial current at the Low magnetic Field Side (LFS), at $z_L = -10\,\text{mm}$. I_r^{ellipse} is the total radial current collected on the elliptic metallic part. The current on the other boundaries are negligible throughout the simulation.

$$I_z(z) = \int_0^{2\pi} \int_{r_a}^{r_b} \int_{\mathbb{R}^3} erv_z(z) f(\vec{r}, \vec{v}) d^3 v dr d\theta, \tag{3.2}$$

establish, leading to charge losses at the boundaries of the simulation domain. Here, L is the axial extent of the cloud, r_+ is the radial upper limit of the cloud and r_- is the radial lower limit of the cloud as illustrated in Figure 3.5. v_r and v_z are respectively the radial and axial components of the electrons' velocity. During the cloud formation, the electrons drift radially because of the effective azimuthal drag caused by electron neutral collisions, see Figure 3.6. This drift induces an outward-going radial motion of the cloud peak density, see Figure 3.7. At the same time, the density increase causes an increase of the radial electric field amplitude due to the important space-charge effects. As the electron perpendicular velocity is strongly dependent on the $\vec{E} \times \vec{B}$ drift, the increase in E_r induces an expansion of the electron Larmor radius ρ_L, which eventually produces particle losses due to gyro-orbits intersecting the wall. This will induce a local loss of electrons with a characteristic time of the order of τ_{ce}, much faster than the characteristic timescale of losses due to drifts imposed by collisional drag that are of the order of τ_d. It is thus useful to define an
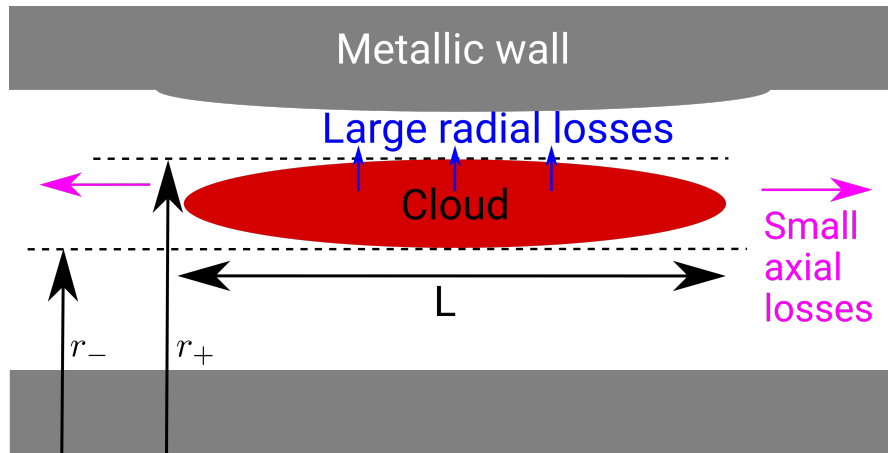
Figure 3.5: Schematic of the trapped electron cloud and of the directions of particle losses. Most electrons drift radially, leading to a strong current in the radial direction (blue) which is collected on the elliptic insert. Fewer electrons are lost along the magnetic field lines causing a weaker current in the axial direction (magenta).

"effective wall" as a virtual surface distanced by two Larmor radii from the metallic wall. This effective wall defines the radial limit above which electrons can potentially hit the metallic boundary. As shown in Figure 3.7, the combination of ρ_L expansion and radial drift of the cloud peak density leads to a moment when the density peak radial position is above the effective wall position. This induces capture of electrons belonging to the cloud peak density by the metallic wall, causing an important radial loss. As the electron source is directly proportional to the electron density, the system is effectively subjected to a modulated source and a modulated sink, and gives rise to oscillations in the cloud density. This effect can be observed in Figure 3.4, where both the maximum cloud density and the boundary currents reach a peak after a few tens of τ_d, when the losses start to dominate and oscillations in the peak density and radial current develop. In the absence of a steady electron seed source, the cloud is completely lost radially after several tens of τ_d. However, the presence of a steady electron seed source can restart the cloud formation process and the cloud density oscillates between a minimum and a maximum value, in a periodic manner, in what could be called "cloud breathing", see Figure 3.4. The seed source amplitude S is selected to be much smaller than the ionization source S_i during the cloud formation, to ensure that its effect is negligible on the radial drifts. It can also be observed from Figure 3.4, that the losses are dominantly radial, while axial confinement remains almost ideal.
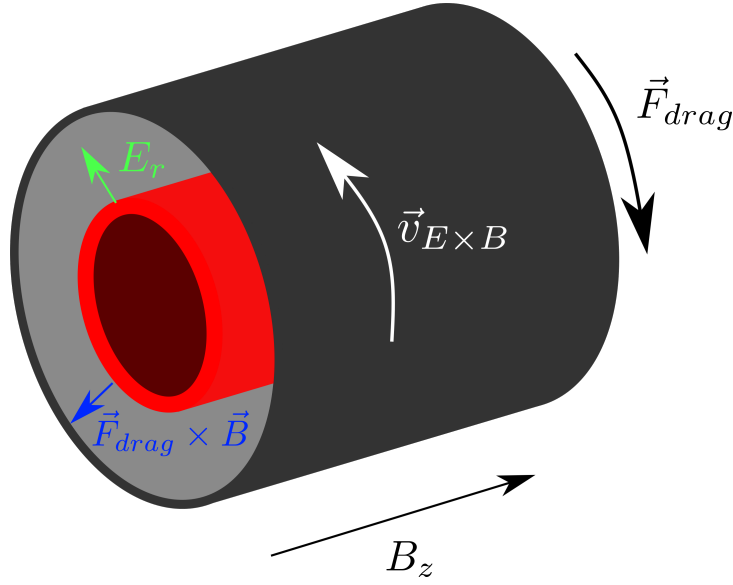
Figure 3.6: Illustration of the radial particle drifts caused by the azimuthal collision drag forces $\vec{F}_{drag}$ and the axial magnetic field B_z.
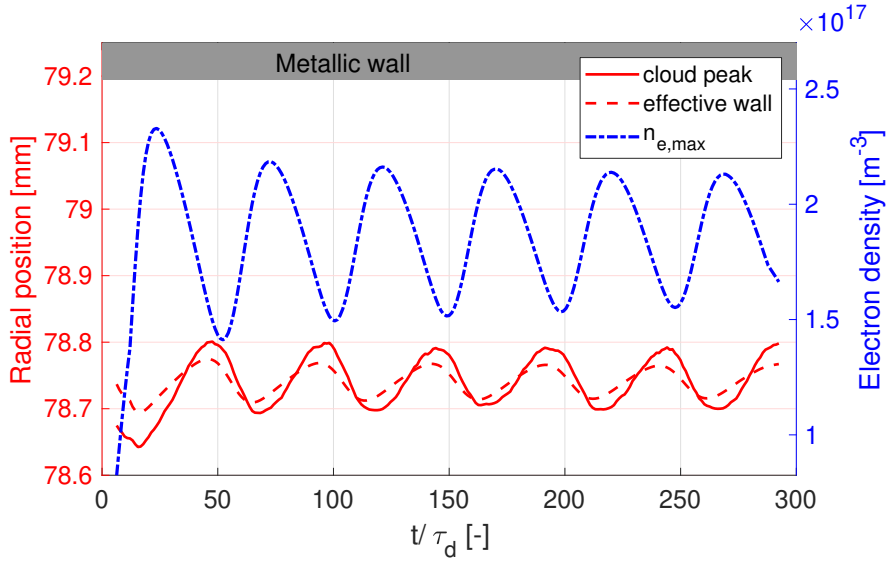
Figure 3.7: Time evolution of the instantaneous spatial cloud peak density radial position (solid red), and of the effective wall radial position (dashed red) for the simulation shown in Figure 3.1 and Figure 3.4. The effective wall is defined as $r_{wall}(z_{peak}) - 2\rho_L(r_{peak}, z_{peak}, t)$ with $r_{wall}(z_{peak})$ the upper metallic wall radial limit at the axial cloud peak position z_{peak}, and $\rho_L(r_{peak}, z_{peak}, t)$ the instantaneous Larmor radius at the cloud peak position (r_{peak}, z_{peak}).

3.2.2 Fluid forces ordering

To derive an analytical model that explains the parametric dependencies observed in the simulations, we evaluate the amplitude of the different forces acting on the electron fluid elements, using simulation results. These forces are evaluated by calculating the moments of the distribution function as extracted from the PIC simulations, at a time when the electron density is maximum, and are then averaged over several electron cyclotron periods to reduce numerical noise. The terms considered in the fluid model are:

- the electric force

$$\vec{F}_E = qn\vec{E}; \tag{3.3}$$

- the magnetic force

$$\vec{F}_B = qn\vec{u} \times \vec{B}; \tag{3.4}$$

- the inertial term

$$\vec{F}_i = -mn(\vec{u} \cdot \boldsymbol{\nabla})\vec{u}; \tag{3.5}$$

- the pressure term

$$\vec{F}_p = -\boldsymbol{\nabla} \cdot \overleftrightarrow{P}; \tag{3.6}$$

- the fluid acceleration term

$$\vec{F}_a = mn\partial_t \vec{u}; \tag{3.7}$$

- the total collisional drag force term

$$\vec{F}_d = -nmn_n \langle \sigma_d v \rangle_f \vec{u} \tag{3.8}$$

which takes into account the effect of elastic collisions, the effect of ionisation collisions on the ionising electrons, and the effective ionisation drag due to the production of new low energy electrons by ionisation.

Here, m and q are the electron mass and charge; n the fluid density; $\vec{E}$ the total electric field taking into account external and self-generated components; $\vec{u}$ the fluid velocity; $\vec{B}$ the external magnetic field; $\overleftrightarrow{P}$ the pressure tensor; $\langle \rangle_f$ denotes the average over the electron velocity distribution function; v is the magnitude of the electron velocity, i.e. the electron speed; σ_d is the total electron-neutral collision cross-section for momentum exchange that is the sum of the effective elastic collision cross-section for momentum exchange σ_{ela}^d, the effective drag caused by the source of cold electrons during ionizations σ_{io}, and the effective drag on the impinging electrons during ionization collisions σ_{io}^d; n_n is the RNG density. It is relevant to observe that the sum of all the force terms in each direction

$$\vec{F}_i + \vec{F}_E + \vec{F}_B + \vec{F}_p + \vec{F}_d - \vec{F}_a \approx 0, \tag{3.9}$$

as this is a strong verification for the implementation of the numerical model. For illustration, the relative error on the force balance $|\Sigma\vec{F}|/|max(\vec{F})|$ is less than 1% in the cloud, for the simulations of this section. In addition, in the plot of the fluid force terms (3.3) to (3.8) in the radial and axial direction (see Figure 3.8 and Figure 3.9 respectively), it can be observed that the dominant terms are the electric and magnetic forces, and that the pressure term is one order of magnitude smaller. In these directions, the inertial force term, and collisional drag term, are completely negligible. In the plot of the fluid force terms (3.3) to (3.8) in the azimuthal direction, represented in Figure 3.10, the dominant terms are the inertial term, the magnetic force and the collisional drag. In this direction, the pressure force is also smaller than all the other terms.

Figure 3.8: Contour plot of the different force terms in the radial fluid force balance equation at a time when the number of trapped particles is maximum. The black dashed-dotted line represents the cloud edge defined as the positions where $n = 0.2\ n_{e,max}$. The red dashed line shows the metallic boundary. Here, the subscript $_r$ denotes the projection along the radial direction.

Figure 3.9: Contour plot of the different force terms in the axial fluid force balance equation at a time when the number of trapped particles is maximum. The black dashed-dotted line represents the cloud edge defined as the positions where $n = 0.2\, n_{e,max}$. The red dashed line shows the metallic boundary. Here, the subscript $_z$ denotes the projection along the axial direction.
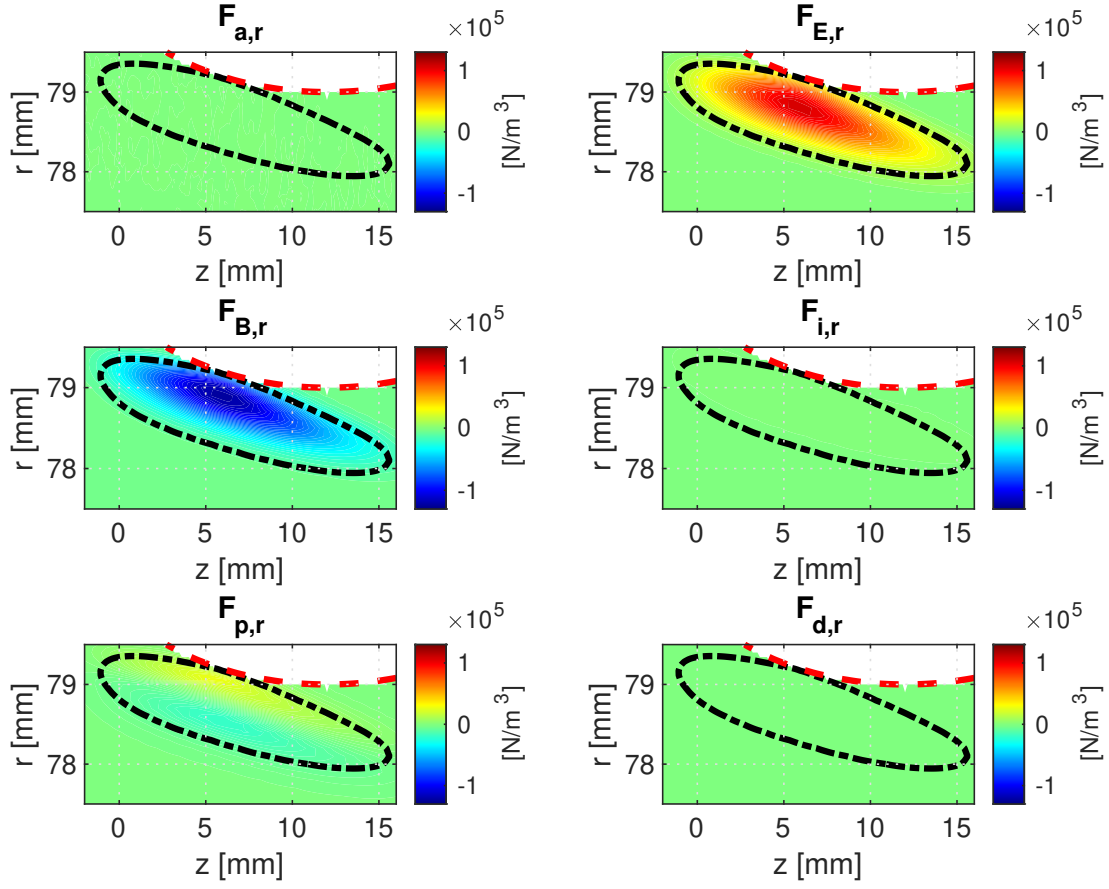
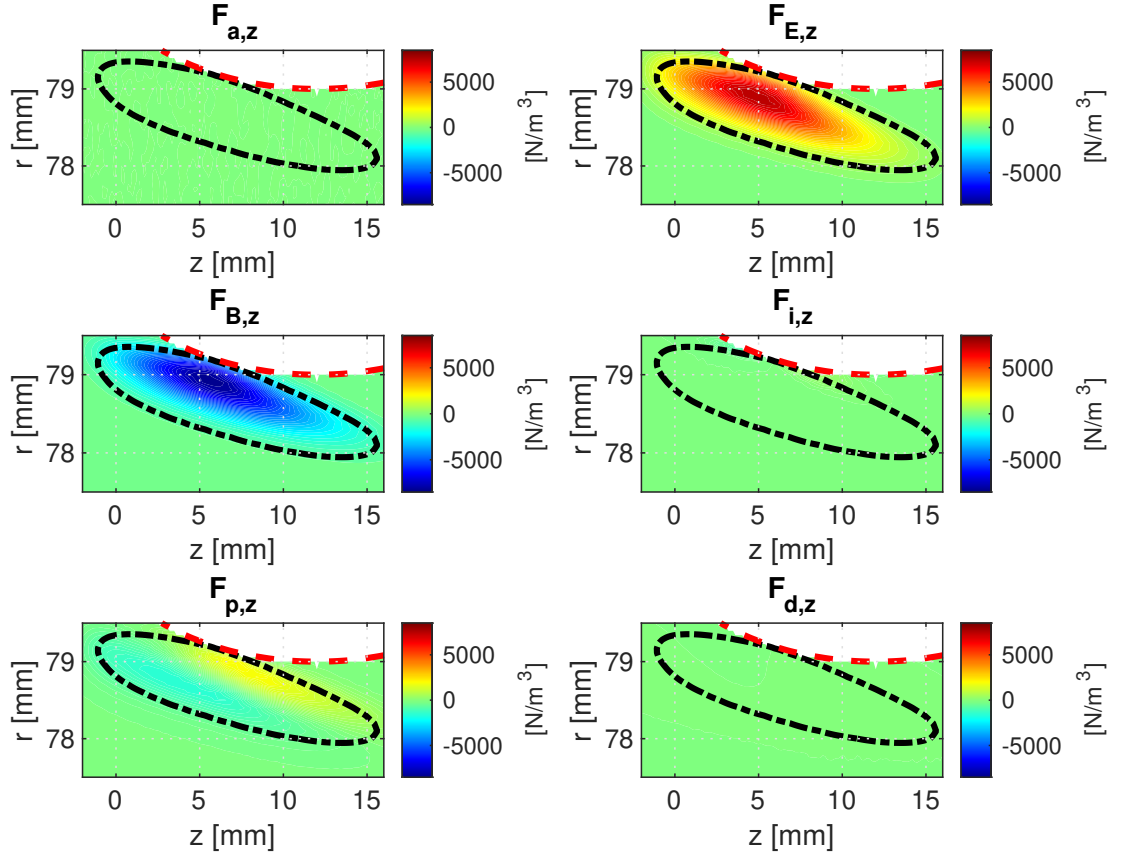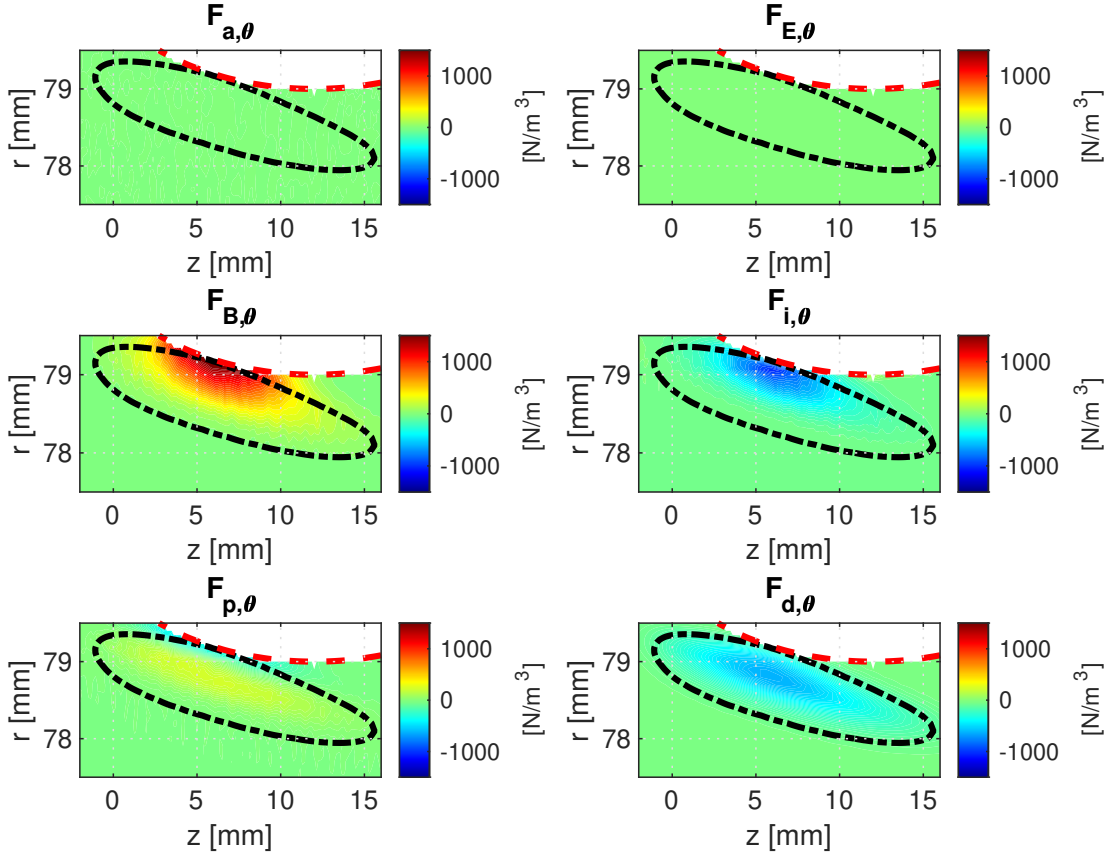Figure 3.10: Contour plot of the different force terms in the azimuthal fluid force balance equation at a time when the number of trapped particles is maximum. The black dashed-dotted line represents the cloud edge defined as the positions where $n = 0.2\, n_{e,max}$. The red dashed line shows the metallic boundary. Here, the subscript $_\theta$ denotes the projection along the azimuthal direction.

3.3 Reduced fluid model

3.3.1 Fluid-Poisson Model

Since FENNECS simulations are numerically expensive, and in order to better understand the underlying mechanisms of cloud build-up and electron losses, a reduced analytical model is desirable. A prediction for the cloud average density and the average radial current density can be derived by considering the electron fluid equations coupled to Poisson's equation (Gauss's law) and neglecting electron pressure effects, which is a simplification that is quantitatively justified by our PIC simulations (see Sec. 3.2.2). We start from the fluid force balance equation:

$$mn\left(\frac{\partial \vec{u}}{\partial t} + (\vec{u} \cdot \boldsymbol{\nabla})\vec{u}\right) = nq(\vec{E} + \vec{u} \times \vec{B}) + \vec{F}_d. \tag{3.10}$$

As shown in Figure 3.8, in the bulk of the cloud, the dominant terms in the radial direction are the electric and magnetic forces, thus the radial component of Eq. (3.10) gives:

$$u_\theta = -\frac{E_r}{B_z}. \tag{3.11}$$

As can be seen in Figure 3.10, the dominant terms in the azimuthal direction are the inertial force ($\vec{u} \cdot \boldsymbol{\nabla}\vec{u}$ term), the magnetic force, and the drag force. Since $B_r \ll B_z$ and in the cloud we also have $u_z \ll u_r$, we can assume $u_z B_r \ll u_r B_z$ and, hence, the azimuthal component of Eq. (3.10) gives, at equilibrium:

$$mu_r \frac{1}{r}\frac{\partial}{\partial r}(ru_\theta) = -qu_r B_z - mn_n\langle\sigma_d v\rangle_f u_\theta. \tag{3.12}$$

Using Gauss's law in cylindrical coordinates,

$$\boldsymbol{\nabla} \cdot \vec{E} = \frac{1}{r}\frac{\partial}{\partial r}rE_r + \frac{1}{r}\frac{\partial}{\partial \theta}E_\theta + \frac{\partial}{\partial z}E_z = \frac{\rho}{\epsilon_0}, \tag{3.13}$$

combined with the azimuthal symmetry ($\partial_\theta = 0$), and assuming an elongated cloud and potential well such that $|\partial_z E_z| \ll |\frac{1}{r}\partial_r(rE_r)|$ we obtain:

$$\frac{1}{r}\frac{\partial}{\partial r}rE_r = \frac{\rho}{\epsilon_0}. \tag{3.14}$$

Here, $\rho = qn$ is the charge density. The left-hand side of Eq. (3.12) can be rewritten by using the expression for the azimuthal velocity, Eq. (3.11), assuming $E_r\partial_r(1/B_z) \ll \frac{1}{rB_z}\partial_r(rE_r)$, and using Eq. (3.14), to obtain:

$$mu_r \frac{1}{r}\frac{\partial}{\partial r}(ru_\theta) = -m\frac{u_r}{B_z}\frac{1}{r}\frac{\partial}{\partial r}rE_r = -m\frac{u_r}{B_z}\frac{qn}{\epsilon_0}. \tag{3.15}$$

Rewriting Eq. (3.12) then gives the radial fluid velocity as:

$$u_r = -\frac{qn_n\langle\sigma_d v\rangle_f}{m}\frac{E_r}{\omega_p^2 - \Omega_c^2}. \tag{3.16}$$

Here, $\Omega_c = qB/m$ is the cyclotron frequency and $\omega_p = \sqrt{q^2 n/(\epsilon_0 m)}$ is the plasma frequency. This equation shows a singularity as the Brillouin ratio f_b approaches 2. We will see however in Sec. 3.3.4, that typical equilibria reach $f_b \le 1$.

The time-averaged density can be obtained by starting from the time average of the continuity equation:

$$\left\langle \frac{\partial n}{\partial t} + \boldsymbol{\nabla} \cdot (n\vec{u}) \right\rangle_T = \left\langle nn_n \langle \sigma_{io} v \rangle_f \right\rangle_T, \tag{3.17}$$

where σ_{io} is the ionisation cross-section and $\langle \rangle_T$ denotes the time average over one cloud breathing oscillation. Considering the case of density oscillations at the spatial peak density:

$$\left\langle \frac{\partial n}{\partial t} \right\rangle_T = 0 \text{ and } \boldsymbol{\nabla} n = 0; \tag{3.18}$$

assuming dominant radial losses, azimuthal symmetry and using the radial velocity obtained in Eq. (3.16), the continuity equation can be rewritten as:

$$-\frac{q}{m} \left\langle \frac{n}{r} \frac{\partial}{\partial r} r \left[\frac{n_n \langle \sigma_d v \rangle_f}{\omega_p^2 - \Omega_c^2} E_r \right] \right\rangle_T = \left\langle nn_n \langle \sigma_{io} v \rangle_f \right\rangle_T. \tag{3.19}$$

Using Gauss's law and the fact that $\boldsymbol{\nabla} n = 0$ at the peak density once more, as well as the assumptions used in Eq. (3.15), we can recover the electron density by isolating ω_p^2, thus obtaining an expression for the time averaged plasma frequency at the spatial peak:

$$\omega_{p,max}^2 = \Omega_c^2 \left\langle \frac{\langle \sigma_{io} v \rangle_f}{\langle \sigma_{io} v \rangle_f + \langle \sigma_d\, v \rangle_f} \right\rangle_T. \tag{3.20}$$

which gives directly the average cloud density at the spatial peak $n_{e,max}$. This result immediately predicts a quadratic dependence of $n_{e,max}$ on the magnetic field amplitude ($n_{e,max} \propto B^2$), as we will see in the parametric scans of Section 3.3.3 (see Figure 3.12).

Using the radial velocity (Eq. 3.16) and average density (Eq. 3.20) previously derived, and assuming zero axial velocity, we can also obtain an estimate for the peak current by integrating the loss term $\boldsymbol{\nabla} \cdot n\vec{u}$ over the cloud volume (see Figure 3.5):

$$I = \int_0^{2\pi} \int_{r_-}^{r_+} \int_{-L/2}^{L/2} \langle q \boldsymbol{\nabla} \cdot (n\vec{u}) \rangle_T r\, d\theta dr dz \approx -2\pi L r_+ \epsilon_0 n_n \langle E_r \langle \sigma_{io} v \rangle_f \rangle_T. \tag{3.21}$$

Where L is the characteristic cloud axial length and r_+ the cloud outer radial limit. These geometric quantities can be estimated from the potential well dimensions in vacuum. It can be observed that this current is linearly proportional to the RNG density n_n, but has a more complex scaling in electric and magnetic field due to the non-trivial dependency of $\langle \sigma_{io} v \rangle$ on these terms. These dependencies are verified with a reasonable accuracy in section 3.3.3, but with more uncertainties on the predicted current due to the assumptions on the final cloud dimensions.

3.3.2 Collision frequencies calculation

To predict the peak electron density and current using Eq. (3.20) and Eq. (3.21), it is necessary to calculate the collision frequencies by averaging σv over the electron velocity distribution function. Figure 3.11 shows the electron velocity distribution function obtained from FENNECS at the position and time where the electron density is maximal. Due to the large $\vec{E} \times \vec{B}$ drift, the average speed of electrons is dominated by the azimuthal component of the average velocity, such that $\vec{u} \approx \vec{E} \times \vec{B}/B^2$. Furthermore, the variance of the speed distribution and the variance of the kinetic energy distribution are relatively small (see first

and second plot of Figure 3.11). We may therefore approximate the collision frequencies ν as follows:

$$\nu = n_n \langle v\sigma(E_k) \rangle_f \approx n_n \left| \frac{\vec{E} \times \vec{B}}{B^2} \right| \sigma \left(\frac{1}{2}m \frac{|\vec{E} \times \vec{B}|^2}{B^4} \right). \tag{3.22}$$

Here, $E_k = mv^2/2$ is the classical kinetic energy of the electrons. The quality of this approximation can be assessed by looking at the figure on the right-hand side of Figure 3.11, where we see a close agreement between the averaged collision frequencies computed using the electron distribution function extracted from the PIC simulations, and the approximate collision frequencies given by Eq. (3.22). With these definitions, Eq. (3.20) and Eq. (3.21) are used to verify the analytic model for the parametric scans of Section 3.3.3.
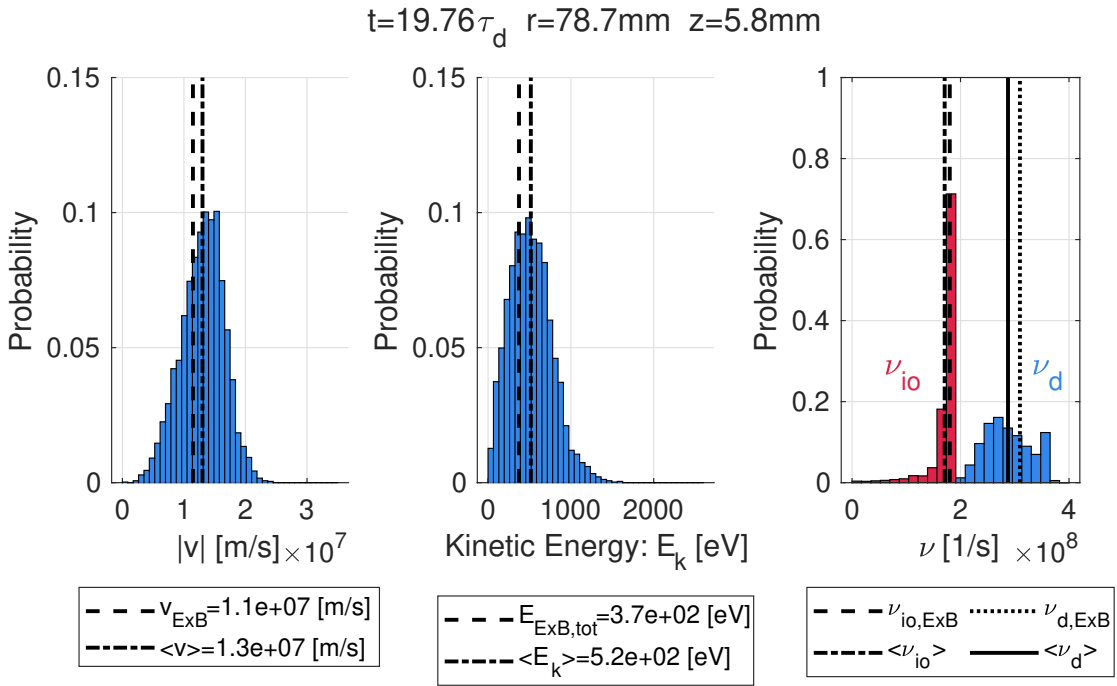
Figure 3.11: Electron velocity distribution (left), kinetic energy distribution (middle), and collision frequencies distribution (right), extracted from the PIC simulation shown in Figure 3.1 and Figure 3.4, and represented at a time when the density is maximum, and at the position of peak density. For comparison, the average is represented by the dash-dotted and solid lines. The dashed lines and the dotted line are the equivalent quantity if the velocity of the electron is exactly the local $\vec{E} \times \vec{B}$ velocity.

3.3.3 Parametric scans

To validate the reduced fluid model derived in section 3.3 and isolate the operational parameters determining the peak electron density and boundary current amplitudes, $n_{e,max}$ and I_{max}, parametric scans are performed. The scanned parameters are:

- the maximum magnetic field amplitude $B_{max} = 0.14 - 0.56\,\text{T}$,

- the applied external bias $\Delta\phi = 5 - 90\,\text{kV}$,

- the RNG density $p_n = 10^{-2} - 10^{-1}\text{mbar}$,

- the gas species $\text{He}, \text{H}_2, \text{Ne}, \text{Ar}$.

The results of the first three scans are shown respectively in Figure 3.12, Figure 3.13, and Figure 3.14. The scan on the gas specie, which modifies the collision cross-sections and the ratio between the ionisation collision frequency ν_{io} and the effective collision frequency for momentum exchange ν_d is shown in Figure 3.15. We find that the peak density has a quadratic dependence on the magnetic field amplitude, see Figure 3.12 (a), it has a non-trivial dependence on the external bias, see Figure 3.13 (a), it is independent of the RNG pressure, see Figure 3.14 (a), and it is linearly proportional to $\nu_{io}/(\nu_d + \nu_{io})$, see Figure 3.15 (a). Based on the PIC simulation results, the radial current appears to scale linearly with B_{max}, see Figure 3.12 (b), to have a non-trivial dependency on the external bias, see Figure 3.13 (b), to be linearly proportional to the RNG pressure, see Figure 3.14 (b), and finally to be linearly proportional to the ionisation frequency ν_{io}, see Figure 3.15 (b).
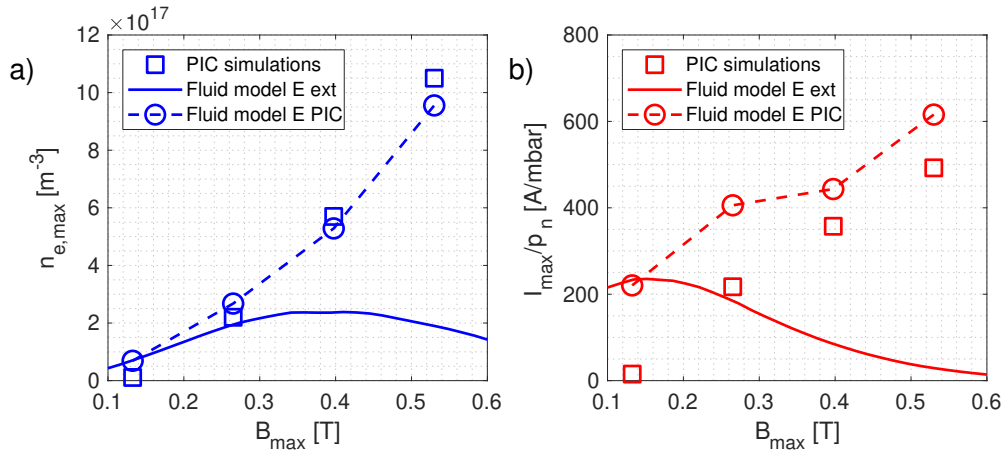
Figure 3.12: a) Evolution of the maximum electron density in the cloud as a function of the maximum magnitude of the magnetic field in the cloud region. b) Evolution of the maximum radial current, normalized to the RNG pressure, as a function of the maximum magnitude of the magnetic field in the cloud region. The applied bias is $\Delta\phi = 30\,\text{kV}$ and the RNG pressure is $p_n = 1 \times 10^{-1}$ mbar. For both a) and b) the squares represent numerical results extracted from the PIC simulations; the solid line is a prediction using the model of Section 3.3 using only the external electric field for calculating the collision cross-sections; and the circle dashed line is obtained from the same model but using the full electric field (external plus self-consistent) extracted from the PIC simulations.
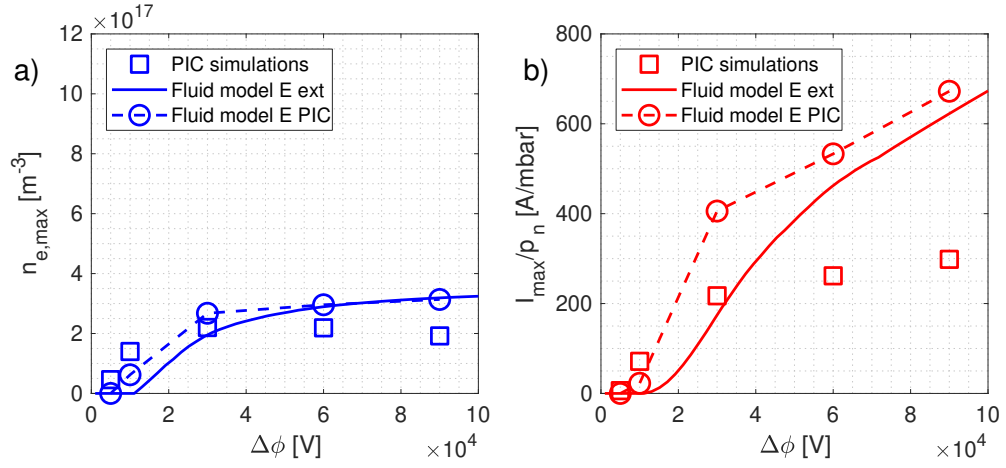
Figure 3.13: Same as Figure 3.12 but as a function of the electric bias. The magnetic field amplitude is set at $B_{max} = 0.28$ T and the RNG pressure is $p_n = 1 \times 10^{-1}$ mbar.

Figure 3.14: Same as Figure 3.12 but as a function of the RNG pressure. The externally applied bias is set at $\Delta\phi = 30$ kV and the magnetic field amplitude is set at $B_{max} = 0.28$ T. In this case, only the self-consistent electric field is considered. We need to remind that I_{max} is normalized by p_n in b) and that the flat response indicates a linear proportionality of I_{max} on p_n.
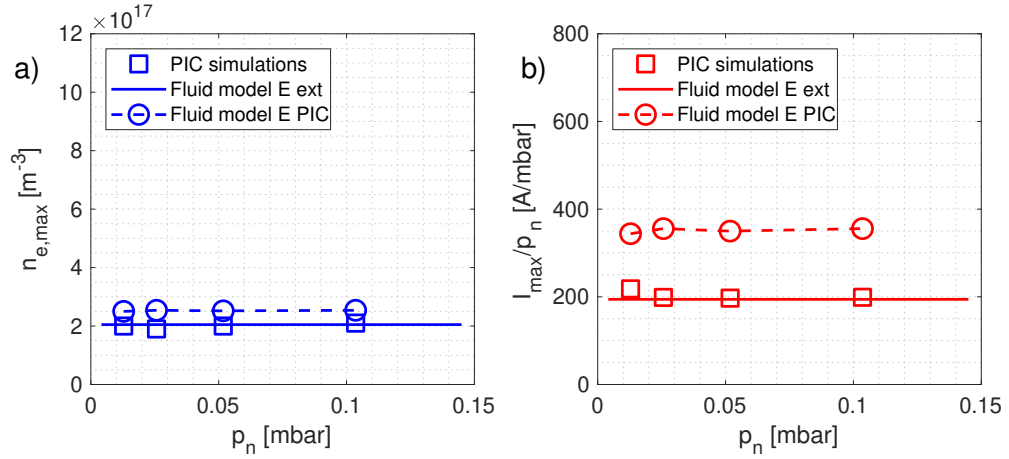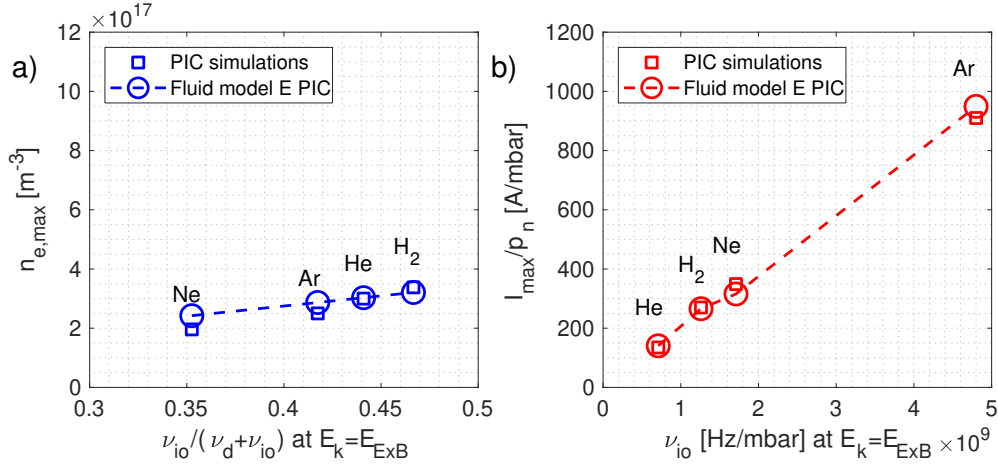
Figure 3.15: Same as Figure 3.12 but as a function of the RNG type. The externally applied bias is set at $\Delta\phi = 30\,\text{kV}$ and the magnetic field amplitude is set at $B_{max} = 0.28\,\text{T}$.

The fluid model is validated using the collision frequencies calculated with Eq.(3.22), and where the drift velocity is calculated once using only the externally imposed electric field (dashed line in Figs. 3.12, 3.13, 3.14), and once using the total electric field extracted from the simulations (circles in Figs. 3.12, 3.13, 3.14). The comparison between the simulation results and the model predictions show that the knowledge of the total electric field is necessary to obtain the correct scaling. When using the total electric field in the model, Eq. (3.20) and Eq. (3.21), the analytical scalings for the scans on B_{max}, see Figure 3.12, on $\Delta\phi$, see Figure 3.13, on p_n, see Figure 3.14, and on the gas type, see Figure 3.15, are well reproduced for $n_{e,max}$, and the correct trends are captured for I_{max}. The slightly worse agreement for the current could be explained by the approximated size of the cloud, which is assumed independent of the external parameters. These results reveal that a model for the self-consistent electric field is needed to have an analytical prediction from the reduced model, and to limit the need for computationally expensive numerical simulations. A first approximation for calculating the self-consistent electric field is presented and discussed in Sec. 3.3.5.

It appears from this reduced model that a fluid code could be sufficient to study the problem at hand. However, this model considers only the time-averaged behaviour of the cloud, and it is not yet known if kinetic effects are important to describe the dynamics (cloud breathing). Moreover, in a fluid code, the implementation of boundary conditions for the fluid would be much more complicated. Furthermore, as seen in Figure 3.10, the amplitude of the pressure force in the azimuthal direction, while small, is not completely negligible. This means that, if this term is important to describe the dynamics of the system, the use of an isothermal fluid model is not justified for a two-dimensional fluid model, and a more complex closure equation is necessary.

One can also remark from these simulations, that the external bias scan (Figure 3.13) suggests the existence of two regimes in the electron peak density and peak current depending on the externally applied bias. Above a certain bias, $\Delta\phi > 30\,\text{kV}$, the slope of the curves changes drastically. This behaviour can be explained by the reduced fluid model derived in section 3.3 and by the two collisionality regimes, where either elastic or ionization collisions dominate, described in section 3.3.4.

3.3.4 Collisionality regimes

In the parametric scans on the external bias of Figure 3.13, two regimes have been identified for both the current and the peak electron density, where a plateau is reached at large biases (above $\Delta\phi = 30\,\mathrm{kV}$). This result can be explained by examining the collision cross-sections, represented in Figure 3.16, and their corresponding effective drag frequencies. Here, two main regimes can be defined. For low electron kinetic energies, $E_k \lesssim 100\,\mathrm{eV}$, the elastic drag dominates, and the peak densities depend directly on the electron energies and by extension on the externally applied electric and magnetic fields, see Eq. (3.22) and Eq. (3.20). On the contrary, for high electron kinetic energies, $E_k \gtrsim 400\,\mathrm{eV}$, the effective drag due to electron creation dominates. This means that in Eq. (3.20), $\sigma_d = \sigma_{io} + \sigma_d^{el} + \sigma_d^{io} \approx \sigma_{io}$ and the peak electron density becomes independent of the electron energies:

$$\omega_{pe,peak}^2 = \left\langle \Omega_{ce}^2 \frac{\langle \sigma_{io} v \rangle_f}{\langle \sigma_{io} v \rangle_f + \langle \sigma_d v \rangle_f} \right\rangle_T \approx \frac{1}{2}\Omega_{ce}^2. \tag{3.23}$$

In the PIC simulations, this change of regime is expected for biases $\Delta\phi \approx 30\,\mathrm{kV}$ where the electron kinetic energy is $E_k \approx 200\,\mathrm{eV}$. Furthermore, as the current is linearly proportional to the cloud electron density, two regimes are also expected in the dependence on the external bias for this quantity. This result also shows that, at equilibrium, $\omega_{pe,peak}^2 \leq \Omega_{ce}^2/2$ or that $f_b \leq 1$, as σ_d contains σ_{io}.
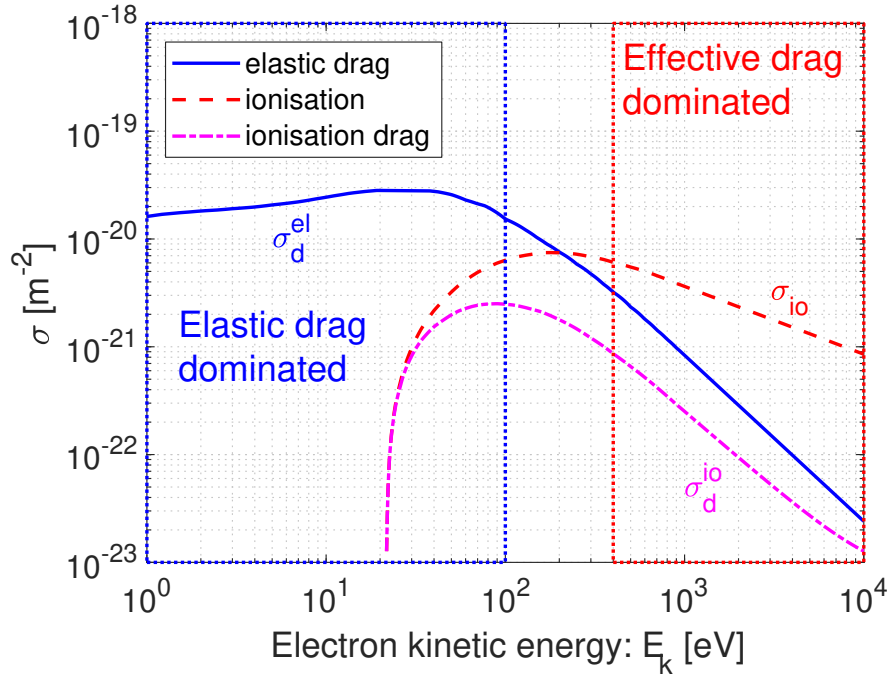
Figure 3.16: Electron collision cross-sections of Ne atoms as a function of the electron kinetic energy. The neutral particles are assumed to have zero velocity.

3.3.5 Improved current and density prediction using an analytical electric field

As presented in Section 3.3.3, the knowledge of the amplitude of the self-consistent electric field is critical to obtain reasonable predictions for the collected current. However, one can go one step further in the

modelling and approximate the electric field using an analytical expression. This can be extremely useful, as rapid estimates of the trapped electron density and collected current could be obtained in a matter of minutes, before running long and numerically expensive FENNECS simulations. As can be seen in Figures 3.1 and 3.3, the cloud is elongated and, at the position where the density is maximum, the axial non-uniformity is small, and the cloud can be approximated by an annular electron cloud of infinite length trapped between coaxial electrodes of constant radius. In this case, the expression for the self-consistent electric field inside the cloud is (see Appendix A):

$$E_r(r) = \frac{qn_e}{2\epsilon_0} r + \left[\Delta\phi + \frac{qn_e}{4\epsilon_0}(r_+^2 - r_-^2) + \frac{qn_e}{2\epsilon_0}\left(r_+^2 \ln\left(\frac{b}{r_+}\right) - r_-^2 \ln\left(\frac{a}{r_-}\right)\right)\right] \frac{1}{r \ln(b/a)},$$ (3.24)

with n_e the electron cloud density, q the electron charge, a and b are respectively the radii of the internal and external electrodes, $\Delta\phi$ is the imposed bias, and r_+ and r_- are respectively the cloud inner and outer radii. As seen in Figure 3.1, the cloud is located close to the outer electrode, and thus $r_+ \approx b$. The lower cloud limit r_- is an input parameter that is in reality defined by the radial limits of the self-consistent potential-well, as seen in Figure 3.3. However, this quantity can be estimated using a worst case scenario where the cloud dimension is maximum. In this case, the lower radial limit of the cloud is taken to be equal to the lower radial limit of the vacuum potential well $r_- = r_{w-}$. Using this value should give an upper limit for the collected electron current.

Combining the expression for equilibrium electron density (3.20), the expression for the collision frequencies (3.22) and the expression for the radial electric field (3.24), gives a closed system of equations. As the collision cross-sections are not known analytically, this problem can be solved numerically. A naive solution would be to use a fixed point iterative scheme starting with $n_{e,0} = 0\,\mathrm{m}^{-3}$ density, calculate the radial electric field, then calculate the predicted electron density $n_{e,1}$ for this electric field. From it, calculate a new electric field $E_{r,2}$ using $n_{e,1}$ and iterate the process until the fixed point is reached. This method is however numerically unstable and, at least for the configuration considered in this section, no fixed point is reached. An alternative is to start with an initial low density $n_{e,0}$ and use it to calculate $E_r(n_{e,0})$. From this the collision frequencies $\nu_{io}(E_r)$ and $\nu_{d,0}(E_r)$ are calculated and the time derivative of the cloud density is evaluated using the continuity equation (3.17) and neglecting density gradients:

$$\frac{\partial n_{e,0}}{\partial t} = -n_{e,0}\nabla \cdot \vec{u} + n_{e,0}\nu_{io}(E_r).$$ (3.25)

In this equation, the velocity $\vec{u}$ is assumed purely radial and given by Eq. (3.16). The new density $n_{e,1}$ is evaluated using an Euler integrator

$$n_{e,i+1} = n_{e,i} + \Delta t \frac{\partial n_{e,i}}{\partial t}.$$ (3.26)

The time-step Δt is adapted during the iteration process for numerical speed and stability with

$$\Delta t = \frac{1}{\eta \nu_d(n_{e,i})};$$ (3.27)

and $\eta = 20$ is a constant defined at the beginning of the simulation. The iterative solver is stopped either if the density reached a fixed point

$$\frac{\Delta t}{n_{e,i}}\frac{\partial n_{e,i}}{\partial t} < \epsilon,$$ (3.28)

with $\epsilon = 10^{-12}$ an input parameter, or if the Larmor radius of a trapped electron ρ_l evaluated in the middle of the cloud is bigger than half of the well radial dimension ($\rho_l > (b - r_{w-})/2$). The predicted collected current is then evaluated using equation (3.21). A simulation result of this reduced model solver

is represented in Figure 3.17 for the geometry represented in Figure 3.1, with a bias $\Delta\phi = 30\,\text{kV}$ and magnetic field $B_0 = 0.265\,\text{T}$. The geometry radial limits are $a = 63.75\,\text{mm}$, $b = 79\,\text{mm}$, $r_- = 76\,\text{mm}$ and $r_+ = 79\,\text{mm}$, $L = 10\,\text{mm}$ and the gas considered is Ne.

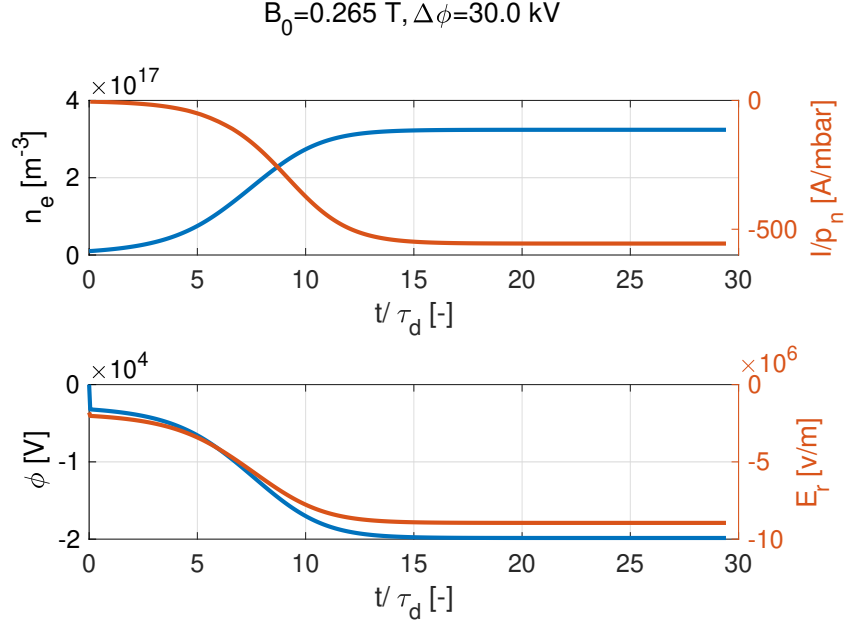$$B_0 = 0.265\ \text{T}, \Delta\phi = 30.0\ \text{kV}$$

Figure 3.17: Top: Time evolution of the electron cloud density (blue) and normalized collected electronic current (red) obtained using the reduced model solver described in Section 3.3.5. Bottom: Time evolution of the self-consistent potential ϕ and radial electric field E_r at $r = (r_+ + r_-)/2$ the middle of the electron cloud.

As the potential well is significantly modified due to the space-charge effects, see Figure 3.3, the effective radial width of the cloud changes in time and is typically smaller than the radial width of the well in vacuum. The reduction of the cloud size will impose a reduction of E_r compared to the one obtained using the vacuum potential well size, and therefore, reduce the predicted $n_{e,max}$ and I_{max}. To take this effect into account, the lower limit of the electron cloud r_- can be adapted at each time-step such that the radial size of the cloud is equal to two Larmor radii up to the width of the vacuum potential well, i.e. $r_- = \max(r_+ - 2\rho_L, r_{w-})$. This choice of r_- gives a lower limit for I_{max} and $n_{e,max}$, while $r_- = r_{w-}$ gives an upper limit.

This analytical reduced model is used to reproduce the results of the parameter scan presented in Section 3.3.3 and shown in Figures 3.18 and 3.19, where the shaded areas correspond to the current estimated with the improved reduced fluid model, and assuming either a large radial well width given by the vacuum potential well size or a small radial well width given by the trapped electrons' Larmor radii. The results show that this model gives predictions in the correct order of magnitude compared to the PIC simulations for the scan in bias $\Delta\phi$ and for low magnetic field amplitudes. However, at high B ($B > 0.5\,\text{T}$) the method looses precision and no meaningful prediction can be obtained. This is mostly due to the very small Larmor radii of the trapped electrons and the inability of the model to predict the effect of space-charge on the axial and radial size of the potential well.
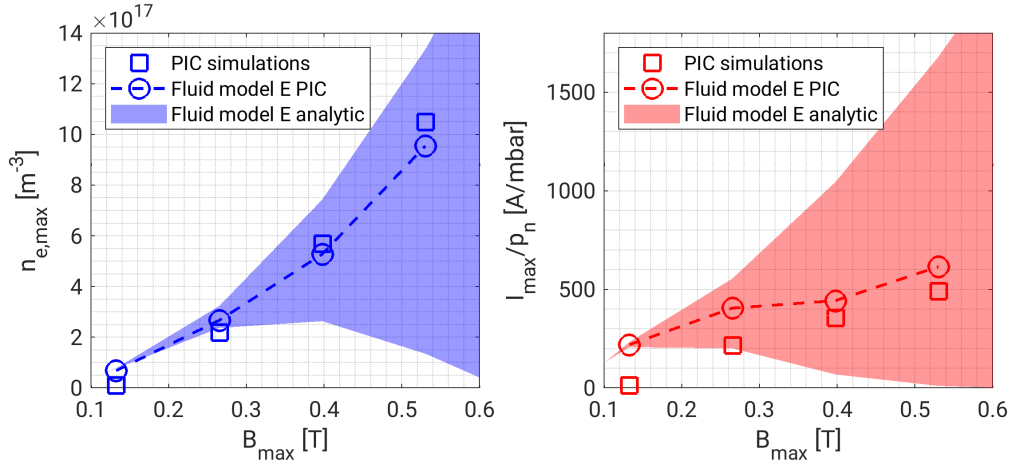
Figure 3.18: a) Evolution of the maximum electron density in the cloud as a function of the maximum magnitude of the magnetic field in the cloud region. b) Evolution of the maximum radial current, scaled by the RNG pressure, as a function of the maximum magnitude of the magnetic field in the cloud region. The applied bias is $\Delta\phi = 30\,\text{kV}$ and the RNG pressure is $p_n = 1 \times 10^{-1}$ mbar. For both figures, the squares represent numerical results extracted from the PIC simulations. The dashed-dotted line is a prediction using the model of Section 3.3 but using only the external electric field for calculating the collision cross-sections, while the shaded region gives the maximum and minimum values obtained with the model of Section 3.3.5 for $r_- = r_{w-}$ and $r_- = \max(r_+ - 2\rho_L, r_{w-})$.

Figure 3.19: Same as Figure 3.18 but as a function of the electric bias. The magnetic field amplitude is set at $B_{max} = 0.28\,\text{T}$ and the RNG pressure is $p_n = 1 \times 10^{-1}$ mbar.

Considering that these simulations are run in the order of seconds compared to the hours or days necessary to run FENNECS, the obtained precision is relevant, and this tool could be useful to do a first scan in the external parameter space. This would allow finding relevant or problematic configurations, which can then be simulated more accurately using FENNECS.

3.4   Summary and conclusions

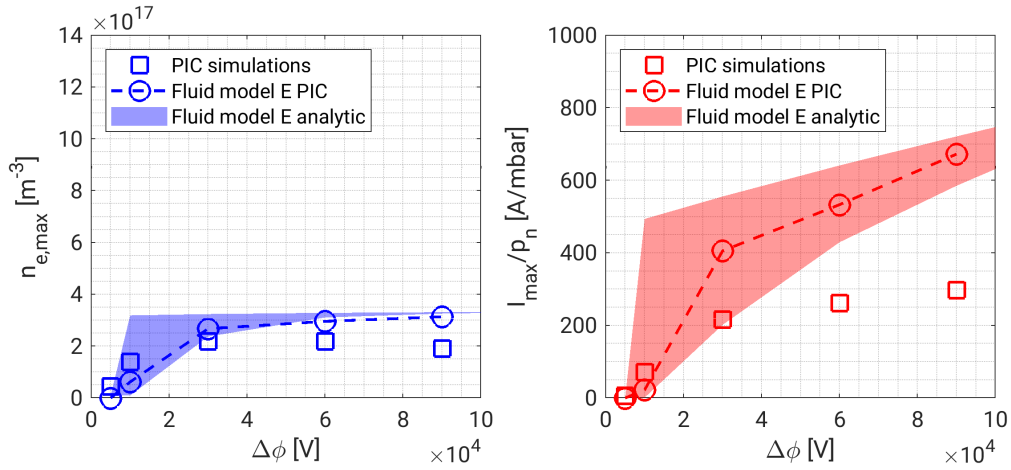The PIC simulations in the simplified geometry show that electron clouds can indeed form self-consistently in potential wells subjected to high external radial electric fields and strong axial magnetic fields by ionising the RNG present in the vacuum vessel. The simulation results also show that these clouds reach high densities with Brillouin ratios $f_b \approx 1$ and that the clouds are mostly axially confined, but lose electrons radially. To understand these phenomena, the nature of the source and sinks have been studied, which show that a pseudo-equilibrium can be reached due to the balance between the electron source caused by ionisation, and the sink due to radial drifts caused by collisional drags. In addition, the study of the individual fluid force terms at equilibrium, allowed the extraction of the order of relevance of the different contributions to the fluid force balance, and showed that pressure effects are negligible in first approximation.

From these observations, a reduced fluid model has been derived that is able to account for these phenomena and to predict the order of magnitude of electron density and current collected on the electrodes. In addition, simulation results show that using the $v_{E \times B}$ velocity to determine the trapped electrons kinetic energy is a good approximation that allows to refine the fluid model and permits the derivation of a closed non-linear 0D set of equations that can estimate the resulting density and current in a limited range of external parameters. However, the physical model used in FENNECS still needs to be validated using realistic geometries and experimental measurements and is the subject of chapter 4.

4 Numerical studies in realistic geometries: simulations of the GT170 gyrotrons

In this chapter, we present the first validation of the code presented in Chapter 2 by comparing experimental results with numerical simulations using the actual geometry of two gyrotron electron guns. This is an important milestone that increases the confidence in the numerical model. It also measures the capability of this model to predict the risk of problematic currents in future gyrotron electron guns, and that this model can facilitate the design phase of the gun geometry. We would like to remark that this work also represents the first validation of simulations of trapped electron clouds in gyrotron guns, ever performed against experiments.

4.1 Challenges in the GT170 gyrotron design

The problem of trapped electron clouds has been observed in some gyrotrons, such as in the magnetron injection gun (MIG) developed for the initial prototype of the European 2 MW 170 GHz coaxial gyrotron planned for ITER [23] (see Figure 4.1). In this gun, the nominal accelerating bias could not be sustained due to trapped secondary electrons, which lead to excessive currents flowing through the body power supply (PS) that imposes the accelerating electric field seen by the beam (see Figure 1.9 on page 10). The presence of a potential well caused excessive currents in CW operation (also without electron beam), and the gun also suffered from adiabatic trapped electrons [21] which did not allow the operation of the gyrotron at the nominal parameters even in short pulses. These effects hindered the nominal operation of the gyrotron and limited the efficiency and power output [20, 102]. A new geometry, referred to as 'refurbished gun', was then designed in which a special attention was paid to avoid the formation of any potential well, for the nominal magnetic field of the gyrotron [30]. This particular geometry is presented in Figure 4.2. The added benefit of this geometry for studying electron trapping, is the capability to create potential wells of different shapes and depths by varying slightly the magnetic field lines topology, from the nominal one, in the gun region. This can be achieved by varying the current I_{cc} flowing through two particular control coils (C3 and C4 in Figure 4.2). It was shown experimentally that for some magnetic field topologies where a potential well is present, the voltage stand-off capabilities of the accelerating electrodes were significantly worsened [30]. This means that the maximum bias $\Delta\phi$ that could be applied to the electrodes, without measuring any current flowing between them, was significantly reduced. To obtain these experimental results, a dummy gyrotron gun was built according to the design of the refurbished prototype of the 2 MW 170 GHz coaxial gyrotron planned for ITER. However, in the dummy-gun, no
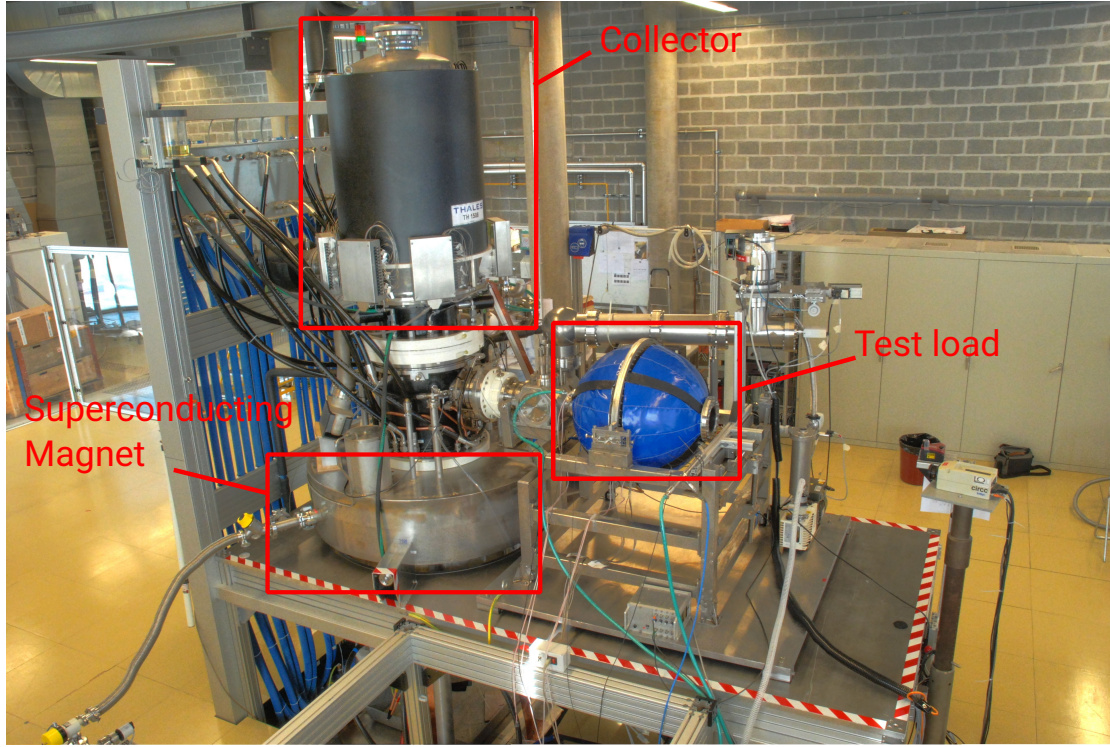
Figure 4.1: Picture of the prototype of the GT170 2 MW 170 GHz coaxial gyrotron initially designed for ITER and installed on the Falcon test stand of SPC [23] (picture courtesy of Jean-Philippe Hogge). The electron gun is not visible here, since the stand table masks it.
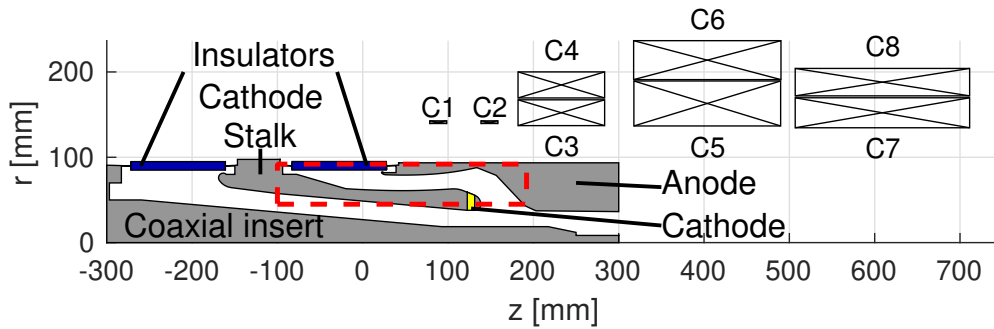
Figure 4.2: Geometry of the refurbished electron gun and of the superconducting coils C1 to C8 generating the magnetic field. An azimuthal symmetry is implied. The red dashed rectangle represents the limits of the simulation domain. Grey denotes a metallic material and blue denotes a ceramic insulator. The yellow section represent the emissive ring where the main electron beam is produced.

emissive ring was installed, therefore no electron beam was produced. The goal of the dummy-gun was to test the voltage stand-off capabilities of the design without magnetic field and at the nominal magnetic field configuration for operating the gyrotron at the nominal power.

4.2 Magnetic field configuration

The magnetic field used for the GT170 gyrotron is generated by a set of 8 superconducting coils (C1-C8 in Figure 4.2) whose characteristics are given in Table 4.1. The coils are powered by 5 power-supplies generating five independent currents $I_1 - I_5$ that are combined differently (see Table 4.1) to produce the desired current flowing in each coil. The nominal currents for operating the gyrotron are: $I_1 = 0.0$ A, $I_2 = 0.0$ A, $I_3 = 6.795$ A, $I_4 = 1.967$ A, $I_5 = 88.278$ A. In this chapter, the two control coils $C3$ and $C4$, also called bucking coils, are controlled by the current $I_{bc} = -I_3 - I_5$, where $I_3 \equiv I_{cc}$ is the controlled current responsible for the change in potential well and the control parameter for Section 4.3. The magnetic field amplitude and field lines are represented in Figure 4.3 for $I_{cc} = 6.8$ A. In the range of values considered in this chapter for I_{cc}, the magnetic field amplitude is only slightly modified with maximum 5% relative difference, but the magnetic field lines topology are strongly changed as shown in Figure 4.4, which leads to significant variations of the generated potential wells size and depth or even to their suppression.

Coil	z_{min} [m]	z_{max} [m]	r_{min} [m]	r_{max} [m]	# of turns	Current
C1	0.07854	0.09846	0.013958	0.142694	218	I_1
C2	0.13854	0.15846	0.013958	0.142694	218	I_2
C3	0.18200	0.28350	0.13710	0.16733	2528.5	$-I_3 - I_5$
C4	0.18200	0.28350	0.16952	0.20005	2626	$-I_3 - I_5$
C5	0.31778	0.48977	0.13670	0.18941	7689	$I_4 + I_5$
C6	0.31748	0.49017	0.19101	0.23666	11517.5	$I_4 + I_5$
C7	0.50685	0.71128	0.13458	0.16972	6110	I_5
C8	0.50685	0.71128	0.17197	0.20412	9656.5	I_5

Table 4.1: Characteristics of the 8 super conducting coils generating the magnetic field of the GT170 gyrotron. The axial reference $z = 0$ m is in the electron gun as shown in Figure 4.2
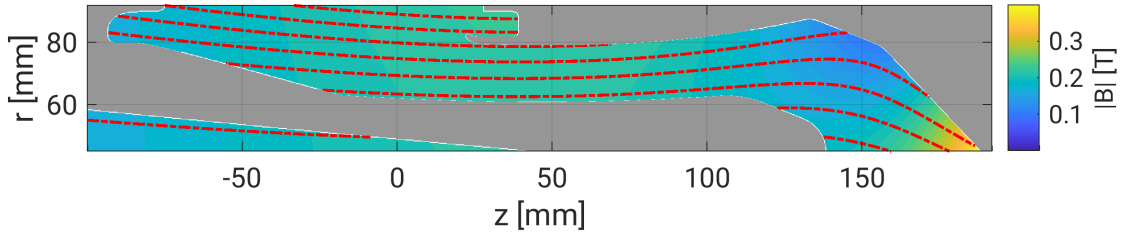

Figure 4.3: Magnetic field configuration generated by the 8 superconducting coils for the nominal control coil current $I_{cc} = 6.8$ A. The colour plot indicates the magnetic field amplitude, and the red lines show the magnetic field lines.

4.3 Simulations in the refurbished geometry

In conjunction to the experimental studies of the dummy gun, a numerical study of the electron clouds dynamics, in the dummy gun geometry, has been performed. The refurbished MIG geometry has been reproduced in FENNECS and used to perform simulations of electron cloud formation for decreasing values of I_{cc} leading to increasing potential well depths U_{well} and size as shown in Figures 4.4 and 4.5. In the simulations, the ions released during the ionization processes are not radially confined due to their large Larmor radius and are accelerated towards the cathode and captured on the electrode surface after a typical time $\tau_{loss} \approx 10^{-8}$ s much faster than the expected cloud formation time $\tau_f \approx 10^{-2} - 10$ s. For this reason, they are initially not simulated. It is important to note that both in the experiment and in the simulations, the cathode was cold and the main electron beam of the gyrotron was therefore not generated. The primary electrons that ionize the RNG and start the cloud formation are expected to be generated either by field-emission [22] or by ionization of the RNG due to background radiation. This effect is simulated in the code by the ad-hoc volumetric source covering the full simulation domain. The electron production rate of this source S is also adapted such that this source is negligible compared to the ionization rate S_i of the RNG by trapped electrons ($S \ll S_i$). The magnetic field applied by the 8 super-conducting coils, C1-C8 in Figure 4.2, is precomputed numerically by solving the Biot-Savart equation and provided as an input to the code. It is then possible from the FENNECS simulations to measure the effect of the potential well shape and depth on the trapped electron cloud density and on the amplitude of the electronic current collected on the electrode surfaces.

In each simulation, the time step is $\Delta t = 8 \times 10^{-12}$ s $\approx 0.05/f_{ce}$, with $f_{ce} = eB/(2\pi m_e)$ the cyclotron frequency and $B \approx 0.23$ T the magnetic field amplitude in the trapping region. The grid used for the Poisson solver is axially uniform with $\Delta z = 0.25$ mm, but radially non-uniform with $\Delta r = 0.05$ mm in the region of cloud trapping (between 59 mm $< r < 65$ mm and 77 mm $< r < 84$ mm), and $\Delta r = 0.25$ mm outside. The RNG is simulated as a uniform background of H_2 at room temperature and at an enhanced neutral pressure $p_n = 1 \times 10^{-2}$ mbar to reduce simulation time (see Chapter 2), but low enough to ensure correct separation of the electron neutral collisions time-scales $\tau_{coll} \approx 8 \times 10^{-8}$ s and the electrons axial bounce time-scale $\tau_b \approx L_{\parallel}/v_{th,\parallel} \approx 1 \times 10^{-8}$ s in the trap along the magnetic field lines. Here $L_{\parallel}$ is the length of the cloud along the magnetic field line and $v_{th,\parallel}$ is the thermal parallel velocity.

4.3.1 Initial simulation results: electron clouds and potential well shapes

The simulation results show that, when present, the potential well is annular and located between the cathode stalk and the anode. As the vacuum potential well shape is purely defined by the magnetic field topology and the electrodes geometries, for a fixed I_{cc}, the vacuum well depth is therefore directly proportional to the applied bias $\Delta\phi$ and a normalized depth can be defined as $U_{well}(r, z)/\Delta\phi$. FENNECS simulations confirm that the potential well size and depths in vacuum are increased as I_{cc} is reduced, as can be seen in Figure 4.4 and Figure 4.5.

The simulations also show the formation of a quasi-steady state with two distinct electron clouds (see Figure 4.7, as a balance between the source of electrons caused by the ionization of the RNG, and a sink imposed by collisional driven cross-field radial drifts causing the electrons of the upper cloud to hit the upper electrode and be captured (see Figure 3.6 on page 58 for an illustration). The electrons of the lower cloud drift outside of the potential well region and stream along $\vec{B}$ toward the anode, where they are collected. Due to the trapping geometry, the electron clouds form a ring radially confined inside coaxial electrodes as seen in Figure 4.6, and are located in the regions where the self-consistent well including

Potential well causing problematic currents

Figure 4.4: Detail of the trapping region and normalized vacuum potential well formed for a control coil current $I_{cc} = 4.6$ A. In the white region, the well depth is 0 and the black dash-dotted lines represent the magnetic field lines for $I_{cc} = 4.6$ A. The blue dashed lines represent the magnetic field lines for a magnetic configuration where $I_{cc} = 6.2$ A and for which no potential well is present.

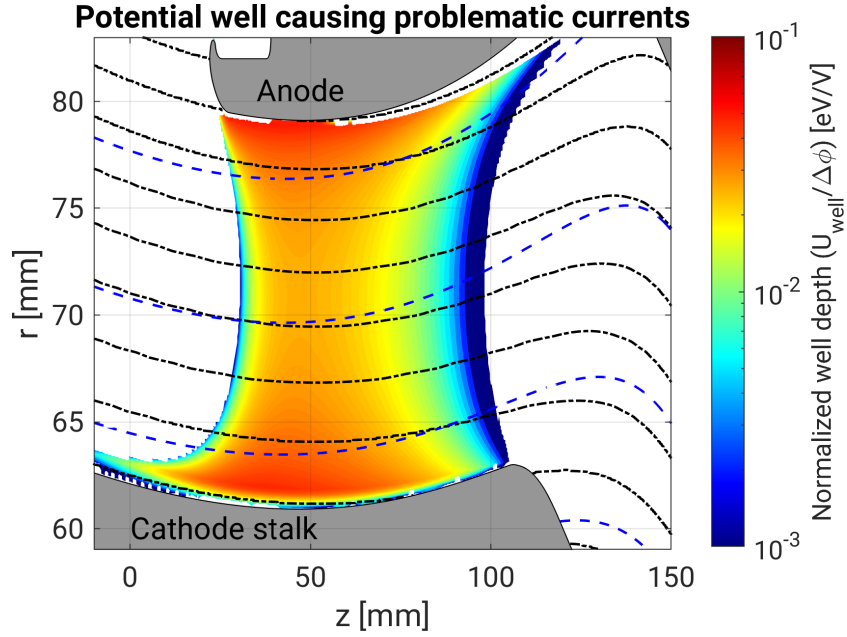**Potential well not causing problematic currents**
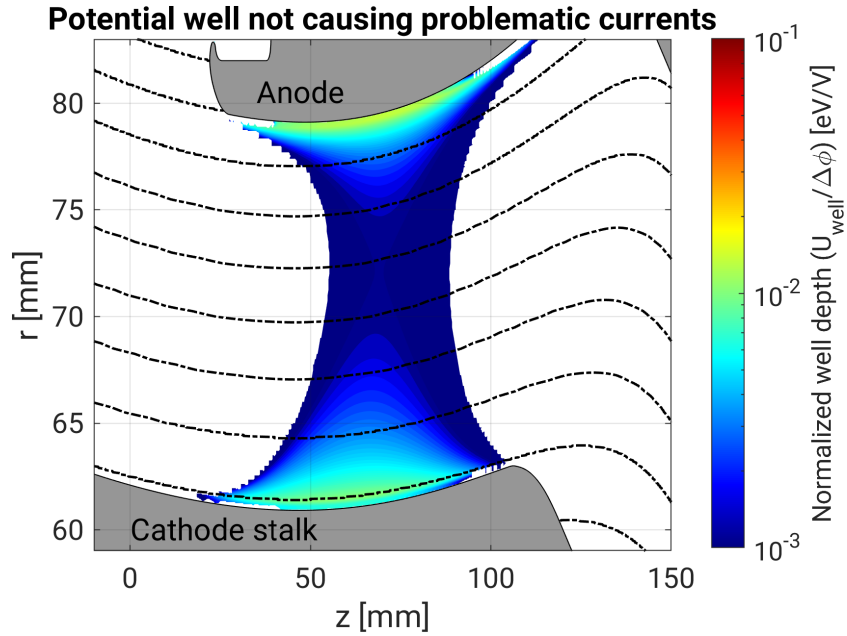
Figure 4.5: Detail of the trapping region and normalized vacuum potential well formed for a control coil current $I_{cc} = 5.6$ A. In the white region, the well depth is 0 and the dash-dotted lines represent the magnetic field lines.
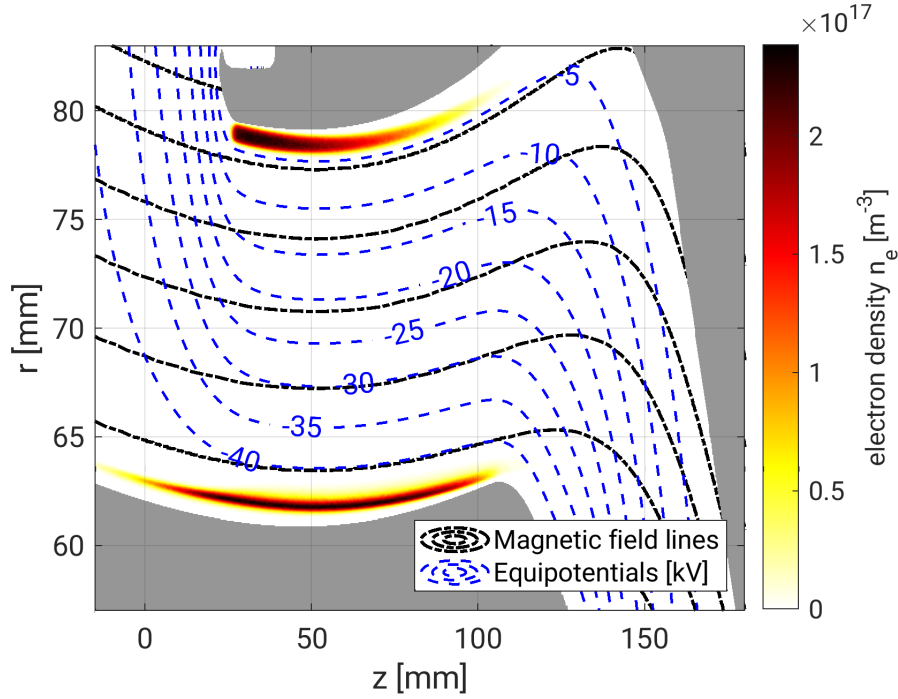
Figure 4.6: Detail of the trapping region and steady-state electron density for a control coil current $I_{cc} = 4.6\,\text{A}$ and an applied PS bias $\Delta\phi = 45\,\text{kV}$. The black dash-dotted lines represent the magnetic field lines and the blue dashed lines represent the electric equipotential lines.

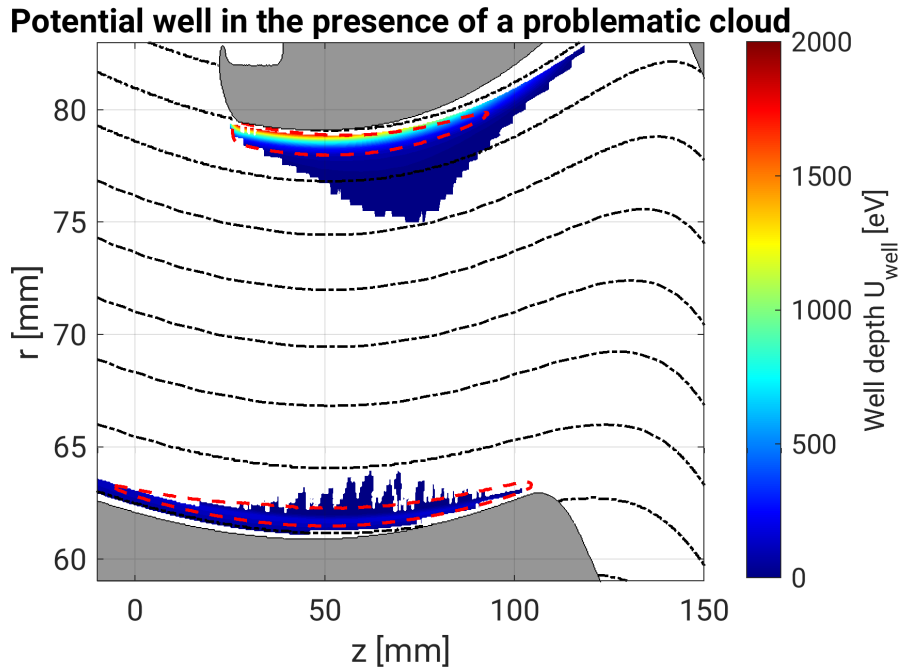Figure 4.7: Detail of the trapping region and self-consistent potential well for a control coil current $I_{cc} = 4.6\,\text{A}$ and an applied PS bias $\Delta\phi = 45\,\text{kV}$. The black dash-dotted lines represent the magnetic field lines and the red dashed line indicate the outline of the cloud where $n_e = 0.1 \cdot \max(n_e)$.

space-charge effects is deepest, as seen in Figure 4.7. Similarly, these simulations show that the two clouds are well separated radially and induce two different contributions to the total collected current. As seen in Figure 4.8, the charges of the upper cloud are mostly lost radially and collected on the corona ring surface at the same axial position of upper electron cloud peak density. In accordance with the results of Chapter 3, the axial confinement of the upper cloud is almost perfect. In the lower cloud, the charges are lost along the magnetic field lines and are collected on the bottom part of the anode, which is called the "Halo shield" (see bottom right part of Figure 4.8).
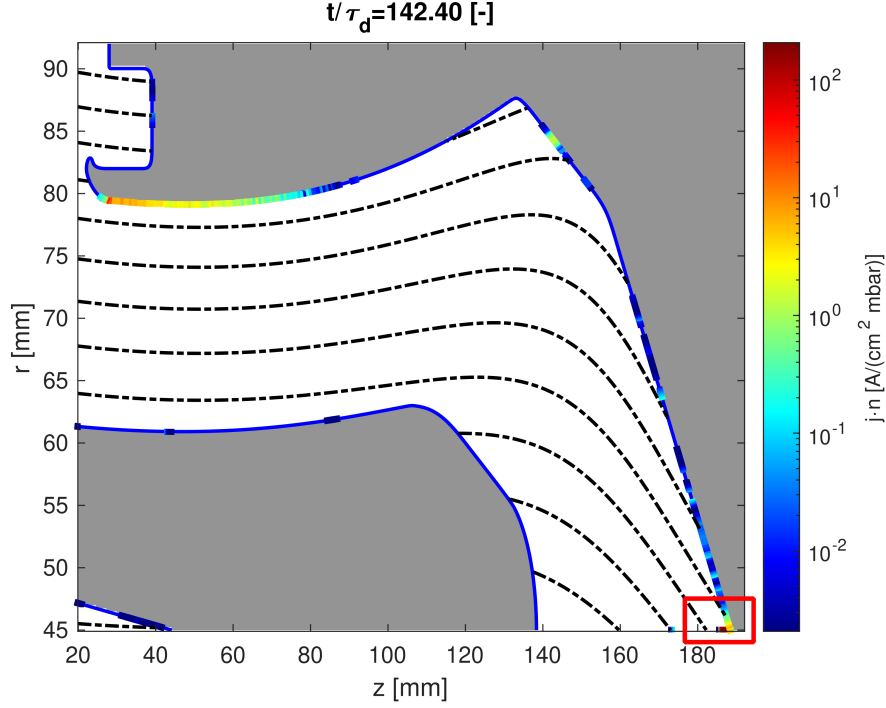
Figure 4.8: Steady state electronic current density collected on the electrodes for the case with $\Delta\phi = 45$ kV and $I_{cc} = 4.6$ A. The red rectangle highlights the collection region of the electronic current generated by the lower cloud.

The reduced fluid model of Chapter 3 also predicts a proportionality between the collected current and the neutral gas density. For this reason, and the fact that the neutral gas temperature is assumed constant, the measured current is then normalized by the neutral pressure p_n. To confirm this proportionality in this specific geometry, simulations have been run at different neutral gas pressure and the steady state current has been measured for the case with $\Delta\phi = 55$ kV and $I_{cc} = 4.8$ A, and represented in Figure 4.9.

4.3.2 Simulation of the parametric scans performed experimentally

During the experimental campaign of the dummy-gun, the voltage stand-off was also tested with increasing potential well depths U_{well} and size by decreasing the control coil current I_{cc}. For a set of control coil currents, the maximum bias $\Delta\phi$ that could be applied without observing problematic currents (without tripping the PS) was measured up to the PS limits of 105 kV [30]. The results of these experiments have been reproduced in Figure 4.10 (red dots and white dashed line), and show a sharp reduction of voltage stand-off below a control coil current of $I_{cc} = 5.3$ A. Figure 4.10 also shows the lines of constant potential

Figure 4.9: Total electronic current, collected in the simulations on the electrodes, in steady state, for various neutral gas pressures, for the case with $\Delta\phi = 55\,\text{kV}$ and $I_{cc} = 4.8\,\text{A}$ (blue crosses). The black dashed line highlights the linear dependency.
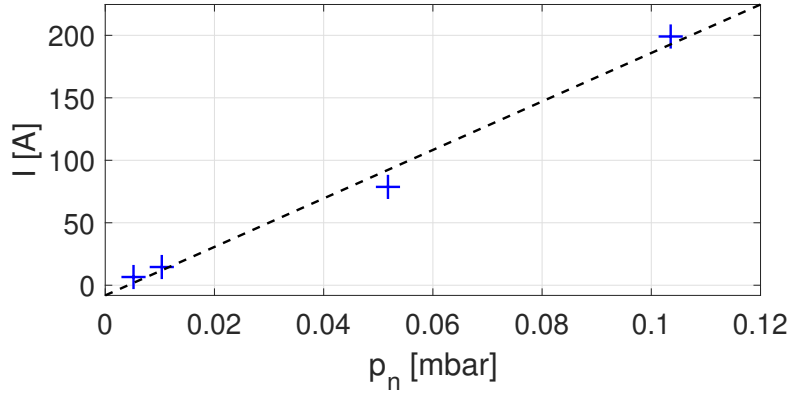
well depth U_{well} (red dashed line). It is important to notice that, for some configurations, a potential well could be present while no problematic currents were measured, which is a good indication that relaxed MIG design criteria could be defined.

To reproduce these results numerically, a set of 136 simulations were carried out with FENNECS by scanning the control coil current in the range $I_{cc} = 4.6 - 6.8\,\text{A}$ with 0.2 A increments and biases in the range $\Delta\phi = 5 - 95\,\text{kV}$ with 10 kV increments covering the scanned parameters of the experimental results. The bias scan was even extended with biases $\Delta\phi = 115, 150$ and $200\,\text{kV}$, shown by the hatched gray region of Figure 4.10, which could not be achieved experimentally due to PS limitations. Each simulation was run on a 36 core node for $\sim 12 - 36$ hours, depending on the bias and control coil parameters, until the system reaches a quasi-equilibrium. From the simulation results, the maximum electronic current collected on the electrodes is then calculated and plotted as a rectangle on the colour plot in Figure 4.10. As mentioned earlier, these simulations neglect the ionic current but in steady state, as will be presented in Section 4.3.3, this contribution changes the measured current by a factor of order 1 and will not change the separation between regions with and without problematic currents, in the parameter space $(\Delta\phi, I_{cc})$.

As the total collected current was not measured during the experiments and the pressure in the vessel is uncertain, no direct comparisons of the current amplitude can be done between simulations and experiments. However, the simulation results show the same trend of high problematic currents for low I_{cc} and low or no problematic currents for high I_{cc}. Furthermore, the range of I_{cc} marking the limit between these two regions is in good agreement with the sharp decrease of voltage stand-off at $I_{cc} = 5.3\,\text{A}$. The simulation results also show that, as in the experiments, a region exists where some potential well is present, but no problematic current is measured between $I_{cc} = 5.3\,\text{A}$ and $I_{cc} = 6.2\,\text{A}$. This is relevant for the development of future gyrotron electron guns, as it means that the current design criteria of avoiding any potential well in the gun region can be relaxed. To this end, FENNECS could be used as a useful design tool to predict the risk of problematic currents for a given gun geometry. We would like to remind that the formed annular electron clouds are susceptible to the diocotron instability which develops azimuthally and can, therefore, not be simulated in FENNECS [103–105]. However, the agreement between experiment and simulations is a strong sign that the diocotron instability might not play an important role for the amplitude of the collected current in this configuration, therefore supporting the use of axisymmetry for the simulations.

The extended scan in applied bias (gray hatched region in Figure 4.10) gives further insight on the conditions
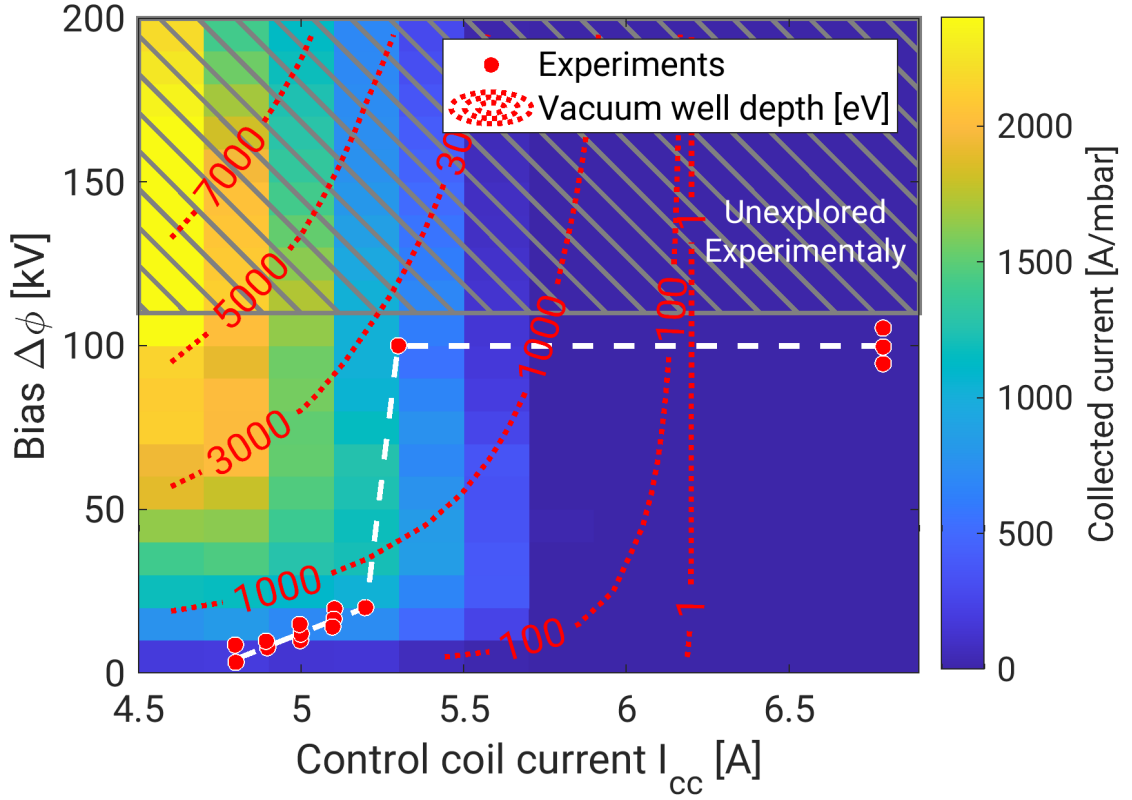
Figure 4.10: Numerically measured total electronic current collected on the electrodes and stand-off voltage achieved in the experiments. The maximum voltage of 105 kV was limited by the PS capabilities and not the stand-off properties of the gun. The red dotted contour gives the maximum potential well depth in vacuum. The gray hatched rectangle show the bias range unexplored experimentally due to PS limitations, but explored numerically.

of electron trapping. It shows that, for a given I_{cc}, increasing the bias voltage increases the collected current until a maximum is reached. If the bias is increased further, the collected current decreases again, which can lead to new regions where no problematic currents arise. This result, and the fact that for some potential wells no problematic current was observed, show that the vacuum potential well depth and volume is not a sufficient measure to predict the amplitude of the current collected on the electrodes. This is visible by following the isolines of maximum potential well depth at 1 keV and 3 keV (Figure 4.10), where a problematic current is observed for low I_{cc} but no problematic current is observed for high I_{cc}. The current hypothesis to explain the decrease of collected current at very high biases is that a larger bias $\Delta\phi$ increases the Larmor radius for the electrons, due to larger $\vec{E} \times \vec{B}$ velocity imposing a larger electron perpendicular velocity. This could lead to Larmor radii of the order of the radial dimensions of the potential well, and could limit the trapped electron cloud density by a reduction of the axial confinement. Indeed, at order 0 the Larmor radius is defined by the $E \times B$ drift velocity and the magnetic field amplitude $\rho_L = v_\perp/\Omega_{ce} = m_e|E_r|/eB_z^2$. Using only the external electric field, $\rho_L \approx 5.7 \times 10^{-3}$ mm kV^{-1}, which for a bias $\Delta\phi = 150$ kV lead to $\rho_L = 0.85$ mm that is of the order of the potential well radial dimension in some configurations and in presence of the electron cloud (see Figures 4.5 and 4.7).

4.3.3 Importance of ion contribution and IIEE effects on the collected current

In Sections 4.3.1 and 4.3.2, the ions were neglected due to their rapid loss compared to the time of cloud formation. However, to study the validity of this approximation, simulations have been run, in the frame of an internship [91], including the ions and using the ion induced electron emission (IIEE) module (see Section 2.2.9). For this comparison, the GT170 refurbished geometry is simulated using the magnetic field generated with $I_{cc} = 4.6\,\text{A}$, an applied bias $\Delta\phi = 25\,\text{kV}$, and the electrode material is assumed to be aluminium, even if the actual anode material is copper and the cathode material is molybdenum. The system is initialized with an electron cloud of density $n_{e,0} = 1 \times 10^{13}\,\text{m}^{-3}$ covering the trapping region and run without a volumetric source. The simulated neutral gas is H_2. Two cases are then compared, one with IIEE enabled and one where it is disabled.
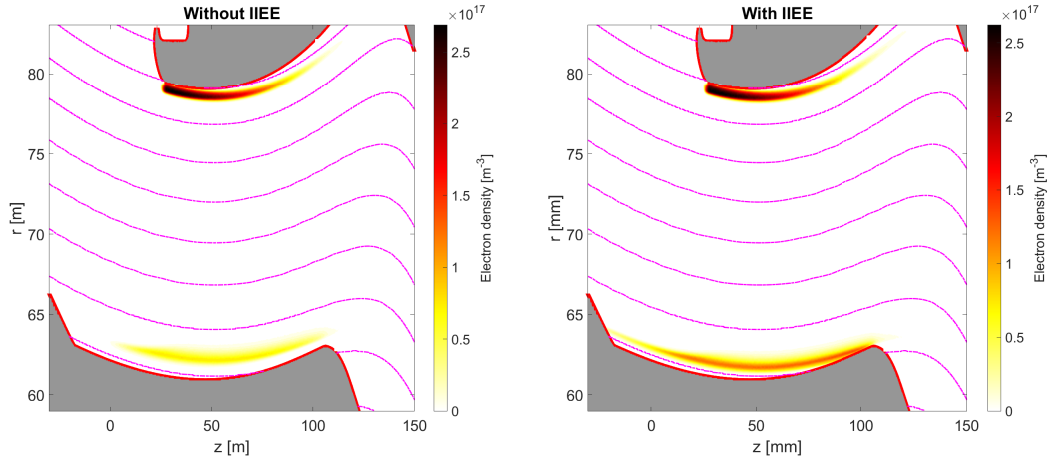

Figure 4.11: Left: Steady state electron density in the case where IIEE effects are not considered. Right: Steady state electron density in the case where IIEE effects are simulated. In both plots, the solid red lines represent the boundary limits and the magenta dashed dotted lines represent the magnetic field lines.

In both cases, the simulations show the formation of two concentric annular electron clouds, as expected from the results of Section 4.3.1 (see Figure 4.11). In addition, the ions generated by ionization are collected on the cathode stalk as seen on Figure 4.12 (right plot). Upon impact with the electrodes, the ions can release electrons at the impact position due to IIEE. This IIEE source is therefore located on the cathode stalk surface and modifies only the behaviour of the lower cloud, as the emitted electrons become trapped in the lower potential well and cannot reach the upper cloud. This additional source induces an increase in the lower cloud density in steady state, as represented in Figure 4.11. The effect of this source is also observed on Figure 4.13 representing the time evolution of the total electronic charge in the simulation domain. This shows that the total electronic charge is larger in the case with IIEE, as expected from the results of Figure 4.11. Similarly, the charge evolution curve for the IIEE case shows two regimes of growth with a transition around $25\tau_d$. In the first part, the IIEE source and the ionization sources contribute to the increase of total charge until the lower cloud reaches its maximum charge. In the second part, the growth rates with and without IIEE effects are almost identical. This can be explained by the fact that at this time, only the charge of the upper cloud is increasing (see Figure 4.14), and only due to the ionization of the RNG, which is equivalent to the case without IIEE effects. In addition, the timescale of formation of the total charge appears to be dictated by the upper cloud filling time and is comparable between both simulation cases. It can also be observed that the total trapped charge is of the same order of magnitude
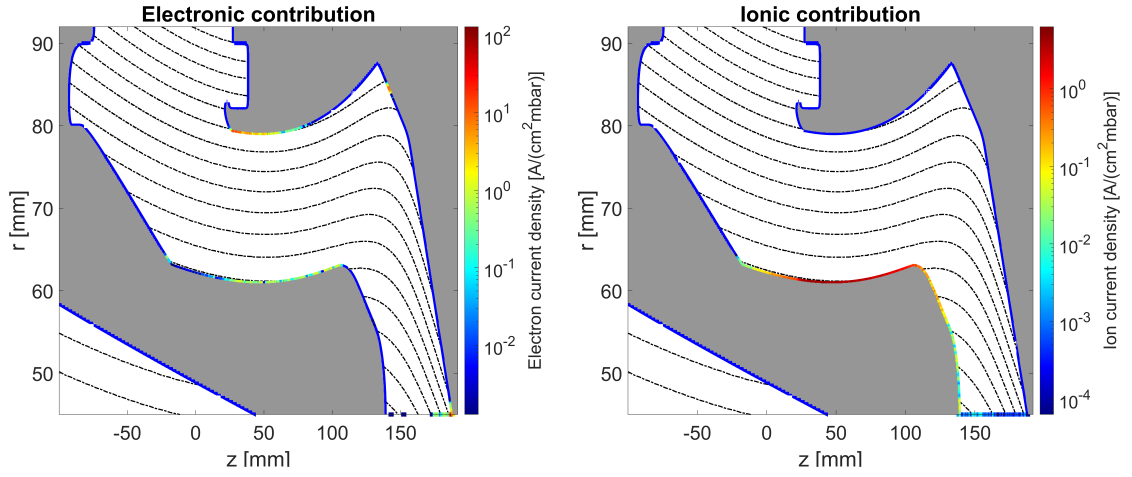
Figure 4.12: Left: Absolute value of the steady state current density collected on the domain boundaries caused by the electrons. Right: Steady state current density collected on the domain boundaries caused by the ions. The solid blue lines represent the boundary limits and the black dashed dotted lines represent the magnetic field lines.
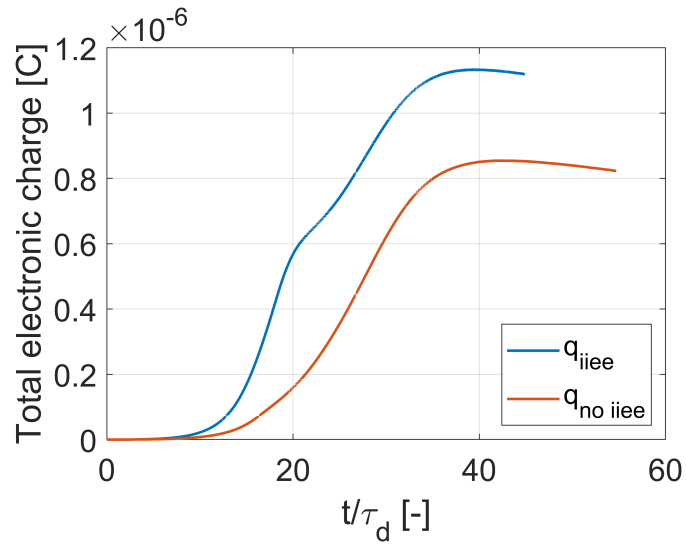
Figure 4.13: Time evolution of the total electronic charge in the simulation domain for the simulations with IIEE effects (blue) and without IIEE effects (red).
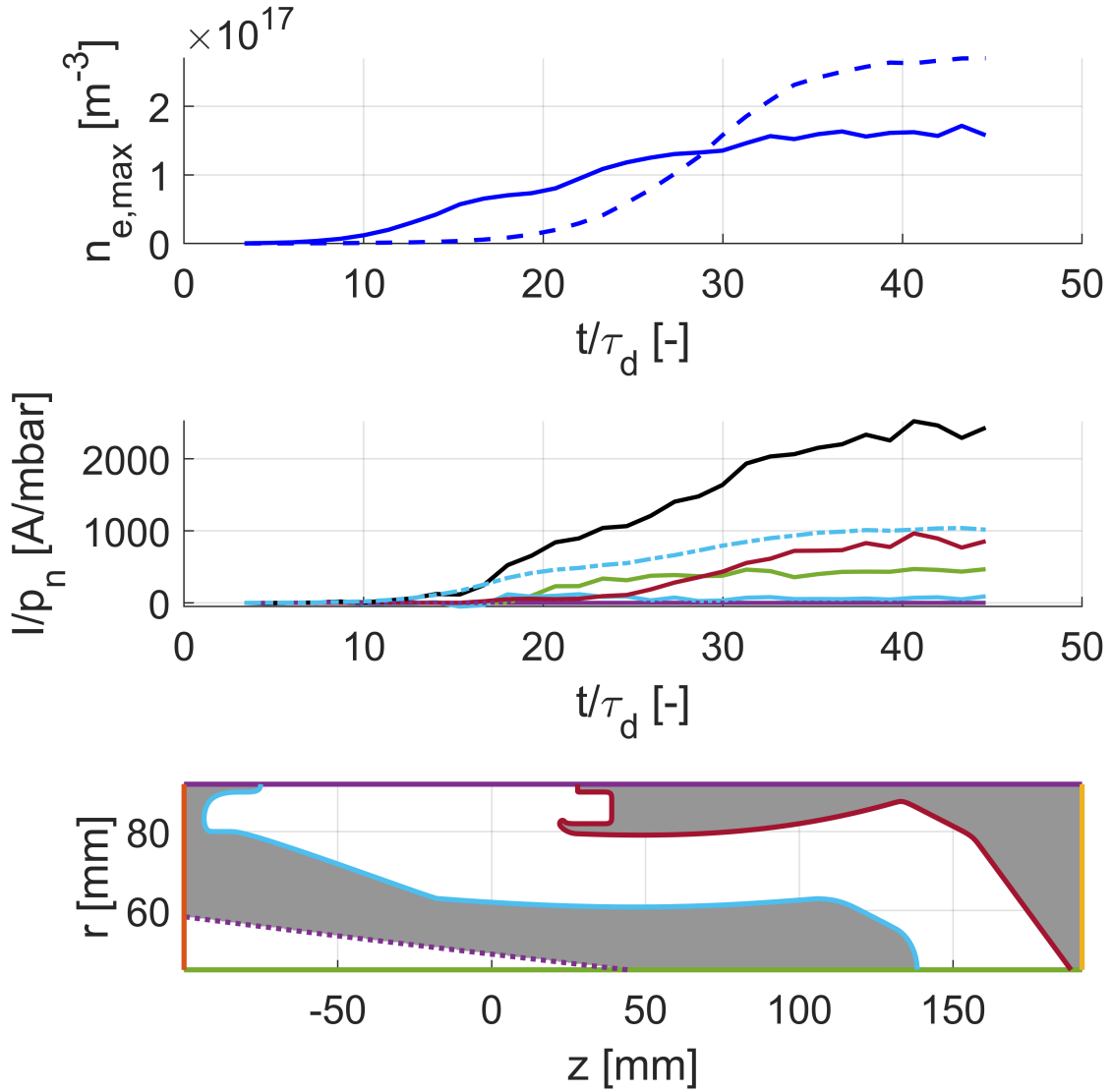
Figure 4.14: Top: Time evolution of the maximum electron density in the upper cloud (dashed) and in the lower cloud (solid). Middle: Time evolution of the collected current on the system boundaries for the simulation considering IIEE effects. The colour code indicates the boundary on which the current is collected, according to the colour code in the bottom plot. The dashed-dotted line is the ion contribution. If a colour is absent from the top plot, it is identically zero. The solid dark line represents the total collected current, including ion and electron contributions. Bottom: Geometry of the simulation and colour coded electrode surfaces.

between the two types of simulations. Indeed, the IIEE induce an increase of the total charge of 30%.

The increase in total confined charge due to the IIEE source leads to an increase of $\sim 20\%$ in the total collected current on the electrodes, as seen in Figure 4.15. This figure shows that the current contribution of the upper cloud (red curve) is unchanged when IIEE effects are included. However, the current leaving the lower cloud (green), the current due to emitted electrons (solid blue) and the ion contribution (dashed-dotted blue) all contribute to an increase of the current flowing through the PS (black). This is particularly relevant for gyrotron guns, as an increased collected current could lead to the PS shutdown. It is however important to notice that while the IIEE effects and ion contribution are significant, they "only" change the total collected current by a factor of order 1, here ~ 2.2, compared to the cases where only electrons are considered. This effect would thus not significantly change the transition presented in Figure 4.10 where differences in currents span several orders of magnitude. For this reason and due to the numerical cost of simulating the ions' trajectory, simulations with IIEE might not be crucial in the first phase of new gyrotron gun design but should be included at a later stage.
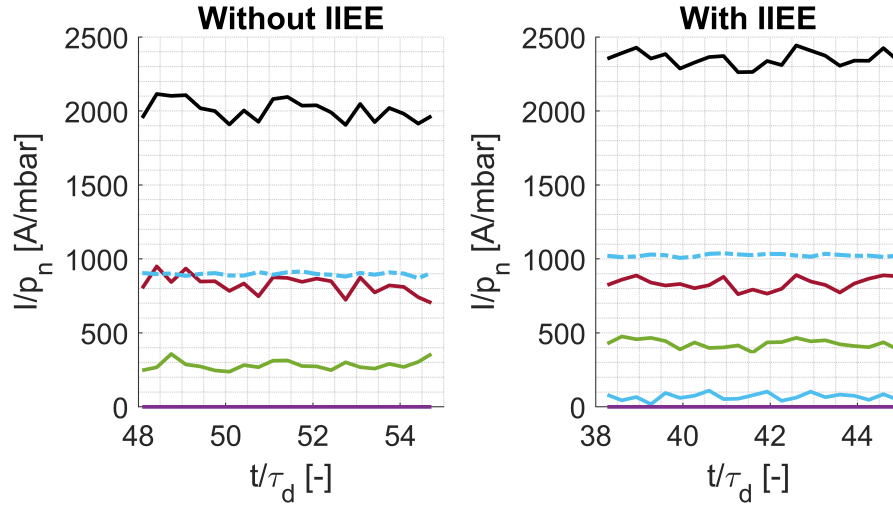
Figure 4.15: Left: Steady state collected current on the system boundaries for the simulation, not considering IIEE effects. Right: Steady state collected current on the system boundaries for the simulation considering IIEE effects. The colour code indicates the boundary on which the current is collected, according to the colour code in Figure 4.14. The solid black line represents the total collected current, including ion and electron contributions. The dashed-dotted line is the ion contribution.

4.4 Simulations in the prototype geometry

Simulations were also performed in the prototype (original) geometry of the GT170 gyrotron. In this geometry, represented in black in Figure 4.16, the anode geometry around the corona ring is strongly modified and leads to a potential well, between the cathode stalk and the anode, in the nominal magnetic field configuration (see Figure 4.17). Figure 4.16 allows the comparison of the prototype and the refurbished geometries, and shows that the most important changes are on the anode. As previously mentioned, during the experimental campaign of this gyrotron, detrimental currents were measured between the cathode and the body of the gyrotron. These were observed after a time of the order of hundreds of milliseconds and
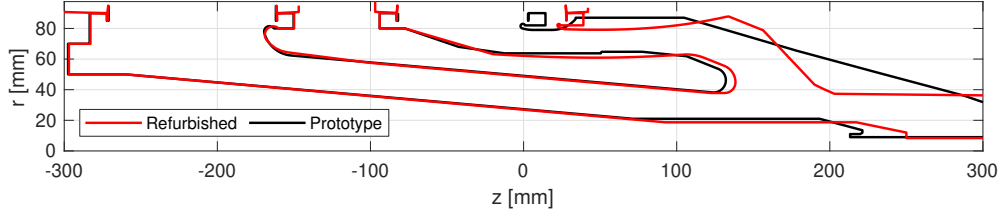
Figure 4.16: Representation and comparison of the prototype geometry (black) and the refurbished geometry (red) of the GT170 coaxial electron gun. The insulators are not shown in this plot to increase the readability.
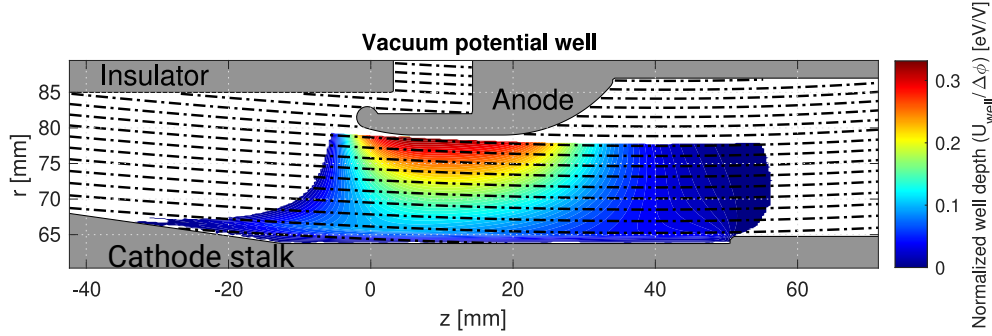
Figure 4.17: Potential well depth in vacuum close to the corona ring region of the GT170 prototype, normalized by the applied accelerating potential on the cathode stalk. The black dashed dotted lines show the magnetic field lines.

prevented the operation of the gyrotron for shots longer than a few tens to hundreds of milliseconds, even at a reduced power.

During the experimental campaign, voltage stand-off measurements were performed using the prototype geometry and a reduced magnetic field amplitude $B_{exp} = 0.6B_{nom}$ compared to the nominal configuration. To this end, the current collected on the body of the gyrotron was measured for several values of applied bias $\Delta\phi$ between the cathode stalk and the rest of the gyrotron. The results of these measurements are represented in yellow on Figure 4.20. In this experiment, the neutral gas pressure was measured at the collector, far from the electron gun region $p_{n,\text{collector}} \approx 1 \times 10^{-8}$ mbar and is estimated to $p_{n,\text{gun}} \approx 1 \times 10^{-6}$ mbar in the electron gun. This value is unfortunately only estimated and could be off by one order of magnitude, which is relevant when comparing FENNECS simulations and experimental measurements.

To validate FENNECS quantitatively, simulations have therefore been run in the prototype geometry with the reduced nominal magnetic field configuration. These simulations show the formation of two electron clouds in a configuration similar to the one obtained in the refurbished geometry when a potential well was present (see Figure 4.6). One cloud is of high density located close to the corona ring and one is elongated with a lower density close to the cathode stalk (see Figure 4.18). Electrons belonging to the clouds drift outwards of the trapping region and lead to the collection of electronic currents on the simulation boundaries. The upper cloud current is collected on the anode, also called body, and the electrons from the lower cloud drift radially outside of the potential well and free stream along the magnetic field lines toward the gyrotron cavity (see Figure 4.19). These lost electrons are replaced by electrons freed from the RNG atoms by ionization, leading to a steady-state density in the clouds (see Figure 4.19).
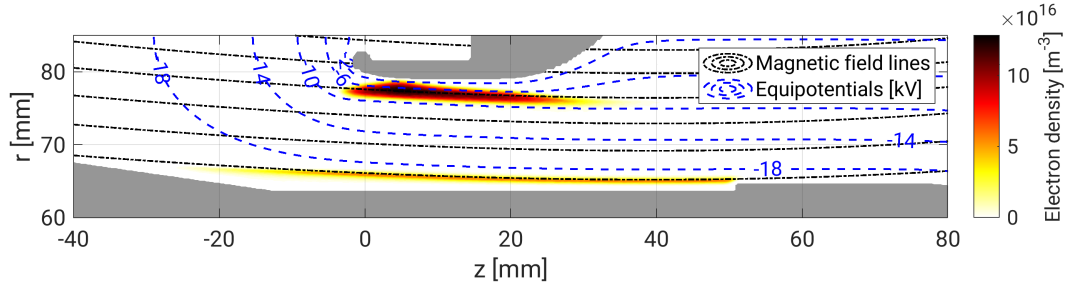
Figure 4.18: Steady-state electron density in the GT170 prototype electron gun for a bias $\Delta\phi = 20\,\text{kV}$ and a reduced magnetic field amplitude $B_{exp} = 0.6B_{nom}$. The blue dashed lines represent the electric equipotential lines and the black dashed-dotted lines show the magnetic field lines.
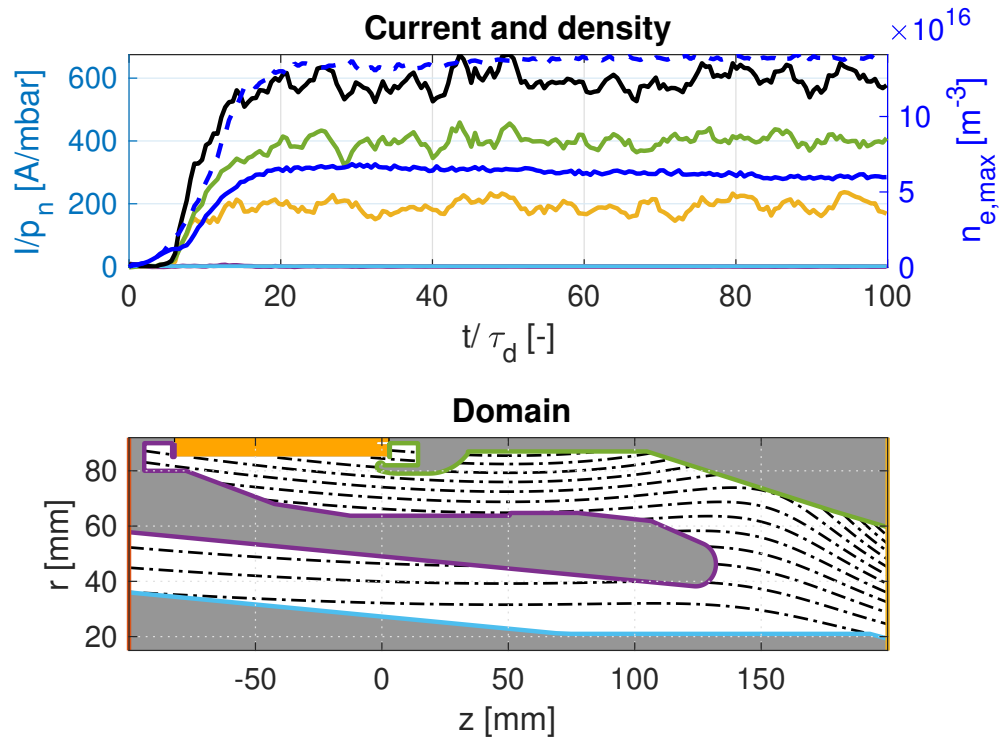
Figure 4.19: Top: Normalized time evolution of the maximum electron density in the upper cloud (solid blue) and the lower cloud (dashed blue), and of the normalized collected current on the electrode surfaces (solid colour) and total collected current (solid black). The geometry is that of the GT170 prototype, the applied bias is $\Delta\phi = 20\,\text{kV}$ and $B = 0.6B_{nom}$. The colour code of the currents correspond to the colour code of the electrodes in the bottom plot. Bottom: Geometry used in the simulation and colour coding of the current collection surfaces. The black dashed-dotted lines show the magnetic field lines.

4.4.1 FENNECS quantitative validation

To quantify the accuracy of FENNECS, simulations were run, in the geometry of the GT170 prototype gun, for several values of applied bias in the same range as the experimental measurements. The simulations

were run with the nominal magnetic field at 60% amplitude and with the IIEE module deactivated. The total current in steady-state is measured as well as the current collected only on the anode/body and represented in Figure 4.20. The simulations show that the current is overestimated below $\Delta\phi < 100\,\mathrm{kV}$ and underestimated above $\Delta\phi < 120\,\mathrm{kV}$. However, the predicted current is in the correct order of magnitude between $80\,\mathrm{kV} < \Delta\phi < 120\,\mathrm{kV}$. It is interesting to note that for $\Delta\phi = 150\,\mathrm{kV}$, the current decreases again, similarly to what was observed in the refurbished geometry. The discrepancy between simulation and experiments cannot be explained by an error in the RNG pressure as the exponential increase of the experimental current as a function of the applied bias is not reproduced in the simulations, and the RNG pressure would just scale the current by a constant factor. However, it is possible that p_n is a function of the applied bias or of the electron cloud dynamics, which would add non-linear effects in the predictions that are not included in FENNECS. Similarly, the electrodes could be heated by ion bombardment and lead to the onset of thermionic emission of electrons on the electrodes surfaces, thus increasing the collected current. However, the inclusion of IIEE effects in the simulations would not help in explaining the overestimation of the current, as it would only increase the total collected current. This difference between experiments and simulations suggests that additional physics might be missing in the model used by FENNECS.
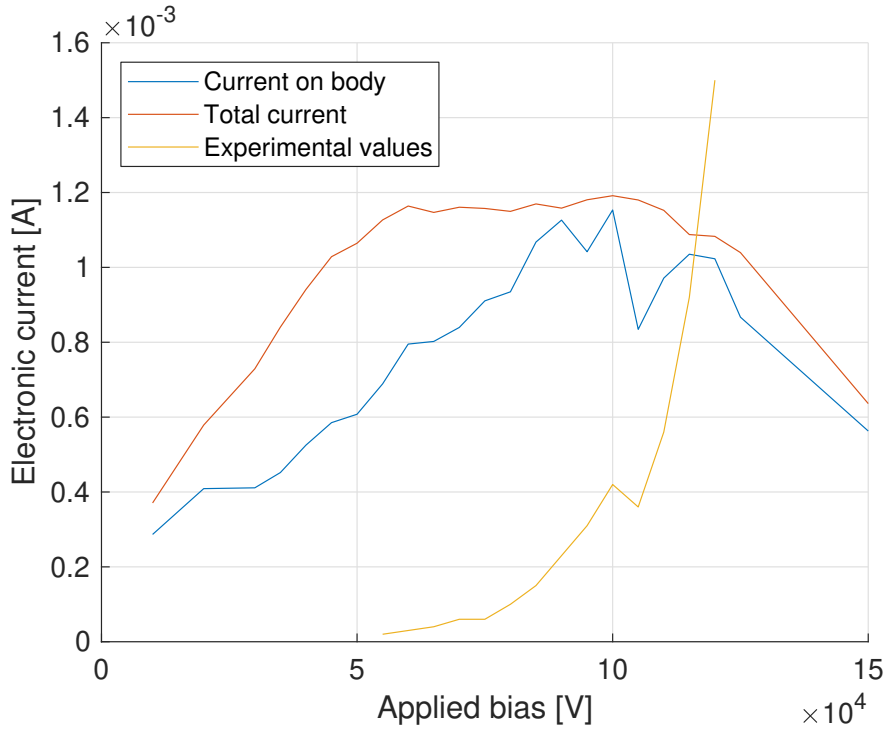
Figure 4.20: Electronic currents collected on all boundaries (red) and on the anode/body (blue) in the simulated prototype geometry obtained from FENNECS simulations as a function of the applied bias. The experimental current measurements (yellow) on the anode/body of the GT170 prototype measured as a function of the applied bias are also represented.

Another hypothesis to explain the overestimation of the current, which can presently be studied, is the onset of diocotron instabilities during the cloud formation. This instability could lead to radial drifts of the electrons, causing additional losses of particles either at the electrodes or in the region between the inner and outer potential wells. This would lead to a reduced trapped electron density, imposing a reduced ionization source and leading to a reduced collected current. A preliminary study of this configuration and

of the linear stability of these clouds to diocotron normal modes is presented in Chapter 6.

4.5   Summary and conclusions

In this chapter, we have shown that FENNECS is able to accurately simulate the complex geometry of a realistic gyrotron MIG. Furthermore, it can reproduce the same regions of problematic and non-problematic currents observed experimentally for the dummy-gun geometry. We have shown that a new region devoid of problematic currents could be accessed if the electric bias could be increased above the 105 kV experimental limit. However, this additional result still needs to be verified experimentally. The simulations including IIEE effects have shown that these effects lead to a change in the total collected current of about 20% compared to the simulations without IIEE. This result and the numerical cost of simulating the ion trajectories motivates the use of FENNECS without IIEE effects during initial exploratory studies of a new gun geometry. It might however be important to use this module in the final steps of a gun design to obtain more precise predictions. Finally, the simulations in the GT170 prototype geometry show a discrepancy in the collected current amplitude between simulations and experiment. This difference could be explained by diocotron instabilities not simulated by FENNECS and motivates a study of this phenomenon. To this end, both theoretical studies of the diocotron instability in the configuration of the GT170 prototype, and experimental measurements of trapped electron clouds in configurations similar to gyrotron electron guns are relevant. Concerning experimental studies, a new flexible experiment called T-REX is being built at SPC [99]. This new experiment will study the electron cloud dynamics with more precise and dedicated diagnostics than what is physically possible in gyrotrons. T-REX will allow for different geometries and field topologies, and thus more direct comparisons between the simulations and experiments will be possible. Numerical studies of electron cloud formation in the T-REX geometry have already been performed and are the subject of the next chapter.

5 T-REX

One of the initial goals of this thesis was to design, build and operate an experiment to study the problem of trapped electron clouds in gyrotron guns. This experiment will allow better control on the trapping potential well, and the use of more precise diagnostic tools than what is possible on existing gyrotron guns. The experimental part of this project has been led by Francesco Romano, a post-doctoral fellow at SPC. However, the design of the electrodes geometry and of the relevant operating parameters has been supported by FENNECS simulations, which will be the subject of this Chapter. These simulations also contributed to the selection of the appropriate measuring devices planned for this experiment (physical quantity being measured) and of the range in which the devices must be sensitive.

5.1 The T-REX device

The TRapped Electrons eXperiment (T-REX) has been designed to allow the study of electron clouds trapped in coaxial geometries by electrostatic potential wells and subjected to strong externally applied azimuthal flows. As seen in Figure 5.1, the geometry consists of two concentric electrodes immersed in a strong axial magnetic field ($B \approx 0.3\,\mathrm{T}$ at the potential well location) generated by a 10 T superconducting magnet. The inner and outer electrodes are interchangeable to allow large freedom in potential well shapes and depths, thus to allowing electron trapping close to the inner, outer, or both electrodes. This allows the study of different trapping configurations that better reproduce potential wells happening in actual electron guns. A bias of up to $\Delta\phi = 20\,\mathrm{kV}$ can be applied between the inner and outer electrode, which, combined with the magnetic field, allows the formation of deep potential wells ($U_{well} \approx 3\,\mathrm{keV}$). To control the background gas composition in the chamber, a mass flow controller is installed to regulate the desired gas input flow, therefore also controlling the pressure. In addition, a two stage vacuum pumping system is installed to ensure that the required high vacuum level in the vacuum chamber during experiment, $p > 1 \times 10^{-7}\,\mathrm{mbar}$, can be reached. This pump is coupled to a residual gas analyser, which allows the measure of the gas composition inside the vacuum vessel.

To measure the behaviour of the electron cloud, current and voltage probes are planned. Those are to provide information on the currents collected on individual electrode surfaces and to determine where the electrons and ions are lost. In addition, a phosphor screen coupled with an imaging camera is installed on the top of the vacuum chamber, through the viewport it is expected to determine the spacial distribution of the clouds line integrated over the magnetic field lines. This is a destructive measurement that will be used by rapidly removing the bias on the electrodes, which will in turn lead to the suppression of the
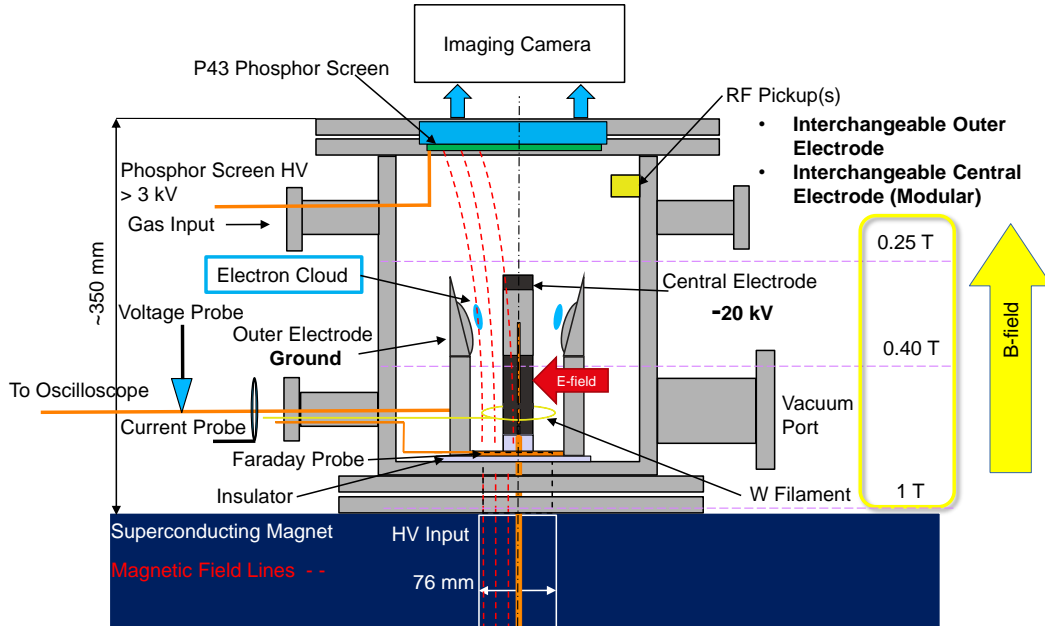
Figure 5.1: Schematic of the T-REX device as considered for the first experimental campaign, with the phosphor screen and camera configuration at the upper end. The vertical dashed line indicates the z-axis of cylindrical symmetry. (Courtesy of Francesco Romano)

trapping potential well. This allows the initially trapped population of electrons to free stream along the magnetic field lines toward the phosphor screen. The electrons reaching the phosphor screen will cause photoemission on the screen surface and produce an image that can be captured by a digital camera. The light intensity of this image will finally be used to obtain the relative line-integrated density of the cloud along the magnetic field lines and should permit the study of the radial and azimuthal density profile of the clouds. In addition, the screen can serve as a Faraday cup and allow the measure of the total trapped charge in the cloud. A Faraday cup is also present at the bottom of the device to collect the remaining released electrons that free-stream toward the bottom of the device.

From experimental results of gyrotron guns and FENNECS simulations, it is expected that the source of primary initial electrons, imposed by field emission on the electrodes or by background ionization of the residual neutral gas present in the vessel, will be sufficient to initiate the formation of electron clouds in T-REX. However, if this turns out not to be the case, a circular tungsten filament has been planned. It will be located between the electrodes, at the bottom of the vessel. This filament could then also serve as a controlled source of primary electrons to perturb the system and to better understand the effect of external electron sources.

5.1.1 Magnetic field configuration

The magnetic field used for the T-REX experiment is generated by a magnet composed of 13 superconducting coils whose characteristics are given in Table 5.1. This magnet was previously used for a low power frequency tunable 263.5 GHz CW gyrotron designed for dynamic nuclear polarization-nuclear magnetic resonance applications [106] that has been decommissioned. The coils are powered by one power supply generating a control current I_c to produce the desired magnetic field. At the nominal current for operating

T-REX, I_c = 100.0 A, the magnetic field amplitude in the centre of the magnet ($r = 0$, $z = 0$) is B_0 = 10 T. However, the experiment is placed on top of the magnet for accessibility, therefore the magnetic field amplitude in the vacuum vessel will be lower. The magnetic field amplitude and field lines, inside the T-REX vacuum vessel, are represented in Figure 5.2 for the nominal case.

Coil	z_{min} [mm]	z_{max} [mm]	r_{min} [mm]	r_{max} [mm]	# of turns
C1	-145.0	145.0	52.592	60.069	1670
C2	-145.0	145.0	60.069	66.051	2217
C3	-150.0	150.0	76.919	82.502	2960
C4	-150.0	150.0	82.502	90.129	4995
C5	-150.0	150.0	90.129	103.638	12793
C6	-150.0	-112.66	103.638	104.187	59
C7	-150.0	-113.66	104.187	104.735	57
C8	-150.0	-114.66	104.735	105.283	56
C9	-150.0	-115.65	105.283	105.832	54
C10	112.66	150.0	105.638	104.190	59
C11	113.66	150.0	104.187	104.735	57
C12	114.66	150.0	104.735	105.283	56
C13	115.65	150.0	105.283	105.832	54

Table 5.1: Characteristics of the 13 super conducting coils generating the magnetic field of the 10 T magnet used for T-REX. The axial reference $z = 0$ m is defined in the middle of the coil assembly, and is also used as axial origin for the simulations.
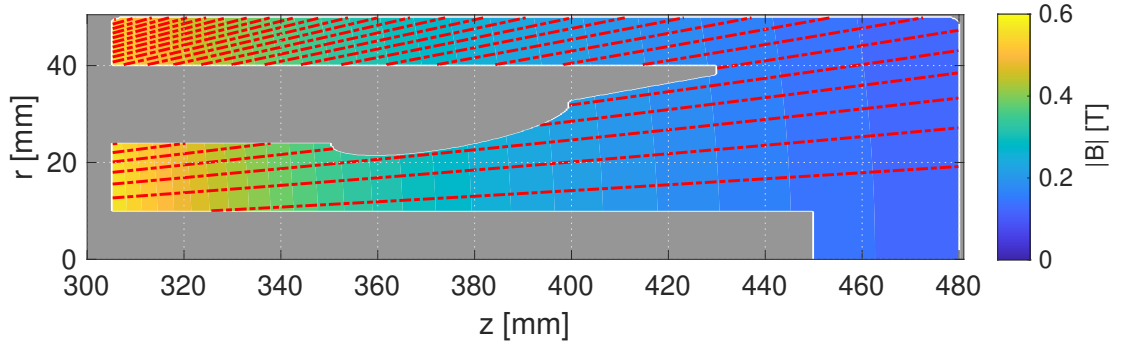
Figure 5.2: Magnetic field configuration generated by the 13 superconducting coils for the nominal coil current I_c = 100.0 A. The colour plot indicates the magnetic field amplitude, and the red lines show the magnetic field lines. The gray parts show one of the electrodes configurations.

5.1.2 Electrodes configurations and relevance for studying electron trapping in MIGs

The T-REX device has been built with the capability to change both the inner and the outer electrodes geometries. In the current version of the experiment, three configurations have been considered, allowing to change the location and shape of the potential well, and to study the different types of electron clouds that can form inside gyrotron electron guns. The first configuration, named configuration 1 in this chapter,
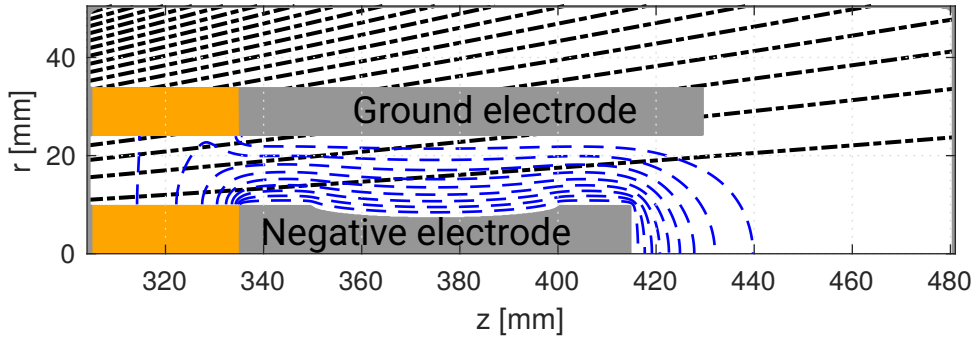
Figure 5.3: Geometry of the T-REX device used for the simulations in the case where the potential well is formed close to the inner electrode (configuration 1). Gray denotes metallic boundary conditions and yellow denotes an insulator with zero surface charge. The black lines show the magnetic field lines and the blue dashed lines show the electric equipotential lines.
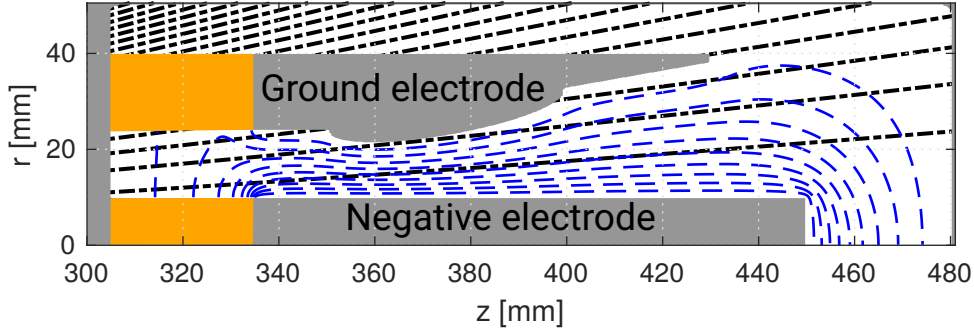
Figure 5.4: Geometry of the T-REX device used for the simulations in the case where the potential well is formed close to the outer electrode (configuration 2). Gray denotes metallic boundary conditions and yellow denotes an insulator with zero surface charge. The black lines show the magnetic field lines and the blue dashed lines show the electric equipotential lines.

Figure 5.5: Geometry of the T-REX device used for the simulations in the case where the potential well covers the gap between the electrodes (configuration 3). Gray denotes metallic boundary conditions and yellow denotes an insulator with zero surface charge. The black lines show the magnetic field lines and the blue dashed lines show the electric equipotential lines.

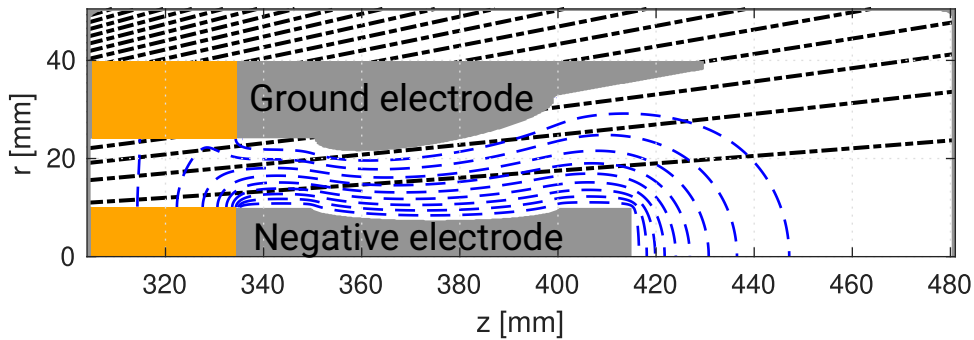leads to the formation of a potential well close to the inner electrode by creating an elliptic cut inside the coaxial insert (see Figure 5.3). In the second configuration, a potential well is formed against the outer electrode by creating an elliptic protrusion on the outer electrode (see Figure 5.4), and will be referred to as configuration 2. These two configurations are relevant as different steady-state behaviours have been observed between the clouds confined close to the outer electrode, leading to cloud breathing, and the ones confined close to the inner electrode, leading to a stable cloud. Finally, in configuration 3 (see Figure 5.5), both types of potential wells exist at the same time by combining the carved inner electrode and shaped outer electrode, which creates a deeper and wider potential well spanning the gap between the electrodes. This third configuration allows to better reproduce the kind of trapping that was observed for the GT170 gyrotron of Chapter 4, as the potential well spans the vacuum region between the electrodes, and should lead to the formation of two concentric annular electron clouds.

As can be seen in Figures 5.6, 5.7 and 5.8, potential wells with sizes similar to the ones found in gyrotron guns are formed with depths of a few keV for the maximum applied bias of 20 kV. Similarly, as seen in Figure 5.2 the magnetic field amplitude in the trapping region ($B \sim 0.3$ T) is consistent with the ones present in gyrotrons. While the applied bias in T-REX is smaller than the ones found in gyrotrons, the gap between the electrodes is also smaller, which leads to vacuum radial electric fields of the order of $E_r \sim 1 \times 10^6$ V m^{-1} consistent with magnetron injection guns (MIG) configurations. In the T-REX configurations, the trapped electrons gain a kinetic energy, due to the $\vec{E} \times \vec{B}$ drift, of the order of several tens to hundreds of eV and are therefore capable of ionizing the residual neutral gas present in the vacuum vessel. These facts show that T-REX is relevant to study electron trapping in regimes similar to the ones happening in gyrotron electron guns.

Figure 5.6: Vacuum potential well formed for the electrode configuration 1 and an applied bias of 20 kV. The black lines show the magnetic field lines.

5.2 Numerical simulations and predictions

To characterize the design of the geometries for T-REX and predict the range of signals collected by the measurement devices, simulations have been run in FENNECS using mainly configurations 1 and 2. The geometries represented in Figures 5.3 and 5.4 are implemented in FENNECS with a default bias voltage $\Delta\phi = 20$ kV and using the magnetic field generated by the 10 T magnet at an operating current $I_c = 100$ A. Unless specified, the residual neutral gas considered is argon and the ion induced electron emission (IIEE) effects are neglected (see Section 2.2.9). As in Chapter 3, the system is loaded with a low density electron cloud ($n_{e0} = 1 \times 10^{13}$ m^{-3}) spanning the trapping region, to initiate the cloud formation. In addition, a
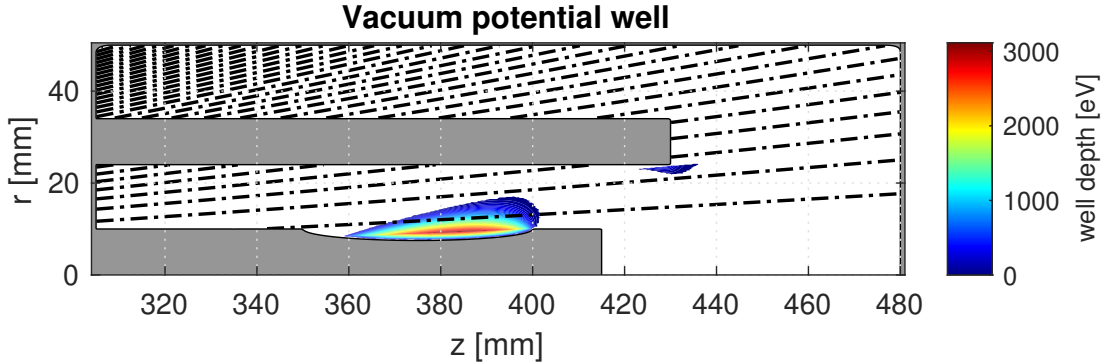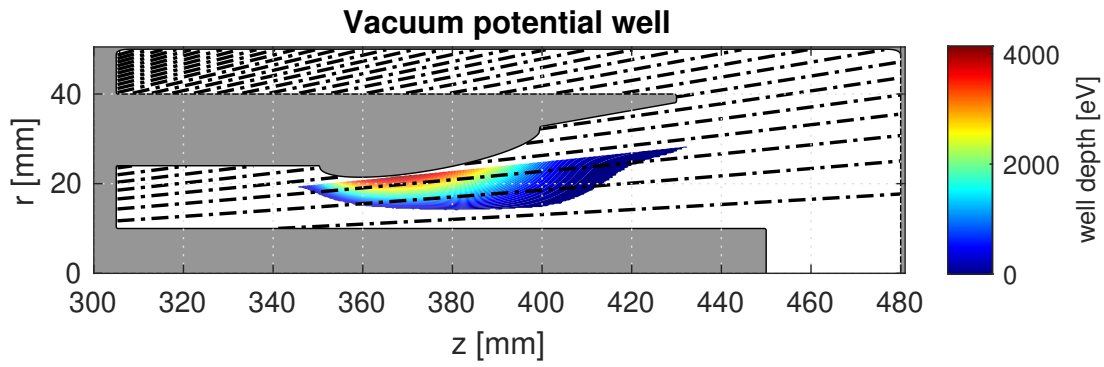
Figure 5.7: Vacuum potential well formed for the electrode configuration 2 and an applied bias of 20 kV. The black lines show the magnetic field lines.
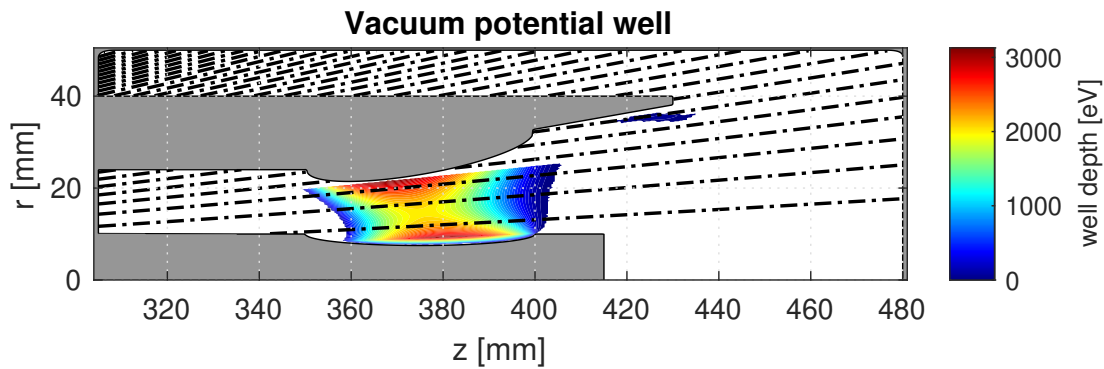
Figure 5.8: Vacuum potential well formed for the electrode configuration 3 and an applied bias of 20 kV. The black lines show the magnetic field lines.

volumetric electron source of small intensity, compared to the ionization source intensity, is activated to sustain or enable the restart of the cloud formation.

5.2.1 Time evolution

In both configurations, the simulations show the formation of electron clouds in the potential well region with densities of the order of $n_e \approx 1 \times 10^{17}$ m^{-3}. As seen in Figure 5.9, the upper cloud configuration (configuration 2) shows the same type of density and current oscillations as observed in Chapter 3 with a periodicity of $\sim 20\,\tau_d$. We recall that $\tau_d = 1/(n_n < \sigma_d v >_f)$ is the effective collisional drag characteristic timescale, which is inversely proportional to neutral gas density n_n, the averaged effective drag cross-section $\sigma_d \approx \sigma_{io} + \sigma_{ela}^d$ and the averaged electron velocity v. The cross-sections σ_{io} and σ_{ela}^d are respectively the ionization and effective elastic collision cross-sections for momentum exchange (see Section 3.3.4). As an illustration, for the experimental parameter planned for T-REX (Ar gas and $p_n = 1 \times 10^{-5}$ mbar) $\tau_d \approx 20\,\mu$s. The cloud remains mainly axially trapped, with an axial current 10 times lower than the radial current. This observation is consistent with the results of Chapter 3. In this configuration, the total current reaches $I_{outer} = 1 \times 10^3$ A mbar^{-1}, with a maximum total trapped charge of $Q_{outer} = 2.4 \times 10^{-7}$ C.
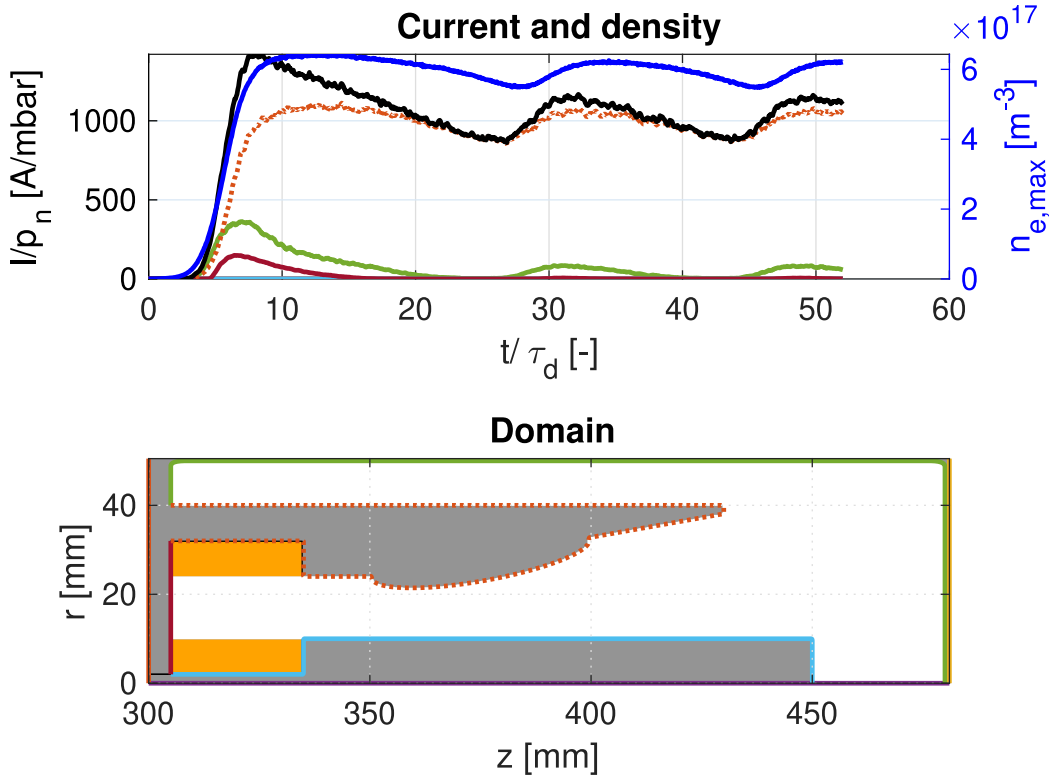
Figure 5.9: Top: Normalized time evolution of the maximum density in the electron cloud (blue solid line) and respective normalized collected currents on the electrode surfaces for configuration 2. The solid black line shows the total collected current, and the colour and line style code shows the location of collection of the currents integrated over the corresponding surface. Bottom: Geometry of the electrodes and colour coded surfaces.
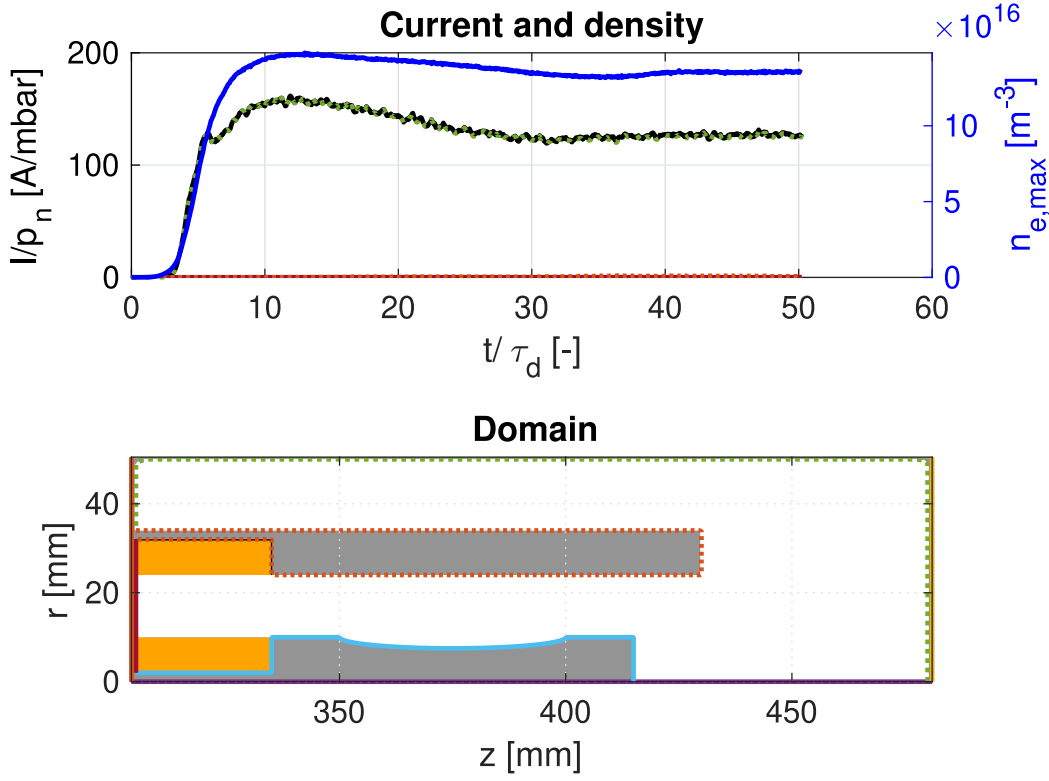
Figure 5.10: Top: Normalized time evolution of the maximum density in the electron cloud (blue solid line) and respective normalized collected currents on the electrode surfaces for configuration 1. The solid black line shows the total collected current, and the colour and line style code shows the location of collection of the currents integrated over the corresponding surface. In this configuration, the total current is dominated by the current on the green dotted surface and the black and green dotted curves overlap. Bottom: Geometry of the electrodes and colour coded surfaces.

In configuration 1 (see Figure 5.10), the cloud reaches an equilibrium in current and density. In this configuration, the current is smaller than for configuration 2 and only collected on the vacuum vessel (green boundary in Figure 5.10) with a steady-state amplitude $I_{inner} = 125\,\mathrm{A\,mbar^{-1}}$. Similarly, the total trapped charge is lower with $Q_{inner} = 4.4 \times 10^{-8}\,\mathrm{C}$.

As seen in Figure 5.11, configuration 3 leads to the presence of two electron clouds: one upper cloud close to the outer electrode and one lower cloud close to the inner electrode. Interestingly, the steady-state clouds' location and size correspond to what a simple combination of configurations 1 and 2 would give. In addition, the electron cloud densities reach similar amplitudes for both the lower and upper clouds as in the individual configurations. However, the system is more stable as the oscillations observed in configuration 2 disappear for a reason that is not yet fully understood (see Figure 5.12). Similarly, the current collected on the outer electrode is reduced by 15% compared to configuration 2 with $I_{outer,3} = 870\,\mathrm{A\,mbar^{-1}}$. The current collected on the vacuum vessel is here similar to configuration 1 with $I_{inner,3} = 130\,\mathrm{A\,mbar^{-1}}$. In steady-state, the total trapped charge is lower than the combination of configurations 1 and 2 with $Q_{both} = 2.15 \times 10^{-7}\,\mathrm{C}$. In addition, this configuration shows that a cloud located close to the ground electrode increases the amplitude of the radial electric field E_r compared to the vacuum one E_r^{vac}, while a

cloud located close to the negative electrode reduces the amplitude of the radial electric field compared to the vacuum one, due to space-charge effects. This result, represented in Figure 5.13, is important because the Larmor radius of the electrons is proportional to the amplitude of E_r, which can lead to an increase of the cloud radial dimensions for the upper cloud and a decrease of the lower cloud radial dimensions. Furthermore, as shown in the fluid model of section 3.3, the radial drift velocity is proportional to E_r (see equation (3.16) of page 63), which leads to different behaviour of the clouds as the density increases. This effect, combined with the differences in the self-consistent potential well dimensions between the configurations, is a good candidate to explain the difference in stability of the clouds between configuration 1 and configuration 2.
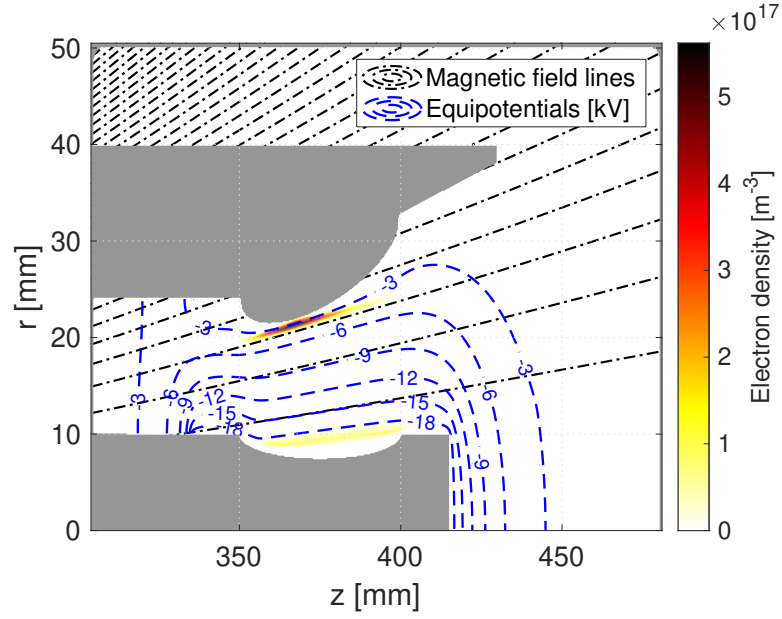
Figure 5.11: Steady-state electron clouds positions and densities for electrode configuration 3. The magnetic field lines (dashed dotted black) and the electric equipotential lines (dashed blue) are also represented. Here, the aspect ratio is not respected to increase readability.

5.2.2 Finite Larmor radius limit of confinement in configuration 2

In configuration 2, a set of simulations have been run with different magnetic field amplitudes to study how this parameter can be used to control the trapped electron cloud density and the total collected current. These results will be particularly important during the commissioning of T-REX to protect the electrodes and the measurement devices. In these simulations, the reference is the nominal magnetic field B_{nom} generated when the superconducting coils are powered at the nominal current $I_c = 100\,\text{A}$.

As predicted by the analytical fluid model of Section 3.3, the maximum trapped density shows a B^2 proportionality as B is decreased until $B \approx B_{nom}/2$ (see Figure 5.14 left). At lower magnetic field amplitudes, the Larmor diameter starts to be of the same order of magnitude as the radial dimensions of the vacuum potential well (see Figure 5.14 right). This fact strongly limits the confinement properties of the well, as space-charge effects will further reduce the potential well dimensions and therefore limit the maximum trapped electron density. This effect induces a reduction of the total collected current, as
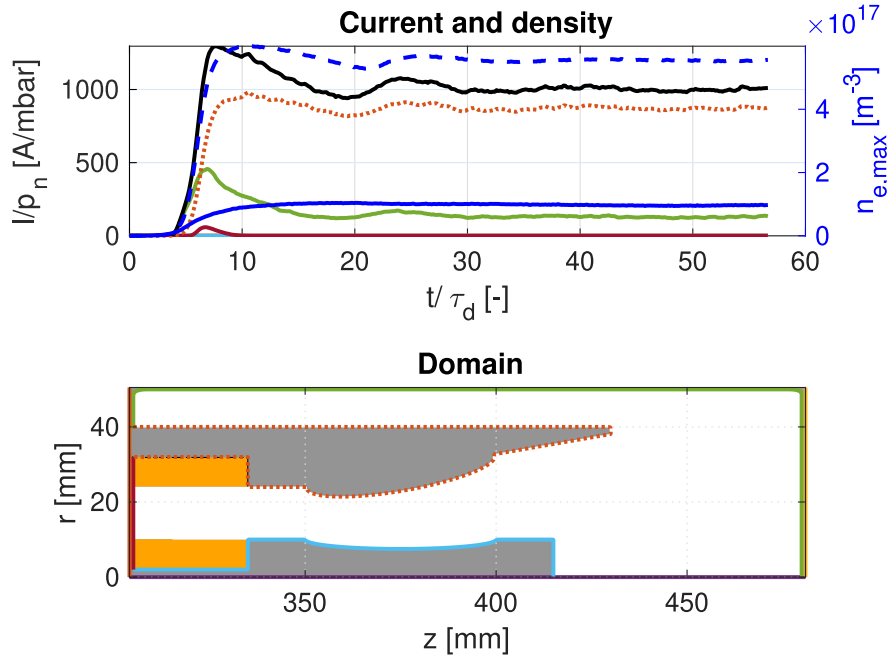
Figure 5.12: Top: Normalized time evolution of the maximum density in the upper cloud (blue dashed line) and lower cloud (blue solid line), and respective normalized collected currents on the electrode surfaces for configuration 3. The solid black line shows the total collected current, and the colour and line style code shows the location of collection of the currents integrated over the corresponding surface. Bottom: Geometry of the electrodes and colour coded surfaces.
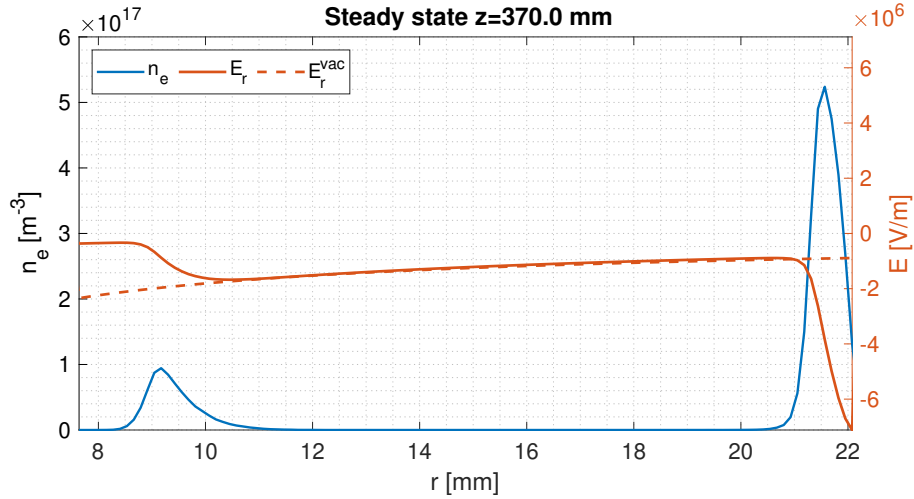

Figure 5.13: Steady-state (solid orange) and vacuum radial (dashed orange) electric fields for electrode configuration 3 at the position $z = 37$ mm. In addition, the steady-state electron radial density profile (solid blue) is plotted. The radial limits are set for the vacuum region between the negative and ground electrodes, where the electron clouds are present.
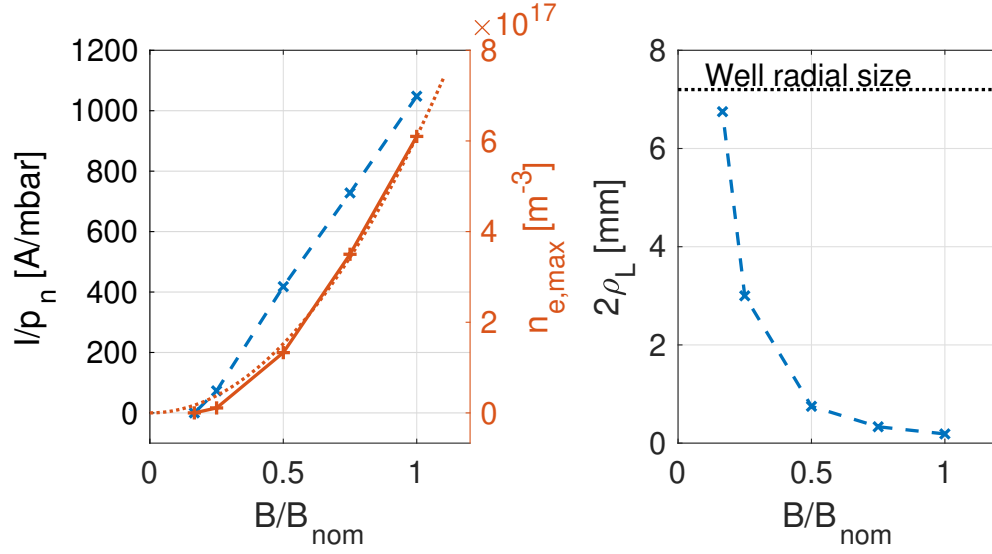
Figure 5.14: Left: Steady-state maximum current (blue) and density (red) for the scan in magnetic field amplitude in configuration 2. The gas considered is Ar, and the bias is $\Delta\phi = 20\,\mathrm{kV}$. The red dotted line shows the B^2 proportionality of the density predicted by the analytical model of Section 3.3. Right: Larmor diameter in vacuum for electrons generated in the region of deepest potential well in configuration 2. For comparison, the radial dimension of the well in vacuum at the axial position where the well is deepest is highlighted by the black dotted line.

can be observed in the left plot of Figure 5.14. These observations support the hypothesis advanced in Section 4.3.2, regarding the GT170 prototype geometry, which states that finite Larmor radius effects lead to the reduction in collected current when the bias voltage was increased above a certain threshold. This result is important for T-REX because it shows that the experiment can be run in a configuration where a deep potential well is present, and no electron cloud build-up can be achieved. It also shows that control parameters of the experiment can be changed to limit the total collected current, which should prevent damages to the measurement devices during the commissioning of T-REX. In addition, since a high impedance power supply will be used to impose the bias, high amplitude currents will cause the shutdown of the power supply to protect its internal components. Therefore, the control of the current generated by the cloud will become important to prevent damages to the power supply and to ensure long operations of the experiment in the presence of the clouds.

5.2.3 Capacitive and resistive effects of the power supply

Since the power supply (PS) selected for T-REX has a high-impedance and is connected to the electrodes by capacitive coaxial cables, simulations have been run using the non-ideal PS module of FENNECS (see Section 2.2.7) to assess its effect on the electron cloud. The technical document of the PS (TREK model 20) specifies that it is capable of delivering 20 mA for a maximum of 20 ms at 20 kV. To simulate this behaviour, an internal resistor of $R_S = 1\,\mathrm{M\Omega}$ is selected. This characteristic of the PS was not disclosed in the manual of the TREK, and a large value is used as an upper bound to simulate a worst case scenario. However, the actual internal resistance of the TREK should be measured experimentally to better reproduce the experimental results. In addition, the capacitive effect of the 3 m cable connecting the PS to the electrodes has been estimated at $100\,\mathrm{pF\,m^{-1}}$. This capacitance is combined with the 37 pF capacitance of

the geometry of configuration 2, which has been calculated using the commercial COMSOL software. This leads to a final simulated capacitance $C_G = 337\,\text{pF}$.

This study was done in configuration 2 as it is the one with the highest collected current and is the only one that shows cloud breathing, which could add resonance effects and unexpected time dependent effects. For the same reasons, the simulations are run with a bias $V_S = 20\,\text{kV}$ and the highest amplitude magnetic field with $I_c = 100\,\text{A}$. The time evolution of the maximum electron density $n_{e,max}$, applied bias V_p, and total collected current i_p was obtained from simulations at three experimental neutral gas pressures from 1×10^{-5} mbar to 1×10^{-3} mbar and plotted in Figure 5.15. On the same figure is also represented the behaviour of the system for an ideal PS at an experimental pressure of 1×10^{-4} mbar. In this set of simulations, the simulated gas is H_2. For this configuration and this gas the maximum normalized current is $I_{H_2,max} = 340\,\text{A mbar}^{-1}$ which is approximately one third of the current generated in the presence of Ar. The simulations show that as expected the applied bias is reduced by the presence of the electronic currents leading to a maximum average collected current in steady-state of $< I_{max} >_t = 20\,\text{mA}$ for pressures $p_n \geq 1 \times 10^{-4}$ mbar. For the case $p_n = 1 \times 10^{-3}$ mbar, this leads to an important reduction of the maximum cloud density in steady-state and a strong reduction of the bias in steady-state to $V_{p,ss,10^{-3}} = 2\,\text{kV}$. Below $p_n = 1 \times 10^{-4}$ mbar, the maximum electron density and collected current using the non-ideal PS, recover the values of the ideal case, with a doubling of the oscillation period. Finally, the simulation at $p_n = 1 \times 10^{-5}$ mbar recovers both the amplitudes and the oscillation periods of the ideal case, leading to a reduced applied bias in steady state of $V_{p,ss,10^{-5}} = 18\,\text{kV}$. For this reason, and to better compare the experimental results with the simulation results obtained using the ideal PS, it is recommended to perform the experiments with a neutral pressure $p_n \leq 1 \times 10^{-5}$ mbar. However, one can note that for all the simulated pressures, the steady-state is reached before the PS trip time of $t_{crit} = 20\,\text{ms}$, which means that in the experiments, the clouds would have time to form, and these simulation results could potentially be validated experimentally.

5.2.4 Importance of IIEE effects

Similarly to what was done in the refurbished GT170 configuration, simulations have been run with the ion induced electron emission (IIEE) module "turned on" to quantify the effect of ion induced electron emission (see Section 2.2.9). These simulations were done in the frame of the internship of an EPFL Master student [91] and were run in the preliminary versions of configurations 1 and 2 both with and without IIEE effects simulated. In these simulations, the enclosing vacuum vessel is not fully simulated, but the trapping region, the electrodes geometry and the magnetic field are identical, allowing for comparisons with the results of the previous section. The simulated neutral gas is H_2, as it is the most relevant gas for gyrotron electron guns, with a numerically increased pressure $p_n = 1 \times 10^{-2}$ mbar. The magnetic field is set at the nominal amplitude with $I_c = 100\,\text{A}$, and an ideal bias $\Delta\phi = 20\,\text{kV}$ is applied between the inner and outer electrode. In accordance with the experimental setup, the electrode material is set to Al in the simulations. In this section, the volumetric source is also deactivated, to isolate the effects of the IIEE source and determine if the IIEE source is sufficient to sustain the cloud formation.

Configuration 1

In configuration 1, a cloud of density $n_{e,0} = 5.5 \times 10^{13}\,\text{m}^{-3}$ is loaded in the region where the potential well is deepest, as represented in Figure 5.16. The simulations show the formation of an elongated electron cloud trapped in the elliptic cut of the inner electrode (see Figure 5.17), and that a steady-state is reached.
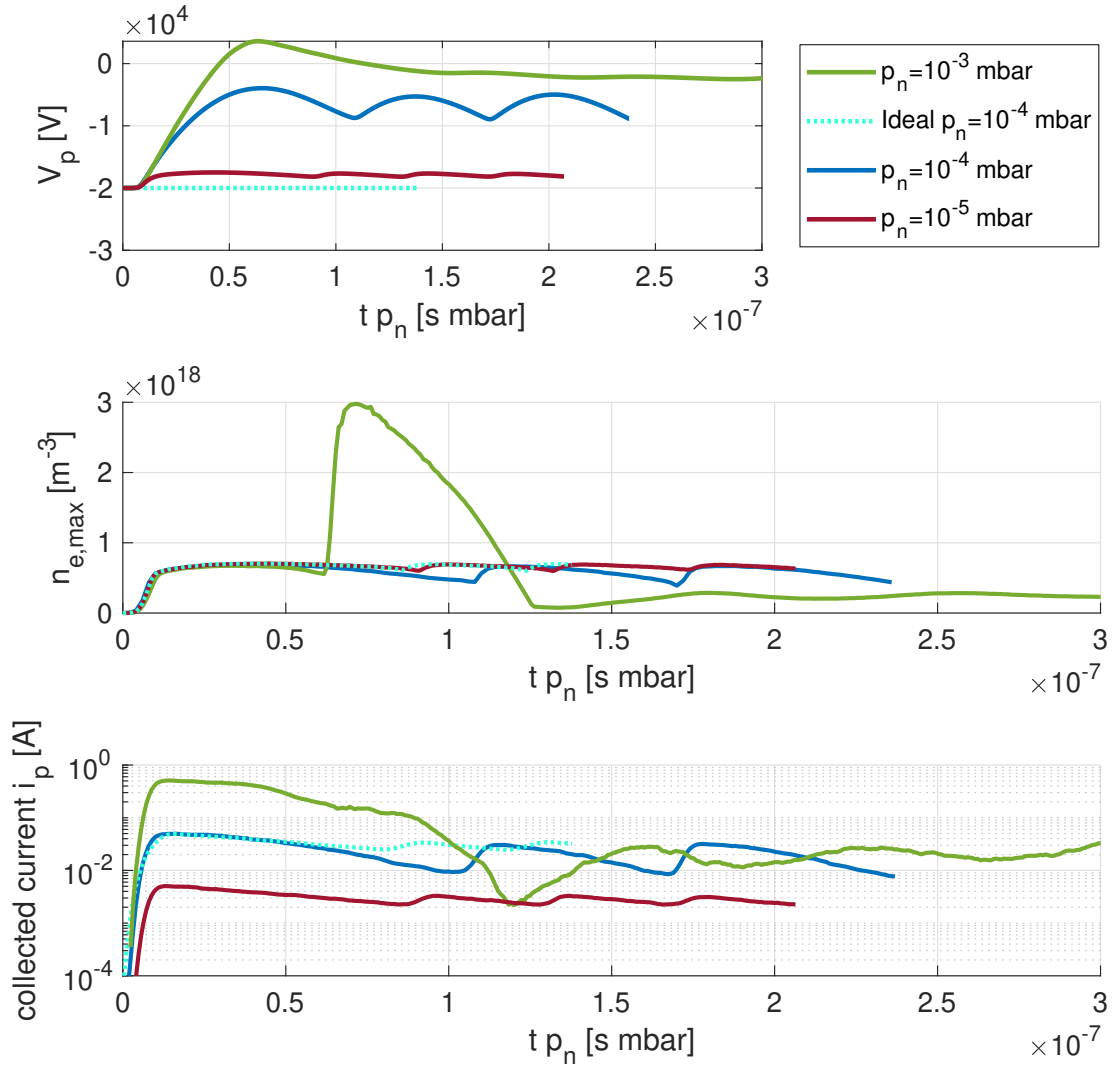
Figure 5.15: Normalized time evolution of the applied bias (top), maximum electron cloud density (middle) and collected current (bottom) in configuration 2 for various neutral gas pressures using the non-ideal PS module. As a comparison, a case at $p_n = 1 \times 10^{-4}$ mbar with ideal PS (dotted cyan line) is added. It is important to notice that the time is normalized by p_n as the collision time-scales are inversely proportional to the neutral gas pressure. The strong increase of the density at $t p_n \approx 0.7 \times 10^{-7}$ s mbar for $p_n = 1 \times 10^{-3}$ mbar is due to a compression of the cloud close to the bottom of the geometry, during the axial loss of the cloud, and not to a rapid increase in trapped charge.
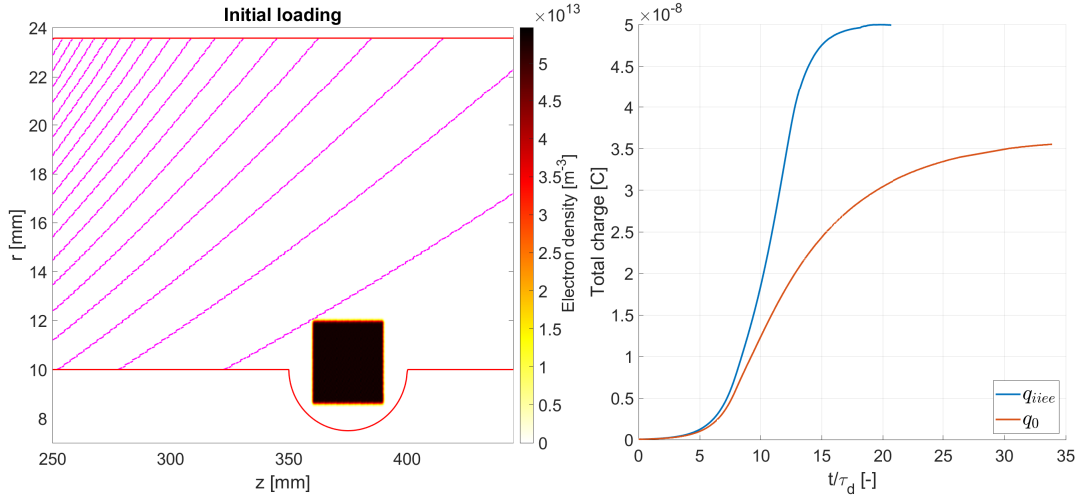
Figure 5.16: Left: Initial electron loading for the study of IIEE effects in configuration 1. Right: Time evolution of the total charge in the simulation with IIEE effects (blue) and without IIEE effects (red) in configuration 1.

As in the simulations of Section 5.2.1 for configuration 1, the cloud reaches a steady-state as a balance between the electron sources from ionization and additional electron emission on the inner electrode surface due to IIEE effects, and the sinks caused by radial drifts imposed by electron-neutral collisional drag. The simulations results show an increased trapped charge for the simulations with IIEE effects compared to the one without, and the maximum charge is reached faster due to the added electron source (see the right plot of Figure 5.16).

Considering the collected currents, the simulation results presented in Figure 5.18 show an increase of 20% of the total collected current in steady-state for the case with IIEE compared to the case without. As expected, these results are similar to the ones of Section 4.3.3. This result means that in the case of a H_2 RNG, the simulations without IIEE effects can serve as a baseline for predicting the order of magnitude of the total collected current by doubling the collected electronic current measured in the simulations. This allows the simulations to run faster without the costly ion trajectory computations (1.5 to 2 times more CPU hours), while still having numerical results comparable with experiments.

Configuration 2

In configuration 2, a cloud of density $n_{e,0} = 5.5 \times 10^{13}\,\mathrm{m^{-3}}$ is loaded in the region where the potential well is deepest. For simulations with and without IIEE, this initial population leads to the formation of an elongated electron cloud trapped close to the outer electrode with maximum densities close to the ones obtained without IIEE effects (see Figures 5.9, 5.19 right and 5.20). The ions generated in the electron cloud are accelerated by the strong radial electric field and collide with the inner electrode. In the IIEE simulations, these collisions lead to electron emission on the inner electrode surface and cause the formation of an electron cloud, highlighted in the green rectangle of Figure 5.19, that is not trapped by a potential well, and has a lower density than the main trapped cloud. This added electronic population causes an increased total electronic charge in the simulation of 15% but with almost identical formation time-scales for the cases with and without IIEE (see Figure 5.19 left). This can be explained by the fact
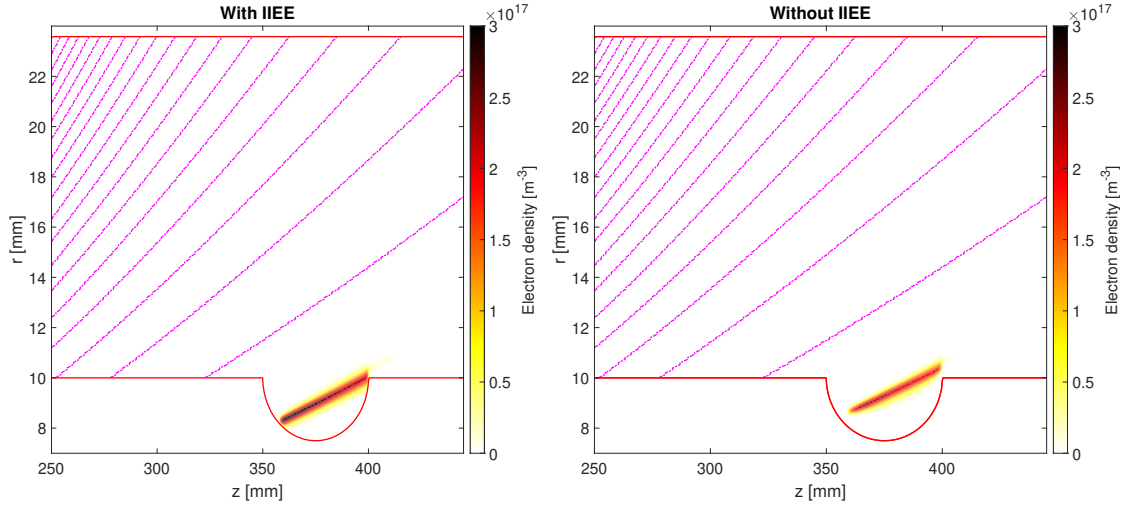
Figure 5.17: Left: Steady state electron cloud density in the simulation using IIEE effects in configuration 1. Right: Steady state electron cloud density in the simulation without IIEE effects in configuration 1. The red lines show the boundary of the electrodes, and the magenta dashed dotted lines represent the magnetic field lines. The aspect ratio is changed for readability.

that the IIEE source is located outside the potential well region, where the emitted electrons have a Larmor radius too small to allow them to reach the upper electrode. For this reason, they cannot influence the electron cloud trapped by the potential well, but they free-stream along the magnetic field lines and are collected at the top of the device.

The study of the collected currents, in configuration 2, shows that the inclusion of IIEE effects leads to an important axial current, similar in amplitude to the radial current, which increases the total collected current by about 40% (see Figure 5.20). This additional axial current on the phosphor screen could be well distinguished from the one coming from the main electron cloud, due to its location and its permanent presence, and should allow the experimental study of IIEE effects in T-REX. In addition, Figure 5.20 shows that the electronic current leaving the inner electrode (solid green curve of the top plot) is almost equal in amplitude to the electronic current collected at the right limit of the simulation domain (solid yellow curve of the top plot of Figure 5.20) confirming that the axial current is dominated by the IIEE emissions. The solid green curve is negative due to the definition of the positive direction of the current as entering the simulation boundaries. It is also important to note that since the solid green and solid yellow contributions of the currents are due to the same electronic population, the solid green curve is not used to calculate the total collected current. Indeed, the current of interest is the one flowing through the power supply and not the total current flowing through the vacuum vessel. In other words, the currents traversing the vacuum region need to be counted only once.

The result of the simulations with configurations 1 and 2 including IIEE effects confirm that these effects add contributions of order less than one to the total current, and are therefore not always crucial. In addition, it is interesting to note that the results of the GT170 simulations using the IIEE module (see Section 4.3.3) can be explained by combining the IIEE effects observed in configuration 1 (faster cloud build-up, higher current, higher density), and the ones observed in configuration 2 (higher total current, similar density, similar cloud build-up time) thus supporting further the relevance of T-REX to study the trapping conditions of electrons in gyrotron electron guns.

Figure 5.18: Top: Normalized time evolution of the maximum electron density (blue) and collected currents on the electrodes for the simulations with IIEE. The black line represents the total collected current and the green dashed-dotted line represents the ionic contribution of the current. Middle: Normalized time evolution of the maximum electron density (blue) and collected current on the electrodes for the simulations without IIEE. The black solid line represents the total collected current without IIEE and the dashed black line shows the total collected current for the case with IIEE for comparison. Bottom: Colour coded simulation boundaries for configuration 1 used to determine the location of the current collection for the top and middle plots.
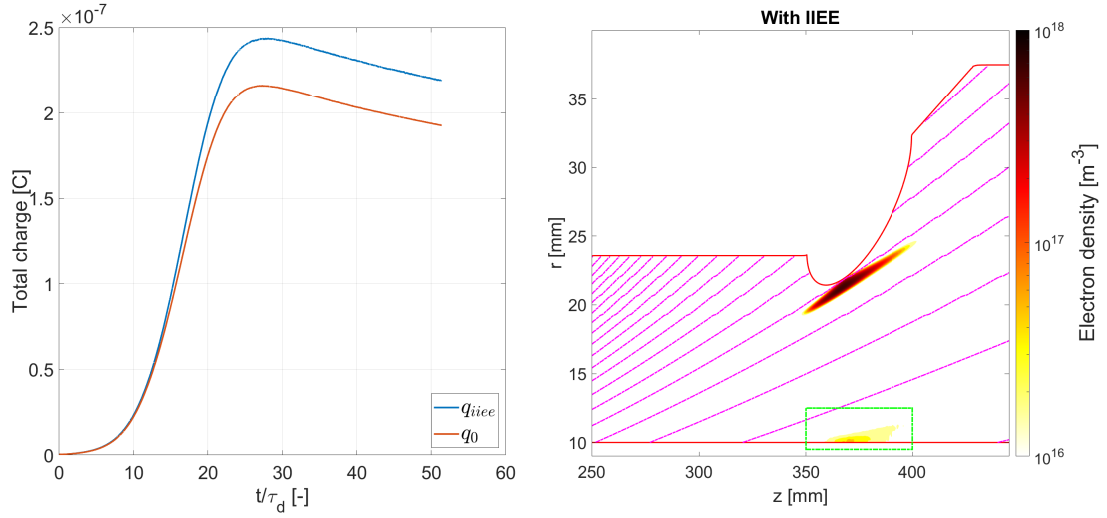
Figure 5.19: Left: Time evolution of the total charge in the simulation with IIEE effects (blue) and without IIEE effects (red) in configuration 2. Right: Steady state electron cloud density in the simulation with IIEE effects in configuration 2 represented in logarithmic scale. The red line shows the boundary of the electrodes and the magenta dashed dotted line represent the magnetic field lines. The green dotted rectangle highlights the location where ions are collected and where IIEE emissions are present, leading to a lower density electron cloud. The aspect ratio is changed for readability.

5.3   Summary and conclusions

This chapter, shows that T-REX is an experiment where electron trapping conditions are consistent with the ones happening in gyrotron electron guns. In particular, the vacuum potential wells are of similar depth and size as the ones found in the GT170 gyrotron gun (see Chapter 4). Similarly, strong azimuthal flows are imposed externally, causing the electrons to gain sufficient kinetic energy to be able to ionize the RNG present in the vessel.

The multiple simulations show that high density electron clouds can spontaneously form, reaching densities of the order of $1 \times 10^{17}\,\mathrm{m}^{-3}$ and reproducing individually the two general categories of electrostatically trapped electron clouds that are expected to be found in gyrotron electron guns. These are compact breathing clouds formed close to the anode, and elongated stable clouds close to the cathode. The simulation results also showed that a fundamental difference exists between the effect on E_r of the clouds formed close to the negative electrode versus clouds formed close to the ground electrode. In addition, the scan in magnetic field amplitude shows that the dependencies of the electron density on the magnetic field, derived in Section 3.3, are recovered and that this parameter can be used to control the total generated current and the electron cloud density. This result, combined with the scan in neutral gas pressure for the cases with the non-ideal power supply module, shows that T-REX can be operated in regimes where direct comparisons between the idealized simulations and the experiment should be possible.

Finally, the simulations with IIEE show that the IIEE effects increase the total collected current by a factor between 1 and 2, which is consistent with the factor obtained in the GT170 refurbished geometry of Section 4.3.3. In addition, the simulations using the IIEE module in configuration 2 show that the IIEE contribution to the current can be well separated from the one coming from the main trapped electron
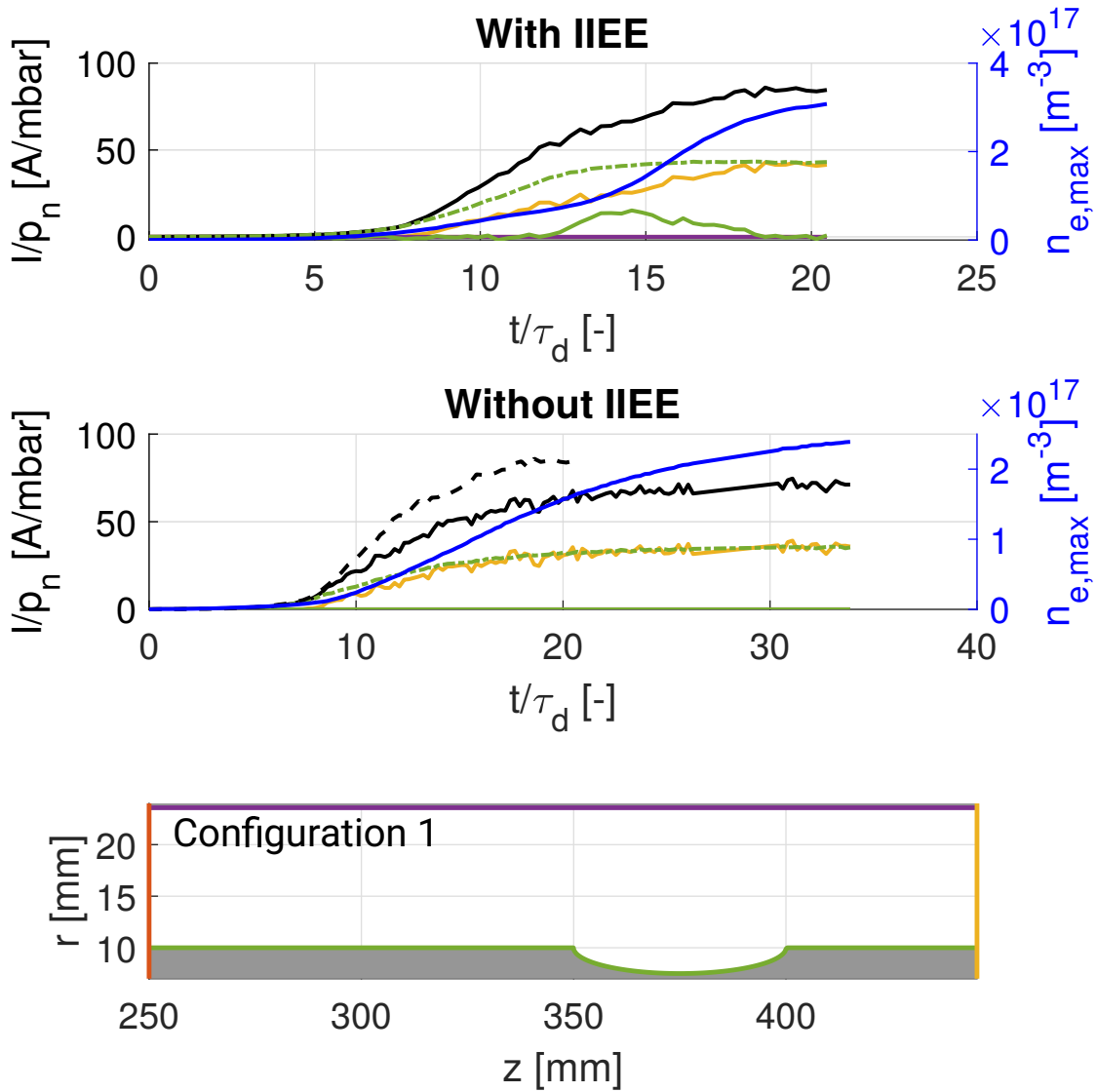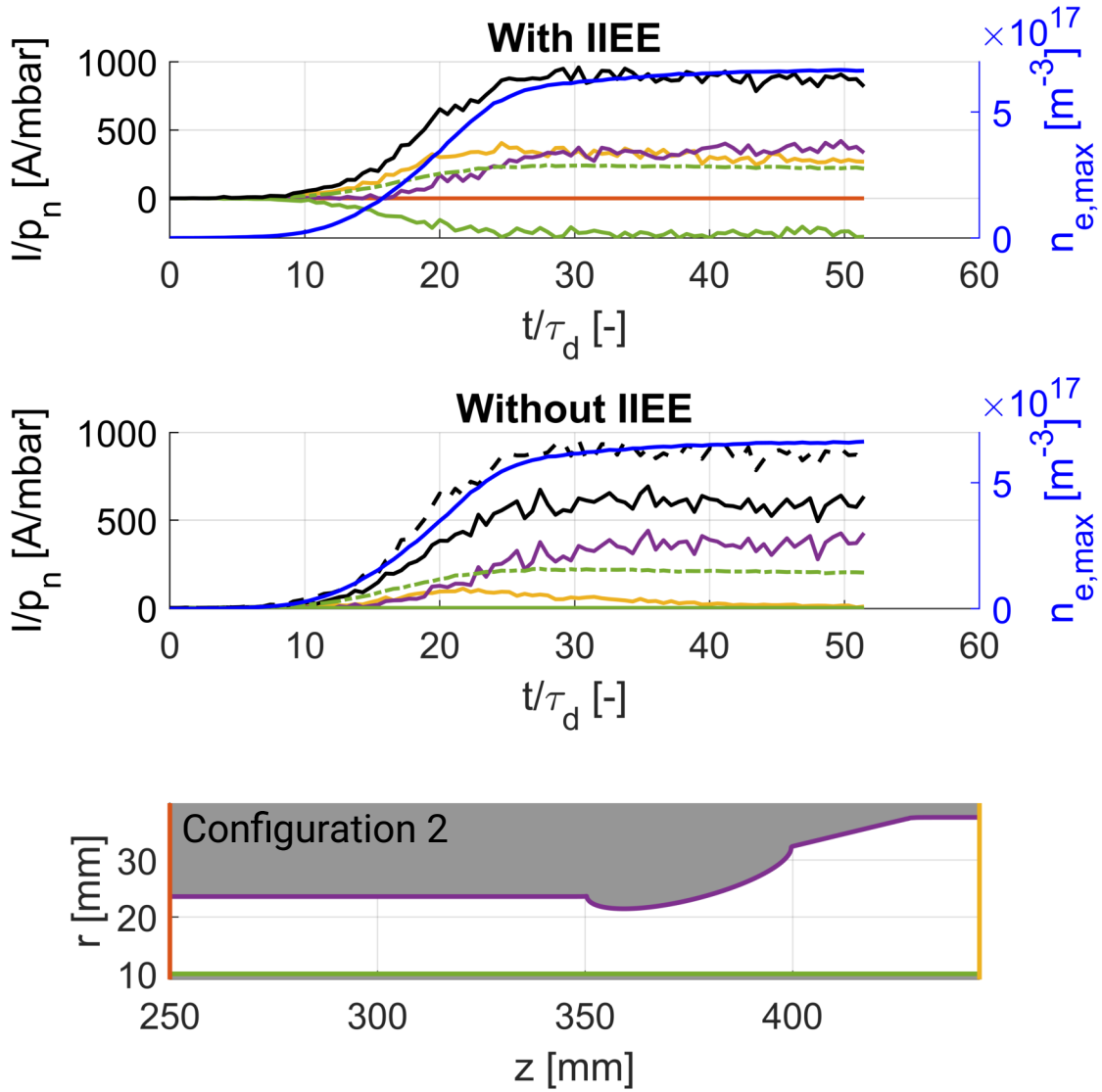
Figure 5.20: Top: Normalized time evolution of the maximum electron density (blue) and collected current on the electrodes for the simulations with IIEE. The black line represents the total collected current and the green dashed-dotted line represents the ionic contribution of the current. Middle: Normalized time evolution of the maximum electron density (blue) and collected currents on the electrodes for the simulations without IIEE. The black solid line represents the total collected current without IIEE and the dashed black line shows the total collected current for the case with IIEE for comparison. Bottom: Colour coded simulation boundaries for configuration 2 used to determine the location of the current collection for the top and middle plots.

cloud. This means that this configuration is a good candidate to study the effect of IIEE and to eventually study the impact of using different gases or electrode materials for IIEE.

All these results are important quantitative predictions for the T-REX device, which should allow further validation of FENNECS once T-REX is commissioned and the first experimental results are available. At the same time, FENNECS simulations could be performed with additional synthetic diagnostics mimicking for example the phosphor screen, pick-up coils or Faraday cups, to improve the understanding of the experimental measurements. Additional simulations, using the current version of the code, could also predict the total charge deposited on the phosphor screen and Faraday cup when the applied bias is rapidly decreased, as this allows the electrons to free-stream along the magnetic field lines and be collected on the walls.

As stated before, FENNECS is neglecting by construction the diocotron instability that is azimuthal in nature. This assumption is currently only partially supported by simulations in the refurbished GT170 geometry and should be studied further using the T-REX device. Should diocotron instabilities be observed in T-REX, one could as a first step use linear stability models, as the one presented in Chapter 6, to study the steady-state density profiles obtained by FENNECS. In a second step, FENNECS could also be adapted to simulate a 2D (r, θ) slice of the geometry in the trapping region. The goal of these simulations would be to study the effect of a limited radial section where the axial trapping is present. This would mimic the effect of a radially limited potential well compared to the radial distance between the inner and outer electrodes. This could potentially change the response of the cloud to diocotron instabilities, as this adds a "virtual" electrode and effectively reduces the maximum radial extent of the cloud. This also corresponds to a configuration that has not yet been used in diocotron instability studies, both with and without an inner electrode, and could lead to new properties or types of diocotron modes. In a third step, the full 3D geometry of T-REX could be simulated. To reduce the computation time, the 3D simulations could be started from density profiles generated by the 2D (r, z) FENNECS version of the code. In these 3D simulations, a synthetic diagnostic could also be implemented to simulate the signal measured on potential future segmented outer electrodes.

6 Preliminary studies of the diocotron instability in gyrotron gun geometries

The diocotron or "slipping-stream" instability is an instability with azimuthal mode structure that can arise in nonneutral plasmas due to a shear in the cloud angular velocity. It is similar in nature to the Kelvin-Helmholtz instability and can be used to study constant density inviscid fluids due to the isomorphism between the 2D drift-Poisson equations of diocotron instabilities and the 2D Euler equations of an inviscid fluid of constant density [107]. These modes cannot be simulated in the current version of FENNECS due to the assumed azimuthal symmetry. However, they could potentially play a role in cloud dynamics and confinement, and lead to a reduction of the maximum trapped density and to significant differences in the predicted current collected on the electrodes in gyrotron electron guns. In this chapter a cold-fluid guiding centre model, assuming an infinitely long electron cloud in presence of an homogeneous magnetic field and neglecting electrons inertial effects, is presented to study the linear stability of low density ($\omega_{pe}^2 \ll \Omega_{ce}^2$) annular electron clouds to diocotron normal modes. This model is then implemented in a finite difference eigenvalue solver and used in the configuration of the GT170 prototype geometry to estimate the importance of the diocotron instability for the trapped electron clouds.

6.1 The linear stability model to diocotron normal modes [32, 103]

In the limit of small amplitude flute perturbations ($\partial_z = 0$) of a cold low density nonneutral plasma equilibrium ($f_b \ll 1$), the linear stability to diocotron normal modes can be studied using a cold-fluid guiding centre formalism [32, 107, 108]. This model assumes an annular electron cloud of infinite length ($\partial_z = 0$) trapped radially between coaxial electrodes by a strong uniform axial magnetic field $\vec{B} = B_0\hat{e}_z$ and subjected to an externally applied electric field (see Figure 6.1). In addition, this model neglects the inertial effects of the electrons and assumes low-frequency flute perturbations $|\omega - l\omega_{re}| \ll \Omega_{ce}$ with ω the diocotron mode frequency, ω_{re} the equilibrium azimuthal rotation frequency of a fluid element, and l the azimuthal mode number. The inner electrode is characterized by a radius a and an applied bias ϕ_a on its surface. The outer electrode has radius b and is set to ground. The electron density $n_e(\vec{r}, t)$ is non-uniform and the ion density is $n_i = 0$. The momentum equation, at equilibrium, in this model is

$$0 = -en_e(\vec{r}, t)\left[\vec{E}(\vec{r}, t) + \vec{u}(\vec{r}, t) \times B_0\hat{e}_z\right], \tag{6.1}$$
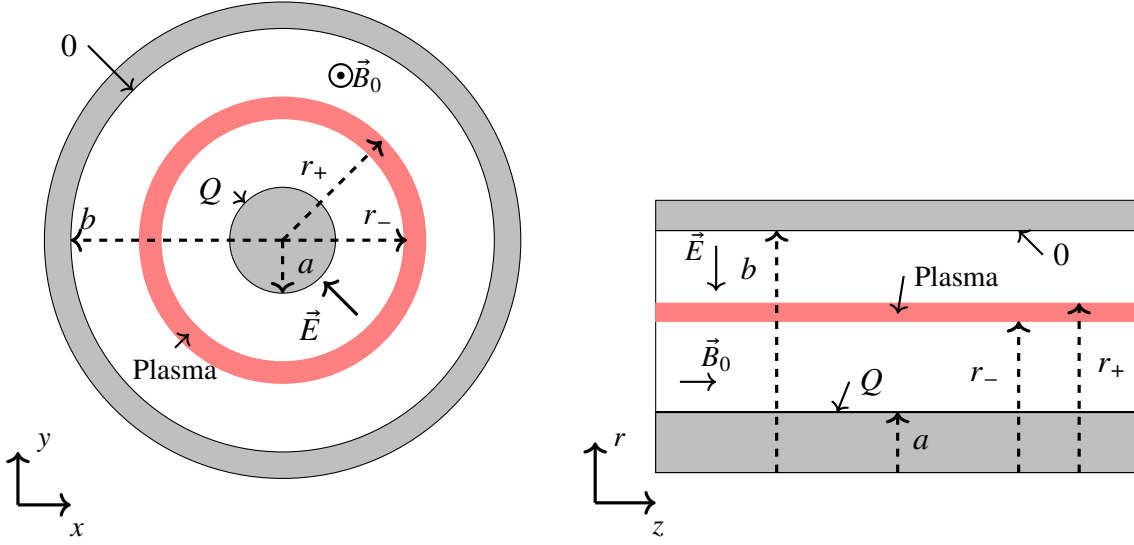
Figure 6.1: Considered geometry for the diocotron linear instability study, seen in the (x, y) and (r, z) plane. Grey denotes a conductor, red denotes the plasma, and white is vacuum.

which in the electrostatic approximation ($\vec{E} = -\nabla\phi$) gives the equilibrium fluid velocity

$$\vec{u}(\vec{r}, t) = -\frac{\nabla\phi(\vec{r}, t)}{B_0} \times \hat{e}_z. \tag{6.2}$$

This result imposes $\nabla \cdot \vec{u} = 0$ and the continuity equation becomes

$$\frac{\partial n_e}{\partial t} + \vec{u} \cdot \nabla n_e = 0. \tag{6.3}$$

The continuity equation can be combined with Poisson's equation,

$$\left(\frac{1}{r}\frac{\partial}{\partial r}r\frac{\partial}{\partial r} + \frac{1}{r^2}\frac{\partial^2}{\partial\theta^2}\right)\phi(r, \theta, t) = \frac{en_e(r, \theta, t)}{\epsilon_0}, \tag{6.4}$$

and the boundary conditions $\phi(a, \theta, t) = \phi_a$ and $\phi(b, \theta, t) = 0$. Equations (6.3) and (6.4) represent a closed nonlinear system of equations. The linearized eigenvalue equations of the diocotron normal modes are obtained by considering an azimuthally symmetric equilibrium ($\partial_\theta = 0$) with small-amplitude perturbations in the electron cloud density δn_e and electric potential $\delta\phi$ of the form

$$\delta n_e(r, \theta, t) = \sum_{l=-\infty}^{\infty} \delta n_e^l(r) \exp(il\theta - i\omega t), \tag{6.5}$$

and

$$\delta\phi(r, \theta, t) = \sum_{l=-\infty}^{\infty} \delta\phi^l(r) \exp(il\theta - i\omega t). \tag{6.6}$$

Here, l is the azimuthal mode number of the perturbation, and ω is the complex oscillation frequency of the mode. The linearized continuity equation (6.3) gives

$$(\omega - l\omega_{re}^-(r))\delta n_e^l(r) = -\frac{l\delta\phi^l(r)}{B_0 r}\frac{\partial n_e^0(r)}{\partial r},$$
(6.7)

where $\omega_{re}^-(r)$ is the slow equilibrium $\vec{E}\times\vec{B}$ drift angular velocity (see section 1.4.1) defined by

$$\omega_{re}^-(r) = -\frac{E_r^0}{rB_0}.$$
(6.8)

Here, the equilibrium density $n_e^0(r)$ and electric potential $\phi^0(r)$ are noted with the 0 superscript. Combining the linearized continuity equation (6.7), the expression of the perturbations (6.5) and (6.6), and Poisson's equation (6.4), we obtain the eigenvalue equation

$$\frac{1}{r}\frac{\partial}{\partial r}r\frac{\partial}{\partial r}\delta\phi^l(r) - \frac{l^2}{r^2}\delta\phi^l(r) = -\frac{l}{\Omega_{ce}r}\frac{\delta\phi^l(r)}{\omega - l\omega_{re}^-(r)}\frac{\partial}{\partial r}\omega_{pe}^2(r).$$
(6.9)

Here, $\omega_{pe}^2(r)$ is the equilibrium electron plasma frequency. The metallic boundary conditions on the electrodes surfaces impose $\partial_\theta\delta\phi(r)|_{r=a,r=b} = 0$ or

$$\delta\phi^l(a) = \delta\phi^l(b) = 0$$
(6.10)

6.2 The finite difference eigenvalue solver

To study the linear stability of arbitrary density profiles to diocotron normal modes, an eigenvalue solver based on finite differences has been developed. In this solver, the physical quantities are discretised on a uniform grid at $N_r + 1$ radial positions r_i from $r_0 = a$ to $r_{N_r} = b$, with a spacing $r_{i+1} - r_i = (b-a)/N_r \equiv \Delta r$. The first and second radial derivatives are expressed using a centred finite difference scheme

$$\frac{\partial\delta\phi^l(r_i)}{\partial r} \approx \frac{\delta\phi_{i+1}^l - \delta\phi_{i-1}^l}{2\Delta r},$$
(6.11)

and

$$\frac{\partial^2\delta\phi^l(r_i)}{\partial r^2} \approx \frac{\delta\phi_{i+1}^l - 2\delta\phi_i^l + \delta\phi_{i-1}^l}{\Delta r^2}.$$
(6.12)

The electric potential eigenvalue equation (6.9) is also rewritten as

$$\left[l\omega_{re}^-(r)\left(\frac{1}{r}\frac{\partial}{\partial r}r\frac{\partial}{\partial r} - \frac{l^2}{r^2}\right) - \frac{l}{\Omega_{ce}r}\frac{\partial}{\partial r}\omega_{pe}^2(r)\right]\delta\phi^l(r) = \omega\left(\frac{1}{r}\frac{\partial}{\partial r}r\frac{\partial}{\partial r} - \frac{l^2}{r^2}\right)\delta\phi^l(r)$$
(6.13)

to obtain a general eigenvalue problem of the form:

$$\overleftrightarrow{A}_l \cdot \vec{\delta\phi}^l = \omega\overleftrightarrow{B}_l \cdot \vec{\delta\phi}^l,$$
(6.14)

with $\overleftrightarrow{B}_l$ and $\overleftrightarrow{A}_l$ two tri-diagonal matrices. In the configurations studied in this chapter, the matrix $\overleftrightarrow{B}_l$ is non-singular and can be inverted, leading to the traditional eigenvalue problem

$$\overleftrightarrow{B}_l^{-1}\overleftrightarrow{A}_l \cdot \vec{\delta\phi}^l = \omega \cdot \vec{\delta\phi}^l,$$
(6.15)

with $\overleftrightarrow{B}_l^{-1}$ its inverse. The non-singularity of $\overleftrightarrow{B}_l$ has only been verified numerically, but a rigorous proof could be obtained recursively using the continuant of $\overleftrightarrow{B}_l$. Using the boundary conditions:

$$\delta\phi_0^l = \delta\phi_{N_r}^l = 0, \tag{6.16}$$

$\overleftrightarrow{B}_l$ and $\overleftrightarrow{A}_l$ are defined hereafter using the following α and β coefficients:

$$\alpha_i^D = -l\omega_{re}^-(r_i)\left(\frac{2}{\Delta r^2} + \frac{l^2}{r_i^2}\right) - \frac{l}{r_i\Omega_{ce}}\left.\frac{\partial\omega_{pe}^2}{\partial r}\right|_{r=r_i}, \tag{6.17}$$

$$\alpha_i^\pm = l\omega_{re}^-(r_i)\left(\frac{1}{\Delta r^2} \pm \frac{1}{2r_i\Delta r}\right), \tag{6.18}$$

$$\beta_i^D = -\left(\frac{2}{\Delta r^2} + \frac{l^2}{r_i^2}\right), \tag{6.19}$$

and

$$\beta_i^\pm = \frac{1}{\Delta r^2} \pm \frac{1}{2r_i\Delta r}. \tag{6.20}$$

The matrix $\overleftrightarrow{A}_l$ is defined as

$$\overleftrightarrow{A}_l = \begin{bmatrix} \alpha_1^D & \alpha_1^+ & 0 & \dots & 0 \\ \alpha_2^- & \alpha_2^D & \alpha_2^+ & \ddots & \vdots \\ 0 & \ddots & \ddots & \ddots & 0 \\ \vdots & \ddots & \alpha_{N_r-2}^- & \alpha_{N_r-2}^D & \alpha_{N_r-2}^+ \\ 0 & \dots & 0 & \alpha_{N_r-1}^- & \alpha_{N_r-1}^D \end{bmatrix}, \tag{6.21}$$

and the matrix $\overleftrightarrow{B}_l$ is defined as

$$\overleftrightarrow{B}_l = \begin{bmatrix} \beta_1^D & \beta_1^+ & 0 & \dots & 0 \\ \beta_2^- & \beta_2^D & \beta_2^+ & \ddots & \vdots \\ 0 & \ddots & \ddots & \ddots & 0 \\ \vdots & \ddots & \beta_{N_r-2}^- & \beta_{N_r-2}^D & \beta_{N_r-2}^+ \\ 0 & \dots & 0 & \beta_{N_r-1}^- & \beta_{N_r-1}^D \end{bmatrix}. \tag{6.22}$$

To solve the eigenvalue equation, the matrices $\overleftrightarrow{A}_l$ and $\overleftrightarrow{B}_l$ are computed numerically and used as input to the "eig" function of MATLAB. This function returns $N_r - 1$ complex eigenvalues and their respective eigenvectors $\delta\phi^l$.

6.2.1 Verifications

To verify the implementation of the finite difference eigenvalue solver, a radial density profile with known analytical solution is used. Indeed, the eigenvalue equation for diocotron normal modes (6.9) has an analytical solution for the case of a step density function confined radially inside a coaxial configuration, where the inner conductor has a charge per unit length Q (see Figure 6.1) [32, 103]. For this configuration,

the equilibrium electron density is of the form:

$$n(r) = \begin{cases} 0, & 0 \le r \le r_-, \\ n_0 = \text{const.}, & r_- \le r \le r_+, \\ 0, & r > r_+, \end{cases} \tag{6.23}$$

with cylindrical conducting walls at $r = a$ and $r = b$. The radial electric field at $r = a$, the surface of the inner conductor, is

$$E_r(a) = \frac{Q}{\epsilon_0 a}. \tag{6.24}$$

In this configuration, Q and ϕ_a are related through the following equation:

$$Q = \frac{\phi_a - \phi_-}{2 \ln r_-/a}, \tag{6.25}$$

with

$$\phi_- = \frac{\ln\left(\frac{r_-}{a}\right)}{\ln\left(\frac{b}{a}\right)} \left[\phi_a \frac{\ln\left(\frac{b}{r_-}\right)}{\ln\left(\frac{r_-}{a}\right)} + \phi_b + \frac{q_e n_e}{2\epsilon_0} \left(r_+^2 \ln\left(\frac{b}{r_+}\right) - r_-^2 \ln\left(\frac{b}{r_-}\right) \right) + \frac{q_e n_e}{4\epsilon_0} (r_+^2 - r_-^2) \right] \tag{6.26}$$

the electric potential at the position r_- derived from Poisson's equation and using the step density profile of (6.23) (see Appendix A). The azimuthal angular velocity in the electron cloud is then

$$\omega_{re}^-(r) = -\frac{E_r(r)}{r B_0} = \omega_q \left(\frac{r_-}{r}\right)^2 + \omega_D \left(1 - \left(\frac{r_-}{r}\right)^2\right), \tag{6.27}$$

with

$$\omega_q = -2Q/\epsilon_0 B_0 r_-^2 \tag{6.28}$$

the angular velocity induced by the external radial electric field at $r = r_-$, and

$$\omega_D = \omega_{pe}^2/2\Omega_{ce} \tag{6.29}$$

the diocotron frequency.

One can show [32, 103] that the dispersion relation for the diocotron modes, equation (6.9), in an electron cloud with a step density profile, reduces to

$$\omega = \frac{1}{2}\omega_D \left[b_l \pm \sqrt{b_l^2 - 4c_l} \right], \tag{6.30}$$

with

$$b_l = \left(l \left\{ \left[1 - \left(\frac{r_-}{r_+}\right)^2 \right] + \frac{\omega_q}{\omega_D} \left[1 - \left(\frac{r_-}{r_+}\right)^2 \right] \right\} \left[1 - \left(\frac{a}{b}\right)^{2l} \right] \right.$$
$$\left. + \left[1 - \left(\frac{r_-}{r_+}\right)^{2l} \right] \left[\left(\frac{r_+}{b}\right)^{2l} - \left(\frac{a}{r_-}\right)^{2l} \right] \right) \left[1 - \left(\frac{a}{b}\right)^{2l} \right]^{-1}, \tag{6.31}$$

and

$$c_l = \left\{ l^2 \frac{\omega_q}{\omega_D} \left[1 - \left(\frac{r_-}{r_+}\right)^2 + \frac{\omega_q}{\omega_D} \left(\frac{r_-}{r_+}\right)^2 \right] \left[1 - \left(\frac{a}{b}\right)^{2l} \right] - l \frac{\omega_q}{\omega_D} \left[1 - \left(\frac{a}{r_+}\right)^{2l} \right] \left[1 - \left(\frac{r_+}{b}\right)^{2l} \right] \right.$$

$$+ l \left[1 - \left(\frac{r_-}{r_+}\right)^2 + \frac{\omega_q}{\omega_D} \left(\frac{r_-}{r_+}\right)^2 \right] \left[1 - \left(\frac{r_-}{b}\right)^{2l} \right] \left[1 - \left(\frac{a}{r_-}\right)^{2l} \right]$$

$$\left. - \left[1 - \left(\frac{r_+}{b}\right)^{2l} \right] \left[1 - \left(\frac{a}{r_-}\right)^{2l} \right] \left[1 - \left(\frac{r_-}{r_+}\right)^{2l} \right] \right\} \left[1 - \left(\frac{a}{b}\right)^{2l} \right]^{-1} . \tag{6.32}$$

Using the dispersion relation (6.30), the condition for instability is

$$4c_l > b_l^2, \tag{6.33}$$

and the oscillation frequencies are complex conjugates of the form

$$\omega_\pm = \frac{1}{2} \omega_D \left(b_l \pm i \sqrt{4c_l - b_l^2} \right). \tag{6.34}$$

The analytical solution for the electrostatic mode $\delta\phi^l(r)$ is defined in three different regions: I between the inner electrode and the cloud ($a \le r < r_-$), II in the cloud ($r_- \le r \le r_+$), and III between the cloud and the outer electrode ($r_+ < r \le b$), and the expressions are

$$\delta\phi_I^l(r) = \left[Br_-^l + \frac{C}{r_-^l} \right] \left[\frac{\left(\frac{r}{a}\right)^{2l} - 1}{\left(\frac{r_-}{a}\right)^{2l} - 1} \right] \left(\frac{r_-}{r}\right)^l, \tag{6.35}$$

$$\delta\phi_{II}^l(r) = Br^l + \frac{C}{r^l}, \tag{6.36}$$

and

$$\delta\phi_{III}^l(r) = \left[Br_+^l + \frac{C}{r_+^l} \right] \left[\frac{1 - \left(\frac{r}{b}\right)^{2l}}{1 - \left(\frac{r_+}{b}\right)^{2l}} \right] \left(\frac{r_+}{r}\right)^l, \tag{6.37}$$

where B and C are constants that can be obtained from the matching conditions of E_r at the interfaces. This analytical solution can be compared to the numerical results obtained with the finite-difference eigenvalue solver to verify the code.

The finite difference solver limits the use of step density profiles, as this imposes large values in the α_i^D coefficients and can lead to a loss of numerical accuracy. The density step-function can however be approximated by using one definition of the Heaviside step function

$$H(r - r_0) = \lim_{\sigma \to 0} \left(\frac{1}{2} + \frac{1}{\pi} \arctan\left(\frac{r - r_0}{\sigma}\right) \right), \tag{6.38}$$

and using small numerical values for σ (i.e. $\sigma \ll (r_+ - r_-)$). From this definition, the electron density used in the verification cases becomes

$$n_{e,num}(r) = n_0(H(r - r_-) - H(r - r_+)) \approx \frac{1}{\pi} \left(\arctan\left(\frac{r - r_-}{\sigma}\right) - \arctan\left(\frac{r - r_+}{\sigma}\right) \right). \tag{6.39}$$

This verification configuration is used as input for the eigenvalue solver with parameters consistent with electron trapping in the GT170 geometry and given in Table 6.1. The verification of the code is done in

n_0	$[1 \times 10^{16}\,\mathrm{m}^{-3}]$
σ	$[1 \times 10^{-1}\,\mathrm{mm}, 1 \times 10^{-3}\,\mathrm{mm}]$
l	$[1, 2, 3, 4]$
B_0	$0.3\,\mathrm{T}$
f_b	0.023
N_r	511
a	$65\,\mathrm{mm}$
b	$80\,\mathrm{mm}$
ϕ_a	$[-1\,\mathrm{kV}, -50\,\mathrm{kV}]$
ϕ_b	$0\,\mathrm{kV}$

Table 6.1: Numerical parameters used to verify the implementation of the finite difference eigenvalue solver for diocotron normal modes.

two steps. First, a convergence study for the numerical frequency ω is done for an analytically unstable configuration of a cloud delimited by $r_- = 67.1\,\mathrm{mm}$ and $r_+ = 75.7\,\mathrm{mm}$. The potential on the central electrode is $\phi_a = -50\,\mathrm{kV}$, and two values of $\sigma_1 = 1 \times 10^{-1}\,\mathrm{mm}$ and $\sigma_2 = 1 \times 10^{-3}\,\mathrm{mm}$ are used. The mode number is $l = 1$ and an increasing number of grid points from 32 to 1024 are used for σ_1 and from 32 to 4096 for σ_2. The result of these convergence studies in Figure 6.2 shows that for σ_1 the code converges and that relative errors on $\mathrm{Re}(\omega)$ smaller than 10^{-3} can be reached. For the σ_2 case, the error is still decreasing as Δr is decreased, meaning that the convergence is not yet reached. This is expected until $\Delta r \sim \sigma_2$, since the density profile is not fully resolved. However, at $N_r = 511$ the relative error on $\mathrm{Re}(\omega)$ is below 10^{-6}, which is sufficient for the verification of the solver. In addition, the comparison between the analytical and numerical perturbed $\delta\phi^l(r)$, in Figure 6.3, show a good agreement between the numerical and analytical solutions. Indeed, the amplitude and phase, for the numerical unstable and damped $l = 1$ modes using the two values of σ reproduce correctly the analytical results in Figure 6.3.
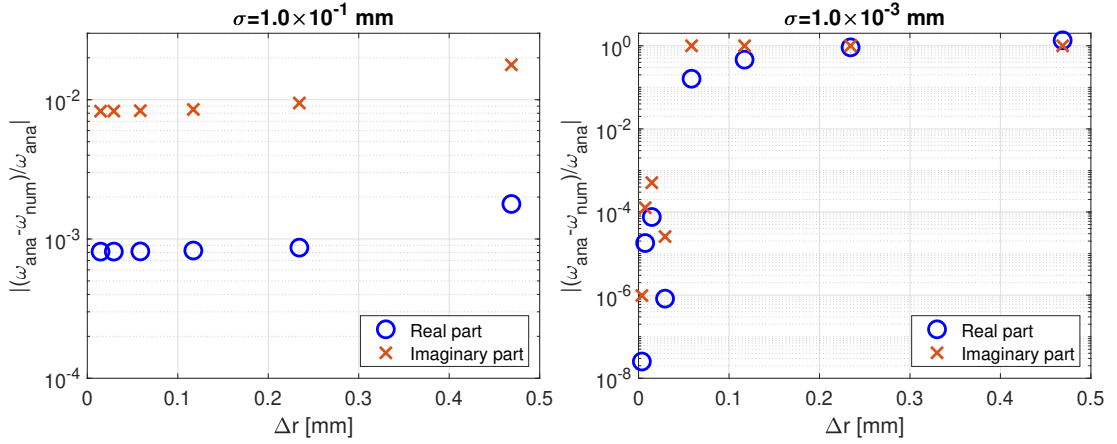
Figure 6.2: Left: Relative error on the real and imaginary part of the diocotron $l = 1$ mode frequency for $\sigma_1 = 1 \times 10^{-1}\,\mathrm{mm}$ as a function of the grid width Δr. Right: Same as Left but for $\sigma_2 = 1 \times 10^{-3}\,\mathrm{mm}$. The cloud is delimited by $r_- = 67.1\,\mathrm{mm}$ and $r_+ = 75.7\,\mathrm{mm}$. The potential on the central electrode is $\phi_a = -50\,\mathrm{kV}$, and the outer electrode is at ground.

In a second step, the code is also verified using a step density profile and the parameters of Table 6.1, but
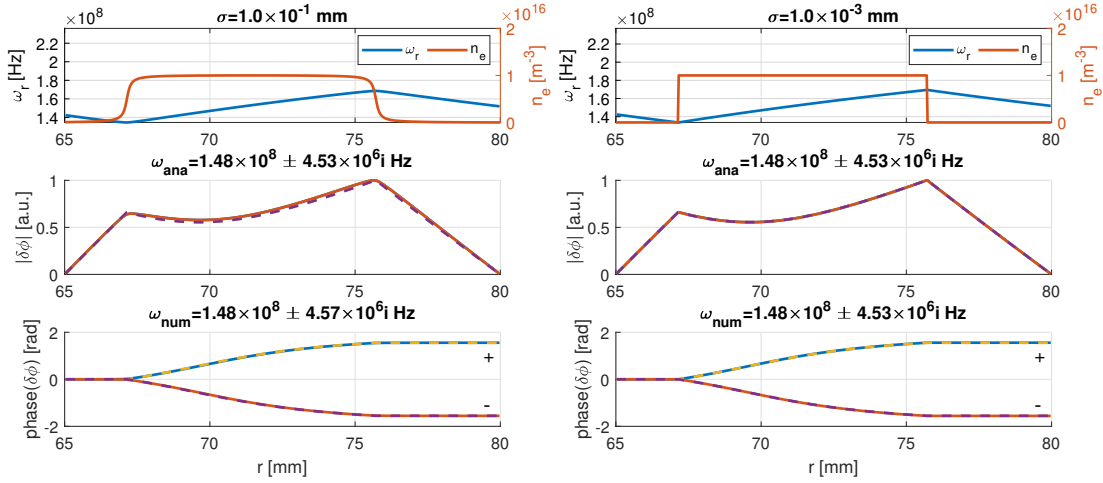
Figure 6.3: Left: From top to bottom: numerical equilibrium electron density $n_{e,num}$ (red) for $\sigma_1 = 1 \times 10^{-1}$ mm, and equilibrium azimuthal angular rotation velocity ω_{re} (blue) used as input; normalized amplitude and phase of the two analytical (dashed) and numerical (solid) $l = 1$ modes with Im(ω) $\neq 0$. The "+" and "-" indicate the modes with Im(ω) > 0 and Im(ω) < 0 respectively. Right: Same as Left but for $\sigma_2 = 1 \times 10^{-3}$ mm. The cloud is delimited by $r_- = 67.1$ mm and $r_+ = 75.7$ mm. The potential on the central electrode is $\phi_a = -50$ kV, and the outer electrode is at ground. The number of grid points is $N_r + 1 = 512$.

scanning the radial limits of the cloud for a shape factor $\sigma_2 = 1 \times 10^{-3}$ mm. For each cloud radial limits, for each mode number $l \in [1, 4]$ and for two inner conductor potentials $\phi_{a,1} = -1$ kV and $\phi_{a,2} = -50$ kV, the stability is evaluated using the finite difference solver and is plotted in Figures 6.4 and 6.5 as a red cross if a mode is unstable, and a white circle if no mode is unstable. In addition, the imaginary part of the unstable analytical mode ω_i is plotted as a contour plot on the same figures. The first scan, with an inner conductor potential $\phi_{a,1} = -1$ kV, is represented in Figure 6.4 and shows an excellent agreement between the code and the analytical solution, as all the positions where $\omega_i > 0$ have a red "x" and all the other positions have a white circle. The second scan, with an inner conductor potential $\phi_{a,2} = -50$ kV, is represented in Figure 6.5 and also presents a good agreement between the code and the analytical solution, as all the positions, where $\omega_i > 0$, have a red "x" and almost all the other positions have a white circle. This shows that the solver has been verified, is able to reproduce the analytical results for a broad range of input parameters, and can be used to study arbitrary density profiles. In addition, the second configuration, with $\phi_{a,2} = -50$ kV, shows that the large inner electrode bias has a stabilizing effect [105], which is relevant for electron trapping in gyrotron electron guns. Indeed, by comparing Figures 6.4 and 6.5, one can see that less cloud configurations are unstable for $\phi_{a,2} = -50$ kV than for $\phi_{a,1} = -1$ kV, and that in the high bias case the cloud needs to be wider, which means a higher total trapped charge, to be unstable. This can be explained by the fact that the external bias term ω_q dominates the equilibrium azimuthal angular velocity in (6.27), thus reducing the shear in angular velocity and preventing the instability.

6.3 Diocotron instabilities in the GT170 prototype geometry

After verification of the eigenvalue solver implementation, it can be used to study the linear stability of electron clouds, trapped in gyrotron electron guns, to diocotron modes. This is relevant to investigate
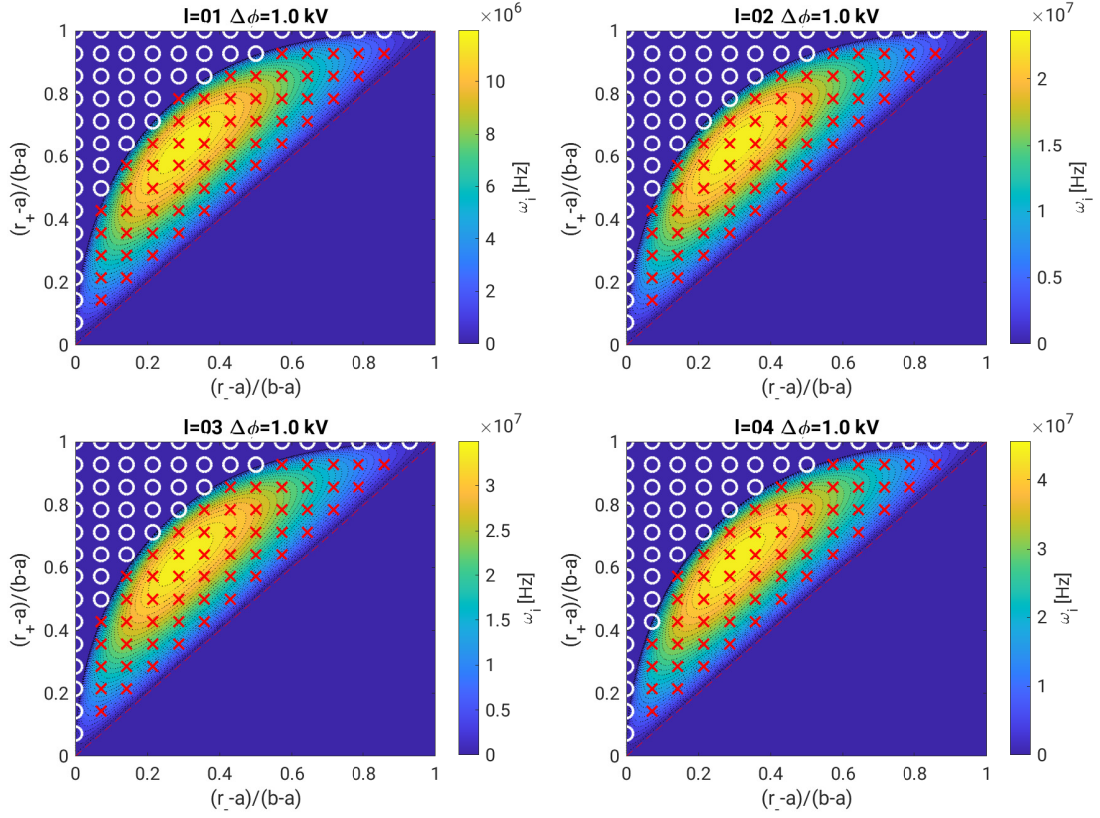
Figure 6.4: Numerical stability of electron clouds with varying radial position and width to diocotron normal modes with mode numbers $l \in [1, 2, 3, 4]$. For each couples of values (r_-, r_+), the numerically unstable modes are marked with a red X and the stable modes with a white circle. The coloured contour shows the imaginary part of the analytical frequency ω_i obtained from (6.34). The potential on the central electrode is $\phi_a = -1\,\text{kV}$, and the outer electrode is at ground.
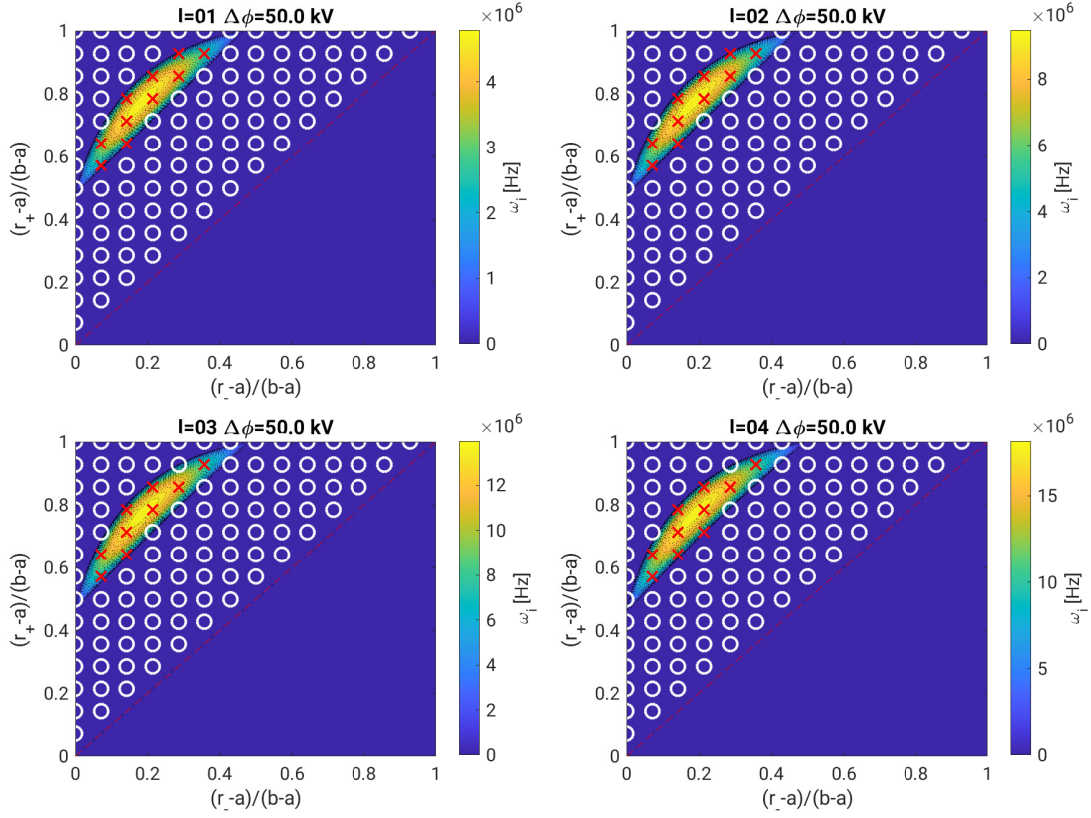
Figure 6.5: Numerical stability of electron clouds with varying radial position and width to diocotron normal modes with mode numbers $l \in [1, 2, 3, 4]$. For each couples of values (r_-, r_+), the numerically unstable modes are marked with a red X and the stable modes with a white circle. The coloured contour shows the imaginary part of the analytical frequency ω_i obtained from (6.34). The potential on the central electrode is $\phi_a = -50\,\text{kV}$, and the outer electrode is at ground.

the discrepancy observed between the collected current predicted by FENNECS simulations and the experimental measurements for the GT170 prototype geometry presented in section 4.4.1. Indeed, as mentioned in that section, this difference could be explained by the onset of diocotron instabilities that could limit the electron cloud density. As an initial study, the linear eigenvalue solver described in the previous section is run by using the steady-state radial density profiles extracted from FENNECS at different axial positions and different applied biases $\Delta\phi$ and using the same simulation parameters as in section 4.4.1. This includes the reduced magnetic field amplitude $B = 0.6\,B_{nom}$ compared to the nominal magnetic field amplitude used to operate this gyrotron, and corresponds to $B_z \approx 0.135\,\mathrm{T}$ in the potential well. We need to underline that the eigenvalue equation of the diocotron solver (described in Sec. 6.2) is not perfectly well suited for studying the electron clouds trapped in gyrotron electron guns, since the clouds have a finite length, are subjected to non-uniform magnetic fields and tend to have high densities with $f_b \approx 1$. This is indeed the case for the steady state density profiles obtained with FENNECS simulations in the GT170 prototype geometry. However, this model can serve as an initial indicator for the relevance of diocotron instabilities and to justify the importance of more elaborate linear simulations, relaxing the assumptions of the current model, and of non-linear diocotron simulations that would allow studying the effect of the diocotron modes on the collected currents. The current model was initially chosen for its simplicity of implementation and verification, allowing preliminary studies of the diocotron instabilities. An implementation of a more general eigenvalue equation, called the macroscopic electrostatic eigenvalue equation in chapter 5.3 of [32], that relaxes the low density and $\partial_z = 0$ assumptions, has been attempted, and its numerical implementation is discussed in Appendix C. However, the verification of the code showed mixed-results due to numerical challenges, and the code was not deemed accurate enough to be used for studying the electron clouds trapped in gyrotron electron guns.

In FENNECS simulations the magnetic field is non-uniform, but for the diocotron solver the magnetic field amplitude is assumed constant. The input magnetic field for the diocotron solver is thus taken as the axial magnetic field amplitude at the axial position considered but averaged over the radial dimension in the vacuum region. The axial points considered for the diocotron study are represented in Figure 6.6 for two biases $\Delta\phi = 20\,\mathrm{kV}$ and $\Delta\phi = 100\,\mathrm{kV}$. The radial density profiles are then linearly interpolated from the 153 grid points of the simulation results to a uniform grid with 1536 points to increase the numerical accuracy of the solver. Figure 6.6 shows the most unstable mode frequency ω and mode number l, for three different axial positions, and for both low and high bias. For both clouds, we observe that the diocotron modes are unstable and with similar growth rates. Thus, the applied bias does not play an important role on the diocotron marginal stability of the steady-state density profiles obtained by FENNECS in this configuration. However, the applied bias seems to increase the mode number l of the most unstable mode (see Figure 6.6). One can also note that the magnitude of ω is close to ω_D, which is in the $10\,\mathrm{GHz}$ range. As an illustration of the typical perturbed potential profile, the most unstable mode for the equilibrium cloud density obtained with a bias $\Delta\phi = 100\,\mathrm{kV}$ is represented in Figure 6.7. This figure shows once again that the radial perturbation profile $\delta\phi^l(r)$ is maximum in a region where the cloud density is high and the shear in ω_{re} is also high, in agreement with the results obtained for flat density profiles.

To complement this study, the linear stability of the equilibrium density profiles to diocotron modes with $l \in [1, 30]$ has been performed for a set of applied biases between $\Delta\phi = 20\,\mathrm{kV}$ and $\Delta\phi = 100\,\mathrm{kV}$ and represented in Figure 6.8. This scan shows that all the modes are unstable, and that the most unstable mode number is correlated with the applied bias. Low biases are most unstable at low mode numbers, and high biases are more unstable at high mode numbers. In addition, for low mode numbers $l \in [1, 5]$, the simulation results show a brusque reduction in growth rate around $50\,\mathrm{kV}$, where the experimental leaking current increases drastically in the results of section 4.4.1. If the low mode numbers have the strongest effect on electron transport, as is often the case for electrostatic plasma instabilities, the simulation results are
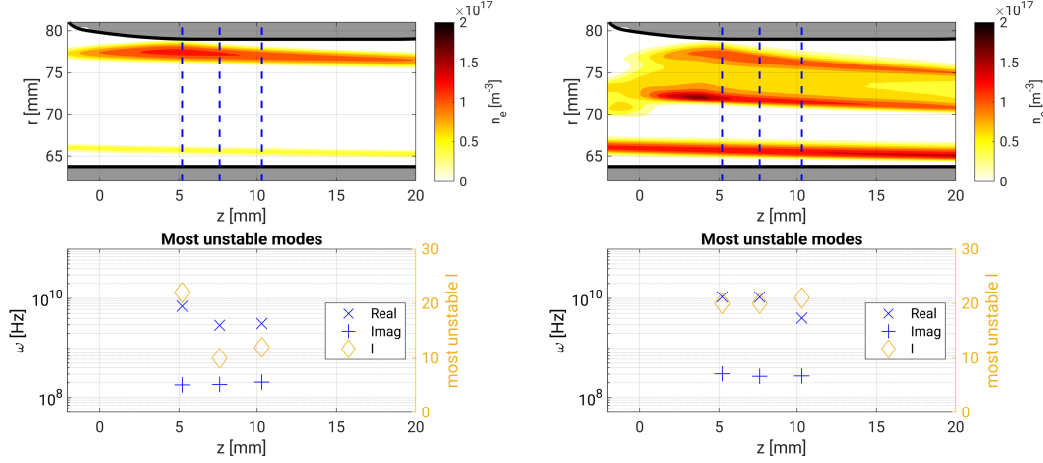
Figure 6.6: Left top: zoom on the steady state electron cloud density obtained in the geometry of the GT170 prototype electron gun for a bias $\Delta\phi = 20\,\text{kV}$. The blue dashed lines highlight the axial positions considered for the diocotron stability study, and the gray parts show the electrodes' geometry. Left bottom: real (blue +) and imaginary (blue x) part of the most unstable mode frequency and corresponding mode number (yellow) for the three considered axial positions. Right: same as left but for a bias $\Delta\phi = 100\,\text{kV}$. The two upper density peaks are formed by electrons trapped in the upper potential well, due to their large Larmor radius and cycloid trajectory. The peaks correspond to the upper and lower positions of the electrons' Larmor motion.
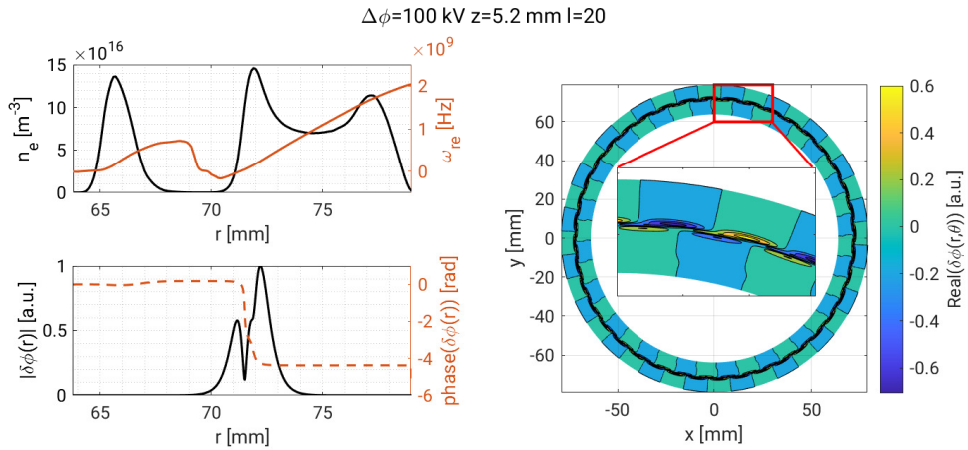
Figure 6.7: Top left: radial density profile (black) and azimuthal rotation frequency (red) used as input for the leftmost axial position of Figure 6.6 and a bias $\Delta\phi = 100\,\text{kV}$. Bottom left: normalised amplitude (black) and phase (red) of the most unstable diocotron mode using the profiles plotted on the top left. Right: real part of the most unstable electrostatic perturbation, represented on the transverse plane (x, y). The centre plot shows a zoom of the perturbation, on the red rectangle portion of the full profile.
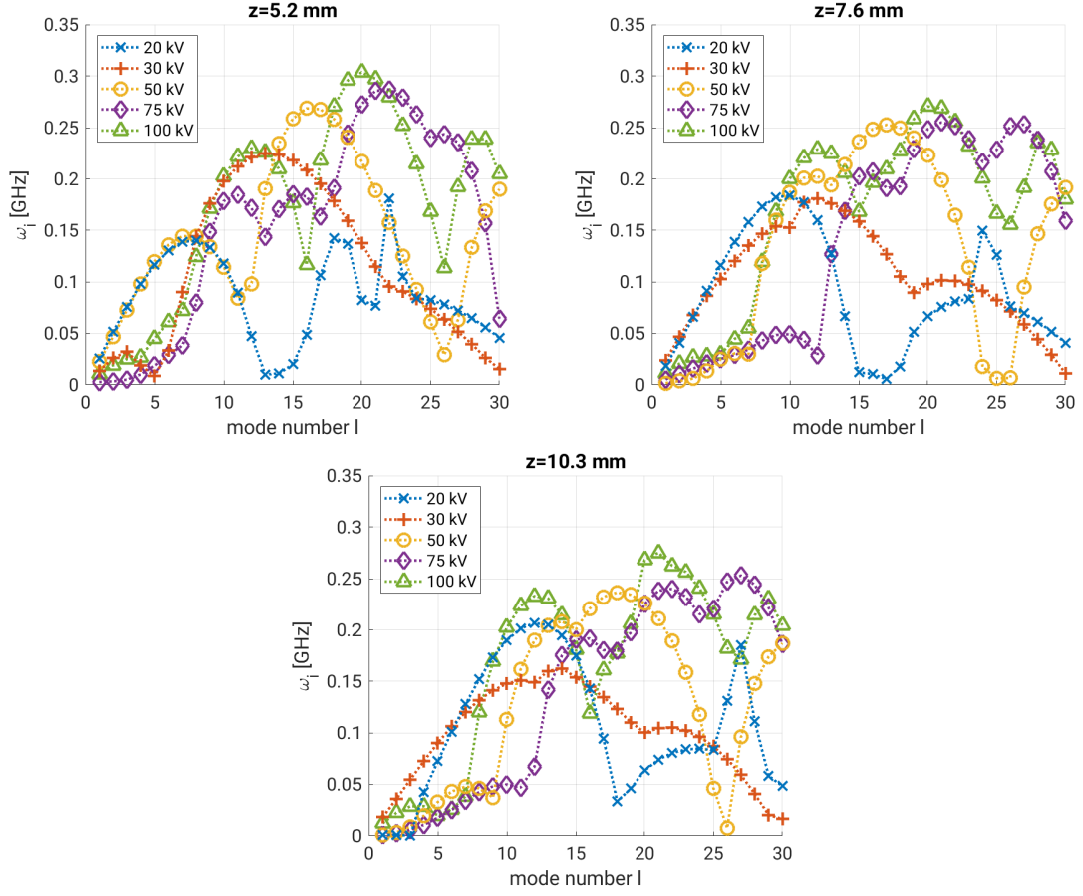
Figure 6.8: Growth rate of the most unstable modes for equilibrium density profiles obtained with a set of applied biases $\Delta\phi$ using FENNECS simulations, for the three positions considered in Figure 6.6 and for each mode number $l \in [1, 30]$. Each colour and marker represent a different applied bias, and the dashed lines are only there to help the reader follow the markers.

consistent with the fact that diocotron instabilities might influence the leaking current. This initial diocotron study also shows that the equilibrium radial density profiles are susceptible to azimuthal instabilities with a fast characteristic timescale $1/\omega_i \approx 10$ ns much faster than the ionisation timescale $\tau_{io} \approx 10$ ms of the RNG ($1/\omega_i \ll \tau_{io}$), at realistic gyrotron gun pressures. This timescale ordering indicates that, even during the cloud formation, the electron cloud can be assumed to be at a pseudo-equilibrium and can be studied with the diocotron eigenvalue solver.

Using this observation, linear instability studies have been run using density profiles extracted from FENNECS simulations at various time-steps during the cloud formation, leading to different values of maximum electron cloud densities $n_{e,max}$ along the radial dimension. These studies have been done with the two extreme applied biases $\Delta\phi = 20$ kV and $\Delta\phi = 100$ kV and at the two leftmost positions ($z = 5.2$ mm and $z = 7.6$ mm) highlighted in Figure 6.6. The result of these studies are represented in Figures 6.9 and 6.10, and show that for low densities, the clouds are less unstable or even stable for $\Delta\phi = 100$ kV compared to $\Delta\phi = 20$ kV. In addition, these results show that the growth-rate does not follow a linear dependency on ω_{pe}^2 and n_e as expected by equation (6.34). This is most likely due to strong modifications of the trapped cloud size due to the modification of the potential well size caused by important space-charge effects. This

Figure 6.9: Top: growth rate of the most unstable modes for density profiles obtained with a bias $\Delta\phi = 20\,\text{kV}$ using FENNECS simulations, at several times of cloud formation, for the left position considered in Figure 6.6 and for each mode number $l \in [1, 30]$. Each colour and marker represent a different time during the cloud formation, corresponding to a different maximum electron density. If a marker is missing, the mode frequency is real and the mode is stable. Bottom: same as top but for a bias $\Delta\phi = 100\,\text{kV}$

difference in growth rate is more salient for the middle axial position $z = 7.6$ mm of Figure 6.10. As seen in Figures 6.9 and 6.10 the values of $\omega_{pe}^2/\Omega_{ce}^2$ are relatively high and questions the validity of the results. Indeed, for densities above $n_{e,max} > 2 \times 10^{16}$ m^{-3}, $\omega_{pe}^2/\Omega ce^2 > 0.1$, which means only the low density simulations are reliable. It is also important to note that in some of these configurations the "Brillouin limit" is exceeded, $f_b > 1$, which seems to contradict the results of Section 3.3. However, due to the large Larmor radius of the trapped electrons, the guiding centre approximation of Section 3.3 cannot be justified any more, which means $u_\theta \neq -E_r/B_z$ at the peak density, and corrections would need to be added to take this effect into account. In addition, the results of Appendix B show that, in some regimes, equilibrium can exist where $f_b > 1$, due to pressure effects.

The difference in growth-rate as a function of the applied bias, while not fully conclusive due to the limitations of the eigenvalue solver, supports further the hypothesis that high biases stabilize the diocotron modes and could explain the discrepancy observed in Section 4.4.1 between the numerical and experimental collected currents. However, more detailed studies of the diocotron modes are necessary. Indeed, the current model is unable to consider high-densities, axial non-uniformities and electron-neutral collisions, and non-linear effects will play a role in the development of the diocotron modes. In this regard, the modification of FENNECS to allow 2D (radial-azimuthal) and 3D simulations will be of great interest to study the effect of the diocotron instability on the collected current.

6.4   Summary and conclusions

This chapter presents an eigenvalue equation used to study the linear stability to diocotron normal modes, of low density annular electron clouds ($\omega_{pe}^2 \ll \Omega_{ce}^2$) radially confined in coaxial geometries of infinite length. This eigenvalue equation is derived from a continuity-Poisson system, neglecting the electrons' inertia and assuming no axial variation. A finite difference spectral solver, implementing this diocotron eigenvalue equation, is then described and successfully verified against analytical solutions for electron plasmas with step density profiles.

The spectral solver is then used to study the stability of steady-state electron clouds trapped in the prototype electron gun of the GT170 coaxial gyrotron by extracting the radial density profile of clouds obtained with FENNECS simulations at several axial positions. The stability of these clouds to diocotron normal modes with mode numbers $l \in [1, 30]$ and externally applied biases between $\Delta\phi = 20$ kV and $\Delta\phi = 100$ kV is then established. This study shows that all equilibrium density profiles are unstable with growth-rates of similar magnitude. It also shows that more in-depth simulations breaking the azimuthal symmetry should be performed to study the impact of this instability on the electron clouds densities and resulting collected currents. Similarly, the combination of high trapped electron cloud densities ($f_b \approx 1$), and axial non-uniformity of the clouds and magnetic field, are breaking the assumptions of the eigenvalue solver and motivates either a more complex eigenvalue equation, such as the macroscopic electrostatic eigenvalue equation given in chapter 5.3 of [32] and [57] and briefly described in Appendix C, or an adaptation of FENNECS to simulate 2D (radial-azimuthal) or 3D geometries.

Finally, to study the onset of diocotron modes as a function of the trapped electron density, simulations have been run using two applied biases ($\Delta\phi = 20$ kV and $\Delta\phi = 100$ kV) to obtain the clouds' radial density profiles at several instants during the clouds' formation. These profiles are used as input for the eigenvalue solver to determine if a critical density exists above which the clouds become diocotron unstable, and if this density is bias dependent. The result of these simulations show that, while most of the modes are unstable at all time frames and both biases, their growth-rates are significantly lower for the high-bias

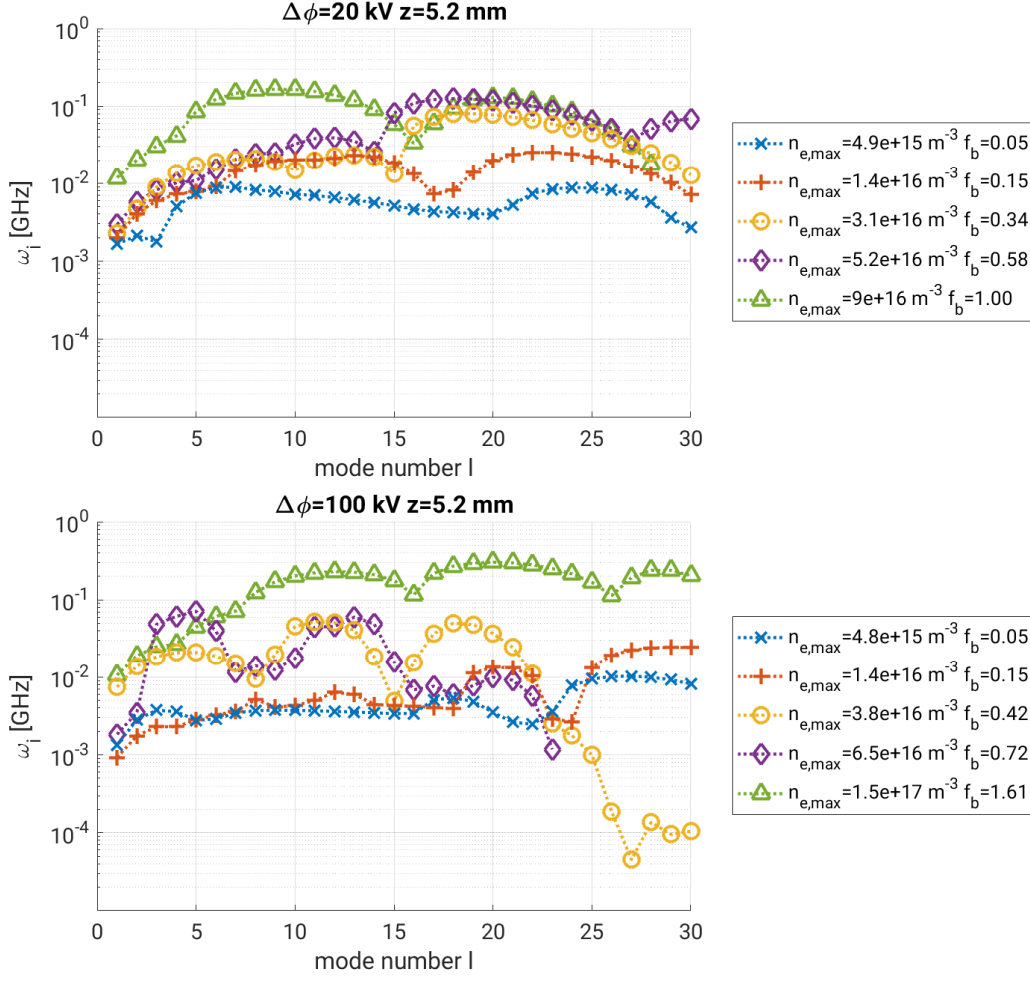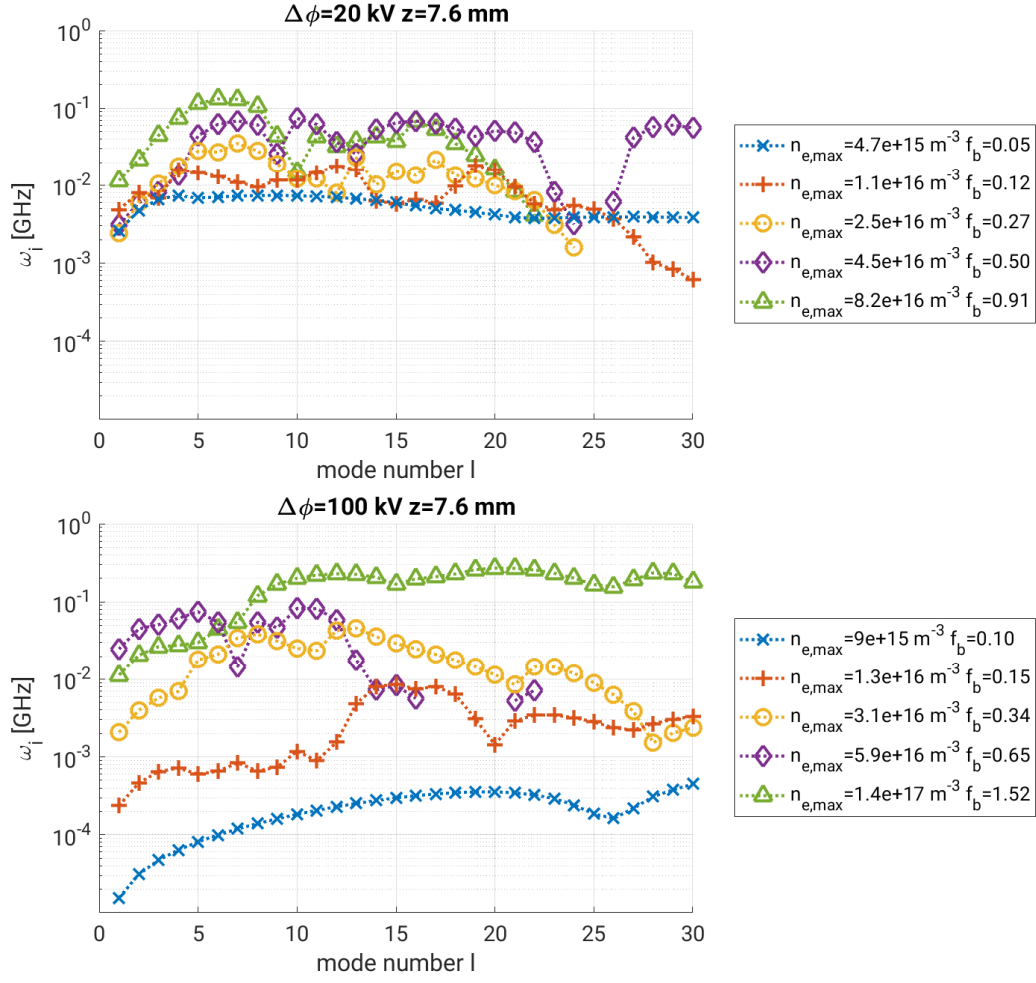Figure 6.10: Top: growth rate of the most unstable modes for density profiles obtained with a bias $\Delta\phi = 20\,\text{kV}$ using FENNECS simulations, at several times of cloud formation, for the middle position considered in Figure 6.6 and for each mode number $l \in [1, 30]$. Each colour and marker represent a different time during the cloud formation, corresponding to a different maximum electron density. If a marker is missing, the mode frequency is real and the mode is stable. Bottom: same as top but for a bias $\Delta\phi = 100\,\text{kV}$

compared to the low-bias at equivalent maximum density. This result is consistent with the hypothesis that imposing larger biases stabilizes the diocotron modes, and that electron clouds need to reach larger densities to become unstable at large biases. This supports the mechanism proposed to explain the discrepancy between numerically and experimentally observed collected currents in the GT170 prototype gyrotron electron gun geometry (see Section 4.4.1). However, this result is preliminary, as the assumptions used in the derivation of the eigenvalue equation are not all respected. This also motivates further study of the diocotron instability in gyrotron electron guns.

7 Conclusions and Outlooks

This thesis investigated the problem of trapped electron clouds in gyrotron electron guns, which emerge due to the presence of deep potential wells formed by the electrodes geometries and the magnetic field lines topology, and the challenge they pose for the design of future gyrotrons. It is clear that preventing the formation of any potential well in gyrotrons is a complex task and a stringent constraint, as many design requirements need to be fulfilled to obtain a reliable continuous wave gyrotron with sufficient efficiency. For this reason, a better understanding of the trapped electron cloud formation conditions inside a gyrotron electron gun was necessary. In addition, the exotic parameter regime of the clouds make their study interesting for the nonneutral plasma physics community and for increasing our understanding of nonneutral plasma confinement. In this chapter, the main results of this thesis are summarized and possible future extensions to this work are proposed.

The 2D (axial-radial) FENNECS particle-in-cell code has been developed as a numerical tool to study the formation and dynamics of trapped electron clouds in realistic gyrotron electron guns. To this end, a novel numerical method has been implemented in the code to solve the Poisson equation in domains with Dirichlet and Neumann boundary conditions defined on curved surfaces while keeping a structured grid. This finite element method called weighted-extended-b-splines is based on bivariate b-splines of any order, which allows numerically efficient charge deposition and electric field evaluation at the particles' position and allows both h and p convergence to reduce the error on the electrostatic potential. Compared to unstructured grids, this novel method also allows for rapid implementation of new geometries, as it does not require the costly and cumbersome generation of meshes. This makes FENNECS particularly relevant as a design tool for gyrotron electron guns, since many geometries need to be tested during the design phase. FENNECS is also capable of simulating electron-neutral collisions in gyrotrons, considering both elastic and inelastic (ionization) collisions, and secondary electron emission on electrodes caused by energetic ions hitting the metallic surfaces. The code has been verified against manufactured solutions and physical problems with known analytical solutions, which allowed its use in both simplified and realistic gun configurations.

With FENNECS verified, the conditions of formation and dynamics of electron clouds have been studied numerically using simplified electrodes geometries, while retaining the key characteristics of gyrotron electron guns. These are: (i) a strong externally applied and mostly axial magnetic field; (ii) two biased coaxial electrodes imposing a strong azimuthal flow; (iii) the formation of a deep (several keV) trapping potential well in vacuum; (iv) the presence of a residual neutral gas that can be ionized by an initial population of electrons. The simulation results showed that electron clouds form spontaneously, from

an initial small trapped electron population, by ionizing the residual neutral gas present in the vessel. The initial population can be extremely small and is expected to come from uncontrolled source such as ionization of the neutral gas by background radiation or field emission on the electrode surfaces. The simulations also showed that electrons are lost from the clouds due to radial drifts imposed by collisional drag forces caused by electron-neutral collisions. A reduced analytical fluid model was then derived that is capable of describing the mechanisms of formation and loss of the electron clouds. This model can also produce fast reasonable estimates of the trapped electron cloud density and its resulting leaking current using only a few key external parameters, in a relevant range of values, that are known and controlled externally. These are the magnetic field amplitude, the potential well size, the applied bias, the distance between the electrodes, and the RNG specie. In particular, the model shows that the steady-state electron density n scales with the square of the magnetic field amplitude B^2 and is independent of the neutral gas density n_n, the leaking current I is linearly proportional to n_n, and both n and I have more complex dependencies on the applied bias $\Delta\phi$ through the collision cross-sections of the electrons with the neutral gas. However, the model still lacks a self-consistent description of the potential well dimensions, which adds uncertainty to the predictions at large magnetic field amplitudes. This is due to the important space-charge effects of the trapped electrons, that significantly modify the potential well size and depth. The model and simulations also showed that for typical configurations obtained in gyrotron electron guns, the clouds will reach high densities with Brillouin ratios $f_b \approx 1$.

Leveraging FENNECS' capabilities and the increased understanding of electron trapping conditions in MIGs, validation simulations have been performed using the geometry of an actual gyrotron electron gun (the refurbished GT170 coaxial gyrotron initially designed for ITER) where experimental data was available. These simulations were run in a configuration where the potential wells size and depth can be controlled precisely by modifying slightly the magnetic field lines topology in the gun region, and where experimental results showed a sharp transition, as a function of a controlled current flowing through one of the superconducting coil, from a region where problematic currents were measured to a region where no problematic currents were observed. The simulations showed that not all potential wells are problematic, and that FENNECS is able to reproduce the region where the gun goes from inoperable to operational in the applied bias and magnetic field topology parameter space. This result is particularly promising for the design of future MIGs as it means that the "no potential-well" constraint can be relaxed, and that FENNECS can guide the design of future MIGs. However, other simulations in the prototype geometry of the GT170 gyrotron, where experimental measurements are also available, showed that FENNECS lacks accuracy in the predicted collected current and that some physical phenomena might be missing from its model. Ion induced electron emission on the electrodes have been included to try explaining the discrepancies, but their effect is too small and do not improve the agreement.

In parallel to the numerical and analytical studies of trapped electron clouds in gyrotron electron guns, a dedicated experiment, called T-REX, which is capable of reproducing the key parameters of MIGs relevant for the study of trapped electron clouds, is under construction at SPC. This experiment allows an easier optical access to the cloud, a broader range of measurable quantities and more precise diagnostics than what can be achieved in a sealed operational gyrotron. While the experimental part of the project is being led by Francesco Romano, a post-doctoral fellow of SPC, the design of the experiment and the selection of the type and sensitive range of the diagnostics, have been supported by FENNECS simulations. Three electrode configurations have been selected for T-REX, allowing the study of two different types of cloud trapping: one close to the anode, one close to the cathode, and a combination of the two. FENNECS simulations in the 3 T-REX configurations have shown that electron clouds are expected to form in the region where a potential well is present, and that the resulting nonneutral plasmas parameters ranges are consistent with the ones present in gyrotron electron guns. In addition, predictions of the total trapped

charge and time-scales of formation and oscillations of the cloud densities have been achieved, using both an ideal power-supply and simulating a realistic high-impedance power-supply that mimics the one that will be used during the experiments. These simulations show that it is recommended to operate T-REX at a high vacuum $p \leq 1 \times 10^{-5}$ mbar. In addition, simulations with IIEE effects show that this effect only brings corrections to the total collected current, and that one of the three electrodes configurations can be used to isolate electrons generated by IIEE from the ones generated by ionization of the RNG, thus allowing an experimental characterization of IIEE effects.

Finally, the linear stability of electron clouds obtained with FENNECS simulations to diocotron normal modes was studied using a finite difference eigenvalue solver. The eigenvalue equation implemented in this solver considers a low density annular electron cloud ($f_b \ll 1$) of infinite length trapped inside a coaxial electrode configuration and subjected to an externally applied radial electric field and a strong uniform axial magnetic field. The studies performed with this solver indicate that diocotron instabilities should develop in electron clouds if they reach a sufficient critical density that is typically reached in MIGs. However, high applied biases between the electrodes have a stabilizing effect, which means that this critical density is bias dependent. We need to stress that these results are still preliminary as the eigenvalue equation chosen for this study is used in regimes where its underlying assumptions (low density, low frequency, axial uniformity) are not fully applicable. For this reason, more general eigenvalue equations relaxing the violated assumptions, such as the macroscopic electrostatic eigenvalue equation given in chapter 5.3 of [32] and [57], need to be implemented, verified and applied to MIGs configurations. Similarly, the diocotron instability could be studied non-linearly by extending FENNECS to allow 2D (radial-azimuthal) or 3D simulations. In the meantime, T-REX experiments will soon be able to determine if diocotron instabilities develop in the trapped clouds and if they lead to a significant discrepancy between measurements and numerical predictions.

In the near future, T-REX will be commissioned and more quantitative validations of FENNECS will be possible, leading to a more robust code. In addition, the experiments will allow the validation of the reduced fluid model and deepen our understanding of the electron clouds formation and loss mechanisms. In parallel, it would be interesting to improve FENNECS to allow 2D (radial-azimuthal) and 3D simulations and to add secondary electron emission due to electrons colliding with the electrodes, enabling the study of electrons trapped by magnetic mirrors in electron guns and their effect on the voltage stand-off of the gun. These improvements should also permit a thorough study of the onset of diocotron instability in electron clouds trapped in MIGs. Furthermore, without any modifications to the code, the effect of ionisation of the RNG in the main electron beam, that lead to the presence of ions along the beam trajectory, and its consequences on the accelerating electric field seen by the beam could already be studied. Indeed, due to the presence of trapped ions along the beam path, generating significant space-charge effects, and due to the beam self-generated electric field, the electrons of the beam are subjected to a different electric field than the one generated by the electrodes in vacuum. This effectively changes the electrons kinetic energy, which in turns changes the beam-wave interaction efficiency [109–111]. Currently, the ion density in the gyrotron is only estimated, leading to uncertainties on the electron beam kinetic energy. To increase the confidence and accuracy of the predicted ion density in the gyrotron, first-principle simulations using FENNECS in the full gyrotron geometry, and considering electron-neutral collisions, could be run. This type of simulation could be used to predict the ion density profile along the beam trajectory and simulate the electron beam distribution function at the entrance of the cavity, which is capital for beam-wave interaction simulations. This will improve the accuracy and confidence on the neutralization fraction used in several beam-wave interaction codes developed for gyrotron design. Similarly, FENNECS could be simplified to run as an iterative equilibrium solver to simulate the electron beam trajectory and characterize the electron beam distribution function, in particular α and γ, at the entrance of the cavity. This, combined with the

flexibility of FENNECS to rapidly implement new geometries, should make it a powerful design tool for the future generation of gyrotron electron guns needed for future fusion reactors.

A Self consistent ϕ calculation for an annular electron plasma trapped in a biased coaxial cylinder

This section presents the analytical solution of the electrostatic potential for an annular electron cloud of infinite length, with step density profile, and encased in a coaxial geometry made of two biased concentric electrodes. Considering an annular electron plasma confined in a coaxial geometry of infinite length, as represented in Figure A.1, with the following density:

$$n(r) = \begin{cases} 0 & a < r < r_- \\ n_e & r_- \le r \le r_+ \\ 0 & r_+ < r < b \end{cases} \tag{A.1}$$

and electric potential boundary conditions:

$$\phi(a) = \phi_a; \quad \phi(b) = \phi_b; \quad \phi(r_+) = \phi_+; \quad \phi(r_-) = \phi_-. \tag{A.2}$$

With a, b, r_+, r_-, n_e, ϕ_a, and ϕ_b constants defining the problem, and $q_e = -e$ is the electron charge. In addition, an axial uniformity is assumed imposing $\frac{\partial}{\partial z} = 0$ and $\frac{\partial}{\partial \theta} = 0$. In this configuration, the Poisson equation is solved analytically in the three radial regions of the coaxial geometry:

$$\nabla^2 \phi(r) = \frac{1}{r}\frac{\partial}{\partial r}\left(r\frac{\partial \phi}{\partial r}\right) = \begin{cases} 0 & a < r < r_-, \\ -q_e n_e / \epsilon_0 & r_- \le r \le r_+, \\ 0 & r_+ < r < b. \end{cases} \tag{A.3}$$

In the vacuum regions the electric potential can be written as:

$$\phi(r) = A_\pm \ln(r) + B_\pm \quad | \, a < r < r_- \text{ or } r_+ < r < b, \tag{A.4}$$

and in the nonneutral plasma region:

$$\phi(r) = \frac{-q_e n_e}{4\epsilon_0}r^2 + C \ln(r) + D \quad | \, r_- \le r \le r_+. \tag{A.5}$$

Appendix A. Self consistent ϕ in coaxial geometry
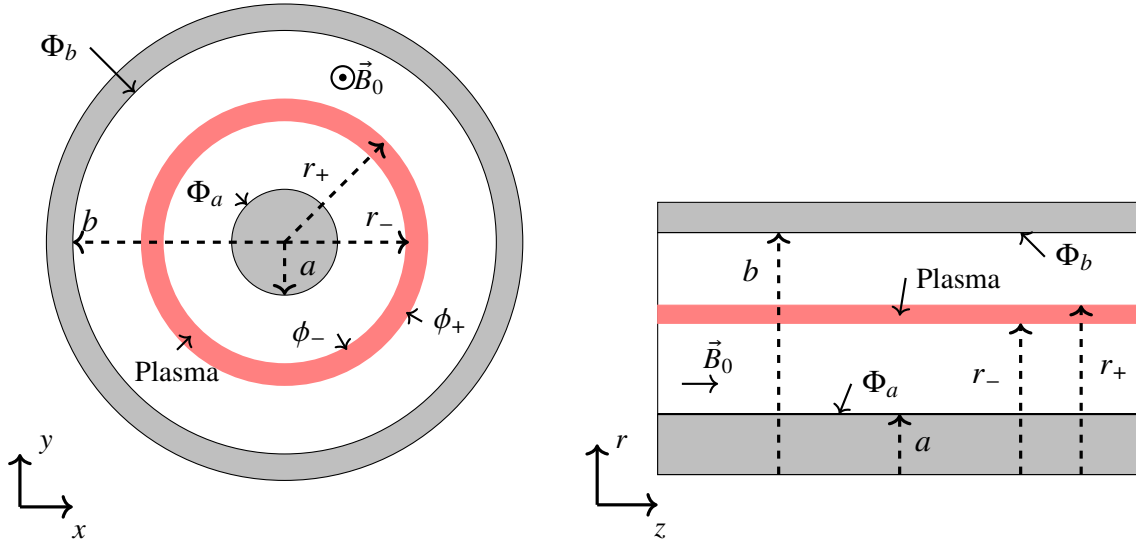
Figure A.1: Considered geometry seen in the (x, y) and (r, z) plane. Grey denotes a conductor, red denotes the plasma, and white is vacuum.

Here A, B, C and D are constants that can be calculated using the continuity of the potential at the interfaces:

$$A_- \ln(a) + B_- = \phi_a, \tag{A.6}$$

$$A_- \ln(r_-) + B_- = \phi_-, \tag{A.7}$$

$$A_+ \ln(r_+) + B_+ = \phi_+, \tag{A.8}$$

$$A_+ \ln(b) + B_+ = \phi_b, \tag{A.9}$$

and the matching conditions for the electric field, at r_- and r_+:

$$\lim_{r \nearrow r_-} E_r = \lim_{r \searrow r_-} E_r \tag{A.10}$$

$$\lim_{r \nearrow r_+} E_r = \lim_{r \searrow r_+} E_r. \tag{A.11}$$

This imposes:

$$-\frac{A_-}{r_-} = \frac{q_e n_e}{2\epsilon_0} r_- - \frac{C}{r_-}, \tag{A.12}$$

$$-\frac{A_+}{r_+} = \frac{q_e n_e}{2\epsilon_0} r_+ - \frac{C}{r_+}. \tag{A.13}$$

Solving for $A^\pm, B^\pm, C$ and D gives

$$A^+ = (\phi_b - \phi_+)/\ln(b/r_+), \tag{A.14}$$

$$A^- = (\phi_- - \phi_a)/\ln(r_-/a), \tag{A.15}$$

$$B^+ = \phi_+ - (\phi_b - \phi_+)\frac{\ln(r_+)}{\ln(b/r_+)}, \tag{A.16}$$

$$B^- = \phi_a - (\phi_- - \phi_a)\frac{\ln(a)}{\ln(r_-/a)}, \tag{A.17}$$

$$C = \left[\phi_+ - \phi_- + \frac{q_e n_e}{4\epsilon_0}((r_+)^2 - (r_-)^2)\right]\frac{1}{\ln(r_+/r_-)}, \tag{A.18}$$

$$D = \frac{q_e n_e}{4\epsilon_0}(r_+)^2 + \phi_+ - C\ln(r_+). \tag{A.19}$$

Where ϕ_+ and ϕ_- are the value of the potential at the cloud boundaries, and can be written as:

$$\phi_+ = \phi(r_+) = \frac{\ln\left(\frac{b}{r_+}\right)}{\ln\left(\frac{b}{a}\right)}\left[\phi_b\frac{\ln\left(\frac{r_+}{a}\right)}{\ln\left(\frac{b}{r_+}\right)} + \phi_a + \frac{q_e n_e}{2\epsilon_0}\left(r_+^2\ln\left(\frac{r_+}{a}\right) - r_-^2\ln\left(\frac{r_-}{a}\right)\right) - \frac{q_e n_e}{4\epsilon_0}(r_+^2 - r_-^2)\right], \tag{A.20}$$

$$\phi_- = \phi(r_-) = \frac{\ln\left(\frac{r_-}{a}\right)}{\ln\left(\frac{b}{a}\right)}\left[\phi_a\frac{\ln\left(\frac{b}{r_-}\right)}{\ln\left(\frac{r_-}{a}\right)} + \phi_b + \frac{q_e n_e}{2\epsilon_0}\left(r_+^2\ln\left(\frac{b}{r_+}\right) - r_-^2\ln\left(\frac{b}{r_-}\right)\right) + \frac{q_e n_e}{4\epsilon_0}(r_+^2 - r_-^2)\right]. \tag{A.21}$$

In addition, the following coefficient can be defined and used in C.

$$
\begin{aligned}
\Delta\phi_{+-} = \phi_+ - \phi_- = \frac{\ln\left(\frac{r_+}{r_-}\right)}{\ln\left(\frac{b}{a}\right)}&\left[\phi_b - \phi_a + \frac{q_e n_e}{4\epsilon_0}(r_+^2 - r_-^2)\frac{\ln\left(\frac{ar_+}{br_-}\right)}{\ln\left(\frac{r_+}{r_-}\right)}\right.\\
&\left.+ \frac{q_e n_e}{2\epsilon_0}\left(r_+^2\ln\left(\frac{b}{r_+}\right) - r_-^2\ln\left(\frac{a}{r_-}\right)\right)\right].
\end{aligned}
\tag{A.22}
$$

B Equilibrium density limit for a mono-energetic electron cloud trapped in a magnetic mirror (chapter 4.3.4 of [32])

This section considers the equilibrium distribution function of an electron cloud trapped radially by a strong magnetic field and axially by a magnetic mirror of length L [32, 97], that is used as a FENNECS test case in Section 2.4.2. This configuration is of interest, because it can allow equilibria with $f_b > 1$ contrary to what is possible in the rigid rotor equilibria of Section 1.4.1, as we will show in this section and as described in chapters 4.2.4 and 4.3.4 of [32].

We remind here that the configuration is shown in Figure 2.14 of page 44, and recall the magnetic field configuration and the Vlasov electrostatic equilibrium distribution function of the annular electron cloud. The magnetic vector potential for an externally imposed mirror field, that is needed to compute the canonical angular momentum, is described analytically by

$$A_0^{\text{ext}}(r, z) = \frac{1}{2} B_0 \left[r - \left(\frac{L}{\pi} \frac{R-1}{R+1} \right) I_1 \left(\frac{2\pi r}{L} \right) \cos \left(\frac{2\pi z}{L} \right) \right], \tag{B.1}$$

with B_0 the magnetic field amplitude on axis at $z = \pm L/4$, I_1 the modified Bessel function of order one, L the distance between the mirror coils, and R the mirror ratio defined by $R \equiv B_{max}/B_{min} = B_0^{\text{ext}}(r = 0, z = \pm L/2)/B_0^{\text{ext}}(r = 0, z = 0)$. In this configuration, the magnetic field generated by the trapped cloud is neglected.

The equilibrium distribution function, solution of the Vlasov equation, is written in terms of conserved quantities, namely the total energy $H = p^2/(2m_e) - e\phi(r, z)$, with $\vec{p} = m_e \vec{v}$, and the canonical angular momentum $P_\theta = r[p_\theta - e A_0^{\text{ext}}(r, z)]$,

$$f_e(H, P_\theta) = \frac{n_0 R_0}{2\pi m_e} \delta(H - H_0) \delta(P_\theta - P_0). \tag{B.2}$$

Here, n_0 is the maximum electron density in the cloud, R_0 is the lower radial limit of the cloud at $z = 0$, H_0 and P_0 are positive constants, and p_θ is the electron momentum in the azimuthal direction. For this equilibrium, an envelope function $\zeta(r, z)$ can be defined [97] such that the curve where $\zeta(r, z) = 0$ denotes the limit of the electron cloud. This function is derived from the definition of H, the conditions $H := H_0$

and $P := P_0$, and the need for the radial and axial kinetic energies to be positive:

$$\zeta(r,z) = \frac{p_\perp^2(r,z)}{2m_e H_0} = 1 + \frac{e\phi}{H_0} - \frac{1}{2m_e H_0}\left[\frac{P_0}{r} + eA_0^{\text{ext}}\right]^2. \tag{B.3}$$

Here, $p_\perp$ is the momentum perpendicular to $\hat{e}_\theta$ and ϕ is the self-consistent electric potential. The electron density can be calculated from the 0th order moment of the distribution function (B.2) leading to:

$$n_e(r,z) = \int_{\mathbb{R}^3} f_e d^3v = \frac{R_0}{r} n_0 U[\zeta(r,z)], \tag{B.4}$$

with $U[x]$ the Heaviside step function.

In this configuration, the radial equilibrium can be characterized, as was done for the rigid rotor equilibria of Section 1.4.1, using the fluid force balance for a fluid element in the radial direction and including pressure effects:

$$-m_e\omega_{re}^2 r = -eE_r(r) - e\omega_{re}rB_z(r) - \frac{\nabla \cdot \mathcal{P}}{n} \cdot \hat{e}_r, \tag{B.5}$$

with ω_{re} the equilibrium azimuthal angular velocity, and $\mathcal{P} = n\mathcal{T}$ the pressure tensor dependent on the temperature tensor:

$$\begin{aligned}\mathcal{T} &= \frac{1}{n}\int_{\mathbb{R}^3}\frac{(\vec{p} - m_e\vec{u})(\vec{p} - m_e\vec{u})}{2m_e}f_e d^3\vec{p} \\ &= \left[H_0 + e\phi(r,z) - \frac{1}{2m_e}\left(\frac{P_0}{r} + eA_0^{\text{ext}}(r,z)\right)^2\right](\hat{e}_{rr} + \hat{e}_{zz}).\end{aligned} \tag{B.6}$$

Here $\vec{u}$ is the mean electron velocity. From this definition, and the equation for the density (B.4), the pressure force in the radial direction becomes:

$$-\frac{\nabla \cdot \mathcal{P}}{n} \cdot \hat{e}_r = -\frac{1}{rn}\frac{\partial}{\partial r}(rnT_{rr}) = -\frac{1}{r}\frac{\partial}{\partial r}(rT_{rr}) - \frac{T_{rr}}{n}\frac{\partial}{\partial r}(n) = -\frac{\partial T_{rr}}{\partial r}. \tag{B.7}$$

Using the definition of the axial magnetic field

$$B_z(r,z) = \frac{1}{r}\frac{\partial rA_0^{\text{ext}}}{\partial r}, \tag{B.8}$$

combined with the radial fluid force balance (B.5), the expression of the pressure force term (B.7) and (B.6) we obtain:

$$m_e\omega_{re}^2 r - e\omega_{re}\frac{\partial}{\partial r}(rA_\theta(r,z)) + e\frac{\partial\phi(r,z)}{\partial r} - e\frac{\partial\phi(r,z)}{\partial r} + \frac{1}{2m_e}\frac{\partial}{\partial r}\left(\frac{P_0}{r} + eA_0^{\text{ext}}(r,z)\right)^2 = 0. \tag{B.9}$$

One can see that the two terms including ϕ cancel out, which removes the density dependency in this equation. This lead to a quadratic equation in ω_{re} with the two solutions:

$$\omega_{re}^\pm = \frac{eB_z(r,z)}{2m_e} \pm \frac{e}{2m_e}\sqrt{\left(\frac{1}{r}\frac{\partial rA_0^{\text{ext}}}{\partial r}\right)^2 - \frac{4}{re^2}\left(\frac{P_0}{r} + eA_0^{\text{ext}}\right)\left(\frac{\partial}{\partial r}eA_0^{\text{ext}} - \frac{P_0}{r^2}\right)}. \tag{B.10}$$

These can be rewritten as

$$\omega_{re}^+ = \frac{eA_0^{\text{ext}}(r,z)}{rm_e} + \frac{P_0}{r^2 m_e}, \tag{B.11}$$

and

$$\omega_{re}^{-} = \frac{e}{m_e} \frac{\partial A_0^{\text{ext}}(r, z)}{\partial r} - \frac{P_0}{r^2 m_e}, \tag{B.12}$$

showing that the radial equilibrium is independent of the peak electron cloud density n_0, and, provided that the magnetic mirror ratio R and the total energy H_0 are sufficiently large, an equilibrium for trapped electron clouds with densities $f_b > 1$ can exist.

C Finite difference discretization of the electrostatic eigenvalue equation for Diocotron instability studies

In this section, we consider the linear stability of non-relativistic nonneutral plasma equilibria to small-amplitude electrostatic perturbations [32], using an eigenvalue equation for the perturbed potential $\delta\phi(r,\theta,z,t)$ that is derived from a linearized cold fluid-Poisson system. This model assumes an electron cloud of arbitrary radial density profile $n_e^0(r)$ and infinite length in cylindrical coordinates and subjected to a uniform axial magnetic field $\vec{B} = B_0\hat{e}_z$. The plasma is assumed to have a uniform axial velocity $u_z = $ cst., and the magnetic field generated by the cloud is neglected. This model also assumes normal mode perturbations of the electrostatic potential and considers spatially periodic perturbations along z with a wave number k_z leading to perturbations of the form:

$$\delta\phi(r,\theta,z,t) = \sum_{l=-\infty}^{\infty} \sum_{k_z=-\infty}^{\infty} \delta\phi^l(r,k_z)\exp(il\theta + ik_zz - i\omega t). \tag{C.1}$$

Contrary to the model presented in Chapter 6, this model retains the electrons' inertial effects, makes no assumptions on the plasma density and does not assume low frequency perturbations.

After the linearisation of the fluid-Poisson system and some algebra (chapter 5.3 of [32]), the eigenvalue equation can be written as

$$\frac{1}{r}\frac{\partial}{\partial r}\left[r\left(1 - \frac{\omega_{pe}^2}{v^2}\right)\frac{\partial}{\partial r}\delta\phi^l\right] - \frac{l^2}{r^2}\left(1 - \frac{\omega_{pe}^2}{v^2}\right)\delta\phi^l$$

$$-k_z^2\left(1 - \frac{\omega_{pe}^2}{(\omega - k_zu_z - l\omega_{re})^2}\right)\delta\phi^l \tag{C.2}$$

$$= -\frac{l\delta\phi^l}{r}\frac{1}{\omega - k_zu_z - l\omega_{re}}\frac{\partial}{\partial r}\left[\frac{\omega_{pe}^2}{v^2}(2\omega_{re} - \Omega_{ce})\right],$$

where ω is the mode complex frequency, $\omega_{pe}^2(r)$ is the local equilibrium electron plasma frequency squared, Ω_{ce} is the classical electron cyclotron frequency, ω_{re} is the equilibrium angular rotation velocity, and

$$v^2 = (\omega - k_zu_z - l\omega_{re})^2 - (2\omega_{re} - \Omega_{ce})\left[\frac{1}{r}\frac{\partial}{\partial r}\left(r^2\omega_{re}\right) - \Omega_{ce}\right]. \tag{C.3}$$

Appendix C. Discretization of the electrostatic eigenvalue equation

For a cloud confined in a cylindrical electrode of radius b set at ground, the boundary conditions impose $\partial_\theta \delta\phi(r)|_{r=0, r=b} = 0$ or

$$\delta\phi^l(0, k_z) = \delta\phi^l(b, k_z) = 0. \tag{C.4}$$

Similarly, in the case of a coaxial configuration with an inner electrode of radius a, the boundary conditions become:

$$\delta\phi^l(a, k_z) = \delta\phi^l(b, k_z) = 0. \tag{C.5}$$

The compact form of the eigenvalue equation (1.6) cannot be solved directly by numerical eigenvalue solvers, but can be rewritten with some algebraic manipulation to obtain a 6th order polynomial eigenvalue equation of the form:

$$(B_6\Omega^6 + B_5\Omega^5 + B_4\Omega^4 + B_3\Omega^3 + B_2\Omega^2 + B_1\Omega)\delta\phi^l = A\delta\phi^l, \tag{C.6}$$

where we have introduced $\Omega = \omega - l\omega_{re}(r)$ and the operators A and B_1 to B_6 that will be discretized using a finite difference scheme and described hereafter.

This system can be solved numerically on a discretized grid constructed from N points r_i and grid width $\Delta r = r_{i+1} - r_i$, using a centred finite difference method. In this case, we define the first and second derivative operators using finite differences leading to

$$D_1 = \begin{bmatrix} 0 & \frac{1}{2\Delta r} & 0 & \dots & 0 \\ -\frac{1}{2\Delta r} & 0 & -\frac{1}{2\Delta r} & \ddots & \vdots \\ 0 & \ddots & \ddots & \ddots & 0 \\ \vdots & \ddots & -\frac{1}{2\Delta r} & 0 & \frac{1}{2\Delta r} \\ 0 & \dots & 0 & -\frac{1}{2\Delta r} & 0 \end{bmatrix}, \tag{C.7}$$

and

$$D_2 = \begin{bmatrix} -\frac{2}{\Delta r^2} & \frac{1}{\Delta r^2} & 0 & \dots & 0 \\ \frac{1}{\Delta r^2} & -\frac{2}{\Delta r^2} & \frac{1}{\Delta r^2} & \ddots & \vdots \\ 0 & \ddots & \ddots & \ddots & 0 \\ \vdots & \ddots & \frac{1}{\Delta r^2} & -\frac{2}{\Delta r^2} & \frac{1}{\Delta r^2} \\ 0 & \dots & 0 & \frac{1}{\Delta r^2} & -\frac{2}{\Delta r^2} \end{bmatrix} \tag{C.8}$$

respectively. To improve the readability of the operators A and B_1 to B_6, we also define the two quantities

$$\alpha(r) = (-\Omega_{ce} + 2\omega_{re})(5\frac{\partial}{\partial r}\omega_{re} + r\frac{\partial^2}{\partial r^2}\omega_{re}) - 2r(\frac{\partial}{\partial r}\omega_{re})^2, \tag{C.9}$$

and

$$\beta(r) = (-\Omega_{ce} + 2\omega_{re})(-\Omega_{ce} + 2\omega_{re} + r\frac{\partial}{\partial r}\omega_{re}). \tag{C.10}$$

With these definitions and the identity matrix I, the matrices A and B_1 to B_6 can be written as

$$A = -k_z^2\omega_{pe}^2\beta^2 I, \tag{C.11}$$

$$B_1 = -\frac{l}{r}\omega_{pe}^2\left[2\beta\frac{\partial}{\partial r}\omega_{re} + (2\omega_{re} - \Omega_{ce})\left(2\beta\frac{1}{\omega_{pe}}\frac{\partial}{\partial r}\omega_{pe} - \alpha\right)\right]I, \tag{C.12}$$

144

$$B_2 = \beta(\beta + \omega_{pe}^2)(\frac{1}{r}D1 + D2 - \frac{l^2}{r^2}I) + \omega_{pe}^2(\beta\frac{2}{\omega_{pe}}\frac{\partial}{\partial r}\omega_{pe} - \alpha)D_1$$
$$- [\beta k_z^2(\beta + 2\omega_{pe}^2) - \frac{2l^2}{r}\omega_{pe}^2(2\omega_{re} - \Omega_{ce})\frac{\partial}{\partial r}\omega_{re}]I, \tag{C.13}$$

$$B_3 = -2l\omega_{pe}^2\frac{\partial}{\partial r}\omega_{re}D_1 + \left[\frac{2l}{r}\omega_{pe}^2\left(\frac{\partial}{\partial r}\omega_{re} + \frac{(2\omega_{re} - \Omega_{ce})}{\omega_{pe}}\frac{\partial}{\partial r}\omega_{pe}\right)\right] \tag{C.14}$$

$$B_4 = -(2\beta + \omega_{pe}^2)\left(\frac{1}{r}D_1 + D_2 - \left(\frac{l^2}{r^2} + k_z^2\right)I\right) - 2\omega_{pe}\frac{\partial}{\partial r}\omega_{pe}D_1 \tag{C.15}$$

$$B_5 = 0, \tag{C.16}$$

and

$$B_6 = \frac{1}{r}D_1 + D_2 - (k_z^2 + \frac{l^2}{r^2})I. \tag{C.17}$$

All the quantities that depend on r are also discretized and are defined as the coefficients of a diagonal matrix but are not written as such for readability. For example, the plasma frequency ω_{pe} becomes

$$\omega_{pe} \equiv \begin{bmatrix} \omega_{pe}(r_1) & 0 & 0 & \dots & & 0 \\ 0 & \omega_{pe}(r_2) & 0 & \ddots & & \vdots \\ 0 & \ddots & \ddots & \ddots & & 0 \\ \vdots & \ddots & 0 & \omega_{pe}(r_{N-1}) & & 0 \\ 0 & \dots & 0 & 0 & & \omega_{pe}(r_N). \end{bmatrix} \tag{C.18}$$

The radial derivatives can then either be calculated analytically, if they are known, or calculated using a centred finite difference scheme.

Equation (C.6) represents a first step towards the numerical solution of the problem. However, the frequency of interest is ω and since Ω is a function of $\omega_{re}(r)$ which depends on the radial position, we need to modify equation (C.6) to obtain an eigenvalue problem for ω and $\delta\phi$. With some more algebraic manipulations, we can obtain a polynomial eigenvalue equation in ω of the form:

$$(\tilde{B}_6\omega^6 + \tilde{B}_5\omega^5 + \tilde{B}_4\omega^4 + \tilde{B}_3\omega^3 + \tilde{B}_2\omega^2 + \tilde{B}_1\omega)\delta\phi^l = \tilde{A}\delta\phi^l, \tag{C.19}$$

where the new matrices are

$$\tilde{A} = A - (l\omega_{re})^6 B_6 - (l\omega_{re})^4 B_4 + (l\omega_{re})^3 B_3 - (l\omega_{re})^2 B_2 + (l\omega_{re})B_1, \tag{C.20}$$

$$\tilde{B}_1 = B_1 - 6(l\omega_{re})^5 B_6 - 4(l\omega_{re})^3 B_4 + 3(l\omega_{re})^2 B_3 - 2(l\omega_{re})B_2, \tag{C.21}$$

$$\tilde{B}_2 = B_2 - 15(l\omega_{re})^4 B_6 - 6(l\omega_{re})^2 I B_4 - 3(l\omega_{re})B_3, \tag{C.22}$$

$$\tilde{B}_3 = B_3 - 20(l\omega_{re})^3 B_6 - 4(l\omega_{re})B_4, \tag{C.23}$$

$$\tilde{B}_4 = B_4 + 15(l\omega_{re})^2 B_6, \tag{C.24}$$

$$\tilde{B}_5 = -6(l\omega_{re})B_6, \tag{C.25}$$

and

$$\tilde{B}_6 = B_6. \tag{C.26}$$

These matrices have been implemented in a Matlab code and the polynomial eigenvalue equation has been

solved numerically using the "polyeig" Matlab function. A verification of the solver was attempted during an internship project by Viktoriia Zakharova, but was unsuccessful. Some similarities between analytical solutions and numerical solutions were obtained, but were not sufficient to support the use of the solver for studying cases relevant to gyrotron electron guns. The discrepancies between the numerical and analytical results were attributed to numerical errors, and further study of this problem will be necessary to have sufficient confidence in the implementation. One possibility of improvement of the code, could be to use a finite element method to increase the accuracy of the solver, while keeping the problem size and numerical costs to a minimum.

D FENNECS input parameters

In complement to the description of the model implemented in FENNECS (see Chapter 2) we present here a list of the input parameters of the code that can be defined in the input files. This appendix combined with Chapter 2 can serve as a manual for future FENNECS users.

To define the simulation parameters for a run of FENNECS, a single text file containing Fortran namelists is given as a command line parameter to the executable. In this subsection, the current namelists and their parameters are defined and all the quantities must be written in SI units unless specified.

D.1 &BASIC

Defines the general parameters of the run, the loading of the particles, the FEM grid, the magnetic field and how the momentum equation is solved. The following parameters can be defined:

Variable (default value) Description

job_time (3600) Wall plug time in seconds allowed for the simulation to run. The simulation will be stopped safely at the end of job_time.

extra_time (60) Extra time in seconds allowed for the simulation to finish a loop and save data to disk, once job_time is finished.

nrun (1) Number of time-steps to run.

tmax (100000) Physical simulation time in seconds after which the run must be stopped.

dt (1) Time step expressed in seconds.

it0d (1) Defines the number of steps between the saving of each scalar variable not depending on r and z (E_{pot}, E_{kin} ...).

it2d (1) Defines the number of steps between each write to the hdf5 file of the 2d variables (Φ, E, moments of the distribution ...).

itparts (1) Defines the number of steps between each write to the hdf5 file of the full particles' position and velocity.

ittracer (1) Defines the number of steps between each write to the hdf5 file of the particles' position and velocity if they are defined with the tracer property.

ittext (1) Defines the number of steps between each write to the program standard output of the total potential energy, kinetic energy and error in the energy and of the population of macro-particles in each specie.

itgraph () Defines the number of time steps between the updates of the graphical interface in case FENNECS is compiled with XGRAFIX and run using **nlxg=**.TRUE..

nbcelldiag (0) Defines the number of &celldiagnostics groups in &celldiagparams.

itcelldiag (100000) Defines the number of steps between each write of the cell diagnostic data to the hdf5 file.

resfile ('results.h5') Name and path of the hdf5 file containing the simulation results.

rstfile ('restart.h5') Name and path of the hdf5 file containing the simulation and particle data at the last time-step of the simulation, to allow the restart of the run.

nlres (.FALSE.) Sets if this run is a restart. This means that during the program initialization, the particles position and velocities will be read from a "restart.h5" file, and the new simulation data will be appended to the existing **resfile**.

nlsave (.TRUE.) Defines if the simulation data at the final time-step is saved in **rstfile** as a checkpoint to allow for a restart.

newres (.FALSE.) Sets if the result file **resfile** is a new file (.TRUE.) and should be created in the case of a restart. This means that during the program initialization, the particles position and velocities will be read from a "restart.h5" file, and the new simulation data will be saved in the new **resfile**.

nlxg (.FALSE.) Sets if the graphical interface and plots should be displayed. The code should be compiled with the XGRAFIX library and run on a personal computer.

nlPhis (.TRUE.) Sets if the macro particles will interact through the self-consistent electric field. If set to .FALSE. the self-consistent electric potential and fields will be evaluated and saved in the hdf5 result, but not applied to the particles during the momentum update. However, the external electric field is always applied.

nlfreezephi (.FALSE.) If .TRUE. the electrostatic potential is first solved self-consistently at the start or restart of the simulation and not updated afterwards. If .FALSE., ϕ is updated every time-steps.

nlclassical (.FALSE.) If set to .TRUE., γ is set to 1 for every particle throughout the simulation. This is equivalent to solving the momentum equation in the classical limit. Otherwise, the relativistic momentum equations are solved.

potinn () Value of the electric potential on the surface of the inner cylinder($\Phi(r_a)$) for simple geometries. (see &geomparams)

potout () Value of the electric potential on the surface of the outer cylinder($\Phi(r_b)$) for simple geometries. (see &geomparams)

radii () Up to 11 components array containing in order for the r dimension, the lower limit of the mesh, the ith limits for the subdivision of the radial grid, the upper limit of the mesh ($[r_a, r_i, r_{i+1}, ...r_b]$).

lz () Up to 11 components array containing in order for the axial dimension, the lower limit of the mesh, the ith limits for the subdivision of the axial grid, the upper limit of the mesh ($[z^-, z_i, ...z^+]$).

nz () Number of intervals in z for the mesh definition. This variable is overridden if **nnz** is defined.

nnr () Up to 10 components vector containing the number of intervals in *r* for the *n* radial mesh regions ($[n_0, n_i, ..., n_{end}]$).

nnz () Up to 10 components vector containing the number of intervals in *z* for the *n* axial mesh regions ($[n_0, n_i, ..., n_{end}]$).

ngauss () 2 component array containing the number of axial and radial gauss points used for the integration in the FEM method($[ngauss_z, ngauss_r]$).

femorder () 2 component array containing the axial and radial degree of the B-splines polynomials used in the FEM method($[order_z, order_r]$).

nlppform (.TRUE.) Defines if b-splines are evaluated using the ppform or b-spline representation of the field. ppform is usually faster as less polynomial evaluations are necessary.

distribtype (1) Switch parameter defining the distribution function used to load the particles.

1. Uniform distribution in *z*, $1/r$ distribution in *r*, Gaussian distribution in each component of the velocity given the temperature **temp**.

2. Stable distribution for a magnetic mirror, as described in section B and in [97].

3. Same as 2. but with uniform radial density.

7. particles loaded from **partfile** input parameter

nbspecies (1) Number of simulated species and number of **partfile** species to read and load.

partfile ("") array of length 10 to set the filename of the particle input files. The files in this list from 2 to **nbspecies** are always read and loaded. **partfile**(1) is loaded only if **Distribtype**=7.

nbaddtestspecies (0) Number of added simulated species and number of **addedtestspecfile** to read and load during the restart of the simulation.

addedtestspecfile ("") array of length 10 to set the filename of the particle input files read during a restart and added to the simulation.

partperiodic (.FALSE.) If true, sets the axial particle boundary conditions to periodic, otherwise the particles are lost when they reach the axial limits of the simulation domain.

samplefactor (1) During rescale, this parameter allows multiplying the amount of macro-particles by an integer number, while keeping the same moments of the distribution function.

nplasma () Number of macro-particles simulated for the first specie if **distribtype**!=7.

npartsalloc () Size of the allocated memory for particles of specie 1 at the beginning of the simulation. More particles can be generated during the run, but only the first **npartsalloc** particles will be saved to disk. This allows better storage of the results if ionization is used in the simulation. This parameter is only used if **distribtype**!=7.

plasmadim () 4 component array containing the axial and radial limits in m, of the electron cloud used by **Distribtype**=1 at the initialization of the particles' positions ($[z_{min}, z_{max}, r_{min}, r_{max}]$).

n0 () Initial value of the density factor, in m^{-3}, used in the different **Distribtype**, which defines the weight of the macro-particles.

temp () Temperature expressed in Kelvins used for initializing the electron velocities in **Distribtype**=1.

H0 () Initial value of the hamiltonian H_0, in SI units, used in **Distribtype**=2,3 (see Section B).

P0 () Initial value of the Canonical angular momentum P_0, in SI units, used in **Distribtype**=2,3 (see Section B).

nblock () Number of slices in the axial direction used to approximate the electron cloud boundary for particle initialization in **Distribtype**=2,3.

weights_scale (1.0) Allows rescaling the macro-particle weight of the main specie on restart, to artificially increase or decrease the density.

B0 () Magnetic mirror scaling factor, or reference magnetic field amplitude for the time normalisation, expressed in T. This values can also be used with **bscaling** to rescale the maximum magnetic field amplitude from the one loaded from a h5 file.

Rcurv () Magnetic mirror ratio, in the case of a magnetic field defined as a magnetic mirror (see Section B).

width () Magnetic mirror width in meters, in the case of a magnetic field defined as a magnetic mirror (see Section B).

magnetfile ("") Name of the hdf5 file containing the description of the magnetic field.

bscaling (-1) Defines the way the magnetic field is rescaled when read from hdf5 file. (0) no rescale, (1) rescale the maximum value of the magnetic field amplitude in the h5 file (could contain points outside the simulation grid), (-1) Rescale the magnetic field amplitude after calculation of the field at the grid points.

nlmaxwellsource (.FALSE.) Sets is the ad-hoc source module is activated in this run.

D.2   Magnetic field h5 file

To input an external magnetic field a ".h5" file must be generated and loaded by setting the **magnetfile** variable in "&basic". Such h5 files can be constructed using the "savemagtoh5.m" Matlab function in the Matlab subfolder of FENNECS. Using the hdf5 nomenclature, the magnetic field data is saved in the group "/mag/" with the following structure:

r Array of dimension n_r defining the radial grid, in meters, on which the magnetic field is defined.

z Array of dimension n_z defining the axial grid, in meters, on which the magnetic field is defined.

Athet Stores the azimuthal component of the magnetic field potential vector in T m, as a 2D array of dimension (n_z,n_r).

Bz Stores the axial component of the magnetic field vector in T, as a 2D array of dimension (n_z,n_r).

Br Stores the radial component of the magnetic field vector in T, as a 2D array of dimension (n_z,n_r).

D.3   Magnetic field txt file

To input an external magnetic field a ".txt" file must be generated and loaded by setting the **magnetfile** variable and **magnetfiletype**=1 in "&magnetparams". Such text file store on each line a new coil with on the columns from left to right: the axial lower and upper limits of the coil (in m); the radial lower and upper limits (in m); the number of turns; the number of axial and radial subdivisions for the computation of the field using elliptic integrals; the current in amperes. The total magnetic field and the magnetic field potential are then computed on each grid points using elliptic integrals [112].

D.4 &magnetparams

This input parameter allows the definition of the magnetic field using three different methods. Some input parameters are the same as the one used in the "&basic" namelist and will overwrite these values.

magnetfiletype (0) type of magnet definition. If set to 0 and **magnetfile** is empty, then the default mirror magnet definition is used. If it is set to 0 and **magnetfile** is not empty, it will assume a hdf5 input file. If this variable is set to one, the code assumes a text input file describing the geometry and currents of each coils forming the magnet. **bscaling** to rescale the maximum magnetic field amplitude from the one loaded from a h5 file.

magnetfile ("") Name of the hdf5 file containing the description of the magnetic field, or of the text file containing the geometry and currents of the azimuthally symmetric magnet.

D.5 &partsload

Defined in specific particles loading files, this namelist allows more flexibility than the legacy loader. It is also combined with either a list of individual macro particles to load or a list of slices and their respective number of macro-particles to load non-trivial distributions. Each specie should have its own particle file list, leading to a separate storage structure in the code.

Variable (default value) Description

partformat ('slices') Type of particle file.

> **'slices'** the cloud is defined spacially as a list of slices with, on each line, the left axial limit, the lower and upper radial limit and the number of macro-particles to load in this slice. The right limit is given on the next line, and the last line comports only the axial limit.

> **'parts'** the cloud is defined by individual particles with in order: the radial, azimuthal and axial positions, then the radial, azimuthal and axial velocities in SI units.

nblock () number of slices in the 'slices' description or number of particles in the 'parts' description.

mass (m_e) the mass of a physical particle in kg.

charge (q_e) the charge of a physical particle in C.

weight (1) the number of physical particles that one macro-particle represents.

npartsalloc () size of the initial particles array to prepare for an increase of particle numbers. In the diagnostics, only the first **npartsalloc** particles will be saved in the hdf5 file. However, more particles can be created or present in the simulations. The additional particles are simply not saved.

radialtype (2) type of radial distribution used when creating particles:

1. $1/r$ distribution in r.

2. uniform distribution in r.

3. $1/r^2$ distribution in r.

4. Gaussian distribution in r centred at $0.5(rlimits(1)+rlimits(2))$ and with $\sigma = 0.1(rlimits(2)-rlimits(1))$.

151

Appendix D. FENNECS input parameters

velocitytype (1) type of velocity distribution to use when creating particles

1. Maxwellian velocity of mean $< v >= 0 \, \text{m s}^{-1}$ and temperature defined in **temperature**.

2. Davidson stable distribution defined with **H0** and **P0** (see section B).

3. Flat top velocity distribution with mean $< v >=$ meanv and span $\max(v) =$ meanv + spanv, $\min(v) =$ meanv − spanv

temperature (10000) Temperature in Kelvin used for the Maxwellian velocity distribution function.

H0 $(3.2 \cdot 10^{-14})$ Energy in joules of the particles for Davidson distribution function.

P0 $(8.66 \cdot 10^{-25})$ Canonical angular momentum in $\text{kg m}^2 \, \text{s}^{-1}$ of the particles for Davidson distribution function.

is_test (.FALSE.) Defines if the specie is a test specie for which all the particles properties should be saved every **ittest** time steps.

is_field (.TRUE.) If .TRUE. the specie is used to calculate the RHS of Poisson's equation, otherwise the particles see the electric field, but do not participate in its resolution.

calc_moments (.FALSE.) Determines if the moments of the distribution function of this specie needs to be calculated on the grid and saved every **it2d** time steps.

meanv (0,0,0) mean velocity, expressed in m s^{-1}, in the radial, azimuthal and axial directions for the flat-top velocity loading.

spanv (0,0,0) span of the flat-top velocity, expressed in m s^{-1}, in the radial, azimuthal and axial directions for the flat-top velocity loading. Velocities will be contained between meanv-spanv and meanv+spanv.

iiee_id (-1) When positive, defines that this specie contains ions that undergo ion induced electron emission and sets the index of the specie id, in the Fortran array **partslist**, of the electronic specie where to add emitted electrons.

neuttype_id (1) Defines the type of ion simulated to determine the correct yield coefficients used to calculate the number of emitted electrons per collision with an electrode. The implemented values are:

1. H_2 gas.

material_id (1) Defines the type of material for the electrodes during the ion induced electron emission events. The implemented values are:

1. Stainless steel 304.

2. Copper.

3. Aluminium.

zero_vel (.TRUE.) If .TRUE. the electrons emitted during IIEE events are generated at the electrode surfaces with $\vec{v} = 0$, otherwise their velocity is initialized normal to the electrode surface, and with a non-uniform distribution of kinetic energy described in section 2.2.9.

D.6 &celldiagparams

This defines the behaviour of the cell diagnostic that stores the particles' velocity and position for all particles in a given cell, and at every **itcelldiag** steps. The arguments are a list of size **nbcelldiag** that allows you to define several of these diagnostics.

Variable (default value) Description

specieid () List of species with index corresponding to the indices in the Fortran array **partslist**.

rindex () radial index of the cell to consider.

zindex () axial index of the cell to consider.

D.7 &geomparams

Namelist used to define the geometry using weighted-extended-b-splines and allowing the definition of boundary conditions on curved surfaces. Currently, Dirichlet boundary conditions are used on the metallic parts and Neumann are used otherwise. The centre cylinder will be set at a potential **Potinn** and the external cylinder and ellipse are set at a potential **Potout** of the &Basic namelist.

Variable (default value) Description

walltype (0) Type of configuration to consider. A list of predefined weights are given here, but others could be defined. For detailed examples, see the Fortran source files "geometry_mod.f90" and "weighttypes_mod.f90".

- -*. If the **walltype** number is negative, a verification case with an analytical source-term is imposed, and the geometry is defined by the absolute value of **walltype**. With this, the correctness of the Poisson solution can be tested in many geometries. The manufactured electric potential solution has the form: $sin(\pi(z - z_c)/L_z) * sin(\pi(r - r_c)/L_r) + 2$ as in section 2.4.1.

- 0. Coaxial configuration of constant radius with central cylinder and external cylinder.

- 1. Center cylinder of infinite length and external ellipse.

- 2. Center cylinder and combination of external cylinder with a metallic ellipse added. This configuration is used in Chapter 3.

- 3. Two facing ellipses with extended cylinders where the centre ellipse radii are defined with $r_{a,inner} = z_r + r_b - r_a$, $r_{b,inner} = z_r + r_b - r_a$ and the ellipse centres are the same between inner and outer ellipse. The inner ellipse is an enlarged version of the outer ellipse.

- 4. Two facing ellipses with extended cylinders with identical major and minor radii.

- 5. Central cylinder and tilted upper cylinder, combined with tilted ellipse and left and right flat section. Natural boundary conditions are imposed at the left and right boundaries. Used to simulate T-REX in configuration 2 in Section 5.2.4.

- 6. Same as previous but with a metallic wall at ground on the lower axial limit of the simulation grid.

- 7. Same as previous but with a metallic wall at ground on the upper axial limit of the simulation grid.

8. Same geometry as previous but only the right wall has a set potential, the rest of the electrodes are at ground.

9. Geometry read from a b-spline description of the boundaries and defined by the namelist &spldomain and a hdf5 input file.

9. Coaxial configuration closed on both ends. The applied bias is between the end electrodes and the cylindrical electrodes. This approximates an ion pump configuration.

10. Concentric ellipses as used in section 2.4.1.

11. Central electrode with elliptic cut biased at **Potinn**, left disc and outer cylinder are set at a potential **Potout**. This configuration simulates T-REX in configuration 1 as shown in Section 5.2.4.

nlweb (.TRUE.) Toggle if weighted-extended-b-splines (.TRUE.) or simple weighted-b-splines (.FALSW.) must be used. There is better numerical precision and stability if set to true. Most cases will crash with mumps using **nlweb=**.FALSE..

testkr (1) For testing purposes (negative **walltype**), this defines the radial wavelength $L_r = (r_{max} - r_{min})/testkr$ of the imposed source term.

testkz (1) For testing purposes (negative **walltype**), this defines the axial wavelength $L_z = (z_{max} - z_{min})/testkz$ of the imposed source term.

z_0 () axial centre of the ellipse.

r_0 () radial centre of the ellipse.

z_r () axial radius of the ellipse.

r_r () radial radius of the ellipse.

r_a () radius of the central metallic cylinder.

r_b () radius of the external metallic cylinder.

z_a () axial position of a left metallic wall.

z_b () axial position of a right metallic wall.

Interior (-1) Defines if the inside or the outside of the ellipses are considered in the geometry.

above1 (1) Defines if the vacuum region is outside (1) or inside (-1) the cylinder of radius r_a.

above2 (-1) Defines if the vacuum region is outside (1) or inside (-1) the cylinder of radius r_b.

alpha () angle of the tilted wall and tilted ellipse w.r.t. the z axis.

r_bLeft () radial limit of the left wall for T-REX configuration 2 used in Section 5.2.4.

r_bRight () radial limit of the right wall for T-REX configuration 2 used in Section 5.2.4.

D.8 &spldomain

Defines the behaviour of the splinebound module which allows setting boundaries using a b-spline curve representation of the metallic, vacuum and insulating surfaces.

Variable (default value) Description

dist_extent () Set the distance in meters over which the geometric weight goes from 0 to 1 away from the boundary (see section 2.2.6).

h5fname () name of the h5 file containing the boundaries descriptions.

Dvals () array storing the fixed potential in V for each of the metallic boundaries defined in h5fname.

nelexact (.FALSE.) if .TRUE. calculates the geometric weight using the exact blended distance function all the time. If .FALSE., the weight is precomputed at each grid cell and used to generate an interpolant of the weight with bivariate b-splines of degree 3. The weights are then calculated by interpolation. This can add small errors for very coarse grids, but greatly increase the execution speed of the code.

D.9   Geometry h5 file

To input a geometry using a b-spline curve a ".h5" file must be generated and loaded by setting the **h5fname** variable in "&spldomain". Such hdf5 files can be constructed using the "savegeomtoh5.m" Matlab function in the Matlab subfolder of FENNECS. Using the hdf5 nomenclature, the geometry data is saved in the group "/geometry_spl/" with the following structure:

nbsplines Defines the number of spline curves stored in this file

*splineid group named by the identifier of the spline structure written in the form "%2.2i" which give "01" for the first spline, "02" for the second ... In each of the spline curve groups, the following parameters must be defined:

   order order of the spline curve.

   dim dimension of the spline curve.

   name name of the spline curve for easier debugging and post-processing.

   type integer defining the type of boundary condition to apply on the curve surface: 0 Dirichlet constant on the full surface, 2 natural boundary condition.

   periodic if set to 1 the curve is closed and periodic, and if set to 0 the curve is opened.

   pos (dim,n)-array of control points of the spline curve. The first dimension defines the dimension of the spline object and the second dimension is of size n, the number of control points.

&maxwellsourceparams

This section defines the behaviour of a volumetric source creating particles uniformly in the axial direction, according to a specified distribution in the radial direction and according to a Maxwellian distribution in velocity.

Variable (default value) Description

frequency () Number of macro-particles created per second of simulated time.

temperature () temperature in Kelvins used in the Maxwellian distribution function.

rlimits () 2 element array storing the radial extent of the source.

zlimits () 2 element array storing the axial extent of the source.

time_start (-1) time in seconds of the simulation time at which the source must be turned on. -1 means start from the beginning of the simulation

time_end (-1) time in seconds of the simulation time at which the source must be turned off. -1 means, never turn off the source.

radialtype (2) type of radial distribution to use when creating particles. The implemented values are:

1. $1/r$ distribution in r.
2. uniform distribution in r.
3. $1/r^2$ distribution in r.
4. Gaussian distribution in r centred at $0.5(rlimits(1)+rlimits(2))$ and with $\sigma = 0.1(rlimits(2)-rlimits(1))$.

D.10   &neutcolparams

This defines the behaviour of the elastic and ionisation collisions between electrons and the residual neutral gas particles.

Variable (default value) Description

nlcol (.FALSE.) defines if the collisions are active or not. If both ela_cross_sec_file and io_cross_sec_file are empty, the collisions are deactivated.

neutdens ($2.4 \cdot 10^{16}\,m^{-3}$) density of the RNG expressed in m^{-3}.

Eion (21.56 eV) first ionization energy, expressed in eV, of the neutral considered.

scatter_fac (24.2 eV) tabulated scatter factor, expressed in eV, used to compute the fraction of energy between scattered and created electrons in an ionization event. To set this parameter, please refer to [76].

io_cross_sec_file () name of the file containing the table of cross-sections as a function of energy in eV for the ionisation. In this file the comments are indicated with "!" and the table is just a two column list with the energy in eV and the cross-section in m^2. Example files are stored in the "wk" folder of the repository, but can also be downloaded from the LXCat database [74].

ela_cross_sec_file () name of the file containing the table of cross-sections as a function of energy in eV for the elastic collisions. In this file the comments are indicated with "!" and the table is just a two column list with the energy in eV and the cross-section in m^2. Example files are stored in the "wk" folder of the repository, but can also be downloaded from the LXCat database [74].

species (1,-1) The first number sets the colliding specie ID in the **partslist** Fortran array. In the case of an ionisation, the second number defines in which specie the ions should be added with 0 velocity. If the second number is lower than 1, no ions are created.

isotropic (.FALSE.) Defines if the scattering of the velocity vector during collisions is isotropic or anisotropic according to the differential cross-section described in [75]. The default is anisotropic.

itcol (1) allows running the collision routine every **itcol** time steps of the particle pushing. If the pressure is too low, this parameter can reduce unnecessary calculations.

D.11   &psupplyparams

Sets the parameters of the non-ideal power supply described in section 2.2.7. The input parameters are:

Variable   (default value) Description

active   (.FALSE.) Defines if this module is active.

expneutdens   () neutral density, in m^{-3}, measured in the experiment we want to simulate. This permits correct timescale separation and rescaling because we accelerate the ionisation time-scales (see sections 2.2.7 and 2.1.4).

PsResistor   () Internal resistance of the power supply in Ohms.

geomcapacitor   () Total capacitance of the geometry and connecting cables in Farrads.

targetbias   () Set bias v_s in V requested on the power supply.

nbhdt   () Number of Boris algorithm time steps between each half time-steps of the Runge-Kutta algorithm used to compute the time-evolution of the bias at the surface of the electrodes.

bdpos   (0) Array of integers indicating for each boundary the direction of the current for the collected species. The boundaries with **bdpos**(i)=-1 are set to $V_i = -V_s$ and all the other are set to ground.

Bibliography

[1] J. D. Lawson. "Some Criteria for a Power Producing Thermonuclear Reactor". In: *Proceedings of the Physical Society. Section B* 70.1 (Jan. 1957), p. 6. DOI: 10.1088/0370-1301/70/1/303.

[2] H. Reimerdes et al. "Overview of the TCV tokamak experimental programme". In: *Nuclear Fusion* 62.4 (Mar. 2022). Publisher: IOP Publishing, p. 042018. DOI: 10.1088/1741-4326/ac369b.

[3] ITER Physics Basis Editors, ITER Physics Expert Group Chairs and Co-Chairs and ITER Joint Central Team and Physics Integration Unit. "Chapter 1: Overview and summary". In: *Nuclear Fusion* 39.12 (Dec. 1999), p. 2137. DOI: 10.1088/0029-5515/39/12/301.

[4] T. Klinger et al. "Performance and properties of the first plasmas of Wendelstein 7-X". In: *Plasma Physics and Controlled Fusion* 59.1 (Oct. 2016). Publisher: IOP Publishing, p. 014018. DOI: 10.1088/0741-3335/59/1/014018.

[5] S. Li et al. *Schematic of a tokamak chamber and magnetic profile*. Mar. 2014. URL: https://commons.wikimedia.org/wiki/File:Schematic-of-a-tokamak-chamber-and-magnetic-profile.jpg.

[6] ITER Physics Expert Group on Energetic Particles, Heating and Current Drive, and ITER Physics Basis Editors. "Chapter 6: Plasma auxiliary heating and current drive". In: *Nuclear Fusion* 39.12 (Dec. 1999), p. 2495. DOI: 10.1088/0029-5515/39/12/306.

[7] C. Darbos et al. "Achievements and challenges for ITER heating & current drive systems". In: *2020 45th International Conference on Infrared, Millimeter, and Terahertz Waves (IRMMW-THz)*. ISSN: 2162-2035. Nov. 2020, pp. 1–2. DOI: 10.1109/IRMMW-THz46771.2020.9370668.

[8] C. Darbos et al. "Status of the ITER Electron Cyclotron Heating and Current Drive System". In: *Journal of Infrared, Millimeter, and Terahertz Waves* 37.1 (2016), pp. 4–20. DOI: 10.1007/s10762-015-0211-3.

[9] V. Erckmann and U. Gasparino. "Electron cyclotron resonance heating and current drive in toroidal fusion plasmas". In: *Plasma Physics and Controlled Fusion* 36.12 (Dec. 1994), p. 1869. DOI: 10.1088/0741-3335/36/12/001.

Bibliography

[10] F. Felici et al. "Integrated real-time control of MHD instabilities using multi-beam ECRH/ECCD systems on TCV". In: *Nuclear Fusion* 52.7 (July 2012). Publisher: IOP Publishing and International Atomic Energy Agency, p. 074001. DOI: 10.1088/0029-5515/52/7/074001.

[11] R. Prater. "Heating and current drive by electron cyclotron waves". In: *Physics of Plasmas* 11.5 (Apr. 2004), pp. 2349–2376. DOI: 10.1063/1.1690762.

[12] R. Temkin, V. Granatstein, and G. S. Nusinovich. *Introduction to the Physics of Gyrotrons*. Baltimore: Johns Hopkins University Press, 2004. DOI: 10.1353/book.62236.

[13] M. V. Kartikeyan, E. Borie, and M. K. A. Thumm. *Gyrotrons*. Advanced Texts in Physics. Berlin, Heidelberg: Springer, 2004. DOI: 10.1007/978-3-662-07637-8.

[14] M. Thumm. "Recent Advances in the Worldwide Fusion Gyrotron Development". In: *IEEE Transactions on Plasma Science* 42.3 (Mar. 2014). Conference Name: IEEE Transactions on Plasma Science, pp. 590–599. DOI: 10.1109/TPS.2013.2284026.

[15] S. Alberti. "Plasma heating with millimetre waves". In: *Nature Physics* 3.6 (June 2007). Number: 6 Publisher: Nature Publishing Group, pp. 376–377. DOI: 10.1038/nphys637.

[16] K. R. Chu. "The electron cyclotron maser". In: *Reviews of Modern Physics* 76.2 (May 2004). Publisher: American Physical Society, pp. 489–540. DOI: 10.1103/RevModPhys.76.489.

[17] S. Alberti et al. "Dual-frequency, 126/84 GHz, 1MW gyrotron for the upgrade of the TCV EC-system". In: *Proceedings of the 40th International Conference on Infrared, Millimeter, and Terahertz Waves (IRMMW-THz 2015), Hong Kong, China, August 23-28, 2015* (2015). ISBN: 9781479982721, p. 7327860. DOI: 10.1109/IRMMW-THz.2015.7327860.

[18] J. Genoud et al. "Parasitic Oscillations in Smooth-Wall Circular Symmetric Gyrotron Beam Ducts". In: *Journal of Infrared, Millimeter, and Terahertz Waves* 40.2 (Feb. 2019), pp. 131–149. DOI: 10.1007/s10762-018-0548-5.

[19] B. Piosczyk et al. "165-GHz coaxial cavity gyrotron". In: *IEEE Transactions on Plasma Science* 32.3 (June 2004), pp. 853–860. DOI: 10.1109/TPS.2004.827593.

[20] I. G. Pagonakis et al. "Gun design criteria for the refurbishment of the first prototype of the EU 170GHz/2MW/CW coaxial cavity gyrotron for ITER". In: *2009 34th International Conference on Infrared, Millimeter, and Terahertz Waves*. Sept. 2009, pp. 1–2. DOI: 10.1109/ICIMW.2009.5324625.

[21] I. G. Pagonakis et al. "Electron trapping mechanisms in magnetron injection guns". In: *Physics of Plasmas* 23.2 (Feb. 2016), p. 023105. DOI: 10.1063/1.4941705.

[22] R. H. Fowler and L. Nordheim. "Electron emission in intense electric fields". In: *Proceedings of the Royal Society of London. Series A, Containing Papers of a Mathematical and Physical Character* 119.781 (Jan. 1997). Publisher: Royal Society, pp. 173–181. DOI: 10.1098/rspa.1928.0091.

[23] J. P. Hogge et al. "Development of a 2-MW, CW Coaxial Gyrotron at 170 GHz and Test Facility for ITER". In: *Journal of Physics: Conference Series* 25.1 (Jan. 2005), p. 33. DOI: 10.1088/1742-6596/25/1/005.

[24] B. Piosczyk et al. "A 2 MW, 170 GHz coaxial cavity gyrotron - experimental verification of the design of main components". In: *Journal of Physics: Conference Series* 25.1 (Jan. 2005), p. 24. DOI: 10.1088/1742-6596/25/1/004.

[25] M. Vogel. *Particle Confinement in Penning Traps*. Vol. 100. Springer Series on Atomic, Optical, and Plasma Physics. Cham: Springer International Publishing, 2018. DOI: 10.1007/978-3-319-76264-7.

[26] G. Le Bars et al. "Self-consistent formation and steady-state characterization of trapped high-energy electron clouds in the presence of a neutral gas background". In: *Physics of Plasmas* 29.8 (Aug. 2022). Publisher: American Institute of Physics, p. 082105. DOI: 10.1063/5.0098567.

[27] V. N. Manuilov. "Numerical simulation of low-frequency oscillations of the space charge and potential in the electron-optical system of a gyrotron". In: *Radiophysics and Quantum Electronics* 49.10 (Oct. 2006), pp. 786–792. DOI: 10.1007/s11141-006-0113-2.

[28] A. J. Cerfon et al. "Observation and Study of Low-Frequency Oscillations in a 1.5-MW 110-GHz Gyrotron". In: *IEEE Transactions on Plasma Science* 37.7 (July 2009). Conference Name: IEEE Transactions on Plasma Science, pp. 1219–1224. DOI: 10.1109/TPS.2009.2020903.

[29] S. E. Tsimring. "Motion of Electrons in External Electric and Magnetic Static Fields". In: *Electron Beams and Microwave Vacuum Electronics*. John Wiley & Sons, Ltd, 2006, pp. 17–46. DOI: 10.1002/9780470053768.ch1.

[30] I. G. Pagonakis et al. "Status of the EU 170 GHz/2 MW/CW coaxial cavity gyrotron for ITER: The dummy gun experiment". In: *35th International Conference on Infrared, Millimeter, and Terahertz Waves*. ISSN: 2162-2035. Sept. 2010, pp. 1–2. DOI: 10.1109/ICIMW.2010.5613058.

[31] S. Kern et al. "Experimental results and recent developments on the EU 2 MW 170 GHz coaxial cavity gyrotron for ITER". In: *EPJ Web of Conferences* 32 (2012). Publisher: EDP Sciences, p. 04009. DOI: 10.1051/epjconf/20123204009.

[32] R. C. Davidson. *Physics of Nonneutral Plasmas*. Co-published with World Scientific Publishing CO, Oct. 2001. DOI: 10.1142/p251.

[33] F. C. Michel. "Non neutral plasmas in the laboratory and astrophysics". In: *Publications of the Astronomical Society of Australia* 6 (Jan. 1985). ADS Bibcode: 1985PASA....6..127M, pp. 127–129. DOI: 10.1017/S1323358000017914.

[34] W. A. Bertsche et al. "Physics with antihydrogen". In: *Journal of Physics B: Atomic, Molecular and Optical Physics* 48.23 (Oct. 2015). Publisher: IOP Publishing, p. 232001. DOI: 10.1088/0953-4075/48/23/232001.

[35] P. Pérez et al. "The GBAR antimatter gravity experiment". In: *Hyperfine Interactions* 233.1 (Aug. 2015), pp. 21–27. DOI: 10.1007/s10751-015-1154-8.

[36] M. R. Stoneking et al. "A new frontier in laboratory physics: magnetized electron–positron plasmas". In: *Journal of Plasma Physics* 86.6 (Dec. 2020). Publisher: Cambridge University Press, p. 155860601. DOI: 10.1017/S0022377820001385.

[37] R. C. Davidson and N. A. Krall. "Vlasov Equilibria and Stability of an Electron Gas". In: *The Physics of Fluids* 13.6 (June 1970). Publisher: American Institute of Physics, pp. 1543–1555. DOI: 10.1063/1.1693115.

[38] T. Mohamed, A. Mohri, and Y. Yamazaki. "Comparison of non-neutral electron plasma confinement in harmonic and rectangular potentials in a very dense regime". In: *Physics of Plasmas* 20.1 (Jan. 2013). Publisher: American Institute of Physics, p. 012502. DOI: 10.1063/1.4773900.

[39] T. M. O'Neil. "A confinement theorem for nonneutral plasmas". In: *The Physics of Fluids* 23.11 (Nov. 1980). Publisher: American Institute of Physics, pp. 2216–2218. DOI: 10.1063/1.862904.

[40] D. H. E. Dubin and T. M. O'Neil. "Trapped nonneutral plasmas, liquids, and crystals (the thermal equilibrium states)". In: *Reviews of Modern Physics* 71.1 (Jan. 1999), pp. 87–172. DOI: 10.1103/RevModPhys.71.87.

[41] Dhdpla. *Penning Trap*. May 2013. URL: https://commons.wikimedia.org/wiki/File: Penning_Trap.jpg.

[42] J. H. Malmberg and C. F. Driscoll. "Long-Time Containment of a Pure Electron Plasma". In: *Phys. Rev. Lett.* 44 (10 Mar. 1980), pp. 654–657. DOI: 10.1103/PhysRevLett.44.654.

[43] Y. H. Jo et al. "Control of the diocotron instability of a hollow electron beam with periodic dipole magnets". In: *Physics of Plasmas* 25.1 (2018), p. 011607. DOI: 10.1063/1.5018425.

[44] L. F. Ricketson and A. J. Cerfon. "Sparse grid techniques for particle-in-cell schemes". In: *Plasma Physics and Controlled Fusion* 59.2 (2016), p. 024002.

[45] S. Muralikrishnan et al. "Sparse grid-based adaptive noise reduction strategy for particle-in-cell schemes". In: *Journal of Computational Physics: X* 11 (2021), p. 100094. DOI: https://doi.org/10.1016/j.jcpx.2021.100094.

[46] V. V. Mikhailenko et al. "Non-modal analysis of the diocotron instability for cylindrical geometry with conducting boundary". In: *Physics of Plasmas* 21.5 (2014), p. 052105. DOI: 10.1063/1.4875341.

[47] I. N. Kartashov and M. V. Kuzelev. "Nonlinear dynamics of diocotron instability". In: *Plasma Physics Reports* 36.6 (June 2010), pp. 524–532. DOI: 10.1134/S1063780X10060073.

[48] Pétri, J. "Non-linear evolution of the diocotron instability in a pulsar electrosphere: two-dimensional particle-in-cell simulations". In: *A&A* 503.1 (2009), pp. 1–12. DOI: 10.1051/0004-6361/200911778.

[49] I. A. Kotelnikov, R. Pozzoli, and M. Romé. "Diocotron instability in non-neutral plasmas with a stationary point in the rotation frequency profile". In: *Physics of Plasmas* 12.9 (2005), p. 092105. DOI: 10.1063/1.2040177.

[50] T. J. Hilsabek. "Finite Length and Trapped-Particle Diocotron Modes". PhD thesis. UCLA, 2003.

[51] A. A. Kabantsev and C. F. Driscoll. "End shape effects on the m_θ=1 diocotron instability in hollow electron columns". In: *AIP Conference Proceedings* 498.1 (1999), pp. 208–213. DOI: 10.1063/1.1302121.

[52] R. Schuldt and E. Borie. "Diocotron instability of the electron beam in the drift tube of a gyrotron". In: *International Journal of Infrared and Millimeter Waves* 16.10 (1995), pp. 1675–1700. DOI: 10.1007/BF02068682.

[53] C. F. Driscoll. "Observation of an unstable l=1 diocotron mode on a hollow electron column". In: *Phys. Rev. Lett.* 64 (6 Feb. 1990), pp. 645–648. DOI: 10.1103/PhysRevLett. 64.645.

[54] T. M. O'Neil. "Cooling of a pure electron plasma by cyclotron radiation". In: *The Physics of Fluids* 23.4 (Apr. 1980), pp. 725–731. DOI: 10.1063/1.863044.

[55] A. J. Theiss, R. A. Mahaffey, and A. W. Trivelpiece. "Rigid-Rotor Equilibria of Nonneutral Plasmas". In: *Physical Review Letters* 35.21 (Nov. 1975). Publisher: American Physical Society, pp. 1436–1438. DOI: 10.1103/PhysRevLett.35.1436.

[56] K. Höllig, C. Apprich, and A. Streit. "Introduction to the Web-method and its applications". In: *Advances in Computational Mathematics* 23.1 (July 2005), pp. 215–237. DOI: 10. 1007/s10444-004-1811-y.

[57] R. C. Davidson. "Waves and instabilities in nonneutral plasmas". In: *AIP Conference Proceedings*. Vol. 175. ISSN: 0094243X. AIP, 1988, pp. 139–209. DOI: 10.1063/1.37618.

[58] *LSP Suite*. URL: https://www.northropgrumman.com/space/pic-code-software/lsp-suite.

[59] A. J. Woods and L. D. Ludeking. "MAGIC electromagnetic FDTD-PIC code dense plasma model comparison with Lsp". In: *2009 IEEE International Vacuum Electronics Conference*. Apr. 2009, pp. 165–166. DOI: 10.1109/IVELEC.2009.5193488.

[60] S. Mattei et al. "A fully-implicit Particle-In-Cell Monte Carlo Collision code for the simulation of inductively coupled plasmas". In: *Journal of Computational Physics* 350 (Dec. 2017), pp. 891–906. DOI: 10.1016/j.jcp.2017.09.015.

[61] B. Herrmannsfeldt. *ELECTRON TRAJECTORY PROGRAM*. Tech. rep. Stanford Linear Accelerator Center, Stanford University, Stanford, California 94305 U.S.A., 1979.

[62] S. Illy, J. Zhang, and J. Jelonnek. "Gyrotron electron gun and collector simulation with the ESRAY beam optics code". In: *2015 IEEE International Vacuum Electronics Conference (IVEC)*. Apr. 2015, pp. 1–2. DOI: 10.1109/IVEC.2015.7223779.

[63] T. M. Tran et al. *DAPHNE, A 2D Axisymmetric Electron Gun Simulation Code*. Tech. rep. LRP–494/94 INIS Reference Number: 25050357. Switzerland, 1994, pp. 1–4.

[64] I. G. Pagonakis and J. L. Vomvoridis. "The self-consistent 3D trajectory electrostatic code ARIADNE for gyrotron beam tunnel simulation". In: *Infrared and Millimeter Waves, Conference Digest of the 2004 Joint 29th International Conference on 2004 and 12th International Conference on Terahertz Electronics, 2004.* Sept. 2004, pp. 657–658. DOI: 10.1109/ICIMW.2004.1422262.

[65] D. P. Grote et al. "The WARP Code: Modeling High Intensity Ion Beams". In: *AIP Conference Proceedings* 749.1 (Mar. 2005). Publisher: American Institute of Physics, pp. 55–58. DOI: 10.1063/1.1893366.

[66] J.-L. Vay et al. "Novel methods in the Particle-In-Cell accelerator Code-Framework Warp". In: *Computational Science & Discovery* 5 (Dec. 2012), p. 014019. DOI: 10.1088/1749-4699/5/1/014019.

[67] A. Friedman et al. "Computational Methods in the Warp Code Framework for Kinetic Simulations of Particle Beams and Plasmas". In: *IEEE Transactions on Plasma Science* 42.5 (May 2014). Conference Name: IEEE Transactions on Plasma Science, pp. 1321–1334. DOI: 10.1109/TPS.2014.2308546.

[68] G. Apaydin and N. Ari. "Use of WEB-splines of arbitrary domain for waveguides". In: *2008 12th International Conference on Mathematical Methods in Electromagnetic Theory.* ISSN: 2161-1750. June 2008, pp. 385–388. DOI: 10.1109/MMET.2008.4581003.

[69] V. V. K. S. Kumar, B. V. R. Kumar, and P. C. Das. "Weighted extended B-spline method for the approximation of the stationary Stokes problem". In: *Journal of Computational and Applied Mathematics* 186.2 (Feb. 2006), pp. 335–348. DOI: 10.1016/j.cam.2005.02.008.

[70] K. Höllig, U. Reif, and J. Wipper. "Weighted Extended B-Spline Approximation of Dirichlet Problems". In: *SIAM Journal on Numerical Analysis* 39.2 (Jan. 2001). Publisher: Society for Industrial and Applied Mathematics, pp. 442–462. DOI: 10.1137/S0036142900373208.

[71] K. Höllig. *Finite Element Methods with B-Splines*. Frontiers in Applied Mathematics. Society for Industrial and Applied Mathematics, Jan. 2003. DOI: 10.1137/1.9780898717532.

[72] G. Le Bars et al. "First self-consistent simulations of trapped electron clouds in a gyrotron gun and comparison with experiments". In: *Physics of Plasmas* 30.3 (Mar. 2023). Publisher: American Institute of Physics, p. 030702. DOI: 10.1063/5.0136340.

[73] A. Anders. *Cathodic Arcs: From Fractal Spots to Energetic Condensation*. Google-Books-ID: rwIUhsbBHQYC. Springer Science & Business Media, July 2009.

[74] *Biagi-v8.9 database, private communication*. www.lxcat.net. retrieved on June 1. June 2021.

[75] A. Okhrimovskyy, A. Bogaerts, and R. Gijbels. "Electron anisotropic scattering in gases: A formula for Monte Carlo simulations". In: *Physical Review E* 65.3 (Feb. 2002). Publisher: American Physical Society, p. 037402. DOI: 10.1103/PhysRevE.65.037402.

[76] C. B. Opal, W. K. Peterson, and E. C. Beaty. "Measurements of Secondary-Electron Spectra Produced by Electron Impact Ionization of a Number of Simple Gases". In: *The Journal of Chemical Physics* 55.8 (Oct. 1971). Publisher: American Institute of Physics, pp. 4100–4106. DOI: 10.1063/1.1676707.

[77] T. Holstein. "Energy Distribution of Electrons in High Frequency Gas Discharges". In: *Physical Review* 70.5-6 (Sept. 1946). Publisher: American Physical Society, pp. 367–384. DOI: 10.1103/PhysRev.70.367.

[78] S. Yoshida, A. V. Phelps, and L. C. Pitchford. "Effect of electrons produced by ionization on calculated electron-energy distributions". In: *Physical Review A* 27.6 (June 1983). Publisher: American Physical Society, pp. 2858–2867. DOI: 10.1103/PhysRevA.27.2858.

[79] J. P. Boris et al. "Relativistic plasma simulation-optimization of a hybrid code". In: *Proc. Fourth Conf. Num. Sim. Plasmas*. 1970, pp. 3–67.

[80] C. de Boor. "On calculating with B-splines". In: *Journal of Approximation Theory* 6.1 (July 1972), pp. 50–62. DOI: 10.1016/0021-9045(72)90080-9.

[81] Ahlberg, J. H., Nilson, Edwin N., and Walsh, J. L. *The Theory of Splines and Their Applications*. Academic Press New York, 1967. URL: https://www.elsevier.com/books/the-theory-of-splines-and-their-applications/ahlberg/978-1-4831-9792-0.

[82] K. Höllig and J. Hörner. *Approximation and Modeling with B-Splines*. Other Titles in Applied Mathematics. Society for Industrial and Applied Mathematics, Jan. 2013. DOI: 10.1137/1.9781611972955.

[83] K. Höllig. *Finite Element Methods with WEB-Splines*. Oslo, Norway, Feb. 2017. URL: http://www.web-spline.de/publications/oslo07.pdf.

[84] E. T. Y. Lee. "Marsden's identity". In: *Computer Aided Geometric Design* 13.4 (June 1996), pp. 287–305. DOI: 10.1016/0167-8396(95)00027-5.

[85] V. L. Rvachev. "Method of R-functions in boundary-value problems". In: *Soviet Applied Mechanics* 11.4 (Apr. 1975), pp. 345–354. DOI: 10.1007/BF00882900.

[86] V. L. Rvachev et al. "Transfinite interpolation over implicitly defined sets". In: *Computer Aided Geometric Design* 18.3 (Apr. 2001), pp. 195–220. DOI: 10.1016/S0167-8396(01)00015-2.

[87] C. Birdsall. "Particle-in-cell charged-particle simulations, plus Monte Carlo collisions with neutral atoms, PIC-MCC". In: *IEEE Transactions on Plasma Science* 19.2 (Apr. 1991). Conference Name: IEEE Transactions on Plasma Science, pp. 65–85. DOI: 10.1109/27.106800.

[88] S. F. Biagi. *Fortran program, MAGBOLTZ v8.9*. lxcat.net. June 2021.

[89] J. F. J. Janssen et al. "Evaluation of angular scattering models for electron-neutral collisions in Monte Carlo simulations". In: *Plasma Sources Science and Technology* 25.5 (Sept. 2016). Publisher: IOP Publishing, p. 055026. DOI: 10.1088/0963-0252/25/5/055026.

[90] D. Hasselkamp et al., eds. *Particle Induced Electron Emission II*. Vol. 123. Springer Tracts in Modern Physics. Berlin, Heidelberg: Springer, 1992. DOI: 10.1007/BFb0038297.

[91]   S. Guinchard. *Numerical study of the influence of ion-induced electrons on the dynamics of electron clouds in gyrotron-like geometries*. Tech. rep. EPFL, Jan. 2023.

[92]   L. M. Kishinevsky. "Estimation of electron potential emission yield dependence on metal and ion parameters". In: *Radiation Effects* 19.1 (Jan. 1973), pp. 23–27. DOI: 10.1080/00337577308232211.

[93]   J. Schou. "Transport theory for kinetic emission of secondary electrons from solids". In: *Physical Review B* 22.5 (Sept. 1980). Publisher: American Physical Society, pp. 2141–2174. DOI: 10.1103/PhysRevB.22.2141.

[94]   J. F. Janni. "Energy loss, range, path length, time-of-flight, straggling, multiple scattering, and nuclear interaction probability: In Two Parts. Part 1. For 63 Compounds Part 2. For Elements $1 \leq Z \leq 92$". In: *Atomic Data and Nuclear Data Tables* 27.4 (July 1982), pp. 341–529. DOI: 10.1016/0092-640X(82)90005-5.

[95]   J. F. Janni. "Energy loss, range, path length, time-of-flight, straggling, multiple scattering, and nuclear interaction probability: In two parts. Part 1. For 63 compounds Part 2. For elements $1 \leq Z \leq 92$". In: *Atomic Data and Nuclear Data Tables* 27.2 (Mar. 1982), pp. 147–339. DOI: 10.1016/0092-640X(82)90004-3.

[96]   D. Hasselkamp, S. Hippler, and A. Scharmann. "Ion-induced secondary electron spectra from clean metal surfaces". In: *Nuclear Instruments and Methods in Physics Research Section B: Beam Interactions with Materials and Atoms* 18.1-6 (1987), pp. 561–565. DOI: 10.1016/S0168-583X(86)80088-X.

[97]   R. C. Davidson. "Equilibrium and stability of mirror-confined nonneutral E layers". In: *Physics of Fluids* 16.12 (1973), p. 2199. DOI: 10.1063/1.1694287.

[98]   *Jed cluster*. Lausanne, Switzerland. URL: https://www.epfl.ch/research/facilities/scitas/jed.

[99]   F. Romano et al. "The TRapped Electrons eXperiment (T-REX)". In: *2022 13th International Workshop on Non-Neutral Plasmas*. To be published. Milano. URL: https://drive.google.com/file/d/1v77t-8oKMTDmqLGU6fKkSpaZL_cYSYcs/view.

[100]   I. G. Pagonakis et al. "Magnetic field profile analysis for gyrotron experimental investigation". In: *Physics of Plasmas* 24.3 (Mar. 2017). Publisher: American Institute of Physics, p. 033102. DOI: 10.1063/1.4977460.

[101]   S. Mukherjee et al. "Hydrogen outgassing and permeation in stainless steel and its reduction for UHV applications". In: *Materials Today: Proceedings*. International Conference on Materials, Processing & Characterization 44 (Jan. 2021), pp. 968–974. DOI: 10.1016/j.matpr.2020.11.007.

[102]   J.-P. Hogge et al. "First Experimental Results from the European Union 2-MW Coaxial Cavity ITER Gyrotron Prototype". In: *Fusion Science and Technology* 55.2 (Feb. 2009), pp. 204–212. DOI: 10.13182/FST09-A4072.

[103]   R. H. Levy. "Diocotron Instability in a Cylindrical Geometry". In: *The Physics of Fluids* 8.7 (1965). Publisher: American Institute of PhysicsAIP, p. 1288. DOI: 10.1063/1.1761400.

[104] G. N. Kervalishvili, J. I. Javakhishvili, and N. A. Kervalishvili. "Diocotron instability in an annular sheath of a gas-discharge nonneutral electron plasma". In: *Physics Letters A* 296.6 (Apr. 2002), pp. 289–294. DOI: 10.1016/S0375-9601(02)00249-9.

[105] G. Rosenthal, G. Dimonte, and A. Y. Wong. "Stabilization of the diocotron instability in an annular plasma". In: *The Physics of Fluids* 30.10 (Oct. 1987). Publisher: American Institute of Physics, pp. 3257–3261. DOI: 10.1063/1.866501.

[106] S. Alberti et al. "Experimental study from linear to chaotic regimes on a terahertz-frequency gyrotron oscillator". In: *Physics of Plasmas* 19.12 (Dec. 2012), p. 123102. DOI: 10.1063/1.4769033.

[107] C. F. Driscoll and K. S. Fine. "Experiments on vortex dynamics in pure electron plasmas". In: *Physics of Fluids B: Plasma Physics* 2.6 (June 1990), pp. 1359–1366. DOI: 10.1063/1.859556.

[108] R. J. Briggs, J. D. Daugherty, and R. H. Levy. "Role of Landau Damping in Crossed-Field Electron Beams and Inviscid Shear Flow". In: *The Physics of Fluids* 13.2 (Feb. 1970). Publisher: American Institute of Physics, pp. 421–432. DOI: 10.1063/1.1692936.

[109] B. Piosczyk. "Compensation of the beam space charge and consequences for the design of a gyrotron". In: *15th International Conference on Infrared and Millimeter Waves*. Vol. 1514. SPIE, Dec. 1990, pp. 507–509. DOI: 10.1117/12.2301568.

[110] G. Dammertz et al. "Long-pulse operation of a 0.5 MW TE/sub 10.4/ gyrotron at 140 GHz". In: *IEEE Transactions on Plasma Science* 24.3 (June 1996). Conference Name: IEEE Transactions on Plasma Science, pp. 570–578. DOI: 10.1109/27.532939.

[111] I. G. Pagonakis et al. "Parameterization technique for the preliminary gun design of the EU 170GHz 1MW conventional cavity gyrotron for ITER". In: *2008 33rd International Conference on Infrared, Millimeter and Terahertz Waves*. ISSN: 2162-2035. Sept. 2008, pp. 1–2. DOI: 10.1109/ICIMW.2008.4665518.

[112] W. R. Smythe. *Smythe - Static and Dynamic Electricity*. McGraw-Hill Book Company, 1950.

Acknowledgements

Doing a PhD and writing a thesis is not an easy task, but a very rewarding one that helped me grow both academically and personally.

This work would not have been possible without the help of many people that supported me and motivated me along the way. For this, I would like to deeply thank my supervisors, both official: Joaquim and Jean-Philippe, and unofficial: Stefano. First, you have trusted me to do this work and have always challenged me to go deeper in the physics through your carefully chosen questions and suggestions. With you, I have learned the true meaning of curiosity and passion, and for that I am forever grateful. I have truly appreciated your open door policy and all the time you have taken to guide me through complex and sometimes more trivial concepts that were eluding me. I was also lucky enough to do my assistantship duties with you and I enjoyed our collaboration during the courses, as well as the opportunity to follow some of your lectures and learn from you. I hope one day to be able to live up to your example.

In addition to my three supervisors, I was lucky enough to be able to work with two wonderful post-docs, Francesco and Jérémy, who participated in our weekly meetings and prompted captivating discussions. You have allowed me to discover more of the experimental side of research, and it is a joy to see the experiment you have built come to life. I really look forward to seeing more of its results. On a personal level, I am very grateful to have been able to collaborate with such open and friendly human beings and to have shared fun activities with you outside the lab.

I would also like to thank all the Master students that collaborated with me, Marcio, Viktoriia, Salomon and Iris, for the successful and productive work you have performed. Your work was directly applicable to my research and has contributed to my thesis in a very concrete way. For that, I am truly grateful.

I also want to show my gratitude to the different services at SPC, who helped build and design T-REX and who maintain a reliable computer infrastructure which allowed me to run FENNECS simulations efficiently. Finally, I would like to thank the administration for the very efficient work and kind presence when I needed you. You were so effective that I almost never had to ask you for information, as my questions were answered before they could even arise.

Outside of SPC, I would particularly like to thank Antoine Cerfon and Ioannis Pagonakis for always being available to collaborate on zoom or in person. You were always open to discussing new results and sharing your knowledge. I always found your questions insightful, which helped me be more rigorous in my work and in my writing.

A thesis would not be possible without a support system, and I would like to thank all the other PhD students of the lab for the wonderful atmosphere and openness that exist at SPC and that motivated me to come to work and continue research when I was feeling stressed or down. I would like to particularly

169

Acknowledgements

thank the PPH277 officemates, both past and present: Arsène, Lorenzo, Sophie, Claudia, Curdin, Jésus, Filippo, Stefano, Frederico, Mack, Martim, Kenneth, Dahye, Hugo, Frederico, and Yuri. It was a joy to work alongside you and to chat with you during the coffee breaks, the apéros and in-between simulations.

I would also like to thank my close and distant family, who kept believing in me and were there during the easy and difficult times of my studies. I would like to thank you for your interest in my passions and for showing it during many of our discussions. You also helped me enjoy doing something else and remember that there can be other things in life than research.

Finally, I would like to deeply thank Eliane, my wife, who has always been there, during good and stressful times alike. You are my everyday support, my motivation, and you have never lost faith in me. I am deeply thankful for your presence, and your eagerness to learn about my work and to help me unpack my doubts and my more difficult questions or bugs during the thesis. You help me relax and think of something else when I am going crazy on a problem. Furthermore, you make me learn more about some of the challenges in our society and how I can help in my small corner of academia. I will be forever grateful for your support throughout my studies, for your patience during my long and twisty studying path, and for the fact that you always believe in me.

Lausanne, November 9, 2023   G. Le Bars

Guillaume Le Bars

Nationality: Swiss, French   **Date of birth:** 24th August 1990
Address: Av. de Préfaully 38, 1020 Renens, Switzerland

✉ guillaume.lebars@alumni.epfl.ch   in Guillaume Le Bars

Employment History

02-07 2018	🔖 **Internship at ABB research centre in Baden, Switzerland** (6 months) : *User friendly Plasma-Arc-Simulations* Development of a graphical user interface to improve the usability of an in-house switch-breaker simulation tool. Simulations of plasma arcs evolution in switch-breakers for R&D.
2011 – 2016	🔖 **Food sales employee (20%)**, COOP, Lausanne Client advising and inventory management.
06-12 2010	🔖 **Sergeant for the Swiss Military**, Armée Suisse, Frauenfeld (all days served) Training and management of a group of 10-20 soldiers.

Education

2019 – 2023	🔖 **Ph.D., SPC EPFL** in Plasma Physics. Thesis title: *Modelling of nonneutral plasmas trapped by electric and magnetic fields relevant to gyrotron electron guns.* Teaching assistant for a mechanics and an introduction to plasma physics courses. Supervision of three master level student projects.
2011 – 2019	🔖 **B.Sc. and M.Sc. Applied Physics, EPFL** specialization in Plasma Physics. Master thesis at the Swiss Plasma Center: *Velocity spread effects on backward-wave interaction in gyrotron beam-ducts.* Semester projects at the Swiss Plasma Center: *Numerical studies of parasitic oscillations in gyrotron beam-ducts.*

Research Publications

Journal Articles

1. G. Le Bars, S. Guinchard, P. Kaminski, *et al.*, "Fennecs: A novel particle-in-cell code for simulating the formation of magnetized non-neutral plasmas trapped by electrodes of complex geometries," *Computer Physics Communications*, Aug. 2023, Submitted.

2. G. Le Bars, J. Loizu, J.-P. Hogge, *et al.*, "First self-consistent simulations of trapped electron clouds in a gyrotron gun and comparison with experiments," *Physics of Plasmas*, vol. 30, no. 3, p. 030 702, Mar. 2023, Publisher: American Institute of Physics, ISSN: 1070-664X. 🔗 DOI: 10.1063/5.0136340.

3. G. Le Bars, J.-P. Hogge, J. Loizu, S. Alberti, F. Romano, and A. Cerfon, "Self-consistent formation and steady-state characterization of trapped high-energy electron clouds in the presence of a neutral gas background," *Physics of Plasmas*, vol. 29, no. 8, p. 082 105, Aug. 2022, Publisher: American Institute of Physics, ISSN: 1070-664X. 🔗 DOI: 10.1063/5.0098567.

4. J. Genoud, S. Alberti, T. M. Tran, *et al.*, "Parasitic Oscillations in Smooth-Wall Circular Symmetric Gyrotron Beam Ducts," *Journal of Infrared, Millimeter, and Terahertz Waves*, vol. 40, no. 2, pp. 131–149, Feb. 2019, ISSN: 1866-6906. 🔗 DOI: 10.1007/s10762-018-0548-5.

Conferences

1   G. Le Bars, S. Guinchard, J.-P. Hogge, *et al.*, "FENNECS: A flexible code to simulate non-neutral plasmas trapped in penning-like annular potential wells," in *49th EPS Conference on Plasma Physics, EPS 2023*, Publisher: European Physical Society (EPS), Bordeaux, France, 2023.

2   G. Le Bars, J.-P. Hogge, J. Loizu, S. Alberti, F. Romano, and A. Cerfon, "PIC simulations and reduced model of confined ionising electron clouds relevant to gyrotrons," in *48th EPS Conference on Plasma Physics, EPS 2022*, Publisher: European Physical Society (EPS), Online, 2022. 🔗 URL: `https://indico.fusenet.eu/event/28/contributions/338/attachments/352/1042/G_Le_Bars_eps2022_paper.pdf`.

3   G. Le Bars, J.-P. Hogge, J. Loizu, *et al.*, "Modelling of high-density electron clouds in penning-like annular potential wells with large imposed flows and electron-neutral collisions," in *13th International Workshop on Non-Neutral Plasmas 2022*, Milano, Italy, 2022.

4   G. Le Bars, J.-P. Hogge, J. Loizu, S. Alberti, and A. Cerfon, "Modelling of trapped high density electron clouds relevant to gyrotrons," in *47th EPS Conference on Plasma Physics, EPS 2021*, Publisher: European Physical Society (EPS), Online, 2021, pp. 761–764. 🔗 URL: `http://ocs.ciemat.es/EPS2021PAP/pdf/P3.4002.pdf`.

5   G. Le Bars, J.-P. Hogge, J. Loizu, and S. Alberti, "Modelling of trapped high density electron clouds relevant to gyrotrons," in *Theory Of Fusion Plasmas Joint Varenna - Lausanne International Workshop*, Online, 2020.

Skills

Languages	▮	French (native), English (C1), German (comprehension B1, production A2).
Coding	▮	Fortran, Python, Matlab, C, C++, LaTeX, OpenMP, MPI, CMAKE, Bash, HPC stack
Web Dev	▮	HTML, CSS, JavaScript, Apache Web Server, Flask framework.
Misc.	▮	Teaching, training, LaTeX typesetting and publishing, Office suite, Sysops of a personal Debian server.

Miscellaneous Experience

Awards and Achievements

2021   ▮   **School of Basic Sciences Dean's Award for excellence in Teaching** for the assistantship given during the General Physics course for first year students.

172